

Dissertation zur Erlangung des Doktorgrades  
der Fakultät für Chemie und Pharmazie  
der Ludwig-Maximilians-Universität München

Conformational changes of proteins involved in the  
chaperone mediated protein folding cycle  
measured by spFRET

Daniela Wengler

aus

Bielefeld, Deutschland

2016



## Erklärung

Diese Dissertation wurde im Sinne von §7 der Promotionsordnung vom 28. November 2011 von Herrn Prof. Don C. Lamb, PhD betreut.

## Eidesstattliche Versicherung

Diese Dissertation wurde eigenständig und ohne unerlaubte Hilfe erarbeitet.

München, den 23. August 2016

Daniela Wengler

Dissertation eingereicht am 25. August 2016

1. Gutachter Prof. Don C. Lamb, PhD

2. Gutachter Prof. Dr. Christoph Bräuchle

Mündliche Prüfung am 30. September 2016



# Contents

<b>Abstract</b>	<b>1</b>
<b>1 Introduction</b>	<b>5</b>
<b>2 Fluorescence</b>	<b>7</b>
2.1 Light . . . . .	7
2.2 Absorption and emission . . . . .	7
2.3 Quantum yield and fluorescence lifetime . . . . .	10
2.4 Anisotropy . . . . .	10
2.5 Förster Resonance Energy Transfer - FRET . . . . .	11
2.6 Single-molecule fluorescence . . . . .	12
<b>3 Fluorescence microscopy</b>	<b>15</b>
3.1 Optical resolution . . . . .	15
3.2 Confocal microscopy . . . . .	16
3.2.1 Fluorescence correlation spectroscopy - FCS . . . . .	17
3.3 SpFRET using MFD-PIE . . . . .	24
3.3.1 Pulsed interleaved excitation - PIE . . . . .	24
3.3.2 Multiparameter fluorescence detection - MFD . . . . .	25
3.3.3 Data analysis . . . . .	26
3.4 Wide field microscopy . . . . .	35
3.4.1 Total internal reflection fluorescence microscopy - TIRF . . . . .	36
3.5 SpFRET using TIRF microscopy . . . . .	37
3.5.1 Prism type TIRF . . . . .	38
3.5.2 Surface preparation and immobilization . . . . .	39
3.5.3 Encapsulation by vesicles . . . . .	39
3.5.4 Data analysis . . . . .	40
3.5.5 Hidden Markov Model - HMM . . . . .	43
<b>4 Protein folding</b>	<b>45</b>
4.1 Protein . . . . .	45
4.2 Molecular chaperones . . . . .	46
4.2.1 Hsp70 . . . . .	47
4.2.2 Hsp90 . . . . .	48
4.2.3 GroEL with the co-chaperone GroES . . . . .	49
<b>5 BiP's interaction with BAP</b>	<b>53</b>
5.1 Introduction . . . . .	53
5.2 Sample Preparation . . . . .	54
5.3 Nucleotide dependent chaperone cycle of BiP . . . . .	56

5.4	BAP influences the nucleotide dependent chaperone cycle of BiP . . . . .	59
5.5	ATP analogues do not behave like ATP in the presence of BAP . . . . .	65
5.6	The N-terminal domain of BAP interacts with the lid . . . . .	68
5.7	The function of BAP as a nucleotide exchange factor . . . . .	73
5.8	BAP and C <sub>H</sub> 1 compete for binding to BiP with each other . . . . .	76
5.9	Discussion and Outlook . . . . .	80
<b>6</b>	<b>Sti1 mediates the interaction of Hsp70 and Hsp90</b>	<b>83</b>
6.1	Introduction . . . . .	83
6.2	Sample Preparation . . . . .	84
6.3	TPR2A and TPR2B form a rigid module . . . . .	85
6.4	End-to-end distances are too large for detecting conformational changes . . . . .	86
6.5	Linker length is independent of bound Hsps . . . . .	88
6.6	Distance changes between the two modules of Sti1 . . . . .	89
6.7	Binding of Hsp70 to multiple domains . . . . .	92
6.8	TIRF analysis of the dynamic behavior of Sti1 . . . . .	93
6.9	Discussion and Outlook . . . . .	99
<b>7</b>	<b>Microfluidic measurements of the substrate protein MBP</b>	<b>103</b>
7.1	Microfluidics . . . . .	103
7.1.1	Introduction . . . . .	103
7.1.2	Design of the microfluidic device . . . . .	104
7.1.3	Manufacturing of the devices . . . . .	105
7.1.4	Microfluidic flow control system . . . . .	112
7.1.5	Calibration of the flow velocity . . . . .	114
7.2	Folding kinetics of DM-MBP . . . . .	115
7.2.1	Introduction . . . . .	115
7.2.2	Sample Preparation . . . . .	116
7.2.3	Spontaneous refolding of DM-MBP . . . . .	117
7.2.4	GroEL mediated conformational changes of DM-MBP . . . . .	121
7.2.5	GroEL and GroES mediated refolding of DM-MBP . . . . .	125
7.3	Discussion and Outlook . . . . .	128
<b>8</b>	<b>Summary</b>	<b>131</b>
	<b>Bibliography</b>	<b>V</b>
	<b>Acknowledgments</b>	<b>XIII</b>

# List of Figures

2.1	Franck-Condon-Principle of transitions . . . . .	8
2.2	Jablonski diagram . . . . .	9
2.3	Stokes shift . . . . .	9
2.4	A simplified Jablonski diagram for FRET . . . . .	11
3.1	Intensity distribution of an Airy disk . . . . .	16
3.2	Schematic of a confocal microscopy setup . . . . .	17
3.3	Jablonski Diagram with rates . . . . .	21
3.4	Correlation function of freely diffusing Cy5 . . . . .	22
3.5	Correlation function of ATTO 532 with external applied flow . . . . .	23
3.6	MFD-PIE setup . . . . .	25
3.7	Microtime histogram of a MFD-PIE experiment . . . . .	26
3.8	Intensity trace of a burst measurement. . . . .	27
3.9	Stoichiometry versus FRET efficiency scheme . . . . .	28
3.10	Relation between species and intensity weighted lifetime . . . . .	30
3.11	FRET efficiency versus the donor lifetime . . . . .	31
3.12	PDA fit of measured data . . . . .	35
3.13	Schematic of a wide field setup . . . . .	35
3.14	Various TIRF modalities . . . . .	37
3.15	Prism type TIRF setup . . . . .	38
3.16	Prism preparation and immobilization . . . . .	39
3.17	Molecule encapsulated in a vesicle . . . . .	40
3.18	Time traces of non-dynamic molecules . . . . .	41
3.19	Transition density plot . . . . .	44
4.1	The energy landscape of protein folding . . . . .	45
4.2	Crystal structure of Hsp70 in the ER . . . . .	47
4.3	Crystal structure of Hsp90 . . . . .	49
4.4	Crystal structure of the GroEL/GroES complex . . . . .	50
4.5	Nucleotide cycle of the GroEL/GroES complex . . . . .	51
5.1	Known crystal structure of BiP in the presence of ATP . . . . .	53
5.2	SpFRET analysis of BiP. . . . .	57
5.3	Model for the nucleotide dependent chaperone cycle . . . . .	59
5.4	Known crystal structure of a BAP homolog bound to the NBD of ScBiP . . . . .	60
5.5	Analytical ultracentrifugation measurements of BiP with BAP . . . . .	60
5.6	SpFRET analysis of BiP in the presence of BAP . . . . .	61
5.7	Interaction of BAP with BiP when ATP is bound . . . . .	62
5.8	Model for the nucleotide dependent chaperone cycle in the presence of BAP . . . . .	64
5.9	Nucleotide analogues for ATP . . . . .	65

5.10	SpFRET analysis of BiP in the presence of BAP and nucleotide analogues . . .	66
5.11	SpFRET analysis of BiP-167-519 labeled with ATTO 647 or Alexa Fluor 647	68
5.12	SpFRET analysis of BiP in the presence of BAP- $\Delta$ N . . . . .	69
5.13	SpFRET analysis of BiP- $\Delta$ lid with BAP and BAP- $\Delta$ N. . . . .	73
5.14	Calculation of the $K_d$ of ATP in the presence and absence of BAP by using spFRET . . . . .	74
5.15	Conformational effect of pyrophosphate for BiP with ADP in the presence and absence of BAP . . . . .	75
5.16	SpFRET analysis of BiP with BAP and $C_{H1}$ . . . . .	76
5.17	Analytical ultracentrifugation measurements of BiP with BAP and $C_{H1}$ . . .	80
5.18	Model for the BAP-regulated chaperone cycle of BiP . . . . .	82
6.1	Different tested labeling positions of Sti1 . . . . .	85
6.2	SpFRET analysis of the Sti1 mutant G309C-S523C . . . . .	85
6.3	SpFRET analysis of Sti1 mutants with large dye distances . . . . .	87
6.4	SpFRET analysis of the Sti1 mutant G193C-S258C . . . . .	88
6.5	SpFRET analysis of the Sti1 mutant G193C-G309C . . . . .	90
6.6	FRET efficiency versus lifetime plots of the Sti1 mutant G193C-G309C . . .	91
6.7	SpFRET analysis of the Sti1 mutant G193C-G309C N39A and G193C-G309C N435A . . . . .	92
6.8	Comparison of the spFRET measurement of the Sti1 mutant G193C-G309C free in solution and encapsulated in vesicles . . . . .	93
6.9	Representative traces from spFRET TIRF experiments of Sti1 . . . . .	95
6.10	Transition density plots from the spFRET TIRF experiments of the Sti1 mu- tant G193C-G309C . . . . .	97
6.11	Model for the Hsp-mediated cycle of Sti1 . . . . .	100
7.1	Design of the microfluidic device . . . . .	104
7.2	Dose test for the maskaligner . . . . .	107
7.3	Light microscopy images of the dose test sample . . . . .	107
7.4	SEM images of the dose test pattern . . . . .	109
7.5	Device positions on the wafer . . . . .	110
7.6	Microfluidic flow control system . . . . .	113
7.7	Device connected with tubes . . . . .	113
7.8	FCS curves with different flow rates . . . . .	114
7.9	Calibration curve for the flow rate . . . . .	115
7.10	Crystal structure of MBP . . . . .	116
7.11	DM-MBP measured in different GuHCl concentrations in equilibrium . . . .	117
7.12	Spontaneous folding of DM-MBP . . . . .	118
7.13	Kinetic of the spontaneous refolding of DM-MBP . . . . .	121
7.14	DM-MBP measured in equilibrium in the presence of GroEL . . . . .	121
7.15	Timescale of the refolding kinetics of DM-MBP mediated by GroEL . . . . .	123
7.16	FCS curves of DM-MBP mixed with GroEL . . . . .	124
7.17	Kinetic of the GroEL mediated refolding of DM-MBP . . . . .	124
7.18	DM-MBP measured in equilibrium in the presence of GroEL, GroES and ATP	125
7.19	Timescale of the refolding kinetics of DM-MBP mediated by GroEL, GroES and ATP . . . . .	127
7.20	Kinetic of the GroEL, GroES and ATP mediated refolding of DM-MBP . . .	128

# Abstract

Heat shock proteins, like Hsp70, Hsp90 and Hsp60, act as chaperones. This class of proteins assist nascent unfolded proteins in reaching their final functional structure and conformation in the appropriate location within the cell. For the development of treatment for various disorders such as Alzheimer or Parkinson's disease, it is essential to understand the underlying mechanisms of chaperone-assisted protein folding. Here, we investigated multiple chaperone systems according to their conformation, which can be one of the first steps in understanding the functional mechanisms. Therefore, we studied different chaperone systems related to their conformation upon the addition of interaction partners or with respect to the structural changes they introduce in a substrate protein. To monitor distance changes on a nanometer scale, the proteins were labeled with two dyes, the donor and acceptor dye. By exciting the donor, parts of the energy are transferred to the acceptor. This process is called Förster Resonance Energy Transfer (FRET) and is distance dependent. Furthermore, we chose single-pair FRET (spFRET) instead of ensemble due to the fact that multiple conformations of a protein can be monitored, which has been shown to be impossible with ensemble measurements. Two different types of experiments were performed. On the one side, solution based experiments using a Multiparameter Fluorescence Detection (MFD) setup combined with Pulsed Interleaved Excitation (PIE) were performed to detect snapshots of single proteins. On the other side, total internal reflection fluorescence (TIRF) microscopy was used to study the dynamics of a single protein over time.

The Hsp70 in the endoplasmic reticulum (ER) is called BiP. It consists of two domains that are connected by a short linker, the nucleotide binding domain (NBD) and the substrate binding domain (SBD). The SBD contains a flexible, alpha helical lid that can open or close the substrate binding pocket of the SBD. When a client protein enters the ER, its charged regions are initially protected by BiP to avoid non-specific interactions. One of the regulating factors in this process is the BiP associated protein, BAP, a nucleotide exchange factor (NEF) of BiP. BAP controls the binding and release of the nascent proteins from BiP by accelerating the ATP/ADP exchange. To analyze the conformational changes BAP introduces in BiP, BiP was fluorescently labeled with a donor and acceptor dye. Three different mutants were used. The first one is the interdomain-mutant, which gives information about the distance between NBD and SBD. The second mutant is the lid-mutant, which monitors the lid opening and closing, and the last mutant is the combined-mutant, which has labels on the NBD and the lid to observe the distance between NBD and the C-terminal end of the lid. The results show that BAP can stably bind to BiP in the ADP and the nucleotide free conformation, but only transient interaction were detected in the presence of ATP. This transient interaction is mediated by the N-terminal domain of BAP. Together with the lid of BiP, this domain of BAP was identified to keep the NBD and SBD of BiP apart from each other. Furthermore, it was found that BAP speeds up the nucleotide cycle and, thus, act as a NEF. From our results, the idea arises that BAP mediates an open nucleotide binding pocket, which promotes the release of the nucleotide. In addition, BAP was identified to compete with a nature substrate and is kicked out of the complex when the substrate binds or the other way around. Thus,

our results clarify the interaction of BAP with BiP and show that BAP can mediate the nucleotide cycle of BiP.

In another set of experiments, we analyzed how a substrate, which has been caught by Hsp70, is handed over to Hsp90, the next interaction partner in the folding machinery. The co-chaperone, which is known to act as a kind of scaffold in this process, is called Sti1. Sti1 was labeled with a FRET pair to study the conformational changes and dynamics introduced by binding of Hsp70 and Hsp90. Sti1 consists of two modules. The first one has an aspartate and proline rich (DP) domain and a tetratricopeptide repeats (TPR) domain. The TPR domain can interact with Hsp70. This module is connected by a flexible linker with the second module, which consists of a TPR2A, TPR2B and a DP2 domain. Hsp90 can interact with the TPR2A domain and Hsp70 has a second interaction domain, the TPR2B. Hsp70 was found to bind preferably to the TPR1 domain, when Hsp90 is bound to Sti1. In addition, it was detected by spFRET that Sti1 is already dynamic on its own but, upon binding of Hsp70, Hsp90 or both, the number of dynamic molecules increases. These dynamics are important for bringing the two modules closer together and, thus, mediate the transfer of the substrate from Hsp70 to Hsp90. Afterwards, Hsp70 is transferred back to the TPR1 binding domain and Sti1 opens up. Due to the low affinity of Hsp70 to the TPR1 binding domain, Hsp70 is released and the cycle can start over again. Thus, Sti1 has the important role of binding to Hsp70 and Hsp90 and dynamically connects the two chaperones as a scaffold and assists in substrate transfer.

Another important chaperone is the Hsp60. In bacteria, it is called GroEL and consists of two identical rings, which stick together. Each of them form a cavity. Inside the cavity, substrate proteins can be trapped. Binding of ATP to GroEL mediates the binding of GroES, a co-chaperone for GroEL and the lid for the cavity. Inside the cage, the substrate protein can fold to its final conformation. To study the effect of GroEL on a substrate, the maltose binding protein (MBP) was chosen. From a previous investigation it is known that a double mutant of MBP (DM-MBP) is not a native substrate for GroEL. It can fold by its own. However, the interaction of GroEL and GroES with DM-MBP makes the folding kinetics faster. To monitor the changes on the timescale of folding, the N-terminal domain of DM-MBP was labeled with ATTO 532 and Alexa Fluor 647 and a home-built microfluidic add-on for the MFD-PIE setup was implemented. Microfluidic provides the possibility to mix different buffers or interaction partners directly on top of the microscope and, thus, makes it possible to measure the conformational changes within a time window of 33 ms to 1.07 s. DM-MBP was found to fold spontaneously on this timescale to an intermediate state, but not to the final conformation. The timing of this folding process was found to depend only on the chaotropic agent concentration, in our case GuHCl, but not on the concentration of other salts. By adding GroEL, it was found that DM-MBP gets partly unfolded on a timescale of 343 ms. The other fraction of molecules shows only slight conformational changes, which are related to a more compact conformation and occurs on a timescale between 343 ms and 512 ms. Furthermore, the addition of GroEL and GroES speeds up the folding process. From the unfolded to the intermediate state, the conformational changes gets 5 to 6 times faster. Afterwards, the DM-MBP gets more and more compact and after 1.07 s a fraction of molecules reach their final folded conformation. Taken together, the timescales of DM-MBP folding that was monitored with microfluidics depends on the GuHCl concentration. The addition of GroEL alone unfolds DM-MBP within the first 512 ms of interaction but GroEL together with GroES speeds up the folding kinetics.

In summary, it was possible to study different chaperone systems with respect to their conformational changes by using spFRET. Our spFRET results reveal new insights that could

not be detected before by ensemble methods. Furthermore, MFD-PIE and TIRF microscopy offers the opportunity to detect conformations under equilibrium conditions. Microfluidic widen up the range of questions that can be answered by these methods. It makes it possible to mix different components of the sample direct ontop of the microscope and, thus, enables to detect fast kinetics and conformational changes on short time scales.



# 1 Introduction

Misfolded proteins can cause various disorders such as Alzheimer or Parkinson's diseases. To figure out ways to cure the patients with diseases connected to misfolded proteins, the first step in this process is to understand the folding pathway of proteins. A polypeptide chain, which is a string of amino acids, has to be brought to a structure consisting of  $\alpha$ -helices and  $\beta$ -sheets. These secondary structures have to be further arranged into complex modules. For most proteins, this is a very time consuming process and the overall folding would, according to the Levinthal's paradox, take longer than the cycle of the universe. Therefore, the polypeptide chain, here also called the substrate, needs assistance by chaperones. Chaperones are defined as 'any protein that interacts with, stabilizes or helps another protein to acquire its functionally conformation, without being present in its final structure' [Hartl et al., 2011]. Thus, protein folding is one of the most complex systems within a cell and differs from organism to organism and depends on the location in the cell. However, different chaperones act in different ways to assist the proper folding of an unfolded or misfolded protein. Some of the chaperones act together and the substrate is handed over from one chaperone to the other, when they are done. Others work on its own and only need the assistance of a co-chaperone. In this work, different chaperone systems were studied under the aspect of conformational changes, to understand the mechanism behind an interaction. The tool used for monitoring the changes in conformation in vitro was single-pair Förster Resonance Energy Transfer (spFRET). SpFRET studies, compared to ensemble measurements, have the big advantage of being able to monitor multiple conformations of a protein in a single measurement. Dynamics between different conformations can be detected, which is also not possible in ensemble measurements.

SpFRET measured on a microscope setup with a combination of 'pulsed interleaved excitation' (PIE) and 'multiparameter fluorescence detection' (MFD) makes it possible to detect at the same time information about the FRET efficiency, the stoichiometry, the lifetime of the dyes and the anisotropy. Changes in all these parameters can be determined due to the addition of an interaction partner or changes in the buffer conditions. However, the measurements only show a snapshot of the protein diffusing through the focal volume. One alternative is to immobilize the protein on the surface and detect conformational changes over time. This technique is based on a total internal reflection fluorescence (TIRF) microscope. To immobilize the protein on the surface, the protein has to bind to a linkage, which is bound to the surface. This induces very often unspecific interactions between the surface and the protein. The second approach used commonly in our lab is to encapsulated the protein in vesicles, but not all proteins stay free in the vesicles. Some proteins stick to the lipids and change their conformation or function due to this unwanted interaction. Therefore, every protein has to be tested before it can be studied on the TIRF microscope.

We studied different chaperone systems using these methods. The first chaperone system is the heat shock protein 70 (Hsp70) in the human endoplasmic reticulum (ER). This protein is called BiP and consists of two domains, the nucleotide binding domain (NBD) and the substrate binding domain (SBD) with a lid that can open and close the binding pocket. Three

different double-labeled FRET mutants were generated. By studying the FRET efficiency, conformational changes in all three mutants upon interaction with a nucleotide or another interaction partner were monitored. One of these interaction partners is a nucleotide exchange factor (NEF), the BiP Associated Protein (BAP). BAP is responsible for controlling a wide range of sometimes contradictory functions like protein folding and degradation. Here, we studied how the interaction of BAP influences the nucleotide cycle of BiP and how the addition of a substrate interferes with the interaction. Furthermore, we investigated how BAP speeds up the nucleotide cycle and, thus, acts as a NEF.

Related to the question of how BiP function, it is of interest how the Hsp70, which is known to catch unfolded proteins, transfers the substrate to the next interaction partner in the protein folding machinery. The substrate is handed over with the help of a co-chaperone to a Hsp90 molecule. The co-chaperone that can bind Hsp70 and Hsp90 is called Sti1 in yeast or Hop in mammals. To study the interaction of Hsp70, Hsp90 and Sti1, yeast proteins were used. Sti1 consists of five domains in two modules. The first module has a binding domain for Hsp70 and is connected by a flexible linker with the second module. This module has a binding domain for Hsp90 and an additional one for Hsp70. Sti1 was labeled at different positions with a donor-acceptor-pair. Using spFRET in combination with MFD-PIE and TIRF microscopy, we studied the conformation and the related dynamics of Sti1 and the process of bringing the Hsp70 and Hsp90 together.

Another chaperone system is the GroEL-GroES complex in bacteria, which interacts with Hsp70 instead of the Hsp90 and assists protein folding. GroEL has a ring-like structure and can interact with its co-chaperone GroES in an ATP-dependent manner. Binding of GroES introduces conformational twisting in GroEL and closes the cavity of GroEL wherein a substrate can be trapped. To study the effect of GroEL on a substrate protein, a double mutant maltose binding protein (DM-MBP) was used. It was labeled at two positions to monitor conformational changes in the N-terminal domain of MBP. To address the effect of different concentrations of GuHCl on the timescale of protein folding, a microfluidic approach was added to the used MFD-PIE setup. Different components can be mixed or diluted directly in the device on top of the microscope. The time range between mixing and measuring that can be resolved lies between 33 ms and 1.07 s. The folding kinetics of DM-MBP depending on the GuHCl and the concentration of other salts in the buffer were analyzed and the effect on the conformation and the corresponding timescale by adding GroEL or GroEL, GroES and ATP to MBP was monitored.

In summary, different chaperone systems were studied to determine the effect of interactions with a nucleotide exchange factor or a co-chaperone. Furthermore, the timescale of conformational changes was analyzed with the help of a microfluidic approach in combination with a MFD-PIE setup. Thus, these studies reveal significance new insights in the function of chaperones and their indispensable assistance in protein folding and, therefore, help to clarify one of the most fundamental processes in cells.

## 2 Fluorescence

### 2.1 Light

Light can be, on the one hand, an electromagnetic wave, which travels, without being refracted or reflected, in a straight line from the source. On the other hand, light is like a particle, the so called photon. The energy of one photon can be described by

$$E = h\nu = h\frac{c}{\lambda} \quad (2.1)$$

where  $h$  is the Planck constant,  $\nu$  the frequency,  $c$  the velocity of the light and  $\lambda$  the wavelength of the photon. Consequently, the energy is inversely proportional to the wavelength and quantized with distinct energies.

### 2.2 Absorption and emission

The energy of light can be transferred to atoms and molecules. This process is called absorption and can be easily explained by the Bohr model. According to the Bohr model, electrons travel in circular orbits around the nucleus. In the so called ground state, the electron is in the lowest energy level. From there, an electron can be excited from the ground state to a higher energetic state. It is important that the photon absorbed by the electron has a higher energy than the energetic distance between the two levels.

For molecules the principle stays the same. In the simplest case, the molecule consists of two atoms, but the principle is the same for molecules consisting of more atoms. The orbit of an electron in this molecule is assumed to be one big combined one. The lowest energy state is again called the ground state or the highest occupied molecular orbital (HOMO). From there, a photon can excite one electron to the excited or lowest unoccupied molecular orbital (LUMO) or to higher order states. Each of the states has different energies, because the nuclei can rotate around each other or vibrate, so called rotational or vibrational states, respectively.

To calculate in which of the rotational and vibrational states the electron will be excited, the Frank-Condon-Principle can be used [Franck and Dymond, 1926], [Condon, 1928]. According to the Frank-Condon-Principle, the distance between the two nuclei does not change during the time, the electron needs for changing between HOMO and LUMO. The explanation for this is given by the Born-Oppenheimer approximation [Born and Oppenheimer, 1927], which states that the electron is much faster by interchanging the state than the nuclei could move. This is due to the relative size of the nucleus and the electron. The nucleus is much larger and, therefore, it has a bigger inertia compared to the electron. As a consequence, the movement of the nuclei can be separated from the movement of the electron.

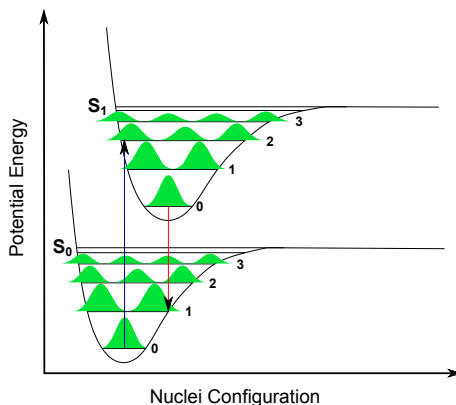


Figure 2.1: Franck-Condon-Principle of transitions. The probability density of the first two singlet states  $S_0$  and  $S_1$  is shown (green rises). Each state is split up into vibrational and rotational states, shown exemplary for three excited states. Transitions happen between wave functions with the highest overlap, i.e. vertically between the vibrational and rotational ground state and an excited vibrational and rotational state (blue arrow). By rotation and vibration the molecule relax to the lowest vibrational and rotational state in the excited state. From there the emission happens again between wave functions with the highest overlap to an excited vibrational and rotational ground state (red arrow).

Figure 2.1 shows the transition of an electron between the singlet ground state ( $S_0$ ) and the second vibrational and rotational state of the first excited singlet state ( $S_1$ ). The probability distribution of the vibrational and rotational states is given by the square of the absolute value of the wave function in the state and is represented by the green rise. The probability of a transition gets higher, when the overlap between the wave functions increases. If the reached state is close to the originally nucleus coordinates, the probability for a transition is maximized. The shift of the excited state potentials to higher nuclei coordinates is given by a slightly larger nucleus distance.

By exciting an electron from the  $S_0$  ground state to one of the singlet excited states ( $S_1, S_2, \dots$ ), the molecule absorbs the energy of the photon (Figure 2.2, green arrow). This process occurs in the time range of about  $10^{-15}$  s [Lakowicz, 2006]. To release this energy, there are different ways. We can distinguish between radiative and non-radiative transitions. In the case of non-radiative transitions, we can additionally differentiate between internal conversion and intersystem crossing. When transforming the energy into vibrations and rotations, energy is given to the environment. This process is called internal conversion (Figure 2.2, dark blue arrows) and the transition happens on a timescale of  $10^{-12}$  s or less [Lakowicz, 2006]. In most cases, the molecule converts by internal conversion parts of energy, that it relaxes to the lowest vibrational state of the  $S_1$  state. This relaxation is a reason for Kasha's rule, which says that all energetic transitions start from the lowest vibrational state in one state.

The spin of the electron does not change during the whole process of absorption and emission, therefore, it is antiparallel to the electron in the  $S_0$  state and a transition back from the  $S_1$  state to the  $S_0$  state is allowed. This transition is called fluorescence (Figure 2.2, orange arrows) and is a radiative transition, i.e. a photon is emitted. By comparing the fluorescence spectra with the excitation spectra, a mirrored spectra is detected. The explanation is given by Kasha's rule, which says that the energetic distance between the different vibrational states is the same for the different electronic states (Figure 2.3).

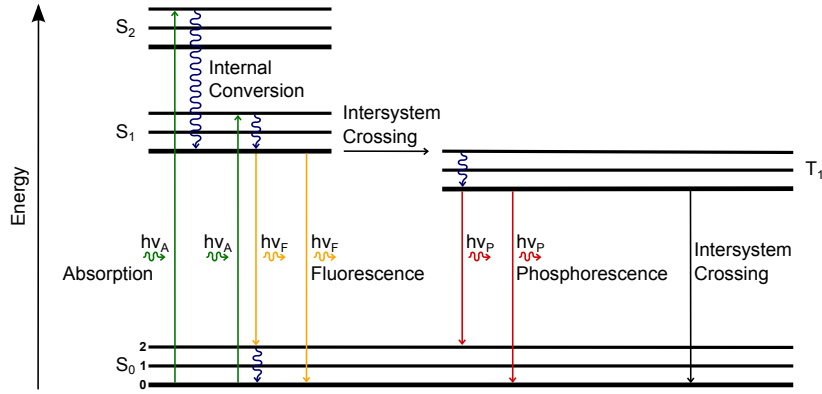


Figure 2.2: Jablonski diagram.  $S_{0/1/2}$  are the energetic states of the singlet system (ground and first and second excited state).  $T_1$  describes the first energetically excited state of the triplet. The absorption of a photon has the energy  $h\nu_A$  (green arrow). By internal conversion the electron can convert to the lowest vibrational and rotational state (dark blue arrow). Transitions between singlet and triplet state are called intersystem crossing (black arrow). The emission of a photon can have the energy  $h\nu_F$  for fluorescence (orange arrow) or  $h\nu_P$  for phosphorescence (red arrow).

The typical fluorescence lifetime is on the order of  $10^{-8}$  s. Thereby, the energy of the fluorescence photon has to be smaller or equal to the energy of the excitation photon due to the energy conversion. By using Equation (2.1), we get that the wavelength of this fluorescence photon is in the most cases larger or equal than the wavelength of the exciting photon. This wavelength shift is called Stokes shift (Figure 2.3).

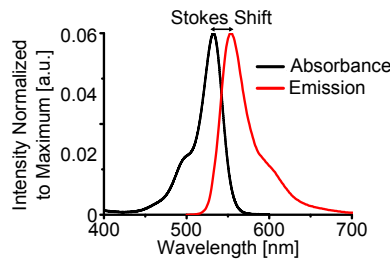


Figure 2.3: Stokes shift. The shift between the maximum of the absorption spectra (black line) and the maximum of the emission spectra (red line) is called the Stokes shift. Here, the spectra of ATTO 532 is shown. Spectra from [ATTO-TEC GmbH, 2016]

An additional radiative transition is phosphorescence. In this case, the electron changes from the first excited triplet state ( $T_1$ ) to the  $S_0$  state by intersystem crossing. For this transition, the electron has to get from the  $S_1$  state to the  $T_1$  state, and, therefore, the electron has to flip its spin, which is then parallel to the one in the singlet ground state. According to the Pauli exclusion principle, this transition is forbidden and the total spin of the system changes. In quantum mechanics, the probability for this transition is quite low and, therefore, it takes longer on average to reach the triplet state. To reach  $S_0$ , the spin has to flip a second time. This transition is either due to a radiative, i.e. phosphorescence, or a non radiative process,

i.e. intersystem crossing. Intersystem crossing and other radiationless pathways compete very successful with phosphorescence and, therefore, phosphorescence (Figure 2.2, red arrows) is usually only seen at low temperature or in high viscous media [Sauer et al., 2011]. Because the spin has to flip two times and the probability for this flipping is very low, phosphorescence takes much longer than fluorescence. The whole absorption and emission cycle is shown in the Jablonski Diagram (Figure 2.2) [Jablonski, 1933], [Jablonski, 1935].

## 2.3 Quantum yield and fluorescence lifetime

A fluorophore has two important attributes, the quantum yield,  $\Phi$ , and the fluorescence lifetime,  $\tau$ .

An electron, which is in an excited state, can be de-excite in different ways. We can distinguish between radiative and nonradiative relaxations. As we are only interested in the fluorescence, the phosphorescence is declared as a nonradiative process. The fraction of emitted to absorbed photons is called quantum yield,  $\Phi$ , and can be expressed in terms of the de-excitation rate  $k_{nr}$ .  $k_r$  is the rate of the intrinsic fluorescence.

$$\Phi = \frac{k_r}{k_r + k_{nr}} \quad (2.2)$$

Equation (2.2) shows that the higher the rate of nonradiative processes,  $k_{nr}$ , the lower the quantum yield  $\Phi$ . The time between excitation and emission is called the fluorescence lifetime  $\tau$  and is defined by the rates as:

$$\tau = \frac{1}{k_r + k_{nr}} \quad (2.3)$$

As fluorescence is a quantum mechanics process, the photon emission is distributed in time. The emission probability is constant in time. This results in an exponential fluorescence intensity decay for an ensemble of fluorophores, which are excited by a short light pulse of the intensity  $I_0$ . The intensity at a certain time point  $t$  is then given for the theoretical case of a quantum yield of one by:

$$I = I_0 \cdot \exp\left(-\frac{t}{\tau}\right) \quad (2.4)$$

## 2.4 Anisotropy

Anisotropy measurements are based on the principle that excitation has the highest probability when the vector of the electric field of the polarized excitation light is parallel to the transition moment of the fluorophore. If the vector of the electric field is not parallel, it can be split up into a parallel and a perpendicular part and, therefore, only the parallel part can excite the molecule with its energy. Thus, the fluorophore can also be excited by polarized light, which is mostly perpendicular to the transition moment of the fluorophore, when the excitation power is high enough.

The transition moment of the emission is in the most cases parallel to the transition moment of the excitation. If the molecule is able to rotate during the time it stays excited, the transition moment also rotates. By detecting this rotation, the size of the molecule can be calculated, as the rotation rate depends on its size. When the size of the molecule gets

too small, the rotation gets too fast and, therefore, the change in polarization and the size cannot be detected anymore. The relationship between the intensity in parallel,  $I_{\parallel}$ , and perpendicular direction,  $I_{\perp}$ , to the excitation light defines the fluorescence anisotropy  $r$  of a sample:

$$r = \frac{I_{\parallel} - I_{\perp}}{I_{\parallel} + 2I_{\perp}} \quad (2.5)$$

Synthetic fluorophores, which are used in this work, are quite small and, therefore, rotate very fast, which results in an anisotropy close to zero. However, when they are used for labeling a larger molecule, for example a protein, the rotational freedom of the fluorophore is confined additionally by the labeled molecule. The dye is attached by a short linker to the molecule and in the ideal case it can freely rotate. If it has no freedom anymore the rotation only depends on the labeled molecule. In reality, it is expected that the anisotropy is a mixture of the rotations of the molecule labeled with the dye and the fluorophore itself.

## 2.5 Förster Resonance Energy Transfer - FRET

Förster Resonance Energy Transfer (FRET) is a nonradiative transition of the energy of one molecule to another [Förster, 1948]. One fluorophore, called the donor, is excited by the absorption of a photon. If a second unexcited fluorophore, called the acceptor, is close enough to the donor, the energy can be transferred. The originally excited electron is then transferred by a nonradiative transition back to the  $S_0$  state and the initially unexcited electron of the acceptor changes to the excited  $S_1$  state. The electron of the excited acceptor changes first by internal conversion to the vibrational ground state of the  $S_1$  state and, afterwards, emits a fluorescence photon (Figure 2.4). The process of FRET is not based on reabsorption of an emitted photon, but on dipole-dipole interactions.

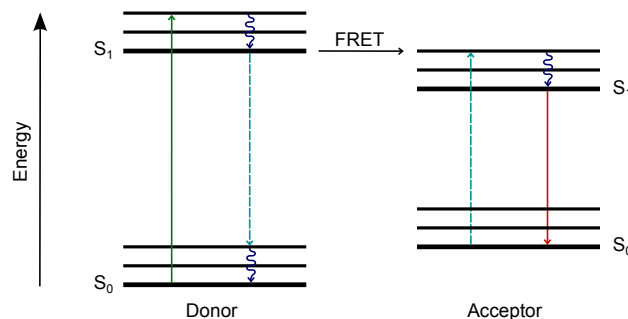


Figure 2.4: A simplified Jablonski diagram for FRET. If the donor dye is excited and a second dye with a longer excitation wavelength, therefore lower energy, is in close proximity to the donor, the excitation energy of the donor can be transferred to the acceptor. This process is based on dipole-dipole-interactions.

The interaction can be characterized by the FRET efficiency  $E$ , which is the fraction of the number of energy transfer processes to the number of all absorption processes. It can be expressed in terms of the de-excitation rates  $k$ :

$$E = \frac{\text{number of energy transfers}}{\text{number of absorbed photons}} = \frac{k_{FRET}}{k_r + k_{nr} + k_{FRET}} \quad (2.6)$$

The FRET efficiency is related to the distance between the two fluorophores and the overlap between the donor emission spectra  $F_D$ , normalized such that  $\int_0^\infty F_D(\lambda)d\lambda = 1$ , and the acceptor absorption spectrum expressed in terms of the extinction coefficients  $\epsilon_A(\lambda)$ . Additionally, the overlap has to be multiplied by the fourth power of the wavelength. The spectral overlap is given as

$$J(\lambda) = \int_0^\infty F_D(\lambda)\epsilon_A(\lambda)\lambda^4d\lambda \quad (2.7)$$

The distance between the donor and acceptor at what 50 % of the excitation results in energy transfer to the acceptor is called the Förster radius  $R_0$ . For most synthetic fluorophore pairs,  $R_0$  is in the range between 30 and 60 Å. The rate of the energy transfer is given by

$$k_{FRET}(r) = \frac{1}{\tau_D} \left( \frac{R_0}{r} \right)^6 \quad (2.8)$$

where  $r$  is the distance between donor and acceptor and  $\tau_D$  is the lifetime of the donor in the absence of energy transfer. By including Equation (2.3) and Equation (2.8) in Equation (2.6), the distance dependency of the FRET efficiency is described by:

$$E(r) = \frac{R_0^6}{r^6 + R_0^6} \quad (2.9)$$

$R_0$  depends on the quantum yield of the donor,  $\Phi_D$ , the overlap integral,  $J$  (Equation (2.7)), between the donor emission and the acceptor excitation spectra and on the relative orientation of the electric dipole moments of donor and acceptor, characterized by  $\kappa^2$  [Förster, 1948], [Lakowicz, 2006].

$$R_0 = \sqrt[6]{\frac{9000\kappa^2 \cdot \Phi_D \cdot \ln(10) \cdot J}{128\pi^5 \cdot N_A \cdot n^4}} \quad (2.10)$$

$N_A$  is Avogadro's number,  $n$  the refractive index of the surrounding medium and  $\kappa^2$  is assumed as 2/3 for a freely rotating dye connected to the molecule of interest.

## 2.6 Single-molecule fluorescence

A lot of biological studies are done in ensemble. If a sample consists only of one species, this results in a clear result with high statistics. The difficulties occur, when different species form one sample. In ensemble measurements, only one population, an average of the different species, will be measured. One idea to distinguish the species is to separate them before measuring and then analyze them individually. The separation could be done by size or charge, for example. An additional difficulty arises when the molecules of interest behave in a dynamic manner. Changing the conformation over time makes a separation impossible. To measure these changes, synchronization of the sample is necessary.

One idea to overcome the difficulties in ensemble is to change to single-molecule measurements. Therefore, the concentration of measured molecules is decreased and only a single-molecule is measured per time interval. This idea has the disadvantage that it takes much longer to collect enough statistics. Furthermore, not all molecules behave well in this low concentrations and tend to aggregate or stick to the walls of the reaction tube. Another disadvantage is that the measurement environment, like the buffer, has to be clean to avoid background signals. In ensemble measurements background is not such a problem, because one is measuring multiple

molecules per time and, therefore, the signal to background ratio is much higher. Overall, single-molecule studies have the advantage of detecting subspecies and dynamics, but they are technically challenging. The two mainly used microscopy schemes for single-molecule studies, confocal and wide field microscopy, are described in the Chapter 3 on page 15.



## 3 Fluorescence microscopy

Two different approaches are mainly used for fluorescence microscopy. On the one hand, the wide field fluorescence microscopy with the extension to total internal reflection fluorescence (TIRF) microscopy and, on the other hand, confocal microscopy. Each method has its advantages and disadvantages. In the following chapter, the basic ideas of microscopy will be discussed along with these two approaches.

### 3.1 Optical resolution

A lot of questions in biology occur on very small dimensions. These objects cannot be detected by eye. To overcome this problem, Förster Resonance Energy Transfer (FRET) can be used in combination with light microscopy to calculate distances on the nanometer scale.

A light microscope consist of a complex system of lenses (objective and ocular), which are used for a magnification of the image. However, very small structures can only be resolved if the magnification as well as the resolution are high enough. The limitation in resolution is given by the diffraction limit. By shining light, emitted from a point emitter, on a circular aperture, the resulting image is blurred. This diffraction image is called an Airy disk and can be explained by the principle of Huygens. Each point of a wave front is a starting point of a new spherical wave. The same diffraction pattern is detected on using an objective, because of the finite size of the objective lenses. The intensity at each point of the Airy disk is the sum of all spherical waves and is given as:

$$I(r) = I_0 \left[ \frac{2 \cdot J_1 \left( 2\pi r \frac{NA}{\lambda_0} \right)}{2\pi r \frac{NA}{\lambda_0}} \right]^2 \quad (3.1)$$

$r$  is the radius of the aperture,  $J_1$  is the first-order Bessel function,  $\lambda_0$  the wavelength of the light in vacuum and  $NA$  the numerical aperture. The numerical aperture depends on the index of refraction  $n$  of the medium in which the lens is working and on the half-angle  $\theta$  of the maximum cone of light that can enter or exit the lens.

$$NA = n \cdot \sin(\theta) \quad (3.2)$$

The intensity distribution of a point light source is called point spread function (PSF). An example for two different points imaged with an objective with  $NA = 1.2$  and a wavelength of 553 nm (the fluorescence maximum of ATTO 532) is given in Figure 3.1. The resolution is defined as the minimal distance between these two objects, which is needed to distinguish them. According to Rayleigh, the distance has to be at least as large as the distance between the maximum and the first minimum of one PSF. This means that the maximum of the first PSF is located in the minimum of the second PSF. This minimum distance is called the lateral resolution.

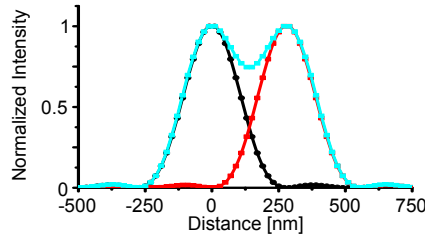


Figure 3.1: Intensity distribution of an Airy disk. The two PSFs are in a distance that corresponds to the resolution limit. The maximum of one PSF is located in the minimum of the other PSF (black and red line). The sum of the two PSFs is plotted in cyan. The PSFs are calculated for an objective with  $NA = 1.2$  and an emission wavelength of 553 nm.

The resolution can be calculated by using the Rayleigh's criteria as given in Equation (3.3). The factor 1.22 is derived from a calculation of the position of the first dark circular ring surrounding the central Airy disc of the diffraction pattern. Equation (3.1) is used for this calculation. In the case of working with the same objective for illumination and detection, the numerical apertures are the same.

$$r_{lateral} = 1.22 \frac{\lambda_0}{NA_{Objective} + NA_{Condensor}} = 0.61 \frac{\lambda_0}{NA_{Objective}} \quad (3.3)$$

## 3.2 Confocal microscopy

Confocal microscopy is based on the idea of illuminating a very small volume and detecting the fluorescence of this area of the sample. The method was first realized by M. Minsky [Minsky, 1961]. For imaging a structure, the sample has to be scanned and, afterwards, reconstructed. A schematic of a confocal microscope is given in Figure 3.2.

A light source, typically a laser, is focused by a lens into a sample. If the light source is not a laser and, therefore, not highly collimated, a pinhole has to be used to clean up the beam profile and make sure that the light is focused only on a small area in the sample.

The so called focal plane is the plane in which the focus has its maximum intensity. The illumination is mainly in this plane and some micrometers above and below the focal point, due to diffraction of the lens. The illuminated volume can be approximated as an ellipsoid with the volume of about a femtoliter.

The fluorescence signal is collected by the same lens, which is used for excitation (Figure 3.2). Because of the Stokes shift of the fluorescent signal, the back scattered excitation light can be filtered out by a beam splitter. Afterwards, the fluorescence is focused on a pinhole. The pinhole has the function to cut off all the fluorescence light, which is not from the focal plane. This means, by adjusting the two pinholes for excitation and for detection, the excitation and detection planes are located at the same position in the sample, i.e. 'con-focal'. The signal is then collected in the back of the pinhole by a photo detector, like an avalanche photon detector (APD).

The advantage of this approach is that the signal to background ratio is very high, because out of focus light is cut off by the pinhole. Furthermore, this method is not limited to structures on the surface like in TIRF microscopy. The disadvantage is that taking an image of a whole

structure with a confocal microscope takes quite long compared to wide field fluorescence microscopy, because the sample has to be scanned.

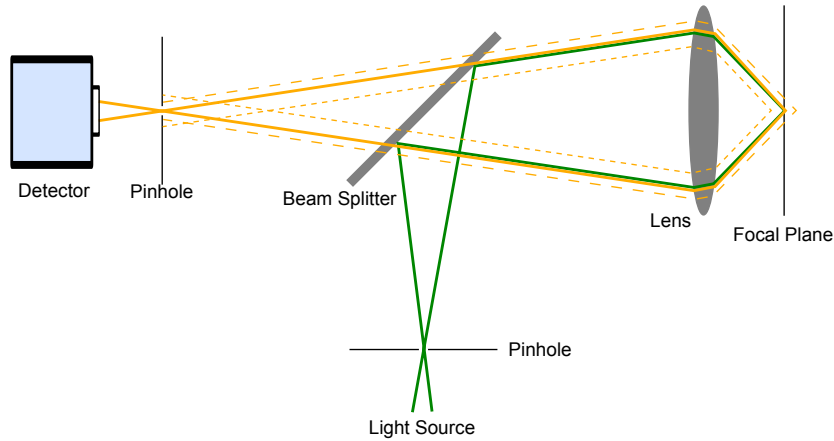


Figure 3.2: Schematic of a confocal microscopy setup. The light source (green) is focused into a sample. The detected fluorescence signal (yellow) is Stokes shifted and can be separated from the excitation wavelength by a beam splitter. The transmitted signal is cleaned up by a pinhole according to the focal plane and then collected by a detector.

### 3.2.1 Fluorescence correlation spectroscopy - FCS

Apart from imaging structures, a confocal microscope can be used for fluorescence correlation spectroscopy (FCS). FCS was first introduced in 1972 by Douglas Magde, Elliot Elson and W.W. Webb [Magde et al., 1972]. This method is based on fluorescence fluctuations. In the easiest way, FCS is performed in solution. Single molecules diffuse by the Brownian motion through a confocal volume. With the help of FCS, we are able to determine the number of particles  $N$  in the detected volume. In addition, this method allows the determination of the diffusion coefficient  $D$ , which is calculated from the average time,  $\tau_D$ , that a molecule spends in the detection volume. This time depends on the hydrodynamical radius and, therefore, on the size of the molecule.

One possible extension for FCS is using an external flow. Then, the time the molecule spends in the focal volume not only depends on the diffusion but also on the applied velocity of the solution. FCS can be used, in this case for example, to determine the flow velocity (for an application see Chapter 7.1.5 on page 114).

#### Principle of FCS

The theory of FCS is based upon Poisson statistics. The probability of finding a molecule in the detection volume is given by

$$P(n, N) = \frac{N^n}{n!} e^{-N} \quad (3.4)$$

where  $N$  is the average number of molecules in the detection volume and  $n$  the actual number of molecules that are detected at one time point.  $N$  and  $n$  do not have to be equal. Therefore, the number of molecules in the focal volume can change over time and, thus, the detected intensities vary. This fluctuations in the intensity are due to molecules diffuses into and out of the confocal volume. When we compare the intensity at one time point,  $t$ , with a slightly later time point,  $t + \tau$ , we can calculate the correlation between these two time points for a range of different  $\tau$ . The result is called autocorrelation function.

### The autocorrelation function

The fluctuations in the detected fluorescence signal are defined as

$$\delta I(t) = I(t) - \langle I(t) \rangle \quad \text{with} \quad \langle \delta I(t) \rangle = 0 \quad (3.5)$$

where  $I(t)$  is the fluorescence intensity at the time point  $t$  and  $\langle I(t) \rangle$  is the temporal average value of the intensity. Additionally, we assumed a constant excitation power to make sure that the detected fluctuations are due to the diffusion of the molecule.

We assume that the process of molecules diffusing in and out of the observation volume is stationary, meaning that the average value does not change over time. Thus, each temporal average of a part of the sample represents the whole sample and, hence, the normalized autocorrelation function [Widengren J., 2002] is defined as:

$$\begin{aligned} g(\tau) &= \frac{\langle I(t)I(t+\tau) \rangle}{\langle I(t) \rangle^2} \\ &= \frac{\langle I(t)I(t+\tau) \rangle - \langle I(t) \rangle^2 - \langle I(t) \rangle^2 + \langle I(t) \rangle^2 + \langle I(t) \rangle^2}{\langle I(t) \rangle^2} \\ &= \frac{\langle I(t)I(t+\tau) \rangle - \langle I(t) \rangle \langle I(t+\tau) \rangle - \langle I(t+\tau) \rangle \langle I(t) \rangle + \langle I(t) \rangle \langle I(t+\tau) \rangle}{\langle I(t) \rangle^2} + \frac{\langle I(t) \rangle^2}{\langle I(t) \rangle^2} \\ &= \frac{\langle (I(t) - \langle I(t) \rangle) \cdot (I(t+\tau) - \langle I(t+\tau) \rangle) \rangle}{\langle I(t) \rangle^2} + 1 \\ &= \frac{\langle \delta I(t) \cdot \delta I(t+\tau) \rangle}{\langle I(t) \rangle^2} + 1 \\ &= \frac{\langle \delta I(0) \cdot \delta I(\tau) \rangle}{\langle I(0) \rangle^2} + 1 = G(\tau) + 1 \end{aligned} \quad (3.6)$$

For this conversion,

$$\langle I(t) \rangle^2 = \langle I(t) \rangle \langle I(t+\tau) \rangle = \langle I(t) \rangle \langle I(t+\tau) \rangle = \langle I(t+\tau) \rangle \langle I(t) \rangle \quad (3.7)$$

and Equation (3.5) are used. The additional constant value 1 in Equation (3.6) shifts the whole correlation function from zero to one.  $G(0)$  is linked to the total number of molecules in the focus. When the number of molecules in the detection volume is large, the fluctuations induced by one molecule, diffusing in and out of the focus, are small compared to the total intensity and the other way around. To calculate the correlation function, the time-depending intensity is needed.

$$I(t) = Q \int p(\vec{r}) \cdot C(\vec{r}, t) dV \quad (3.8)$$

When diffusion is the only reason for the fluctuations, changes in the intensity depend on the changes in the concentration.

$$\delta I(t) = Q \int p(\vec{r}) \cdot \delta C(\vec{r}, t) dV \quad (3.9)$$

where  $C(\vec{r}, t)$  is the concentration of fluorescent molecules depending on the position  $\vec{r}$  and the time  $t$ ,  $Q = q \cdot \sigma_{exc} \cdot \Phi_f$ , where  $q$  is the detection efficiency in the focus of the laser beam,  $\sigma_{exc}$  the excitation cross section and  $\Phi_f$  the fluorescence quantum yield.  $p(\vec{r})$  is the spacial dependence of brightness at which a molecule is seen by the detector, i.e. the PSF. Approximating the focus in all directions to be Gaussian distributed results in:

$$p(\vec{r}) = I_0 \cdot e^{-\frac{2(x^2+y^2)}{\omega_r^2}} e^{-\frac{2z^2}{\omega_z^2}} \quad (3.10)$$

where  $\omega_r$  and  $\omega_z$  are the distances from the center of the volume element in the radial and axial direction, respectively, at which the detected fluorescence intensity has dropped by a factor of  $e^2$ . Instead of computing Equation (3.6), it is combined with Equation (3.9) to yield:

$$g(\tau) = \frac{Q^2 \int_V \int_{V'} p(\vec{r}) p(\vec{r}') c(\vec{r}, \vec{r}', \tau) dV dV'}{(Q \langle C \rangle \int_V p(\vec{r}) dV)^2} + 1 \quad (3.11)$$

where

$$\begin{aligned} c(\vec{r}, \vec{r}', \tau) &= \langle \delta C(\vec{r}, t) \delta C(\vec{r}', t + \tau) \rangle \\ &= \langle \delta C(\vec{r}, 0) \delta C(\vec{r}', \tau) \rangle \end{aligned} \quad (3.12)$$

is the correlation of the concentration fluctuations and  $\langle C \rangle$  is the equilibrium mean concentration. The mean of the fluctuations should be independent of the starting point of the measurement. The fluctuations in the concentration can be expressed as

$$\delta C(\vec{r}, t) = C(\vec{r}, t) - \langle C \rangle \quad (3.13)$$

The temporal evolution of the fluctuations in the concentrations can be described by the continuity equation:

$$\frac{\partial(\delta C(\vec{r}, t))}{\partial t} = D \nabla^2 (\delta C(\vec{r}, t)) \quad (3.14)$$

where  $D$  is the diffusion coefficient. This differential equation can be transformed into the Fourier space<sup>1</sup>.

$$\frac{\partial(\delta \tilde{C}(\vec{\nu}, t))}{\partial t} = -D \vec{\nu}^2 \delta \tilde{C}(\vec{\nu}, t) \quad (3.15)$$

In the Fourier space, this equation can be solved by

$$\delta \tilde{C}(\vec{\nu}, t) = \delta \tilde{C}(\vec{\nu}, 0) \cdot e^{-D \vec{\nu}^2 t} \quad (3.16)$$

In the next step, the fluctuations in concentrations are transformed back.

$$\begin{aligned} \delta C(\vec{r}, t) &= \int e^{i\vec{\nu}\vec{r}} [\delta \tilde{C}(\vec{\nu}, 0) \cdot e^{-D \vec{\nu}^2 t}] d\nu \\ &= \int e^{i\vec{\nu}\vec{r}} \left[ \frac{1}{(2\pi)^3} \int e^{-i\vec{\nu}\vec{r}''} \delta C(\vec{r}'', 0) dV'' \right] e^{-\vec{\nu}^2 D t} d\vec{\nu} \end{aligned} \quad (3.17)$$

<sup>1</sup>The convention for the Fourier transformation used here is:

$$\begin{aligned} \tilde{f}(\vec{\nu}) &= \frac{1}{2\pi} \int_V e^{-i\vec{\nu}\vec{r}} f(\vec{r}) d\vec{r} \\ f(\vec{r}) &= \int_V e^{i\vec{\nu}\vec{r}} \tilde{f}(\vec{\nu}) d\vec{\nu} \end{aligned}$$

This result is included in Equation (3.12) and the assumptions made that a molecule can only be at one place at a time and the concentration is Poisson distributed.

$$\begin{aligned}
\langle \delta C(\vec{r}, 0) \delta C(\vec{r}', \tau) \rangle &= \left\langle \delta C(\vec{r}', 0) \int e^{i\vec{v}\vec{r}} \frac{1}{(2\pi)^3} \int e^{-i\vec{v}\vec{r}''} \delta C(\vec{r}'', 0) dV'' e^{-\vec{v}^2 D t} d\vec{v} \right\rangle \\
&= \frac{1}{(2\pi)^3} \int e^{i\vec{v}\vec{r}} \int e^{-i\vec{v}\vec{r}''} \langle \delta C(\vec{r}', 0) \delta C(\vec{r}'', 0) \rangle dV'' e^{-\vec{v}^2 D t} d\vec{v} \\
&= \frac{1}{(2\pi)^3} \int e^{i\vec{v}\vec{r}} \int e^{-i\vec{v}\vec{r}''} \langle \delta C(\vec{r}', 0) \delta C(\vec{r}'', 0) \rangle \delta(\vec{r}' - \vec{r}'') dV'' e^{-\vec{v}^2 D t} d\vec{v} \\
&= \frac{1}{(2\pi)^3} \int e^{i\vec{v}\vec{r}} \int e^{-i\vec{v}\vec{r}''} \langle \delta C(\vec{r}', 0)^2 \rangle \delta(\vec{r}' - \vec{r}'') dV'' e^{-\vec{v}^2 D t} d\vec{v} \\
&= \frac{1}{(2\pi)^3} \int e^{i\vec{v}\vec{r}} \int e^{-i\vec{v}\vec{r}''} \langle C \rangle \delta(\vec{r}' - \vec{r}'') dV'' e^{-\vec{v}^2 D t} d\vec{v} \\
&= \frac{\langle C \rangle}{(2\pi)^3} \int e^{i\vec{v}\vec{r}} e^{-i\vec{v}\vec{r}'} e^{-\vec{v}^2 D t} d\vec{v} \\
&= \frac{\langle C \rangle}{(2\pi)^3} \int e^{i\vec{v}(\vec{r}-\vec{r}')} e^{-\vec{v}^2 D t} d\vec{v} \\
&= \frac{\langle C \rangle}{(4\pi D \tau)^{\frac{3}{2}}} e^{-\frac{(\vec{r}-\vec{r}')^2}{4D\tau}}
\end{aligned} \tag{3.18}$$

This expression gives the probability of finding a molecule, which was at time point  $\tau = 0$  at the location  $\vec{r}'$  and at the location  $\vec{r}$  at time point  $\tau$ . Implementing the result of Equation (3.18) and Equation (3.10) into Equation (3.11) leads to the correlation function of a molecule, which diffuses through a Gaussian focus.

$$\begin{aligned}
g(\tau) &= \frac{\int_V \int_{V'} I_0 e^{-\frac{2(x^2+y^2)}{\omega_r^2}} e^{-\frac{2z^2}{\omega_z^2}} \cdot I_0 e^{-\frac{2(x'^2+y'^2)}{\omega_r^2}} e^{-\frac{2z'^2}{\omega_z^2}} \cdot \frac{\langle C \rangle}{(4\pi D \tau)^{\frac{3}{2}}} e^{-\frac{(\vec{r}-\vec{r}')^2}{4D\tau}} dV' dV}{\left( \langle C \rangle \int_V I_0 e^{-\frac{2(x^2+y^2)}{\omega_r^2}} e^{-\frac{2z^2}{\omega_z^2}} dV \right)^2} + 1 \\
&= \frac{1}{\langle C \rangle \omega_r^2 \omega_z \pi^{\frac{3}{2}} \left( \frac{1}{1 + \frac{4D\tau}{\omega_r^2}} \right)} \sqrt{\frac{1}{1 + \frac{4D\tau}{\omega_z^2}}} + 1 \\
&= \frac{2^{-\frac{3}{2}}}{N} \left( \frac{1}{1 + \frac{4D\tau}{\omega_r^2}} \right) \sqrt{\frac{1}{1 + \frac{4D\tau}{\omega_z^2}}} + 1 \\
&= G_D(\tau) + 1
\end{aligned} \tag{3.19}$$

This is used to obtain the final form, where the volume is defined as  $V_0 = \left(\frac{\pi}{2}\right)^{\frac{3}{2}} \omega_r^2 \omega_z$  and the average number of molecules in the focus is  $N = \langle C \rangle V_0$ . The diffusion time is  $\tau_D = \frac{\omega_r^2}{4D}$ .

### The autocorrelation function including triplet transitions

The model described in the last pages described an ideal system. In reality different additional effects can change the shape of the correlation function. One of these effects is due to a transition of the fluorophore to the triplet state. Because of the used laser power, the molecule has a relatively high probability of undergoing intersystem crossing from the excited singlet

state to the triplet state. Therefore, the molecule changes from a fluorescent state to a dark state during the time it spends in the focus. From the triplet state, the molecule can convert back to the singlet ground state. In some cases, the molecule is still in the focus when this relaxation occurs and can be excited again. In the other case, it has already left the focus. This effect appears in the autocorrelation function at faster timescales than the diffusion time. A scheme of the rates is shown in Figure 3.3.

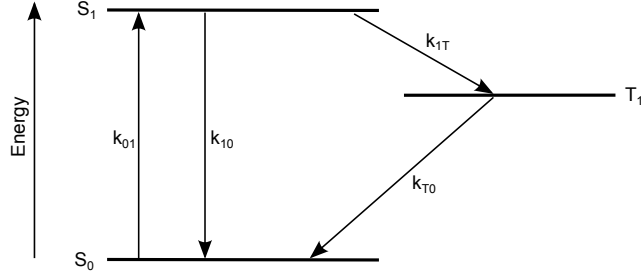


Figure 3.3: Jablonski Diagram with rates. The rate  $k_{01}$  represents the excitation,  $k_{1T}$  the intersystem crossing,  $k_{T0}$  the transition from the triplet state back to the ground state and  $k_{10}$  the rate of fluorescence.

By assuming that the process of changing to the triplet state is faster than the diffusion time, that the diffusion coefficient does not change due to the transitions between singlet and triplet and that the transition to the triplet state is independent of the location, it is possible to create a matrix for the different states.

$$\frac{d}{dt} \begin{pmatrix} S_0(t) \\ S_1(t) \\ T(t) \end{pmatrix} = \begin{bmatrix} -k_{01} & k_{10} & k_{T0} \\ k_{01} & -(k_{1T} + k_{10}) & 0 \\ 0 & k_{1T} & -k_{T0} \end{bmatrix} \times \begin{pmatrix} S_0(t) \\ S_1(t) \\ T(t) \end{pmatrix} \quad (3.20)$$

The eigenvectors and the eigenvalues  $\lambda$  of the equation matrix can be calculated. For more details, see [Widengren J., 1994], [Widengren J., 1995]. The three eigenvalues are:

$$\lambda_1 = 0 \quad (3.21)$$

$$\lambda_2 = -(k_{10} + k_{01}) \quad (3.22)$$

$$\lambda_3 = - \left( k_{T0} + \frac{k_{01} \cdot k_{1T}}{k_{01} + k_{10}} \right) \quad (3.23)$$

The first eigenvalue,  $\lambda_1$ , is 0, which means that the population will go to a steady state at  $t \rightarrow \infty$ . This definition is put into the model, as it is assumed that the system is closed and, therefore, the number of molecules stays constant. Furthermore, it is assumed that photobleaching does not happen.

The second eigenvalue,  $\lambda_2$ , represents the antibunching term. This means that the fluorophore is in the ground state after it has emitted a photon. To emit a second photon it has to be excited again. This takes a certain time in which the probability to detect a photon is very low.

The last eigenvalue,  $\lambda_3$ , represents the rate at which the buildup of the triplet state population takes place. With the help of this rate, it is possible to calculate the correlation function with the inclusion of the triplet state.

$$G(\tau) = G_D(\tau) \left( 1 + \frac{T}{1-T} e^{-\lambda\tau} \right) \quad (3.24)$$

There,  $G_D(\tau)$  is the diffusional autocorrelation function (Equation (3.19)).  $T$  is the fraction of molecules that are in the triplet state in equilibrium. Because of the assumption of a closed system, the populations are normalized  $T + S_0 + S_1 = 1$ . A scheme of a correlation function, including the information about the number of molecules in the focus,  $N$ , and the diffusing time,  $\tau$ , is shown in Figure 3.4.

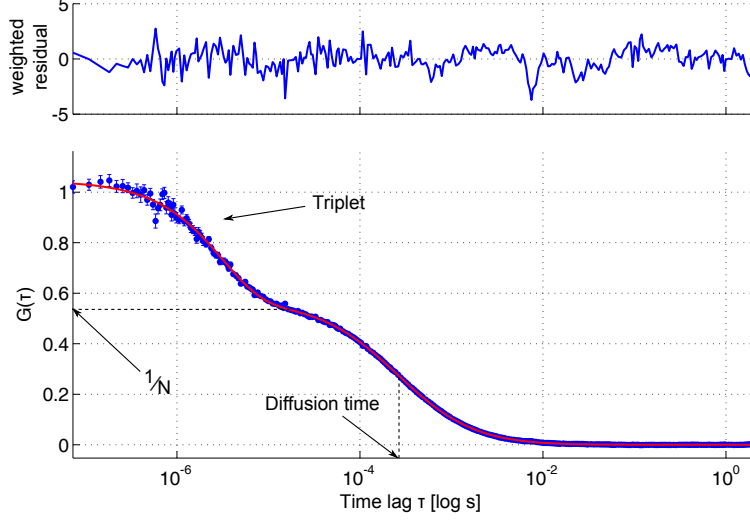


Figure 3.4: Correlation function of freely diffusing Cy5. The correlation time can be fitted by the autocorrelation function including triplet transitions. The curve includes information about the number of particles in the focus,  $N$ , the diffusion time of the molecule,  $\tau_D$ , and about presence or absence of a triplet state.

### The autocorrelation function with flow

In the presence of an uniform external flow, the correlation function of Brownian motion has to be extended. The velocity could be of interest, for example when using a microfluidic system to calculate the time till mixing. For calculating the correlation function under flow, an additional term has to be included into the continuity equation (Equation (3.14), [Widengren J., 2002]):

$$\frac{\partial(\delta C(\vec{r}, t))}{\partial t} = D\nabla^2(\delta C(\vec{r}, t)) - \vec{v}\nabla(\delta C(\vec{r}, t)) \quad (3.25)$$

$\vec{v} = (v_x, v_y, v_z)$  is the vectorial flow speed. Solving this equation is done in the same way as was done for the autocorrelation on page 18. The first step is to transform the equation into Fourier space.

$$\frac{\partial(\delta\tilde{C}(\vec{v}, t))}{\partial t} = -D\vec{v}^2\delta\tilde{C}(\vec{v}, t) - \vec{v}\vec{v}\delta\tilde{C}(\vec{v}, t) \quad (3.26)$$

In Fourier space, this equation can be solved by

$$\delta\tilde{C}(\vec{v}, t) = \delta\tilde{C}(\vec{v}, 0) \cdot e^{-D\vec{v}^2 t} \cdot e^{i\vec{v}\vec{v}} \quad (3.27)$$

Next, the equation has to be transformed back and, afterwards, implemented in Equation (3.25). The resulting equation can be solved and results in the correlation function with flow (but without triplet).

$$g(\tau) = G_D(\tau) \cdot e^{-\left[ \left[ \frac{(v_x^2 + v_y^2)\tau^2}{\omega_r^2} \right] \frac{1}{1 + \frac{4D\tau}{\omega_r^2}} + \left( \frac{v_z\tau}{\omega_z} \right)^2 \frac{1}{1 + \frac{4D\tau}{\omega_z^2}} \right]} + 1 \quad (3.28)$$

For the case of a flow in one direction,  $\vec{v} = (v_x, 0, 0)$ , the Equation (3.28) can be simplified to:

$$g(\tau) = G_D(\tau) \cdot e^{-\left[ \left( \frac{v_x\tau}{\omega_r} \right)^2 \frac{1}{1 + \frac{4D\tau}{\omega_r^2}} \right]} + 1 \quad (3.29)$$

Combining Equation (3.29) with Equation (3.24) leads to the following overall equation, including triplet and flow:

$$G(\tau) = G_D(\tau) \cdot e^{-\left[ \left( \frac{v_x\tau}{\omega_r} \right)^2 \frac{1}{1 + \frac{4D\tau}{\omega_r^2}} \right]} \cdot \left( 1 + \frac{T}{1 - T} e^{-\lambda\tau} \right) \quad (3.30)$$

A scheme of a correlation function with flow (red line) in comparison with a correlation function without flow (black line) is shown in Figure 3.5. The correlation function gets steeper by applying an external flow and the flow component gets more dominant by increasing the flow rate, till the diffusion component can be neglected.

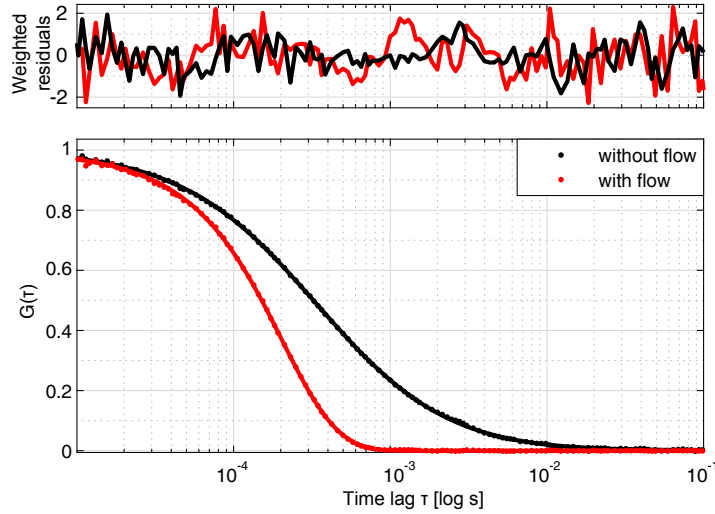


Figure 3.5: Correlation function of ATTO 532 with external applied flow. The correlation time can be fitted by the autocorrelation function including flow. The correlation function of a measurement with flow (red line) is steeper than the correlation function without externally applied flow (black line).

### 3.3 SpFRET using MFD-PIE

For monitoring conformational changes in a molecule, FRET can be used. In a typical FRET measurement, the molecule is labeled with two dyes and the energy transfer is measured. For measuring the molecules in solution, a confocal setup can be used. The concentration of the molecules has to be decreased to the pM range to make sure that only one molecule is in the focus at the time. This is called single-pair FRET (spFRET) measurements. To get as much information as possible, a combination of 'pulsed interleaved excitation' (PIE) [Müller et al., 2005] and 'multiparameter fluorescence detection' (MFD) [Eggeling et al., 2001] is chosen [Kudryavtsev et al., 2012].

#### 3.3.1 Pulsed interleaved excitation - PIE

For studying spFRET, a single color confocal setup, i.e. only exciting the donor, has the disadvantage that blinking or bleaching of one dye changes the FRET efficiency distribution. When the acceptor bleaches or turn for a short period of time to a dark state, the detected FRET efficiency interchanges to a FRET efficiency of zero. This interchanging can not be distinguished from the case that the distance between the two dyes increases during the measurement to a value, which is too long for FRET. To get more information and to account for blinking and bleaching, excitation is done using two lasers, one to excite the donor and one to excite the acceptor. The two lasers are alternating one after the other. We can distinguish between two different approaches: On the one hand, 'alternating laser excitation' (ALEX) [Kapanidis et al., 2005] and, on the other hand, 'pulsed interleaved excitation' (PIE) [Müller et al., 2005]. In the case of ALEX, the two lasers alternate on a timescale between 25 and 3000  $\mu$ s. This means that the switching between the excitation lasers is on a timescale faster than the diffusion. The difference to PIE is the alternating timescale and the use of subnanosecond pulsed lasers. For PIE, alternating is in the range of nanoseconds, e.g. for the used setup 18.8 ns.

In our case, we use a PIE system, consisting of two lasers. For the dye pair ATTO 532 and ATTO 647, a setup like the one shown in Figure 3.6 is used. A frequency-doubled diode laser (PicoTA, PicoQuant, Berlin, Germany) at 530 nm for donor excitation and a diode laser (LDH-D-C-640, PicoQuant) at 640 nm for acceptor excitation is used. Both lasers are coupled into a polarization maintaining single mode fiber (AMS Technologies, Martinsried, Germany) and, afterwards, the laser light is recollimated (60FC-4-RGB11-47, Schäfter + Kirchhoff, Hamburg, Germany). The two lasers are pulsed with a repetition rate of 26.7 MHz. In the back of the fiber, the polarization of both lasers are maximized by a Glan-Thompson polarizer (GTHM Polarizer, Thorlabs, Dachau, Germany). The laser light is adjusted to an average power of 100  $\mu$ W for each wavelength after the polarizer. The light is then reflected by a dichroic mirror (DualLine z532/635, AHF Anaysetechnik, Tübingen, Germany) and focused into the sample by a 60x 1.27 NA water immersion objective (Plan Apo IR 60x/1.27 WI, Nikon, Düsseldorf, Germany).

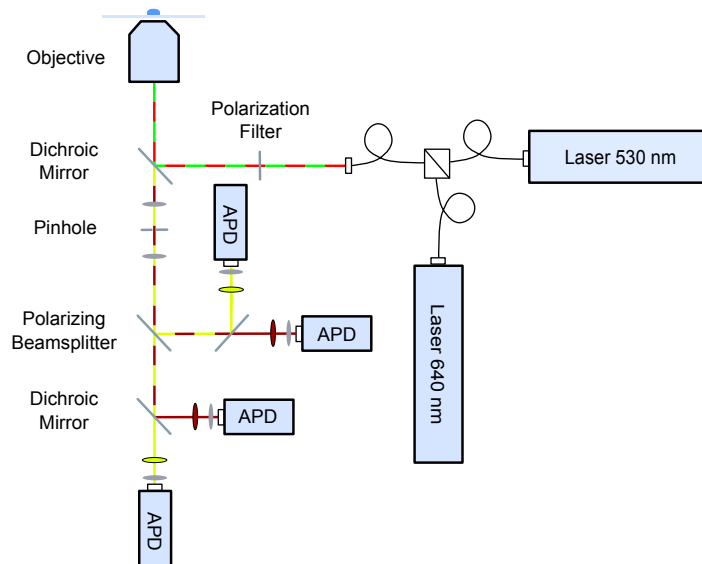


Figure 3.6: MFD-PIE setup. Two pulsed lasers are coupled each in a single mode fiber, the fibers are combined and the polarization of the overlapped signal is after the fiber optimized. The excitation light sources are alternated and the light is focused by an objective in the sample. The fluorescence signal is separated by a dichroic mirror from the excitation light and, afterwards, cleaned up by a pinhole and split by polarization and then by wavelength. The signal is detected by four APDs combined each with a TCSPC card.

### 3.3.2 Multiparameter fluorescence detection - MFD

To maximize the information available from a single measurement, we use the MFD approach. With this setup, we collect information regarding the fundamental anisotropy, fluorescence lifetime, fluorescence intensity, microtime, excitation spectrum, fluorescence spectrum, fluorescence quantum yield and the distance between the fluorophores [Widengren et al., 2006]. We realize this approach by the following detection pathway: The fluorescence signal is collected by the objective and then passes the dichroic mirror (DualLine z532/635, AHF Anaysetechnik), because of the Stokes shift of the fluorescence compared to the excitation, and is focused on a  $75 \mu\text{m}$  pinhole. Out of focus signal is cut off by the pinhole. In the next step, the signal is split in the parallel and the perpendicular components compared to the excitation light by a polarizing beam splitter (05FC16PB.3, Newport, Darmstadt, Germany) and, afterwards, the polarization directions are separated by wavelength to a donor and an acceptor channel (BS 650, AHF Analysentechnik). Before detection, the fluorescence signal passes through emission filters (2x BrightLine HC 582/75 and 2x ET 700/75, AHF Analysentechnik). The detection is done using single photon counting avalanche photodiodes (2x SPQR-14, and 2x SPQR-16, Perkin Elmer, Massachusetts, USA). For getting additionally information about the lifetime of the dye, the detected photons are registered by four individual TCSPC data collection cards (SPC-154, Becker & Hickl GmbH, Berlin, Germany). This cards are synchronized with the laser pulses, which are delayed with respect to each other by about 18 ns. Therefore, every photon can be assigned to the corresponding excitation.

### 3.3.3 Data analysis

To analyze the MFD-PIE data, first the photons have to be extracted by performing a burst search. Afterwards, the double labeled molecules can be selected from a stoichiometry versus FRET efficiency plot and further analysis can be performed. The dynamic behavior of a molecule can be determined by a FRET efficiency versus lifetime plot and changes in the complex size gets visible in the anisotropy. Finally, the FRET efficiencies are transferred to distances and fitted by the photon distribution analysis.

The whole data analysis was performed with the matlab program 'pam', which has been written in our lab.

#### Burst search

In the first step of the single-molecule FRET analysis, the double labeled molecules have to be identified. With the MFD-PIE setup, we can measure and sort the photons with respect to their excitation pulse. We are able to detect a green signal after green excitation and a red signal after red excitation. Additionally, we can measure a red signal after green excitation, which corresponds to the FRET signal. In Figure 3.7, the sum over the microtime of a measurement, the time for one excitation cycle, is shown. First, the green laser pulse excites the sample and after the molecule has time enough to emitted a photon and converted back to the ground state, the next pulse, the red one, excites the sample. The signal in the green channel after red excitation is due to scattered light.

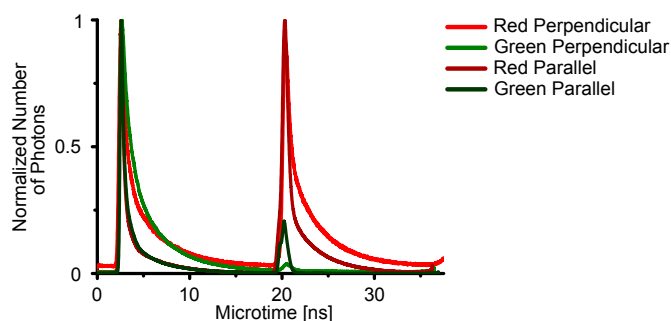


Figure 3.7: Microtime histogram of a MFD-PIE experiment. First a green laser pulse excites the sample. After emitting a photon, the sample is excited by a red laser pulse. The time between two pulses is for the used setup 18.8 ns.

In a sample, molecules are never 100 % double-labeled and sometimes some background signal, for example from a component of the buffer, is detected. The advantage of spFRET measurements on a MFD-PIE setup is that it is possible to sort out the single labeled molecules and the background. Thus, the double-labeled molecules can be selected. The first step for doing this, is to select bursts. Every time, a labeled molecule enters the confocal volume, a signal is detected till it leaves the focus again. This signal appears in the intensity histogram over time as a burst, hence the name burst analysis. In Figure 3.8, the intensity trace of the sum of the two green detection channels (upper part, green) and of the two red detection channels (lower part, red) are shown.

Multiple ways are available to select the bursts [Nir et al., 2006]: The two approaches we

used are either to select all bursts independent of the channel. This method is called the all-photon-burst-search (APBS). The other possibility is to select bursts that appear in the green and at the same time in the red channel. This method is called the dual-channel-burst-search (DCBS) and selects only bursts of double-labeled molecules. In this work, the DCBS method was used. The chosen parameters for the burst-search depend on the background of the sample. For a clean sample, the number of photons per burst in a time window of 500  $\mu\text{s}$  is chosen as 50, whereby in both channels separately a minimum of 5 photons has to be detected.

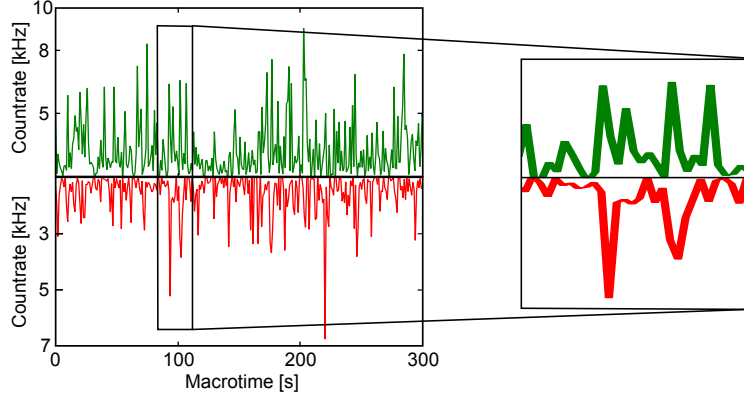


Figure 3.8: Intensity trace of a burst measurement. The upper plot represent the signal detected in the donor channels and the lower plot the signal in the acceptor channel. When a molecule is double-labeled and shows FRET, a burst appears in both channels simultaneously.

### Stoichiometry versus FRET efficiency plot

In the next step, we can calculate the FRET efficiency from the extracted bursts. By using the signal intensity of the acceptor after donor excitation,  $F_{GR}$ , which is the FRET signal, and the signal of the donor after donor excitation,  $F_{GG}$ , the proximity rate is given by:

$$E_{PR} = \frac{F_{GR}}{F_{GR} + F_{GG}} \quad (3.31)$$

Whereby, the signal has been corrected for the background.

To convert the proximity rate into FRET efficiency, we have to correct our signals for detection artifacts. The first correction factor is the spectral crosstalk  $\beta$ , which represents the donor signal detected in the acceptor channel. The second correction factor is the direct excitation  $\alpha$ , which corresponds to the signal of an acceptor excited by the donor laser. The last correction is due to the differences in the sensitivity of the different detection channels, called  $\gamma$ . The correction factors themselves can be determined by

$$\alpha = \frac{\epsilon_A^{\lambda_{exD}} I_D}{\epsilon_A^{\lambda_{exA}} I_A} \quad (3.32)$$

$$\beta = \frac{\eta_A^{\lambda_{emD}}}{\eta_A^{\lambda_{emA}}} \quad (3.33)$$

$$\gamma = \frac{\Phi_A \eta_A^{\lambda_{emA}}}{\Phi_D \eta_D^{\lambda_{emD}}} \quad (3.34)$$

$I_D$  and  $I_A$  are the excitation intensities of the donor and acceptor laser, respectively, which are equal in the measurements shown in this work.  $\epsilon_A^{\lambda_{exD}}$  is the absorption cross section of the acceptor at the donor excitation wavelength and  $\epsilon_A^{\lambda_{exA}}$  at the acceptor wavelength. The detection efficiency of the donor and acceptor fluorescence in the donor and acceptor channel is given by  $\eta_D^{\lambda_{emD}}$  and  $\eta_A^{\lambda_{emA}}$ , respectively.  $\Phi_D$  and  $\Phi_A$  are the quantum yield of the donor and acceptor, respectively. By using this correction factors, the FRET efficiency is given by

$$E = \frac{F_{GR} - \alpha F_{RR} - \beta F_{GG}}{F_{GR} - \alpha F_{RR} - \beta F_{GG} + \gamma F_{GG}} \quad (3.35)$$

Additionally, the stoichiometry can be calculated. The stoichiometry is a factor that takes into account if a molecule is double-labeled or is only labeled with one color and can be calculated by using the signal intensities, which are measured. For the uncorrected case, this results in Equation (3.36).

$$S = \frac{F_{GR} + F_{GG}}{F_{GR} + F_{GG} + F_{RR}} \quad (3.36)$$

By applying the correction factors also to the stoichiometry, the stoichiometry of the double-labeled molecules is shifted to approximately 0.5 and, thus, different measurements can be compared easily. The Equation (3.36) is extended to

$$S = \frac{F_{GR} - \alpha F_{RR} - \beta F_{GG} + \gamma F_{GG}}{F_{GR} - \alpha F_{RR} - \beta F_{GG} + \gamma F_{GG} + F_{RR}} \quad (3.37)$$

The corrected stoichiometry can be plotted versus the corrected FRET efficiency. In this plot, shown schematically in Figure 3.9, we can distinguish between double-labeled molecules with different FRET efficiencies and, therefore, different distances between the dyes, and single-labeled molecules, meaning donor or acceptor only.

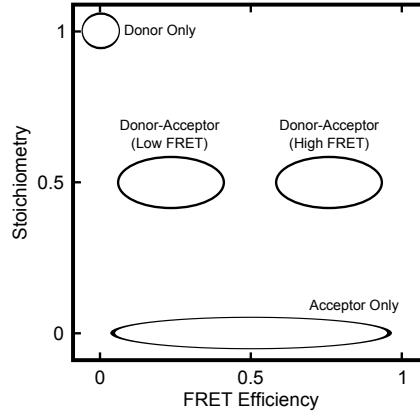


Figure 3.9: Stoichiometry versus FRET efficiency scheme. In this plot, the double-labeled and single-labeled molecules can be distinguished.

To estimate the correction factors, the uncorrected stoichiometry versus FRET efficiency plot can be used. In the case of donor only molecules, the FRET efficiency should be 0. By changing the crosstalk correction factor  $\beta$  from 0, the uncorrected case, to higher values, the donor

only population shifts to lower FRET efficiency values and can be set to 0.

To estimate the direct excitation, the stoichiometry of the acceptor only population has to be zero. By increasing  $\alpha$ , the acceptor only population shifts to lower stoichiometry values. Both correction factors, crosstalk and direct excitation, are in a range of a few percent and below 10 %. For evaluating the values, an APBS has to be done because, otherwise, with the DCBS, the donor and acceptor only populations are not represented in the plot.

The last correction factor,  $\gamma$ , change the stoichiometry value. The changes depend on the FRET efficiency.  $\gamma$  has to be chosen in a way that the FRET populations have the same stoichiometry value in a FRET efficiency versus stoichiometry plot.

The next step in analyzing MFD-PIE data is to select only bursts from double-labeled molecules that do not blink or bleach as long as the molecule stays in the focus. Two possible filters are commonly used for this: One method is to compare between the mean time of detection of the FRET and the acceptor signals. If one of the dyes is in the dark state for a part of the detection time, the mean time the signals in the donor and acceptor channels are detected differs and remained from the further analysis [Kudryavtsev et al., 2012]. A second approach is the so called ALEX-2CDE filter [Tomov et al., 2012]. It takes into account the amount of fluctuations in the brightness ratio of the different bursts. If a molecule stays too long in the dark state, the brightness of this burst is less and the burst is neglected.

## FRET efficiency versus Lifetime

For further analyzing the measured and selected double-labeled molecules, the fluorescence lifetime of the dyes is an important information. By plotting the FRET efficiency versus the fluorescence lifetime, dynamics in the measured system can get visible and the  $\gamma$  value can be optimized.

The dye molecule is excited by the laser pulse and can then emit a photon after a certain delay time. This is a statistic process and can be described by an exponential decay (Figure 3.7). If a part of the energy is transferred from the donor to the acceptor, the time between the excitation and emission gets shorter depending on the FRET efficiency. The time relation is given by Equation (3.38), whereby  $\tau_{D(0)}$  is the lifetime of the donor in the absence of the acceptor and  $\tau_{D(A)}$  the lifetime of the donor in the presence of the acceptor.

$$E = 1 - \frac{\tau_{D(A)}}{\tau_{D(0)}} \quad (3.38)$$

This equation does not take into account that the dyes are not rigidly connected to the molecule of interest. They have some flexibility due to the linker between the dye and attachment point. The distance of the dye to its mean position can be estimated by a Gaussian distribution. The distance between the mean value of the dye and the real value is named  $r$ . The fraction of the time the molecule spends at a particular separation is given by  $x$ . By combining Equations (2.9) and (3.38), the lifetime of the donor in the presence of the acceptor in the dependency of the distance  $r$  can be calculated as

$$\tau_{D(A)}(r) = \frac{\tau_D}{1 + \left(\frac{R_0}{r}\right)^6} \quad (3.39)$$

The species weighted average lifetime  $\tau_{ave,x}$  can be calculated as a fraction of  $\tau_{D(A)}$ . It is the sum over all distances  $r$  weighted by the corresponding donor lifetime

$$\tau_{ave,x} = \sum_r x(r) \tau_{D(A)}(r) \quad (3.40)$$

Additionally, the fluorescence intensity weighted average lifetime  $\tau_{ave,a}$  can be calculated by Equation (3.41).

$$\tau_{ave,a} = \sum_r a(r) \tau_{D(A)}(r) \quad \text{with} \quad a(r) = \frac{x(r) \tau_{D(A)}(r)}{\sum_r x(r) \tau_{D(A)}(r)} \quad (3.41)$$

The plot of the species weighted average lifetime versus the fluorescence intensity weighted average lifetime can be described empirically by a third-order polynomial [Gansen et al., 2009] (Figure 3.10).

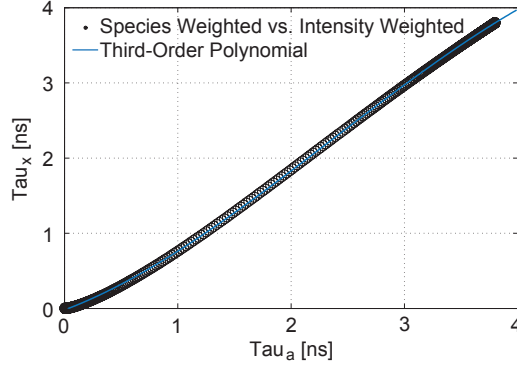


Figure 3.10: Relation between species and intensity weighted lifetime. The dependency can be interpolated by a third-order polynomial.

In the case of ATTO 532 and ATTO 647, the most used dye pair in this work, the lifetime of the donor in the presence of the acceptor can be interpolated by the third-order polynomial fit, which is given in Equation (3.42). For the standard deviation of the distance distribution around the mean value, according to the linker between the dye and the molecule, a value of 6 Å is chosen.

$$\tau_{ave,x} = -0.0195 + 0.5668 \tau_{ave,a} + 0.25 \tau_{ave,a}^2 - 0.03547 \tau_{ave,a}^3 \quad (3.42)$$

With this equation and Equation (3.38), we can calculate the dependency of the FRET efficiency versus the lifetime of the donor.

$$E = 1 - \frac{-0.0195 + 0.5668 \tau_{ave,a} + 0.25 \tau_{ave,a}^2 - 0.03547 \tau_{ave,a}^3}{\tau_{D(0)}} \quad (3.43)$$

In the case of our dye pair, the donor lifetime in the absence of the acceptor is  $\tau_{D(0)} = 3.8$  ns. If the molecule undergoes some conformational changes and, therefore, the FRET distance changes during the time the molecule stays in the focus, the data differs from the theoretical line [Kalinin et al., 2010]. According to Equation (3.38) the lifetime of the donor dye gets larger, when the distance between the two dyes is increased. Thus, the population is in the case of dynamics shifted to higher fluorescence lifetimes for the FRET efficiency values inbetween the start and end population of the dynamics. The interconversion between two FRET states and, therefore, two lifetimes can be described again by a species weighted average lifetime. This is given by:

$$\tau_{ave,x} = x_1 \tau_1 + (1 - x_1) \tau_2 \quad (3.44)$$

The lifetime of the donor in the presence of FRET for state one and state two is  $\tau_1$  and  $\tau_2$ , respectively.  $x_1$  is the species fraction of the first state. By combining Equation (3.41) and Equation (3.44), we can calculate the intensity weighted lifetime for the interconversion between two FRET conformations.

$$\tau_{ave,a} = \frac{x_1\tau_1^2 + (1-x_1)\tau_2^2}{x_1\tau_1 + (1-x_1)\tau_2} \quad (3.45)$$

With this equation, we can express the species weighted average lifetime as a function of the intensity weighted average lifetime.

$$\tau_{ave,x} = \frac{\tau_1\tau_2}{\tau_1 + \tau_2 - \tau_{ave,a}} \quad (3.46)$$

By including Equation (3.46) in (3.38), we can calculate the FRET efficiency.

$$E = 1 - \frac{\tau_1\tau_2}{\tau_{D(0)}[\tau_1 + \tau_2 - \tau_{ave,a}]} \quad (3.47)$$

All lifetimes, the one from the different species and the species weighted, have to be weighted by Equation (3.42). In Figure 3.11, the static line for ATTO 532 and ATTO 647 is given in red. The three dotted lines represent all possible transitions between exemplary states with a lifetime of 0.5 ns, 2 ns and 3.5 ns.

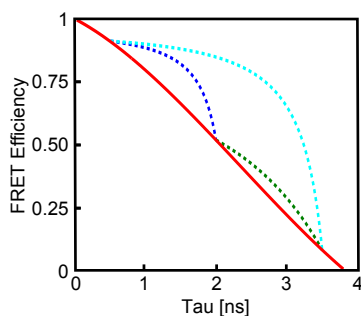


Figure 3.11: FRET efficiency versus the donor lifetime. The theoretical donor lifetime in the presence of the acceptor for a static FRET conformation is shown in red. If the molecule changes between two FRET conformations during the time it stays in the focus, the lifetime shifts to higher values for the same FRET efficiency. Transitions between a lifetime of 0.5 ns, 2 ns and 3.5 ns are plotted.

### Perrin equation

To separate different species in the sample, for example bound and unbound protein, the anisotropy can be used. A molecule is excited with parallel light. For the highest probability of excitation, the transition moment of the dye is in parallel to the vector of the electric field. During the time the fluorophore stays in the excited state, the molecule rotates depending on its size and environment. The orientation of the transition moment of the dye stays according to the molecule of interest constant. Thus, it rotates together with the labeled molecule. The fluorescence signal is then not anymore in the same direction than the excitation light and can be split in a parallel and a perpendicular component. Taking this into account, the two

detectors for one color, parallel and perpendicular, have to be calibrated. The correction factor for the detectors is called the  $G$  factor and corrects for different polarization dependencies in the four channels  $\eta_D^{\lambda_{emD,\parallel}}$ ,  $\eta_D^{\lambda_{emD,\perp}}$ ,  $\eta_A^{\lambda_{emA,\parallel}}$  and  $\eta_A^{\lambda_{emA,\perp}}$ .

$$G_{GG} = \frac{\eta_D^{\lambda_{emD,\perp}}}{\eta_D^{\lambda_{emD,\parallel}}} \quad \text{and} \quad G_{GR} = G_{RR} = \frac{\eta_A^{\lambda_{emA,\perp}}}{\eta_A^{\lambda_{emA,\parallel}}} \quad (3.48)$$

For estimating the  $G$  factors, a freely diffusing dye is measured. Because a free dye rotates faster than it emits a photon, the parallel and the perpendicular signal should be equal. The detected decay of the signal can be fitted by Equation (3.49) of the time resolved anisotropy.

$$r(t) = (r_0 - r_\infty)e^{-\frac{t}{\rho}} + r_\infty \quad (3.49)$$

where  $r_0$  is the fundamental anisotropy given by the angle between excitation and emission dipole.  $r_\infty$  is the residual anisotropy and  $\rho$  is the rotational correlation time. Using the fitted values, the  $G$  factor can be calculated by

$$G = \frac{1 - r_\infty}{2r_\infty + 1} \quad (3.50)$$

With knowledge of the  $G$  factors, the anisotropy (Equation (2.5)) can be corrected for differences in the polarization dependency.

$$r_{green} = \frac{G_{GG} \cdot F_{GG,\parallel} - F_{GG,\perp}}{(1 - 3 \cdot I_2) \cdot G_{GG} \cdot F_{GG,\parallel} + (2 - 3 \cdot I_1) \cdot F_{GG,\perp}} \quad (3.51)$$

$$r_{red} = \frac{G_{RR} \cdot F_{RR,\parallel} - F_{RR,\perp}}{(1 - 3 \cdot I_2) \cdot G_{RR} \cdot F_{RR,\parallel} + (2 - 3 \cdot I_1) \cdot F_{RR,\perp}} \quad (3.52)$$

where  $F$  is the detected signal intensity and  $I_1$  and  $I_2$  account for polarization mixing due to the refraction in the objective and are chosen for the used objective as  $I_1 = 0.0308$  and  $I_2 = 0.0368$ .

The anisotropy of the green or red channel is plotted versus the lifetime of the donor in the presence of the acceptor or the lifetime of the acceptor, respectively. Due to the fact that the anisotropy is size dependent different species can be sorted, for example unbound and bound labeled molecules. The restriction for the binding partner is that it has to be large enough that we can detect changes in the anisotropy. The Perrin equation can be fitted in this plot to distinguish between different species. It describes the relation between the steady-state anisotropy  $r$  and the fluorescence lifetime.

$$r(\tau) = \frac{r_0}{1 + \frac{\tau}{\rho}} \quad (3.53)$$

## Photon distribution analysis - PDA

Due to the fact that distance and FRET efficiency are not forming a linear dependency, FRET efficiency can not easily be converted into distance between the donor and acceptor. Furthermore, every FRET population has a certain center and width. The width depends on photon shotnoise, which is a result of the photon statistics, and on the flexibility in the distance between the acceptor and the donor. Photon distribution analysis (PDA) was developed to

distinguish between underlying inhomogeneities and photon shotnoise [Antonik et al., 2006], [Kalinin et al., 2007], [Kalinin et al., 2010]. It simulates the photon shotnoise under the measured conditions, compares the simulated width with the measured width of the data and can therefore determine underlying donor-acceptor distance distributions.

In spFRET measurements, only a low number of molecules per time is detected and, thus, the signal is, due to the low number of molecules in the focus, very low. Therefore, the background signal of the detector has to be taken into account.  $S$  is the signal produced by a detector and, thus, a mixture of the real detected signal,  $I$ , and the background including the intrinsic detector noise,  $B$ , and, therefore,  $S = I + B$ . In the case of spFRET measurements, the total number of counted events is given by the sum of the donor (D) and acceptor (A) signals,  $N = S_D + S_A = I_D + B_D + I_A + B_A$ .

For obtaining a value, which can be directly compared to the uncorrected and unmodified experimental data, the signal ratio is chosen, which is defined as

$$\frac{S_D}{S_A} = \frac{I_D + B_D}{I_A + B_A} \quad (3.54)$$

Different combinations of  $I_D$ ,  $I_A$ ,  $B_D$  and  $B_A$  can result in the same value of the signal ratio. The probability to measure a certain signal ratio,  $P\left(\frac{S_D}{S_A}\right)$  is therefore the sum of all possible combinations.

$$P\left(\frac{S_D}{S_A}\right) = \sum P(I_D, I_A, B_D, B_A) \quad (3.55)$$

The probability  $P(I_D, I_A, B_D, B_A)$  can be expressed by individual probabilities. The background counts of the different channels are independent from each other and also from the signal that reaches the detector. Furthermore,  $P(I_D, I_A)$  can be given in terms of the total fluorescence intensity  $I = I_D + I_A$ .

$$P(I_D, I_A) = P(I)P(I_A|I) \quad (3.56)$$

where  $P(I_A|I)$  is the probability that exactly  $I_A$  out of  $I$  photons come from the acceptor. Combining these simplifications with Equation (3.55) results in Equation (3.57).

$$P\left(\frac{S_D}{S_A}\right) = \sum P(I)P(I_A|I)P(B_D)P(B_A) \quad (3.57)$$

The different terms in Equation (3.57) have to be described in terms of physically relevant quantities. By assuming that the data is binned into equal time bins, the background of the donor and acceptor channel can be expressed by a Poisson distribution with the average value  $\langle B_D \rangle$  and  $\langle B_A \rangle$ , respectively.

$$P_{\langle B \rangle}(B) = \frac{\langle B \rangle^B e^{-\langle B \rangle}}{B!} \quad (3.58)$$

For expressing the probability of observing exactly  $I_A$  acceptor photons out of  $I$  total photons, we make the assumption of a fixed probability  $\varepsilon$  that any given count is coming from the acceptor and not from the donor detector.  $\varepsilon$  can be assumed as apparent FRET efficiency that has to be corrected for the quantum yield, detection efficiencies, crosstalk and direct excitation. The probability can then be described by a binomial distribution.

$$P(I_A|I) = \frac{I!}{I_A!(I - I_A)!} \varepsilon^{I_A} (1 - \varepsilon)^{I - I_A} \quad (3.59)$$

The last unknown term of Equation (3.57) is  $P(I)$ . It can be calculated analytical, but this is time consuming. The alternative is to describe it with measurable quantities:

$$I = N - B_D - B_A \quad (3.60)$$

With these substitutions Equation (3.57) becomes:

$$P\left(\frac{S_D}{S_A}\right) = \sum P(N)P(I_A|N - B_D - B_A)P_{\langle B_D \rangle}(B_D)P_{\langle B_A \rangle}(B_A) \quad (3.61)$$

Within the duration of a burst under experimental conditions, the number of fluorescence photons exceeds the background photons by at least one order of magnitude. With this restriction,  $P(N)$  can be determined from the distribution of photon counts by normalizing to unity. The expression of the other parts is given in Equation (3.58) and (3.59). If the average background counts are determined from a buffer measurement, the apparent FRET efficiency  $\varepsilon$  is the only free parameter and can be obtained by fitting Equation (3.61) to the measured FRET histograms.

The relation between the apparent FRET efficiency  $\varepsilon$  and the real FRET efficiency, which can be expressed by (2.9), is

$$\varepsilon = 1 - \frac{1}{1 + \frac{\Phi_A \eta_A}{\Phi_D \eta_D} \frac{E}{1-E}} = 1 - \frac{1}{1 + \frac{\Phi_A \eta_A}{\Phi_D \eta_D} \frac{R_0^6}{R^6}} \quad (3.62)$$

Equation (3.61) has to be extended to include a distribution in  $\varepsilon$  as a function of  $R$ , because a molecular system does not exhibit a single distance.

$$P\left(\frac{S_D}{S_A}\right) = \int P(\varepsilon(R)) \sum P(N)P(I_A|N - B_D - B_A)P_{\langle B_D \rangle}(B_D)P_{\langle B_A \rangle}(B_A)d\varepsilon \quad (3.63)$$

Assuming a Gaussian distribution of efficiencies, an explicit expression for  $P(\varepsilon)$  can be given by Equation (3.64) with  $\bar{R}$  and  $\sigma_R$  as the mean value and the standard deviation of the donor-acceptor distances. These two values are the PDA fit parameters.

$$P(\varepsilon) = \frac{R_0}{6\sqrt{2\pi}\sigma_R} \left(\frac{\Phi_A \eta_A}{\Phi_D \eta_D}\right)^{\frac{1}{6}} \frac{1}{(1-\varepsilon)^2} \left(\frac{1}{1-\varepsilon} - (1+\beta)\right)^{-\frac{7}{6}} \cdot \exp\left(-\frac{1}{2\sigma_R^2} \left[R_0 \left(\frac{\Phi_A \eta_A}{\Phi_D \eta_D}\right)^{\frac{1}{6}} \frac{1}{(1-\varepsilon)^2} \left(\frac{1}{1-\varepsilon} - (1+\beta)\right)^{-\frac{1}{6}} - \bar{R}\right]^2\right) \quad (3.64)$$

An example for a PDA fit is shown in Figure 3.12. Two different DNA strands, labeled with ATTO 532 and ATTO 647N, were measured with the described MFD-PIE system (Chapter 3.3 on page 24). The measured data was analyzed and then fitted to a two population PDA model (Figure 3.12A). The fit of one population is shown in red and the other in blue. The mean distance between the two dyes can be assumed as a result of the PDA with  $70 \pm 9 \text{ \AA}$  and  $51 \pm 3 \text{ \AA}$  (Figure 3.12B).

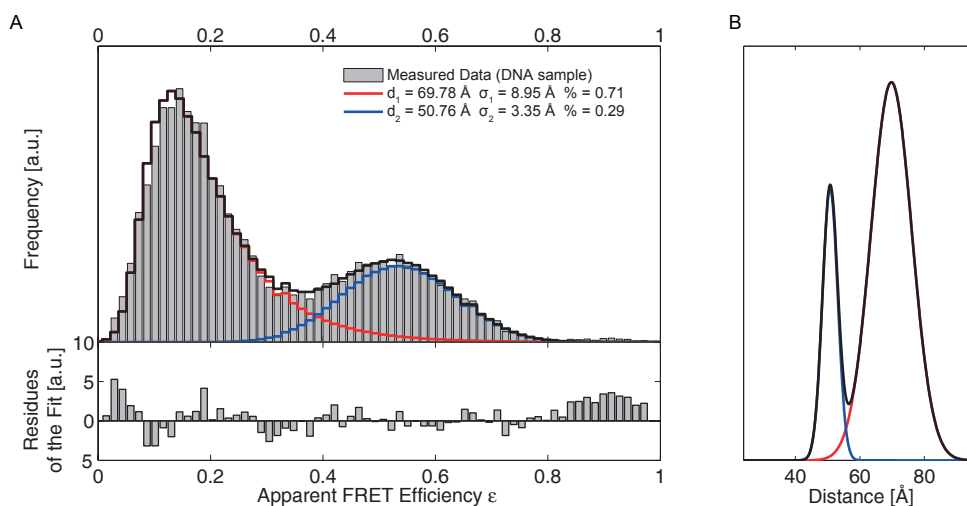


Figure 3.12: PDA fit of measured data. **(A)** Two different DNA strands with different distances between the attached dyes, ATTO 532 and ATTO 647N, were measured with the MFD-PIE system described in Chapter 3.3. **(B)** The fit of the PDA results in the distances  $70 \pm 9 \text{ \AA}$  for the first DNA sample and  $51 \pm 3 \text{ \AA}$  for the second DNA sample.

### 3.4 Wide field microscopy

The second mainly used approach in fluorescence microscopy is wide field microscopy. In this approach, the illuminating light is not focused to a small volume within the sample as it is for confocal excitation, but illuminates a wide range of the sample simultaneously.

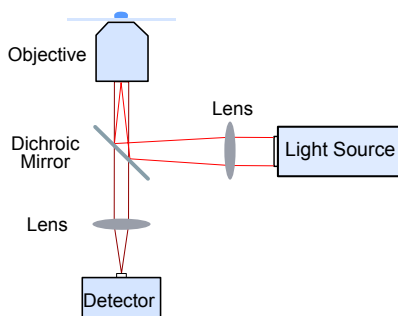


Figure 3.13: Schematic of a wide field setup. The light source is focused on the back focal plane of the objective. The detected signal is Stokes shifted and can be separated from the excitation wavelength by a beam splitter. The passing signal is then collected by a camera.

This can be done by focusing the light on the back focal plane of the objective. The light is then collimated by the complex lens system of the objective to illuminate the sample. The fluorescence signal from the sample is collected by the objective and a dichroic mirror separates the signal from the back reflected light. The fluorescence read out is focused by an additional lens on a detector, in the most cases an electron multiplying charge-coupled device

(EMCCD) or a complementary metal-oxide-semiconductor (CMOS) camera (Figure 3.13). The advantage of this approach is that the light source excites the sample with a high penetration depth. Whole biological structures like cells can be imaged. However, no z-information can be determined. This limits the wide field microscopy in combination with quantitative analysis to thin structures. Additionally, the volume around the structure of interest is excited as well and can result in a high readout noise.

### 3.4.1 Total internal reflection fluorescence microscopy - TIRF

One way to overcome the high background signal of wide field microscopy is the use of total internal reflection. Total internal reflection fluorescence (TIRF) microscopy [Axelrod, 1981] creates an evanescent field on top of the surface between two media with different refraction indexes, commonly a coverslip. The illuminated penetration depth shrinks to a range of 100 nm - 200 nm. This depth is very small and can be extended, by using an angle which is a bit smaller than the critical angle. This creates a thin diagonal plain above the coverslip. The technique is called highly inclined and laminated optical sheet (HILO) [Tokunaga et al., 2008]. The disadvantage of these two methods is that only structures close to the coverslip can be imaged due to the very thin excitation depth on top of the coverslip.

In TIRF microscopy, the light beam hits the surface above the critical angle and the light is totally reflected. However, an evanescent wave propagates parallel to the surface into the sample. Direct on top of the surface the intensity is  $I_0$ . The intensity  $I$  of the evanescent wave decays exponentially with the perpendicular distance  $z$  from the surface.

$$I = I_0 e^{-\frac{z}{d}} \quad (3.65)$$

The characteristic exponential decay depth  $d$  depends on the angle  $\theta$  under which the light hits the surface.

$$d = \frac{\lambda}{4\pi n_2} \left( \frac{\sin^2(\theta)}{\sin^2(\theta_c)} - 1 \right)^{\frac{1}{2}} \quad (3.66)$$

where  $\lambda$  is the wavelength of incident light in vacuum.  $n_2$  is the refractive index of the liquid medium and  $\theta_c$  the critical angle of incidence. Furthermore, Snell's law is used:

$$n_1 \sin(\theta_1) = n_2 \sin(\theta_2) \quad (3.67)$$

where  $n_1$  is the refractive index of the substrate. In the case of the critical angle,  $\theta_2 = 90^\circ$  the equation changes to

$$n_1 \sin(\theta_c) = n_2 \quad (3.68)$$

Three different approaches to TIRF microscopy are used: Prism type TIRF, Objective type TIRF and Waveguide TIRF. All are shown in Figure 3.14.

In the case of prism type TIRF (Figure 3.14A), the exciting laser beam comes from the top. It reaches a prism and hits the bottom surface of the prism above the critical angle. This creates an evanescent wave below the prism, where the sample is placed. The fluorescence signal is collected by an objective. The critical point in this approach is that the space between prism and objective is limited by the working distance of the objective and so the area for the sample is limited. Therefore, the volume of buffer surrounding the sample is very low. This is the reason why this approach is primarily used for single-molecule studies and not for cell imaging, because growing cells in this low amount of media is hard to realize.

Another possibility to create TIRF excitation is objective type TIRF (Figure 3.14B). An objective with a high numerical aperture ( $NA > 1.4$ ) and, therefore, with oil immersion medium is needed. Due to the high numerical aperture, the angle of the light leaving the objective can be larger than the critical angle. Focusing the light in the center of the back focal plane of the objective, generates a collimated beam after passing the objective. By changing the focusing position on the focal plane of the objective from the middle to the edges, the light is leaving the objective under a certain angle. The angle can be adjusted by changing the distance of the incoming light from the center of the objective. The evanescent wave starts on top of the coverslip, because the coverslip has the same refraction index as the objective and, therefore, the interface with the different refraction index is on top of the coverslip. The sample is placed directly on the coverslip. This approach has the advantage that biological structures like cells can be measured easily, but bigger structures are problematic due to the limited excitation depth.

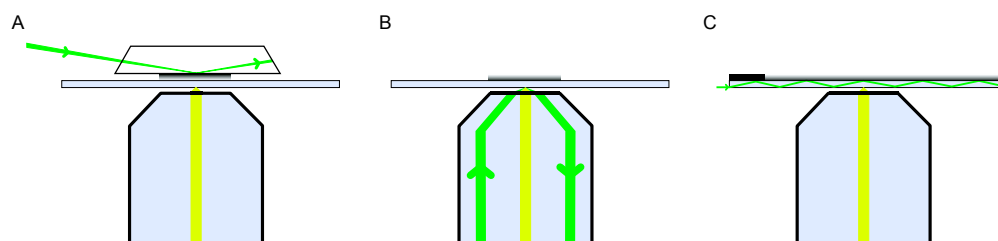


Figure 3.14: Various TIRF modalities. (A) In a prism type TIRF microscope, the evanescent wave starts on the bottom of the prism. (B) In the case of objective type TIRF, the evanescent wave starts from the coverslip. (C) The waveguide TIRF is generated by using the coverslip as a waveguide. The light is coupled into the coverslip on one side and the light with a smaller angle than the critical angle is absorbed by a black rubber on the starting end of the waveguide. The evanescent wave is starting again from the coverslip. The green beam represents the excitation light, which is reflected. The fluorescence signal is presented in light green.

The last approach to create a TIRF excitation is to use a waveguide [Ramachandran et al., 2013]. In Figure 3.14C one example for a waveguide is given. There the coverslip with the sample on top acts as a waveguide. The excitation light is coupled in on one side of the coverslip. Light with an angle smaller than the critical angle is absorbed by a black rubber on the starting end of the waveguide. The remaining light is totally reflected in the coverslip and induces an evanescent field on top of the coverslip. The advantage is that the illumination is homogeneous. Nevertheless, to generate an evanescent field with higher power needs further improvements that makes the excitation more complicated.

### 3.5 SpFRET using TIRF microscopy

SpFRET measurements, as described above, are done in solution and, therefore, give a snapshot of the molecule. To collect information about a single-molecule and how the conformation changes over time, a TIRF system is needed. The molecule of interest has to be fixed to the surface. There are multiple ways of immobilizing the molecule, two are commonly used in

combination with spFRET in our laboratory: First, by direct binding, which can introduce unwanted interactions between the molecule and the surface and, therefore, a loss of functionality. Second, by encapsulating the molecule in vesicles and immobilize then the vesicles on the surface. The following section focuses on the use of prism type TIRF with encapsulation of the labeled molecule.

### 3.5.1 Prism type TIRF

A home-build microscope setup, build by Peter Schlüsche, was used for spFRET TIRF measurements. A scheme of the whole setup is depicted in Figure 3.15. For the excitation, the 532 nm line of a diode-pumped solid-state laser (Cobolt Samba 532 nm, Cobolt, Solna, Sweden) is coupled into a single mode fiber (optimized for 532/647 nm OZ Optics, Carp, Canada). The fiber has the advantage that it cleans up the beam profile and decouples the alignment of the lasers from that of the excitation pathway. The laser is then focused by an achromatic lens on a quartz prism and hits the bottom part of the prism above the critical angle, which corresponds to an exponential decay depth  $d$  of about 100 nm. The evanescent wave excites the molecules in the sample chamber. The sample chamber is formed by a sandwich between the quartz prism and the coverslip using nescofilm, where a channel is cut in.

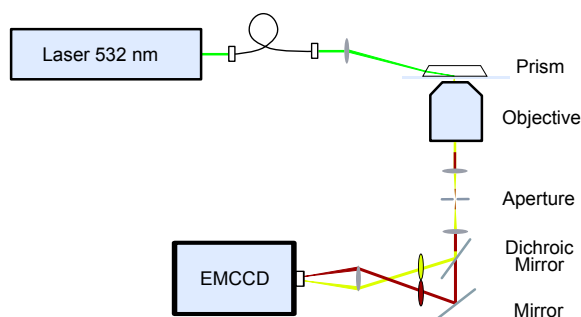


Figure 3.15: Prism type TIRF setup. The laser is coupled into a fiber, recollimated, focus by a lens into the prism, hits the lower side of the prism above the critical angle and introduces an evanescent wave in the sample channel. The fluorescence is collected by an objective, split by color and detected by an EMCCD camera.

The fluorescence signals from the donor and acceptor, due to FRET, are collected by a water immersion objective (CFI Plan Apochromat 60x WI, NA 1.2, Nikon). The objective is positioned below the prism and coverslip. The detected signal is focused by the tube lens ( $f = 200$  nm) of the microscope (TE 2000-U, Nikon). In the image point, a rectangle aperture is placed to cut the signal into a rectangular shape, which allows to place images of two channels next to each other on one chip of the same camera. The light is collimated by a second achromatic lens ( $f = 100$  nm). A dichroic mirror (630DCXR, AHF) is used to split the signal by wavelength. The donor signal is reflected to the camera. The FRET signal in the red channel passes through the dichroic mirror and is then reflected by a mirror to the camera. The fluorescence is cleaned up by a notch filter for both channels (z532/633rpc, AHF) and an additional emission filter per channel (HQ585/80 (green) and HQ715/150 (red), AHF). The different fluorescence signals are then focused ( $f = 200$  nm) on different regions of an EMCCD camera (iXon +, Andor Technology, Belfast, UK).

### 3.5.2 Surface preparation and immobilization

For performing prism type TIRF experiments, the prism has to be connected by a nescofilm with the coverslip and, thus, the channels are generated. Additionally, the surfaces have to be treated in a way that unspecific binding is avoid and the vesicles, encapsulating the molecule of interest, bind reproducibly. Therefore, the surfaces of the sample chambers have to be cleaned and treated with silane and polyethylene glycol (PEG, Sigma-Aldrich, Munich, Germany) to avoid unspecific interactions between the sample and the surfaces. A scheme of the immobilization is shown in Figure 3.16.

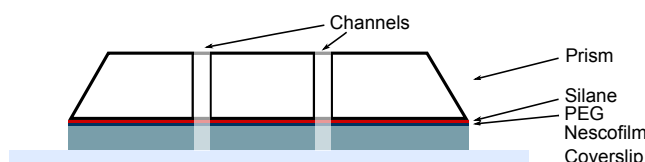


Figure 3.16: Prism preparation and immobilization. The lower side of the prism is treated with silane and PEG to protect the surface for unwanted interactions with the sample. The nescofilm forms the channels, which are sealed by a coverslip.

In the first step, the prisms have to be cleaned with 2 % Hellmanex II (Sigma-Aldrich) to remove all protein rests by heating the solution with the prisms inside in a microwave for two minutes and washing afterwards three times with ddH<sub>2</sub>O. Next, the surfaces are cleaned with a mixture of two parts hydrogen peroxide, H<sub>2</sub>O<sub>2</sub>, and one part hydrogen chloride, HCl. The prisms are kept in this solution for about 45 - 60 min. To get rid of any remaining chemicals, the prisms are washed again with ddH<sub>2</sub>O and dried with nitrogen. The next cleaning step is flaming the prisms. The coverslip, which is used to close the chamber, is cleaned in the same way with Hellmanex II and ddH<sub>2</sub>O and is dried afterwards with nitrogen.

The surface passivation starts with silanization of the prism. 2 % aminosilane in acetone is placed in a petri dish and the prisms are added. Incubation is performed in a closed container for about 20 - 30 min till the acetone is evaporated. Afterwards the prisms are washed again with ddH<sub>2</sub>O and dried with nitrogen. Next, the surface has to be treated with PEG. Approximately 3 - 4 % biotinylated PEG was mixed with normal PEG and one capsule of carbonate-bicarbonate buffer (COO<sup>3</sup>, Sigma-Aldrich) solved in 1  $\mu$ l ddH<sub>2</sub>O per 1 mg PEG. The solution is centrifuged for 2 min at 14000 rpm and added on the bottom side of one prism and a second prism is placed on top of the solution. The prisms are incubated for 30 min at a high humidity, to avoid drying of the PEG. Afterwards, the prisms are washed with ddH<sub>2</sub>O and dried with nitrogen a last time. The nescofilm with the cut channels is placed between the prism and the cleaned coverslip and heated for 10 s to make the nescofilm sticky and, therefore, the prisms are tightly sealed with the coverslip.

### 3.5.3 Encapsulation by vesicles

As mediated above, there are two different possibilities to immobilize the molecules of interest on the surface. The molecule can be labeled with biotin, which binds to a streptavidin that is bound to an immobilized biotin on the surface. This has the advantage that the molecule can easily be given to the sample holder without any further steps. One of the problems with this

immobilization is that the molecule needs a biotin. Another big problem can be the possible interaction of the molecule with the surface and, therefore, it could be that the molecule is not functional anymore. To avoid these disadvantages, the molecule can be encapsulated in vesicles [Boukobza et al., 2001], [Okumus et al., 2004]. Therefore, the molecule is in a closed environment with its interaction partners and can not interact with the surface. Furthermore, no additional labeling with biotin is needed. However, this method can cause difficulties due to nonfunctional and destroyed molecules because of the extruding during the process of making the vesicles. Additionally, some of the molecules tend to stick to the vesicles and, therefore, have the same problems like the molecules on the surface. Thus, every protein has to be tested, which method works best for it. For the used protein in this work, the second method was chosen to measure proteins by TIRF microscopy, because the proteins seems to diffuse freely in the vesicles.

For encapsulation of molecules, the used lipids have to be mixed and prepared ahead of time.  $10 \frac{\text{mg}}{\text{ml}}$  1,3-Dioleoyl-sn-glycero-3-phosphocholine (DOPC, Avanti Polar Lipids, Alabaster, USA) is mixed with  $250 \frac{\mu\text{g}}{\text{ml}}$  1,3-dipalmitoyl-sn-glycero-3-phosphoethanolamine-N-(cap biotinyl) (sodium salt) (PE, Avanti Polar Lipids). These two components are diluted in chloroform and filled in a test tube. The chloroform is evaporated under a stream of nitrogen and any remaining chloroform is removed by applying a vacuum to it. The resulting films are hydrated at room temperature for 30 min with 200 - 340 nM fluorescently labeled molecules in buffer. Multilamellar vesicles are formed in the solution. They are extruded 31 times through a polycarbonate membranes with a pore diameter of 200 nm using an extruder (Mini-Extruder Set, Avanti Polar Lipids) to make unilamellar vesicles with a diameter of 200 nm. To separate the vesicles from free molecules, an Amicon spin column (Merck Millipore, Billerica, Massachusetts, USA) with a molecular weight cutoff of 100 kDa is used.

Before these vesicles can be brought to the channels of the prism, the channels have to be incubated with  $0.3 \frac{\text{mg}}{\text{ml}}$  streptavidin for 20 min. In the mean time the channel surfaces are bleached by a laser. After washing with the measurement buffer, the vesicles can be flushed into the channels. Figure 3.17 depicts (not in scale) a molecule in the vesicle bound to the surface.

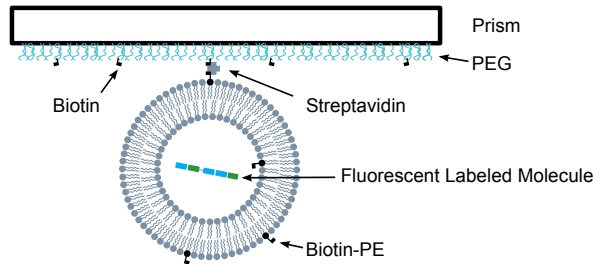


Figure 3.17: Molecule encapsulated in a vesicle. The vesicle is bound by biotin-streptavidin-biotin to the surface passivated with PEG. The scheme is not in scale.

### 3.5.4 Data analysis

The data analysis of single-molecule measurements on a surface is performed with the MATLAB program 'Trace Intensity Analysis' (TRACY) written by Gregor Heiss in our group. To analyze the dynamics of a single-molecule, the intensity in the donor and acceptor channel

have to be extracted. Therefore, the two channels have to be mapped to find the corresponding area in the acceptor and the donor channel. For calculating the map, fluorescent beads are imaged after the measurement each day. Distortions between the two channels can be fitted by a third-order polynomial. With the map, the acceptor channel can be rotated and distorted till it fits to the donor channel. This mapping is then used for all measurements on this particular day to get the right corresponding coordinates in the two channels.

To avoid counting molecules, which have a fluorescent signal in both channels but are not due to the fluorescent labeled molecule, a threshold, which is higher than the background resulting from this molecules, is chosen. Before the threshold is used, the local background around the molecule of interest is subtracted from the intensity. Furthermore, blinking can occur due to the photophysics of the dyes. To take this into account, the intensity of the single images is summed up over 200 images of the movie and the mean intensity is calculated. Thus, molecules that are bleached after a few frames are very dim. The mean intensity has to be higher than a certain threshold to discard background signals and low enough to include as most as possible molecule in the further analysis. We choose that the signal has to be two times higher than the background.

Now all molecules with a signal higher than the threshold are selected. The identified molecules were tested according for their shape. A dye molecule, which is smaller than the PSF is expected to be detected as round. The central pixel is calculated and a circle of seven by seven pixels around the mean pixel is selected. A ring of pixels around the molecule area is used as the local background. If two molecules are too close together or a molecule with a non-round shape is found, the intensity in the background is not constant and, thus, the molecules are removed from the further analysis. For the rest of the selected molecules, the intensity of the circle is plotted over time.

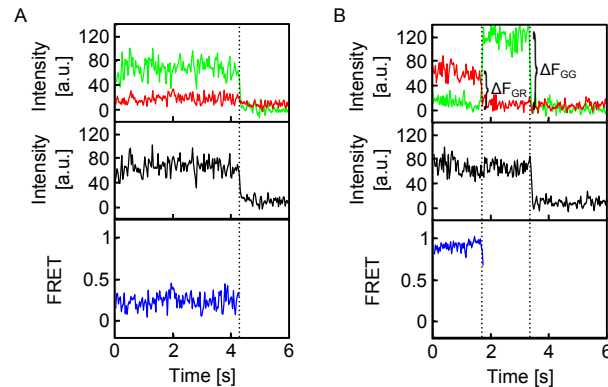


Figure 3.18: Time traces of non-dynamic molecules. Time traces of the background corrected donor intensity (green), acceptor intensity (red, upper graphs), total intensity ( $I_{total} = F_{GR} + \gamma F_{GG}$  where  $\gamma$  is the detection correction factor, black, middle graphs) and FRET efficiency (blue, lower graphs) are shown. **(A)** Characteristic trace where the donor bleaches first and, therefore, the donor and acceptor signals disappear simultaneously due to missing energy transfer. **(B)** A characteristic trace where the acceptor bleaches first. The acceptor signal decreases and the donor signal increases to keep the total intensity constant. From such traces, the detection factor  $\gamma$  can be determined.

The resulting time traces are sorted manually. All time traces where more than one bleaching step is observed are discarded from the analysis. Furthermore, all traces with varying total intensity are discarded. The remaining traces can be sorted into two groups. On the one hand, the donor bleaches first and, therefore, the acceptor signal also decreases to the background level, due to no remaining energy transfer (Figure 3.18A). On the other hand, the acceptor bleaches first and, therefore, the donor signal increases, due to the missing FRET process. After a while the donor bleaches too and the signal decreases to the background level (Figure 3.18B).

For calculating the FRET efficiency from the single time traces, Equation (3.35) can be used. To do this, the correction factors have to be determined from the measurements and applied. The direct excitation can be calculated from a measurement using ALEX excitation, when the donor bleaches first.

$$\alpha = \frac{F''_{GR}}{F_{RR}} \quad (3.69)$$

$F''_{GR}$  is the intensity in the acceptor channel before the donor is bleached.  $F_{RR}$  is the signal in the acceptor channel after acceptor excitation. For the used setup with a laser power of 2 mW for the red laser and 10 mW for the green laser and the dye ATTO 647 the direct excitation can be calculated as 0.037.

The second correction factor describes the spectral cross talk. It can be calculated from the measurements where the acceptor bleaches first and then the donor bleaches afterwards. The mean signal in the acceptor channel  $\overline{F'_{GR}}$ , after the acceptor bleached, but before the donor bleaches, is divided by the mean in the donor channel  $\overline{F'_{GG}}$  under the same conditions (between the two dotted lines in Figure 3.18B).

$$\beta = \frac{\overline{F'_{GR}}}{\overline{F'_{GG}}} \quad (3.70)$$

This value cannot be calculated for all traces, because the acceptor has to bleach first. To apply this correction factor to all traces, the mean value of all possible traces is calculated and then used for all traces of one measurement. For measurements on the described setup with ATTO 532,  $\beta$  was typically around 0.03.

The last correction factor,  $\gamma$ , describes differences in the sensitivity of the different detection channels. It can be calculated from traces where the acceptor bleaches first.  $\gamma$  is defined as the relationship between the decrease of the intensity in the acceptor channel, when the acceptor bleaches ( $\Delta F_{GR}$ ) and the resulting donor intensity after acceptor bleaching ( $\Delta F_{GG}$ ), both background corrected (Figure 3.18B).

$$\gamma = \frac{\Delta F_{GR}}{\Delta F_{GG}} \quad (3.71)$$

For the traces the acceptor bleaches first, we calculated  $\gamma$  and applied the value to the corresponding trace. To correct the other traces, the mean value of  $\gamma$  is used. For the dye pair ATTO 532 and ATTO 647,  $\gamma$  is approximately 1. For a suitable value of  $\gamma$ , the total intensity (Figure 3.18, black line) is constant during the whole trace, till the donor bleaches.

$$I_{total} = F_{GR} + \gamma F_{GG} \quad (3.72)$$

Furthermore, we can distinguish between dynamic and static traces. Static traces mean that the fluorescent signal in both channels show no detectable fluctuations during the whole time

of measurement. This can be due to different reasons. The fluctuations are too small to distinguish them from the noise or the fluctuations are too fast for measuring them on the previously described setup. Another possibility could be that the fluctuations are too slow and can not be detected till the time the dye photo bleaches. Dynamic traces mean that the molecule changes its conformation during the measurement, which introduces a change in the FRET efficiency and, therefore, in the relationship between the intensities in the donor and the acceptor channel.

### 3.5.5 Hidden Markov Model - HMM

A Markov process is a time-dependent random process. A set of parameters can be transferred with the transition probability to another state. This transition does not depend on its past history. A Markov model becomes hidden when not only the transition probability, but also the states themselves are unknown when there is too much noise. This model is called Hidden Markov Model (HMM) and was developed in the 1960s [Baum and Petrie, 1966] for voice recognition. With the help of HMM, the dynamic FRET traces from measurements on the TIRF can be analyzed [McKinney et al., 2006].

In theory, the FRET states are well defined, but in reality, we get a broadening in the FRET distribution due to experimental noise. This makes it hard to distinguish between different states. In the case of FRET traces the real states are hidden under the noise. To digitalize the noise of a trace, a HMM can be used and the traces are fitted to determine the real states that are hidden. Furthermore, we assume that transitions are governed by single exponential decay kinetics and, therefore, a Markov process is given. To describe the probability of a molecule that changes the state from one time point to the next or stays in the same state, we need the transition probability ( $tp_{x \rightarrow y}$  where  $x$  represents the starting state and  $y$  the ending state). All probabilities together form the transition probability matrix.

$$tp = \begin{pmatrix} tp_{A \rightarrow A} & tp_{B \rightarrow A} & \dots \\ tp_{A \rightarrow B} & tp_{B \rightarrow B} & \dots \\ \vdots & \vdots & \ddots \end{pmatrix} \quad (3.73)$$

The second required probability is the emission probability. It describes the relative likelihood of observing a FRET value ( $FRET_{data}$ ) when the system is in a conformation  $\Phi$ . The noise introduced FRET distribution can be described by a Gaussian distribution with the width of  $\delta$ . The emission probability is therefore given as

$$ep_{\Phi}(FRET_{data}) \propto \exp \left[ -2 \cdot \left( \frac{FRET_{data} - FRET_{\Phi}}{\delta} \right)^2 \right] \quad (3.74)$$

With these two probabilities, we can calculate the total probability that a trace can be described by a given state combination  $\alpha(i)$  at one time point  $i$ .

$$prob(i) = ep_{\alpha(i)}(FRET_{data}(i)) \cdot tp(\alpha(i), \alpha(i+1)) \quad (3.75)$$

The probability for the whole trace is then given by

$$total = \prod_{i=1}^N prob(i) \quad (3.76)$$

The total probability is calculated for all possible combinations and, then, the fit with the highest total probability is chosen. To calculate all possible combinations for one trace with  $N$  data points using a two state system, it would take on the order of  $2^N$  ( $O(2^N)$ ) calculations. With the help of the Viterbi algorithm [Viterbi, 1967], the computational power can be reduced to the order of  $N$ .

The problem with this concept is that the FRET states in a real experiment ( $FRET_A$ ,  $FRET_B$ ) and the distribution of the states are unknown. The transition probability is the value, which we want to calculate with the HMM. Therefore, the model parameters ( $FRET_A$ ,  $FRET_B$ ,  $\delta$ ,  $tp_{A \rightarrow B}$  and  $tp_{B \rightarrow A}$ ) need to be varied till the maximal total probability is reached. This can be done using Brent's algorithm [Press et al., 1992]. As a starting parameter, the transition probabilities from one state to another are chosen as 0.005 and the FRET states are defined as uniformly distributed between 0 and 1. By using all traces of an experimental condition of a single day, a global HMM analysis was performed.

To visualize the different transitions of a single trace or of a whole batch of traces with molecules under the same conditions, we use the transition density plot (TDP). It is a two-dimensional pseudo-histogram (Figure 3.19). The horizontal axis corresponds to the starting FRET value and the vertical axis to the final FRET values. The color represent how often a transition is found in the analyzed traces (blue to red). The width of the distributions in the TDP are representing the standard deviation of the fit, due to small fluctuations in the intensity in a real state. Additionally, the transition rates are calculated. The HMM analysis gives back the fit of the traces. Therefore, it is known how long a molecule stays in one particular state and when it interchanges. The cumulated dwell time can be fitted by a mono- or bi-exponential curve and, thus, the transition rates are calculated.

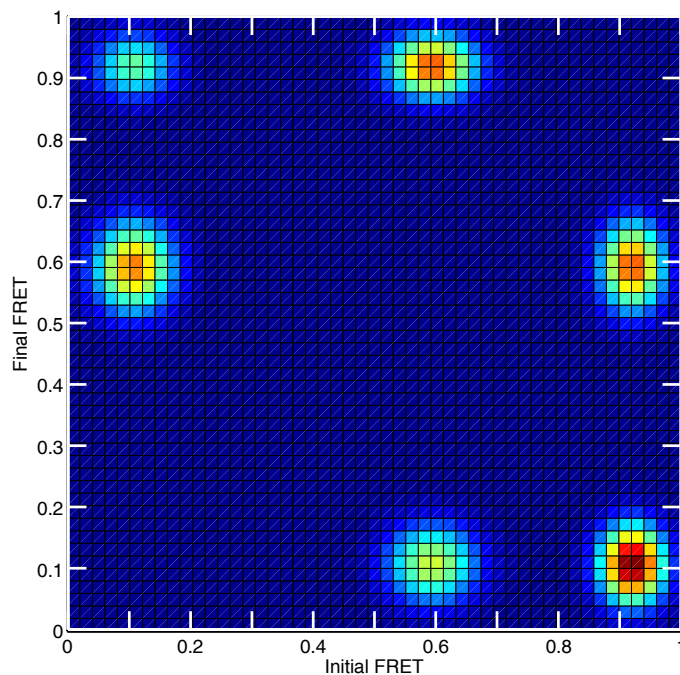


Figure 3.19: Transition density plot. A three state system with FRET efficiencies at 0.1, 0.6 and 0.92 fitted by HMM. The color represents from blue to red how likely a transition is detected.

# 4 Protein folding

## 4.1 Protein

Genetic information flows from DNA to RNA to proteins. In the first step, a gen from the DNA is copied to messenger RNA (mRNA). This process is called transcription. Next, a ribosome decodes the mRNA and produces a polypeptide chain (translation). The resulting polypeptide chain is a string of single amino acids. [Hebert and Molinari, 2007]

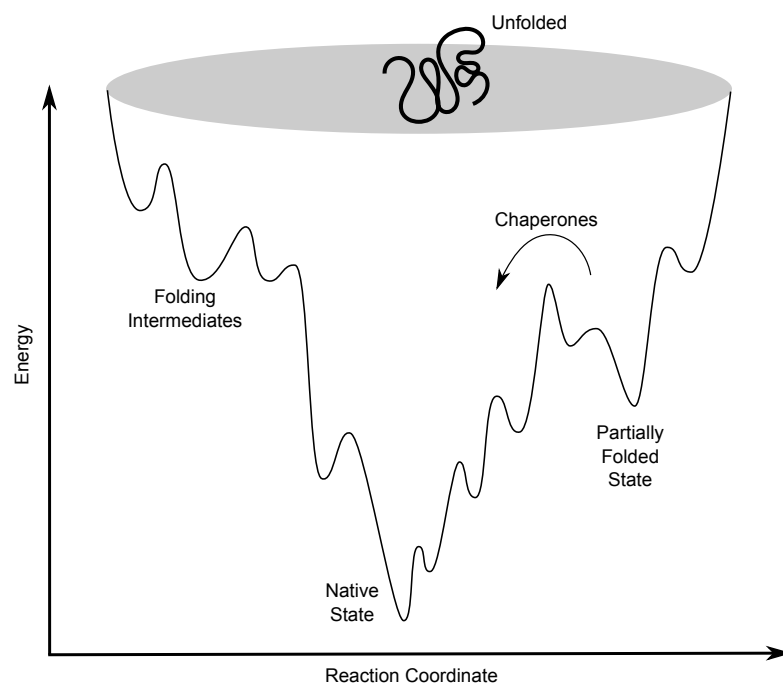


Figure 4.1: The energy landscape of protein folding. An unfolded protein reduces its energy by folding. If it does not reach the total minimum by its own, chaperones can overcome energy barriers and, therefore, help the partly folded protein to reach its final structure, the native state.

There are more than 20 natural amino acids, which form different polypeptide chains. Each chain is specific for one protein and unique in length and amino acid sequence. To form a chain, the carboxy group of one amino acid binds to the amino group of the second amino acid by freeing up one water molecule. The polypeptide chain is called the primary structure of the protein. Interactions between amino acids close to each other can introduce structures like  $\alpha$ -helices or  $\beta$ -sheets. These structures are called secondary structures. In the next structural level, the tertiary structure, amino acids that are further apart interact with each

other and form completely folded domains. The interactions can be non-covalent, interactions such salt bridges, van-der-Waals forces or hydrogen bonds, or can be covalent, like disulfide bridges. If a protein consist of multiple domains the final three dimensional structure, i.e. the combination of the single domains, is the quartary structure, which combines different folded domains to the whole folded protein.

When we talk about protein folding, we refer to a polypeptide chain that builds a final tertiary structure that is thermodynamically preferred. If this process was done by a random search, even for a small 150 residue protein and a folding speed as little as 1 fs per search step, the folding would take several orders of magnitude longer than the age of the universe. In reality, a small protein folds spontaneously on a millisecond to microsecond timescale (Levinthal's paradox) [Levinthal, 1969]. Thus, there must be different mechanisms in folding than trying all possible cominations. One idea to overcome this contradiction is that small areas start folding and stay in this conformation after folding. All the partly folded areas are then rearranged till the whole protein is folded. For parts of the proteins in a cell, this concept is enough to fold correctly, but other proteins need further assistance. This assistance is done by supporting molecules, so called chaperones. Chaperones can overcome energetic barriers and, therefore, inhibit the formation of aggregates and help the protein to fold in the right order [Kim et al., 2013]. The whole folding process can be described by an energy funnel with decreasing free enthalpy, e.g. Gibbs energy (Figure 4.1) [Hebert and Molinari, 2007].

## 4.2 Molecular chaperones

Chaperones can bind to and interact with an unfolded or partly folded protein and protect charged regions to avoid aggregation and misfolding [Feldman and Frydman, 2000]. They are part of the quality control of a cell and classified into different groups by their sequence homology. Most of the chaperones are heat shock proteins (Hsps). The production of Hsps increase when the cell is heated up or undergo other conditions of stress. This is important because, on the one hand, some proteins start refolding at higher temperatures than the physiological one. On the other hand, the tendency for aggregation increases at higher temperatures.

Chaperones have different functions: They support the folding of nascent proteins or help to transport proteins to different areas in the cell because folded proteins cannot pass most membranes. Additionally, they are involved in assembly and disassembly of protein complexes [Lindquist and Craig, 1988], [Doyle et al., 2013].

The members of the Hsp family are named according to their molecular weight. The most famous proteins are Hsp40, Hsp60, Hsp70, Hsp90 and Hsp100. Some proteins can be folded by one of these chaperones, others need multiple chaperones for reaching the final conformation. If different chaperones have to work together to fold a protein, cochaperones are needed to connect multiple chaperones. Additionally, the folding can be also affected by nucleotide exchange factors (NEFs) or other interaction partners. [Kim et al., 2013]

In this study we focused on different chaperone related questions. For example, the first interaction partners in eukaryotes of the unfolded or partly folded proteins are, when chaperone assistance is required, Hsp70 and Hsp90. Thus, the interaction with Hsp70 and the transfer to Hsp90 was studied. Furthermore, in bacteria, Hsp70 interacts with a Hsp60 called GroEL. Unfolded proteins can be trapped in the cavity of GroEL closed by its cochaperone GroES. Inside

the cavity folding is mediated. To understand how the GroEL-GroES complex acts, this system was also studied. [Sigler et al., 1998], [Buck et al., 2007], [Hebert and Molinari, 2007]

### 4.2.1 Hsp70

One of the major classes of molecular chaperones in bacteria and eukaryotic cells is the Hsp70 family. It is an important part of the folding machinery in a cell and does not only work under stress conditions. The Hsp70s can be found in all forms of life. The sequence identity is about 70 % between the different organisms. However, the Hsp70s from different organisms can not be exchanged. Hsp70 is hosted in different regions of the cell, such as in the mitochondria, the chloroplasts or the endoplasmic reticulum (ER) [Wegele et al., 2004]. Two different classes of Hsp70s are distinguishable. Some fulfill important functions under physiological conditions and others are important under stress conditions [Wegele et al., 2004].

The crystal structure of the Hsp70 in the ER is depicted in Figure 4.2. All Hsp70 have two domains, a nucleotide binding domain (NBD, red) and a substrate binding domain (SBD, green). These two domains are connected by a short flexible linker (purple). The NBD binds with a high affinity to ATP and ADP. The different nucleotides induce opening and closing of the binding pocket of the SBD by an alpha-helical lid (blue).

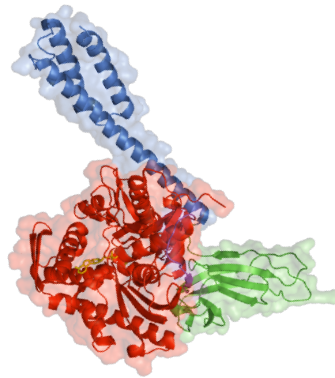


Figure 4.2: Crystal structure of Hsp70 in the ER. The domain architecture of the Hsp70 in the ER binding ATP is shown in the crystal structure (PDB-ID: 5E84). The NBD is depicted in red, the SBD in green, the lid in blue and the linker between NBD and SBD in purple.

The SBD interacts with a low affinity with a substrate in the ATP bound state by van der Waals contacts between the side chains of Hsp70 and the side chains of the unfolded polypeptide [Wegele et al., 2004]. By hydrolyzing ATP to ADP, the affinity increases and the Hsp70s can assist the folding of the substrate. They prevent substrate aggregation by binding to hydrophobic patches of the substrate molecule, which shields them from deleterious inter- and intramolecular interactions. Additionally, they promote folding to the native state. Hsp70-dependent protein folding occurs on the timescale of minutes or longer and aids folding in two different ways. The Hsp70s keep the concentration of free substrate low due to repetitive binding and release of substrate. This results in preventing the substrate from aggregating, while allowing free molecules to fold in the native state. Furthermore, the binding of the

substrate to the Hsp70 induces local unfolding in the substrate, e.g. the untangling of a misfolded  $\beta$ -sheet, which helps to overcome the kinetic barrier for folding to the native state. Additionally, Hsp70s can increase the solubilization and, therefore, assist refolding of aggregated proteins. [Mayer and Bukau, 2005]

The human Hsp70 in the ER, the Binding immunoglobulin heavy-chain Protein (BiP), is used for the work in one part of this thesis. BiP has different functions. It can gate the ER translocon pore, the gateway between the ER and the lumen. To fulfill the gating function, an ADP bound BiP binds to the ER side of the pore and close it. The pore will be filled from the cytoplasm side with a nascent chain. When the chain reaches a certain length, the ADP is exchanged by an ATP and BiP opens up the pore again. The nascent chain is released into the ER and the cycle can start again. [Alder et al., 2005]

When a misfolded protein is in the ER, it has to be brought back to the cytosol for degradation. There, the 26S proteasome digests the misfolded protein. In this cycle, BiP is also involved in catching the misfolded protein in the ER and transporting it to the membrane. [Hebert and Molinari, 2007]

Another very important function of BiP is to assist nascent proteins upon translocation in the ER. Therefore, BiP binds to the charged regions of the unfolded protein, when ATP is bound. The affinity for binding increases when ATP is hydrolyzed to ADP and the binding pocket closes. The unfolded protein is then caught. Thus, BiP protects the charged regions from aggregation and unspecific interactions. The unprotected regions can fold in a proper way. When ADP is released, the binding domain for the nascent chain opens again and the not completely folded protein is released. [Hebert and Molinari, 2007], [Behnke et al., 2015]

Hsp70 does not work in a cell on its own, but rather interacts with a large set of cochaperones, like Hsp40 or J-proteins, and nucleotide exchange factors, like BAP. Additionally, Hsp70 is just a part of the folding machinery and interacts with other chaperones, like Hsp90. [Lindquist and Craig, 1988]

## 4.2.2 Hsp90

Another member of the chaperone family is called Hsp90. It facilitates the final protein maturation, but is not required for *de novo* folding. It exists in different parts of the cell and in different organisms. In yeast, two isoforms of the Hsp90 exist, Hsc82 and Hsp82. The Hsp90 analog in the endoplasmic reticulum of mammalian cells is called Grp84. Hsp90 is involved in the assembly of small nuclear ribonucleoproteins and RNA polymerase, the protein import in mitochondria and chloroplast, the nuclear migration and melanoma progression. It interacts with various clients that are involved, for example, in viral infections, innate immunity and RNA modification. Thereby, Hsp90 helps to fold the client protein correctly, to activate or transport it, or even trigger its degradation. Posttranslational modifications such as phosphorylation, acetylation, nitrosylation and methylation influence the function of Hsp90 and, thus, the maturation of client proteins. In addition, Hsp90 plays a crucial role in the progression of diseases. It is known that the expression of Hsp90 is 2- to 10-fold higher in tumor cells than in normal cells. [Shiau et al., 2006], [Li and Buchner, 2013]

Hsp90 is a homodimer and each subunit consists of three flexibly linked regions. This structure is the same from bacteria to human and is depicted in Figure 4.3. The first domain is the N-terminal ATP-binding domain (N-domain). The nucleotide binding pocket can be opened and closed by a lid depending on the nucleotide state. The second domain, the middle domain (M-domain), is important for the ATP hydrolysis. Additionally, this domain contributes to

the interaction sites for client proteins and co-chaperones, like Sti1. The last domain is the C-terminal dimerization domain (C-domain). This domain is essential for the dimerization of Hsp90 and has a MEEVD motif, which serves as docking site for tetratricopeptide repeat (TPR) domains in co-chaperones. [Shiau et al., 2006], [Li and Buchner, 2013]

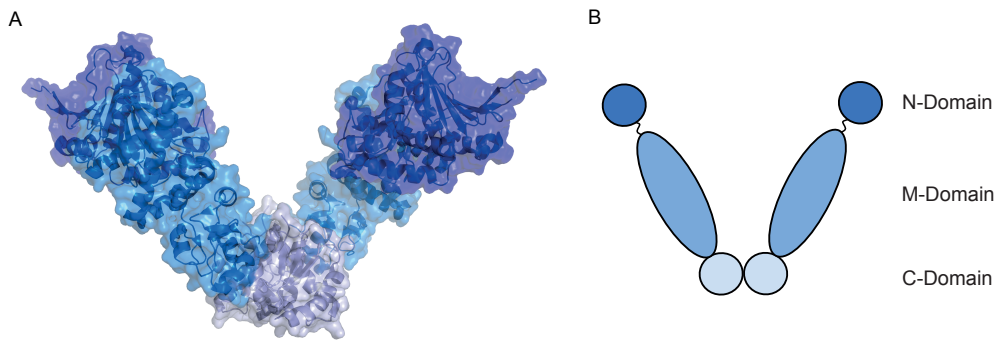


Figure 4.3: Crystal structure of Hsp90. (A) The open conformation of the full-length Hsp90 from *E. coli* (HtpG, PDB-ID: 2IQO). (B) A cartoon representation of Hsp90 shows the different domains. The N-domain is depicted in dark blue, the M-domain in middle blue and the C-domain in light blue.

Nucleotide binding introduces conformational changes [Richter and Buchner, 2006], [Shiau et al., 2006]. In the *apo* state, Hsp90 stays in the open conformation, the V-shaped form. Upon binding of ATP, the lid closes but the rest of the N-domain remains open. The N-domain dimerizes and due to this dimerization, the M-domain repositions and interacts with the N-domain. In the next step, the Hsp90 reaches its final conformation, the closed conformation. In this closed form, ATP is hydrolyzed, the N-domains dissociate and ADP as well as the inorganic phosphate are released. The Hsp90 returns back to the open *apo* conformation. This chaperone cycle can be regulated by different co-chaperones, like Hop [Southworth and Agard, 2011] or p23 [Morgner et al., 2015]. They inhibit or activate the ATPase and are responsible for the recruitment of clients.

### 4.2.3 GroEL with the co-chaperone GroES

GroEL, the Hsp60 chaperone in bacteria, forms a cavity for protein folding and acts in an ATP-dependent manner. It has a barrel-shaped form and is a ~800 kDa large tetradecameric protein complex.

GroEL consists of three domains, the apical domain, the intermediate domain and the equatorial domain. Seven subunits form a ring and two rings interact via the equatorial domains, forming the entire GroEL complex (Figure 4.4, red and blue structure) [Sigler et al., 1998]. The most important interaction partner of GroEL is the co-chaperone GroES. It acts as a kind of a lid and can open and close the GroEL barrel. It is a heptamer of 10 kDa subunits and has a dome-shaped architecture (Figure 4.4, green structure). Each subunit consists of a core  $\beta$ -barrel structure with two  $\beta$ -hairpin loops.

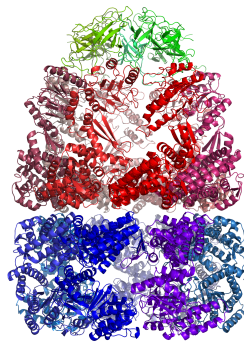


Figure 4.4: Crystal structure of the GroEL/GroES complex. The GroES is depicted in green. GroEL consist of two ring-like structures, depicted in red and blue.

From previous studies, the chaperone cycle is known [Sigler et al., 1998] (Figure 4.5). In the absence of any nucleotide and GroES, a hydrophobic surface inside the ring is responsible for catching an unfolded protein. From previous studies, the chaperone cycle is known [Sigler et al., 1998] (Figure 4.5). In the absence of any nucleotide and GroES, a hydrophobic surface inside the ring is responsible for catching an unfolded protein. Next, seven ATP molecules, one per subunit, bind to the equatorial domain of this ring. It induces conformational changes. Therefore, the ring with bound substrate is called *cis* ring. The GroEL twists anticlockwise by  $60^\circ$  [Sigler et al., 1998], which increases the affinity of the apical domain to the co-chaperone GroES. When a GroES molecule binds to GroEL, the substrate is encapsulated in the *cis* ring. Furthermore, the binding of GroES induces a clockwise twist by  $120^\circ$ . This increases the hydrophilicity of the inner surface and, therefore, promotes the folding of the substrate. In the next step, the seven ATP molecules are hydrolyzed to ADP. The GroES and ADP released from the *cis* ring is triggered by the binding of seven new ATP molecules to the opposite side of the GroEL, to the *trans* ring. Then, the substrate is released, *cis* and *trans* ring exchange their function, i.e. the *trans* ring becomes the new *cis* ring, and the cycle can start again. The overall cycle is depicted in Figure 4.5. Nevertheless, the binding and unbinding of GroES occurs every 10 to 15 s and multiple cycles per substrate are needed to fold the protein to its right conformation, because only 5 % of the molecules are properly folded, when they are released [Sharma et al., 2008].

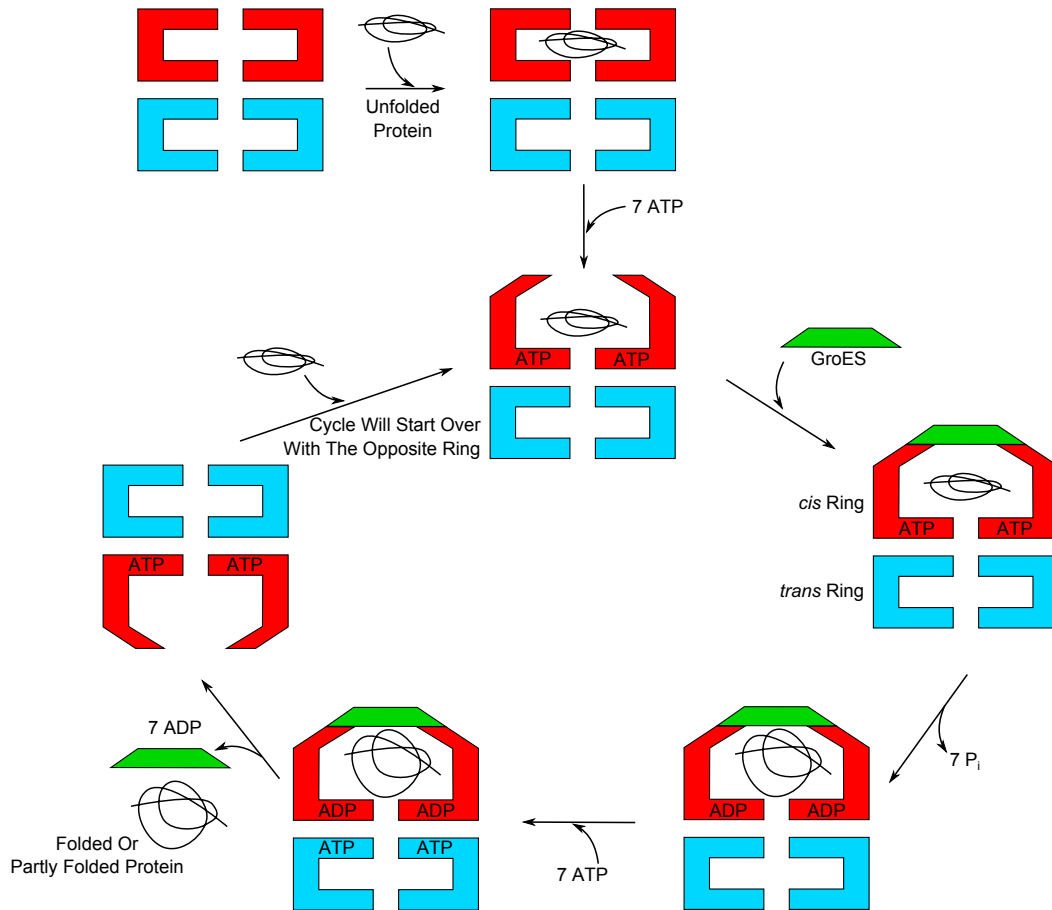


Figure 4.5: Nucleotide cycle of the GroEL/GroES complex. GroEL consist of two ring-like structures, the *cis* and the *trans* ring, which are depicted in red and blue, respectively. An unfolded protein can bind to the *cis* ring. Upon addition of seven ATP molecules, one per GroEL subunit, the conformation of GroEL changes and GroES, depicted in green, can bind and close the GroEL cavity. The GroES binding induces the hydrolysis of the seven ATP molecules to ADP. Inside the cage, the unfolded protein can change its conformation to a folded or partly folded conformation. Next, seven ATP molecules bind to the *trans* ring inducing the release of GroES, the seven ADP molecules and the folded or partly folded protein. The cycle will start over with the opposite ring.



# 5 BiP's interaction with BAP

## 5.1 Introduction

Molecular chaperons play an important role in protein folding, disassembling of aggregates and translocation. The Hsp70 in the human endoplasmic reticulum (ER) is called Binding immunoglobulin heavy-chain Protein (BiP, also known as Grp78 or HSPA5) [Lindquist and Craig, 1988]. It is the only Hsp70 that is located in the ER.

BiP consists of two binding domains. The N-terminal nucleotide binding domain (NBD) is connected by a flexible short linker with the substrate binding domain (SBD). The substrate binding cleft of the SBD can be closed or opened by an  $\alpha$ -helical lid at the C-terminal end. The overall structure of BiP is known from the crystal structure in the presence of bound ATP (PDB-ID: 5E84, [Yang et al., 2015], Figure 5.1A). Additionally, there are crystal structures of the NBD without a nucleotide (PDB-ID: 3LDN), with ADP (PDB-ID: 3IUC) and with ATP (PDB-ID: 3LDL) available.

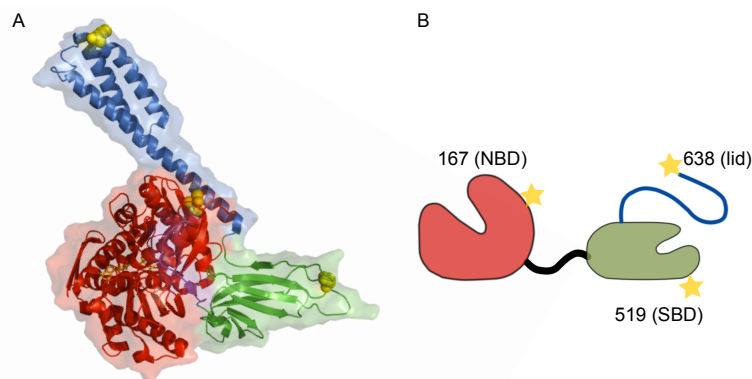


Figure 5.1: Known crystal structure of BiP in the presence of ATP. **(A)** The domain architecture of BiP is shown on the crystal structure of BiP binding ATP (PDB-ID: 5E84). In yellow the labeling positions are marked. **(B)** The cartoon representation of BiP shows the labeling positions as stars. The numbers are the amino acids of the labeling. In red the NBD is depicted, in green the SBD and in blue the lid.

To control the wide range of sometimes contradictory functions like protein folding and degradation, BiP is regulated by a set of cochaperones, which either belong to the class of J proteins or to the nucleotide exchange factors (NEFs). These proteins assist in fine-tuning the ATPase-driven chaperone cycle of BiP.

The binding and release of a substrate to or from BiP, respectively, depends on the nucleotide state. Therefore, the exchange process is important. This process can be catalyzed by a NEF. The first discovered NEF for mammalian cells was BAP, a BiP Associated Protein, also called

SIL1 [Otero et al., 2010]. The exact function of BAP is unknown [Ichhaporia et al., 2015], but mutations in BAP cause the Marinesco-Sjögren syndrome [Howes et al., 2012], which is related to autosomal recessive form of ataxia, cataract and myopathy [Anttonen et al., 2005], [Senderek et al., 2005], [Krieger et al., 2013].

The nucleotide cycle of BiP is already known [Marcinowski et al., 2011] (see also Figure 5.3). In the first step of the nucleotide cycle, ATP binds to BiP. A nascent protein can then interact with a low affinity with BiP. When ATP hydrolyzes to ADP, the binding affinity increases. BiP binds to charged areas of the nascent chain and protects the unfolded protein against unspecific interactions. This interaction happens in the ER during the translocation process of the unfolded protein from the lumen to the ER. Thus, BiP has to interact with many different unfolded or misfolded proteins. One of the most prominent substrates for BiP is C<sub>H1</sub>, an unassembled immunoglobulin heavy chain. C<sub>H1</sub> is an intrinsically disordered protein and unfolded in the absence of the immunoglobulin light chain [Lee et al., 1999], [Feige et al., 2009]. A final exchange of ADP for ATP promotes substrate release and allows the substrate to fold or to re-enter the cycle if there are still hydrophobic patches exposed.

The conformation of BiP in the presence of BAP changes when BiP interacts with a nucleotide or a substrate. In this chapter, the conformational changes of BiP by binding to BAP are analyzed by single-pair Förster Resonance Energy Transfer (spFRET) measurements. A cartoon, which depicts the used labeling positions of BiP, is given in Figure 5.1B.

## 5.2 Sample Preparation

The protein expression, purification and labeling was done by Mathias Rosam and Christina Stutzer in the group of Prof. Buchner (TU Munich, Munich, Germany). The strategy used is briefly presented here.

### BiP expression

BiP and BAP were expressed in *E.coli* culture. Murine spFRET BiP mutants were cloned into a pProEX vector (Thermo Fisher Scientific, Waltham, USA) containing a N-terminal 6x-His tag and a TEV protease cleavage site. The *E.coli* BL21 DE3 grew at 37°C till they had an OD<sub>600</sub> ~ 0.8 (cell density). The BiP mutants were expressed at 37°C for 3 h. Cells were harvested by centrifugation, disrupted at ~ 1.8 kbar, and cell debris was removed by extensive centrifugation at 20 krpm for 1 h. The supernatant was loaded onto a HisTrap FF column (GE Healthcare, Freiburg, Germany) equilibrated in 50 mM Hepes (pH 7.5, KOH), 400 mM NaCl and 20 mM imidazole. Bound BiP was eluted with a linear imidazole gradient from 20 mM to 1 M. The eluted fractions containing BiP were TEV-digested and dialyzed overnight at 4°C to remove the N-terminal His tag. A final size exclusion chromatography step on a Superdex 200 26/60 (GE Healthcare) in HKM buffer (50 mM Hepes (pH 7.5), 150 mM KCl and 10 mM MgCl<sub>2</sub>) was used to remove smaller contaminants.

### BiP labeling

To elucidate the overall BiP conformation, we always used two of three different possible labeling positions for each mutant. The respective labeling positions are located in different regions

of the protein, one in the nucleotide binding domain (NBD, 167), one in the substrate binding domain (SBD, 519) and the last one close to the C-terminal end of the lid (639) (Figure 5.1B). The labeling positions were the same as previously used in [Marcinowski et al., 2011]. The counting starts at the first methionine (UniProt ID: P20029). The chosen labeling positions of BiP were stochastically labeled with the dyes ATTO 532 and ATTO 647 (ATTO-TEC GmbH, Siegen, Germany). For this purpose, BiP was reduced with a 200-fold excess of TCEP for 1 h at 25°C. To reduce the TCEP concentration to an equal molar concentration of BiP, diafiltration in Amicon Ultra-0.5 (Merck Millipore, Billerica, Massachusetts, USA) was used. The dyes were diluted in water-free DMSO. The double-cysteine mutants of BiP were incubated for 2.5 h at 25°C with a two-fold excess of equal amounts of ATTO 532-maleimid and ATTO 647-maleimid. Free dye was removed by diafiltration. The linker between the dye and BiP is a C<sub>6</sub>. The first mutant, BiP-167-519, is the interdomain-mutant and provides information about the linker distance between the two binding domains. The second mutant, BiP-519-638, is the lid-mutant and monitors the lid closing or opening. The last mutant is the combined-mutant, BiP-167-639, which is used to study the distance between the NBD and the lid.

## BAP expression

The plasmid encoding human BAP was produced in the group of Linda Hendershot (St. Jude Children's Research Hospital, Memphis, USA). They cloned the protein without the N-terminal ER import sequence into the pQE10 vector. Expression and purification was done in the group of Prof. Buchner. BAP was expressed in *E.coli* HB101 at 17°C for 18 h. The cells were then harvested, disrupted, and debris removed as was performed for BiP. The supernatant was applied to a HisTrap FF column equilibrated in 50 mM Na<sub>2</sub>HPO<sub>4</sub> (pH 7.5, HCl), 500 mM NaCl, 10 mM imidazole and 10 % (v/v) glycerol. Bound BAP was eluted with 50 mM Na<sub>2</sub>HPO<sub>4</sub> (pH 7.5, HCl), 1 M imidazole, 10 % (v/v) glycerol. Since BAP appeared to be very degradation-prone and protease-sensitive, protease inhibitor HP (Serva, Heidelberg, Germany) was added to every buffer. And to the tubes for elution 5 mM EDTA were added. The BAP-containing fractions in HKM buffer additionally run through a Superdex 200 26/60 (GE Healthcare) column.

## SpFRET experimental conditions

The fluorescently labeled BiP was incubated in a concentration of 1 μM under the following conditions: BiP only diluted in HKM was incubated for 15 min at 37°C. Adding 1 mM ADP, AMP-PNP or ATPγS to BiP did not change the incubation (15 min at 37°C). ATP is always added in the last step of dilution of BiP to avoid hydrolyzes. For measurements of 10 μM BAP with or without a nucleotide, the incubation was chosen as 15 min at 37°C. Adding 10 μM BAP-ΔN instead of BAP to BiP with and without a nucleotide changes the incubation temperature to 20°C for 15 min. The addition of 14 μM C<sub>H</sub>1 changes the incubation time to 120 min at 37°C in the absence or presence of BAP without a nucleotide or BAP with a nucleotide. Combining 10 μM BAP-ΔN with 14 μM C<sub>H</sub>1 with or without a nucleotide reduces the incubation temperature again to 20°C for 120 min. After incubation, the labeled BiP protein was diluted to concentrations lower than 50 pM, while the concentration of the other incubation partners was kept constant.

## ADP purification

Commercially available ADP is contaminated by a few percent with ATP. Due to the higher affinity of BiP to ATP compared to ADP, this results in a mixture of ADP and ATP bound BiP. Therefore, the ADP had to be purified in Hepes buffer by an anion-exchange column using an Äkta system (ÄKTAmicro, GE Healthcare, Uppsala, Sweden). ADP was eluted with a linear salt concentration from 0 to 1 M KCl. Only the ADP fraction was used for the following experiments.

## 5.3 Nucleotide dependent chaperone cycle of BiP

SpFRET measurements of double labeled BiP mutants, like recently developed in [Marcinowski et al., 2011], were performed. On a multiparameter fluorescence detection setup (MFD, see Chapter 3.3.2 on page 25) with pulsed interleaved excitation (PIE, see Chapter 3.3.1 on page 24), the Förster resonance energy transfer efficiency (FRET, see Chapter 2.5 on page 11) was determined and the distance between the two dyes was calculated using photon distribution analysis (PDA, see Chapter 3.3.3 on page 32).

Without any nucleotide (*apo*), the interdomain distance of BiP, measured using the interdomain mutant, had a broad FRET efficiency distribution with a mean at  $\sim 0.4$ . This FRET efficiency corresponded to a distance of  $d = 58 \text{ \AA}$  with a width of  $\sigma = 9 \text{ \AA}$  fitted by a Gaussian (Figure 5.2A and Table 5.1). The broadening is large for spFRET measurements. This suggests that BiP is highly heterogeneous in this conformation and has multiple subconformations. To fit the experimental data in a proper manner, one additional Gaussian distribution was needed, which had a distance of  $d = 39 \text{ \AA}$  and a width of  $\sigma = 5 \text{ \AA}$ .

The analog experiment with the lid-mutant, BiP-519-638, showed that the lid is closed, i.e. the FRET efficiency is high and, therefore, the distance is small. The distance between the two dyes was  $d = 44 \text{ \AA}$  ( $\sigma = 4 \text{ \AA}$ ) for the main population. Two additional Gaussian functions were needed to fit the measured data properly, but they were very broad and, therefore, not clearly defined or much less populated (Figure 5.2B and Table 5.1).

The last mutant is a combination of the two. This mutant shows mostly very similar results than the interdomain-mutant, but also is effected by changes in the lid-mutant. The combined-mutant had one broad peak, which needed two Gaussian functions to be approximated (Figure 5.2C). One with a distance calculated as  $d = 50 \text{ \AA}$  ( $\sigma = 10 \text{ \AA}$ ) and the other, the main conformation, was fitted to  $d = 65 \text{ \AA}$  with a width of  $\sigma = 11 \text{ \AA}$  (Table 5.1). This broad  $\sigma$  is again a sign for a highly heterogeneous conformation and multiple subconformations. This is in a good agreement with the mutant BiP-167-519 and can be explained by a very flexible linker between the two binding domains, when no substrate and no nucleotide is present.

After measuring BiP alone, ATP was added. This shifted the FRET efficiency for the interdomain-mutant to higher values (Figure 5.2A). The distance was calculated by fitting one Gaussian with  $d = 52 \text{ \AA}$  and  $\sigma = 4 \text{ \AA}$  (Table 5.1). The broadening got smaller and, therefore, the conformation is more distinct compared to BiP without a nucleotide.

In the presence of ATP, the lid is in the open conformation (Figure 5.2B and Table 5.1) with a main separation of  $d = 85 \text{ \AA}$  ( $\sigma = 10 \text{ \AA}$ ). The broad  $\sigma$  can be explained by the reduced sensitivity at very high FRET values.

For the mutant BiP-167-638, the FRET efficiency shifted to  $\sim 0.65$  (Figure 5.2C). This corresponded to a distance  $d = 53 \text{ \AA}$  ( $\sigma = 5 \text{ \AA}$ ) (Table 5.1). Consequently, upon ATP binding, the two binding domains come closer together and the lid opens up.

Upon hydrolysis, ADP is bound to BiP. For all three BiP-mutants we measured that BiP is in the *apo* conformation (Table 5.1). The mutant BiP-167-519 had one distance (Figure 5.2A) at  $d = 60 \text{ \AA}$  ( $\sigma = 7 \text{ \AA}$ ). For the mutant BiP-519-638 (Figure 5.2B) the distance was calculated as  $d = 45 \text{ \AA}$  ( $\sigma = 4 \text{ \AA}$ ). The last mutant, BiP-167-638, was fitted similar to the nucleotide free conformation with two Gaussian functions (Figure 5.2C), the amplitudes are  $d = 46 \text{ \AA}$  ( $\sigma = 7 \text{ \AA}$ ) and  $d = 66 \text{ \AA}$  ( $\sigma = 9 \text{ \AA}$ ), respectively.

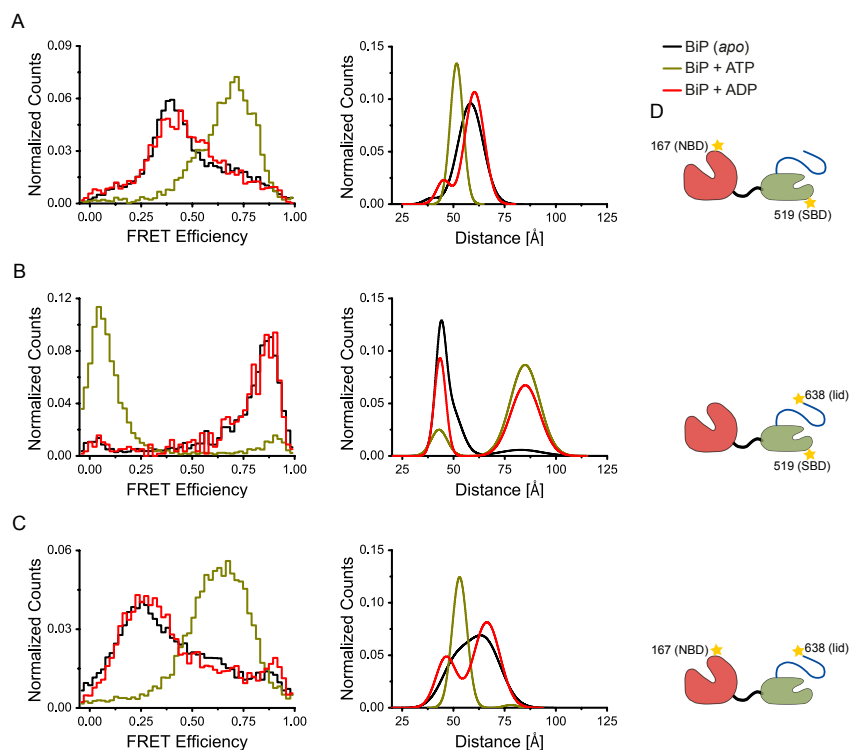


Figure 5.2: SpFRET analysis of BiP. (**A-C**) SpFRET distributions for 25 pM BiP measured without any nucleotide (black line), in the presence 1 mM ATP (dark yellow line) or with 1 mM ADP (red line). In the left panels the FRET efficiency histograms are plotted, the graphs in the middle panels represent the resulting distance distributions from the PDA fit. All these conditions were used for the three labeling constructs shown in **D**. (**A**) BiP-167-519 gives information about the distance between NBD and SBD, (**B**) BiP-519-638 monitors the lid conformation and (**C**) BiP-167-519 has labels on the NBD and on the lid to observe the distance between NBD and the C-terminal end of the lid. (**D**) The labeling sides are shown in the cartoon.

Uncertainties due to small variations in the measurements of different protein purification batches were calculated for all the measurements of BiP without a nucleotide and in the presence of ATP. Therefore, the mean of the fit results from multiple measurements was exemplary determined. The standard deviations for the single distances and widths are given in red in parentheses in Table 5.1. The deviations are determined smaller or equal to  $5 \text{ \AA}$  for all

Table 5.1: Distances calculated by PDA for BiP in the presence and absence of nucleotides. The spFRET mutants (25 pM) were measured in the absence (*apo*) or presence of nucleotides (1 mM ATP or 1 mM ADP). The photons of a burst were divided into bins of 1 ms, summed up in a FRET histogram, and fitted using a single-, double- or triple-Gaussian model. From the PDA, the distance  $d$  between donor and acceptor, the corresponding width  $\sigma$  and the relative weights of the different populations were calculated. An asterisk (\*) indicates that the respective value was fixed for fitting. The error of the fit was calculated from multiple measurements of the same conditions and is given in red in parentheses. The error for the other measurements was approximated from the calculated values and is given in black.

Mutant	Subpopulation 1			Subpopulation 2			Subpopulation 3			Goodness of the fit	
	$d$ [Å]	$\sigma$ [Å]	%	$d$ [Å]	$\sigma$ [Å]	%	$d$ [Å]	$\sigma$ [Å]	%		
167/519	<i>apo</i>	39 ( $\pm$ 3.2)	5 ( $\pm$ 0.8)	2.7			58 ( $\pm$ 1.6)	9 ( $\pm$ 1.3)	97.3	3.1	
167/519	ATP			52 ( $\pm$ 0.9)	4 ( $\pm$ 0.3)	100				2.0	
167/519	ADP	45 ( $\pm$ 4)	5 ( $\pm$ 1)	10.6			60 ( $\pm$ 2)	7 ( $\pm$ 2)	89.4	3.0	
519/638	<i>apo</i>	44 ( $\pm$ 0.7)	4 ( $\pm$ 0.8)	55.4	48 ( $\pm$ 3.5)	8 ( $\pm$ 2.7)	34.9	83 ( $\pm$ 4.0)	14* ( $\pm$ 5.0)	9.7	1.2
519/638	ATP	43 ( $\pm$ 1.0)	6 ( $\pm$ 0.3)	8.9				85 ( $\pm$ 2.1)	10 ( $\pm$ 0.6)	91.1	2.3
519/638	ADP	45 ( $\pm$ 1)	4 ( $\pm$ 1)	88.3				80 ( $\pm$ 4)	16* ( $\pm$ 5)	11.7	1.2
167/638	<i>apo</i>	50 ( $\pm$ 1.6)	10* ( $\pm$ 0.4)	27.6			65 ( $\pm$ 1.3)	11 ( $\pm$ 1.1)	72.4	3.6	
167/638	ATP				53 ( $\pm$ 0.3)	5 ( $\pm$ 0.3)	96.0	78 ( $\pm$ 2.1)	5 ( $\pm$ 3.4)	4.0	1.9
167/638	ADP	46 ( $\pm$ 2)	7 ( $\pm$ 1)	23.4			66 ( $\pm$ 3)	9 ( $\pm$ 4)	76.6	2.5	

distances and widths. Therefore, the overall fit results are very similar and, for the remaining measurements, the deviations are estimated from the standard deviations calculated here. Additionally, the goodness of the PDA fit was calculated. The  $\chi^2$  should be less than 5 for the fit. Numbers above this are an indication that the model is incorrect, that the wrong number of subpopulations and, therefore, a wrong number of Gaussian fits was chosen.

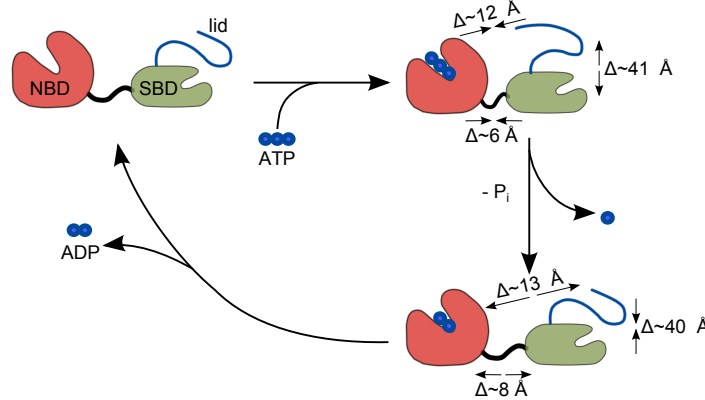


Figure 5.3: Model for the nucleotide dependent chaperone cycle. The NBD is depicted in red, the SBD in green and the lid in blue. The distances between the previous and current nucleotide state are given next to the arrows. The relative changes between the distances were calculated using PDA from the spFRET measurements.

The results indicate that the two binding domains of BiP come closer together in the presence of ATP, compared to the nucleotide-free state and the lid opens up. Upon hydrolysis to ADP, the whole BiP conformation, including the distances between the NBD and SBD and between SBD and lid, takes the form of the nucleotide free conformation. The resulting nucleotide dependent chaperone cycle of BiP is drawn in Figure 5.3, which is in line with the already known nucleotide cycle from [Marcinowski et al., 2011]. Small deviations between the results are due to different BiP concentrations during the measurement. In [Marcinowski et al., 2011] the concentration was chosen much higher than here and, therefore, additional populations were measured. These populations are in between the populations found here and are due to multimolecule events, i.e. multiple molecules are detected at the same time. Furthermore, in the previous study the used ADP was not purified and, therefore, a fraction of BiP molecules was bound to ATP in their measured ADP conformation.

## 5.4 BAP influences the nucleotide dependent chaperone cycle of BiP

The definition of a nucleotide exchange factor (NEF) is that it interacts with the protein itself, in this case BiP, and influences the nucleotide-dependent chaperone cycle [Cyr, 2008]. For BiP, the first discovered nucleotide exchange factor is the BiP Associated Protein, BAP, also known as SIL1 [Chung et al., 2002]. The structure of human BAP is still unknown, but a crystal structure of the yeast BAP (ScBAP) in combination with the NBD of yeast BiP (ScBiP-NBD) (PDB-ID: 3QML) is shown in Figure 5.4. The crystal structure shows that BAP binds to the lobe IIb of the NBD of BiP [Yan et al., 2011]. It is the structure of yeast

BAP but can give a first hint, how the structure of human BAP could be. However, sequence identity between the human and the yeast BAP is only 15 % and, in the case of the crystal structure, the N-terminal domain of BAP and the SBD of BiP including the lid are missing.

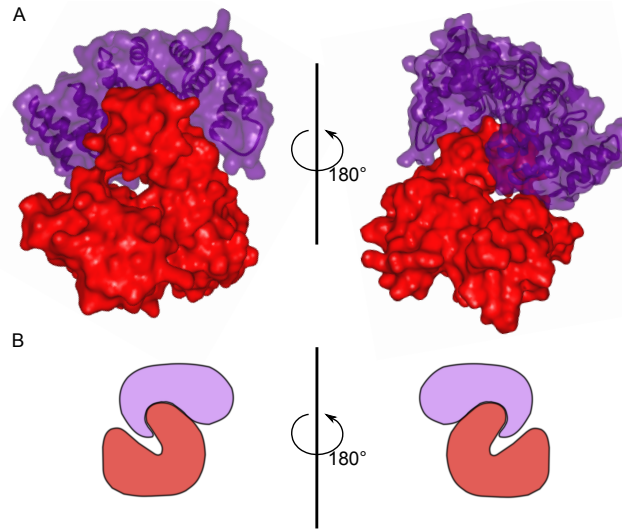


Figure 5.4: Known crystal structure of a BAP homolog bound to the NBD of ScBiP. **(A)** The crystal structure of yeast ScBAP (purple) in complex with yeast ScBiP-NBD (red) identifies lobe IIb as the interacting subdomain in BiP-NBD (PDB-ID: 3QML). The crystal structure is rotated by 180°. **(B)** A cartoon representation of BiP-NBD interacting with BAP.

For testing the binding of BAP to BiP, Mathias Rosam from the group of Prof. Buchner (TU Munich) performed analytical ultracentrifugation (AUC) sedimentation velocity (SV) experiments of labeled BiP with and without unlabeled BAP (Figure 5.5A).

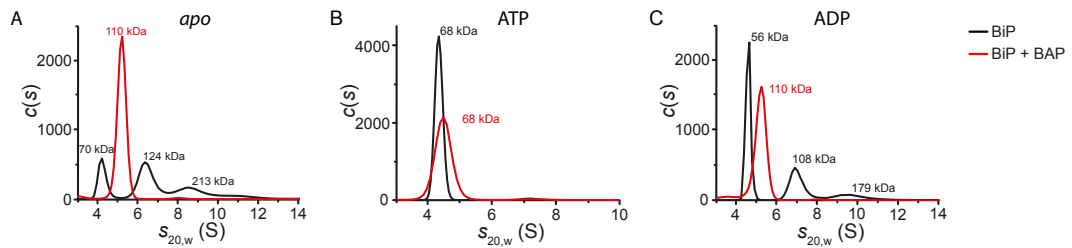


Figure 5.5: Analytical ultracentrifugation measurements of BiP with BAP. **(A-C)** Complex formation by sedimentation velocity (SV) runs of 0.5  $\mu$ M ATTO 488-labeled BiP and 5  $\mu$ M BAP **(A)** in the absence of nucleotide (*apo*), **(B)** in the presence of 1 mM ATP and **(C)** 1 mM ADP. The measurements were performed by Mathias Rosam in the group of Prof. Buchner.

In the *apo*-state, BiP was found as a monomer or formed dimers and trimers. This is in line with the literature, where it can be found that Hsp70s can form noncovalent oligomers in solution [Blond-Elguindi et al., 1993] [Marcion et al., 2014]. Adding BAP to BiP shifted the

oligomeric distribution of BiP to a single species with a higher sedimentation coefficients  $s_{20,w}$  compared to the monomeric population without BAP. This peak corresponded to a complex formed by binding of BiP and BAP (Figure 5.5A).

For getting an idea of how BAP influences the conformation of BiP without and with a nucleotide, spFRET measurements were performed and the distances were calculated from the FRET efficiencies again using PDA. Figure 5.6A depicts the labeling positions of BiP.

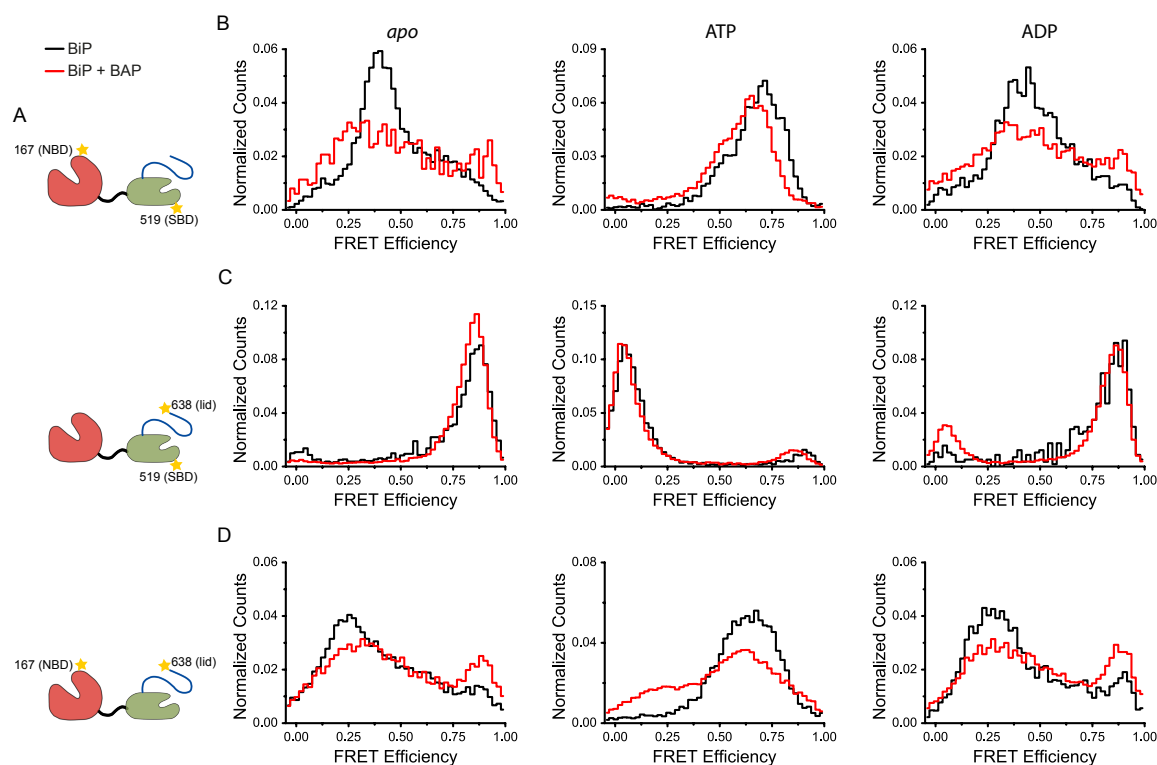


Figure 5.6: SpFRET analysis of BiP in the presence of BAP. (A) The labeling sides are shown in the cartoons. (B-D) SpFRET distributions of 25 pM BiP were measured in the presence of 10  $\mu$ M BAP (first column, red line) or 10  $\mu$ M BAP and 1 mM ATP (second column, red line) or 10  $\mu$ M BAP and 1 mM ADP (last column, red line). All three labeling constructs were measured under these conditions and compared with the measurements without BAP (black lines and Figure 5.2). (B) BiP-167-519 gives information about the distance between NBD and SBD, (C) BiP-519-638 monitors the lid conformation and (D) BiP-167-519 has labels on the NBD and the lid to watch the distance between NBD and the C-terminal end of the lid.

For nucleotide free BiP the measurements reveal that the main conformation of BiP does not change upon binding of BAP, but the FRET efficiency histograms get broader. The mean distance between NBD and SBD was calculated as  $d = 58 \text{ \AA}$  with a width of  $\sigma = 12 \text{ \AA}$  (Figure 5.6B (first column) and Table 5.2). This broadening is large for spFRET measurements, consequential BiP is highly heterogeneous and implies the presence of multiple subconformations, as for BiP without BAP. In about 5 % of the BiP, the two binding domains showed a higher FRET efficiency value and, therefore, came closer together. The mean distance for

this part of BiP-BAP complexes is  $d = 41 \text{ \AA}$  ( $\sigma = 4 \text{ \AA}$ ).

The lid-mutant had a closed lid and a mean distance of  $d = 45 \text{ \AA}$  between the two dyes. As the width of this distance is  $\sigma = 3 \text{ \AA}$ , the conformation is well defined (Figure 5.6C (first column) and Table 5.2). Interestingly, the closed lid without nucleotide is independent from the presence of BAP.

For the combined-mutant, BiP-167-638, two different conformations in the presence of BAP were measured. On the one hand, the same FRET efficiency as without BAP ( $\sim 25 \%$  FRET) was detectable. The corresponding mean distance was  $d = 58 \text{ \AA}$  with a width of  $\sigma = 13 \text{ \AA}$ . This broad distribution again suggests subconformations of the linker between the NBD and SBD. On the other hand, a high FRET efficiency population with  $d = 42 \text{ \AA}$  ( $\sigma = 3 \text{ \AA}$ ) was calculated from the FRET efficiency data (Figure 5.6D (first column) and Table 5.2).

In summary, the lid is closed and two possible conformations of BiP are observed in the presence of BAP when a nucleotide is bound. In the most common conformation, the distances between the domains and the lid are similar to the measurements without BAP. A small percentage of proteins (5-10 %) is in a more compact conformation, the distance between the two binding domains is smaller and, therefore, the distance between the NBD and lid is shorter.

To further analyze the conformation of BiP with BAP, ATP was added to the measurements. In the AUC experiments, only a single species of monomeric BiP was detected. Upon the addition of BAP, the sedimentation coefficient did not change significantly. Therefore, BAP does not bind stably to BiP when ATP is already present.

To get information about the conformation of BiP, spFRET experiments were performed in the presence of ATP and BAP. The FRET efficiencies and the distances between the dyes stayed the same for the interdomain- and the lid-mutant with ATP in the presence and absence of BAP (Figure 5.6B and C (second column) and Table 5.2). This would be explained when BAP does not bind. However for the combined-mutant, a small change with and without BAP was detected. A low FRET peak in the presence of BAP appears (Figure 5.6D). It has the same FRET efficiency as BiP with BAP without a nucleotide.

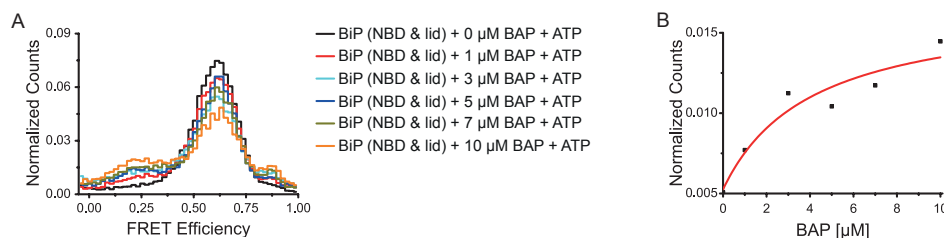


Figure 5.7: Interaction of BAP with BiP when ATP is bound. **(A)** SpFRET distributions of 25 pM BiP-167-638 were measured with different concentrations of BAP in the presence of 1 mM ADP. **(B)** The normalized area under the FRET histogram up to a FRET value of 0.4 was summed up and plotted versus the BAP concentration. The  $K_d$  is given by the fit as  $4.1 \pm 3.7 \mu\text{M}$ .

To further analyze if this additional population is a result of an interaction of BAP with BiP that is bound to ATP, different BAP concentrations were measured for the combined-mutant in the presence of ATP (Figure 5.7A). An increase of the height of the population was found for increasing BAP concentrations. The normalized area under the curve up to a FRET value of 0.4 was plotted versus the concentration of BAP (Figure 5.7B). The values were fitted by

Table 5.2: Distances calculated using PDA for BiP in the presence of BAP and in the absence and presence of nucleotides. The spFRET mutants (25 pM) were measured in the absence (*apo*) and presence of nucleotides (1 mM ATP or 1 mM ADP) and a nucleotide exchange factor (10  $\mu$ M BAP). The photons of a burst were divided into bins of 1 ms, summed up in a FRET histogram, and fitted using a double- or triple-Gaussian model. From the PDA, the distance  $d$  between donor and acceptor, the corresponding width  $\sigma$  and the relative weights of the different populations were calculated. An asterisk (\*) indicates that the respective value was fixed for fitting. The error of the fit values was approximated from the measurements without a NEF as the maximum standard deviation for the fit and is given in parenthesis.

Mutant	Subpopulation 1			Subpopulation 2			Subpopulation 3			Goodness of the fit $\chi^2$
	$d$ [Å]	$\sigma$ [Å]	%	$d$ [Å]	$\sigma$ [Å]	%	$d$ [Å]	$\sigma$ [Å]	%	
167/519 BAP	41 ( $\pm$ 4)	4 ( $\pm$ 1)	5.2	58 ( $\pm$ 1)	12 ( $\pm$ 1)	94.8				1.0
167/519 BAP + ATP				54 ( $\pm$ 1)	6 ( $\pm$ 1)	93.0	79 ( $\pm$ 2)	8* ( $\pm$ 2)	7.0	3.9
167/519 BAP + ADP	42 ( $\pm$ 4)	3 ( $\pm$ 1)	7.6	57 ( $\pm$ 1)	11 ( $\pm$ 1)	92.4				3.5
519/638 BAP	45 ( $\pm$ 1)	3 ( $\pm$ 1)	89.6	52 ( $\pm$ 4)	15 ( $\pm$ 3)	10.4				6.9
519/638 BAP + ATP	45 ( $\pm$ 1)	4 ( $\pm$ 1)	13.4				86 ( $\pm$ 4)	12 ( $\pm$ 5)	86.6	12.7
519/638 BAP + ADP	44 ( $\pm$ 1)	3 ( $\pm$ 1)	67.6	50 ( $\pm$ 4)	9 ( $\pm$ 3)	13.5	91 ( $\pm$ 4)	9 ( $\pm$ 5)	18.9	5.3
167/638 BAP	42 ( $\pm$ 2)	3 ( $\pm$ 1)	10.0	58 ( $\pm$ 1)	13 ( $\pm$ 1)	90.0				2.1
167/638 BAP + ATP	45 ( $\pm$ 2)	6* ( $\pm$ 1)	18.1	55 ( $\pm$ 1)	6 ( $\pm$ 1)	58.9	73 ( $\pm$ 3)	8 ( $\pm$ 4)	23.0	1.3
167/638 BAP + ADP	43 ( $\pm$ 2)	3 ( $\pm$ 1)	13.8	57 ( $\pm$ 1)	13 ( $\pm$ 1)	86.2				1.3

a sigmoid curve and the dissociation constant of BAP was estimated as  $4.1 \pm 3.7 \mu\text{M}$ . The large standard error is due to the low number of molecules in this conformation and the high noise. However, we can state that BAP is not bound stably in the ATP state of BiP, but interacts transiently.

To get an overall picture of the nucleotide cycle, BiP with BAP was also analyzed in the presence of ADP. In the AUC measurements, a similar oligomerization pattern was observed as for the *apo*-state. The monomeric species of BiP was most prevalent while the trimeric population was hardly detectable. Adding BAP shifted the oligomers to a single species, which corresponded to monomeric BiP in complex with BAP.

SpFRET measurements revealed that the mean distance of the interdomain-mutant in the presence of BAP ( $d = 57 \text{ \AA}$ ) had the same value as for measurements without BAP (Figure 5.6A (third column) and Table 5.2). The width of this measurement was  $\sigma = 11 \text{ \AA}$  compared to the  $\sigma = 7 \text{ \AA}$  for the ADP conformation without NEF. Therefore, the conformation gets more inhomogeneous.

The mean distance of BiP's lid-mutant with BAP and ADP was equal to the measurements without BAP. The distance was  $d = 44 \text{ \AA}$  ( $\sigma = 3 \text{ \AA}$ ) (Figure 5.6B (third column) and Table 5.2). Additionally, up to 20 % of the molecules are in a closed conformation with a distance of  $d = 91 \text{ \AA}$  ( $\sigma = 9 \text{ \AA}$ ).

The last mutant, the combined-mutant is similar to the interdomain-mutant and shows two possible conformations. They are calculated as  $d = 43 \text{ \AA}$  ( $\sigma = 3 \text{ \AA}$ ) and  $d = 57 \text{ \AA}$  ( $\sigma = 13 \text{ \AA}$ ), which are similar to the conformation in the absence of ADP. The high FRET peak is again more populated due to the addition of BAP. Thus, in the presence of ADP, BAP forms binary complexes and makes the conformation more heterogeneous.

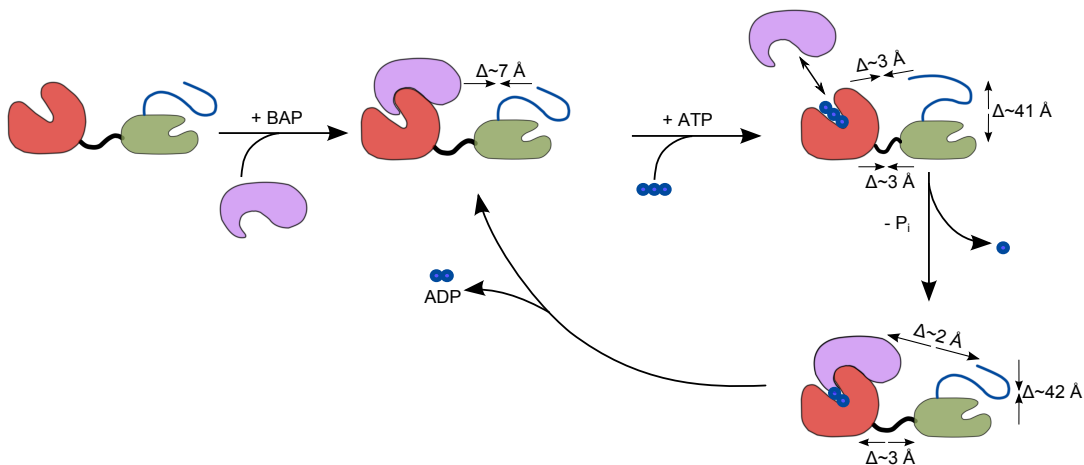


Figure 5.8: Model for the nucleotide dependent chaperone cycle in the presence of BAP. The distances between the previous and current nucleotide state are given next to the arrows. The relative changes between the distances were calculated using PDA from the spFRET measurements. Small distance changes are due to the flexibility of the short linker between BiP and the dye.

To conclude the results of the measurements with BAP, it is again possible to draw an overall picture of the nucleotide cycle (Figure 5.8). When BAP binds to BiP without any nucleotide, the main conformation stays constant, except for minor changes due to an increase in the flexibility of the short linker between the two domains. By adding ATP to BiP with BAP,

BAP unbinds, which allows ATP to bind to BiP. We detect a transient interaction between BAP and BiP with ATP. Nevertheless, the main conformation of BiP with ATP is the same both in the presence and absence of BAP. The lid is in an open conformation and the two binding domains stay close together. In the presence of ADP instead of ATP, BAP can rebind stable. BiP changes back in the nucleotide free conformation. The two domains shift back and separated and the lid closes again.

## 5.5 ATP analogues do not behave like ATP in the presence of BAP

In the middle panel of Figure 5.6D, BiP-167-638 with ATP, a low FRET population was detected although it was expected that the conformation with and without BAP are equal, because BAP can not bind when ATP is bound. One possible explanation for this low FRET

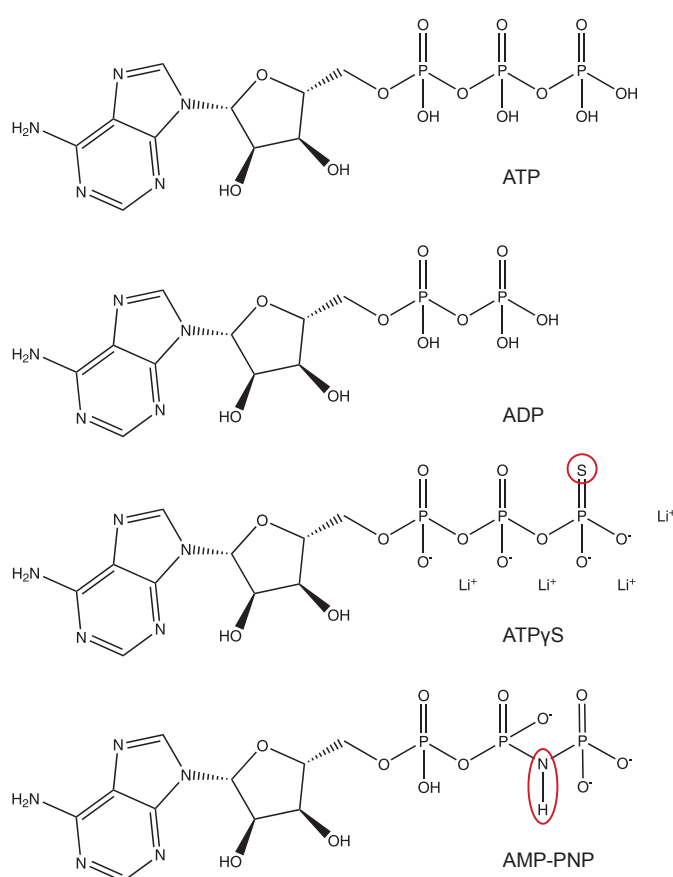


Figure 5.9: Nucleotide analogues for ATP. The structure of ATP and ADP along with the ATP analogues ATP $\gamma$ S and AMP-PNP are depicted. Differences between the analogues and ATP are marked in red.

population could be the hydrolysis of ATP. The additional population with BAP has a similar FRET efficiency as the combined mutant with ADP. For the two other mutants, the effect was not observed. This is an indication for an rotational motion between the NBD and the

SBD-lid. To test if this population is due to the hydrolysis and belongs to an intermediate state in the nucleotide cycle, ATP analogues, which cannot hydrolyze, were used. ATP $\gamma$ S and AMP-PNP were chosen because they are structurally equal except for their phosphate rest (Figure 5.9) [Bagshaw, 2001]. Therefore, they were expected to interact in a similar way as ATP with BiP in complex with BAP, but maybe simulate the hydrolyzed state.

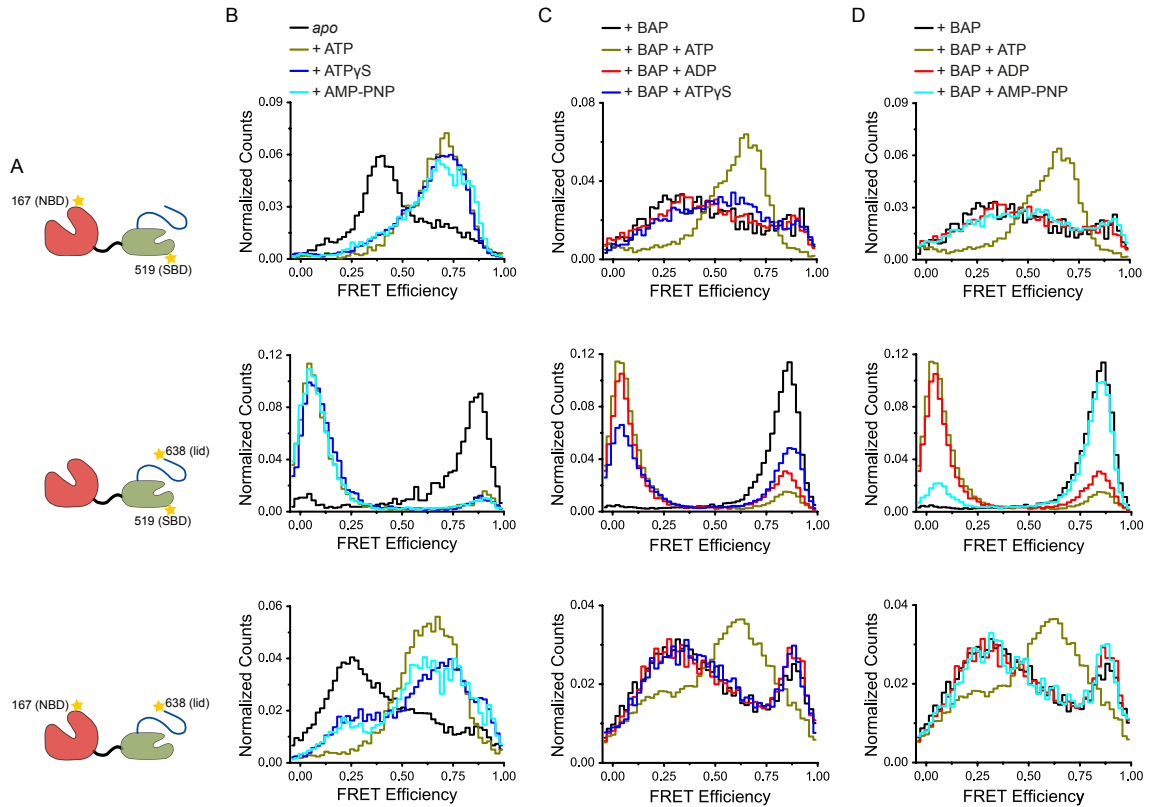


Figure 5.10: SpFRET analysis of BiP in the presence of BAP and nucleotide analogues. **(A)** The labeling sides are shown in the cartoons. **(B)** SpFRET distributions of 25  $\mu$ M BiP were measured without a nucleotide (black line), in the presence of 1 mM ATP (dark yellow line), 1 mM ATP $\gamma$ S (blue line) or 1 mM AMP-PNP (cyan line). **(C)** SpFRET distributions of BiP with 10  $\mu$ M BAP and 1 mM ATP $\gamma$ S (blue line) compared to the measurements with only 10  $\mu$ M BAP (black line), with 10  $\mu$ M BAP and 1 mM ADP (red line) and with 10  $\mu$ M BAP and 1 mM ATP (dark yellow line). **(D)** The same measurements as in **(C)** compared with 10  $\mu$ M BAP and 1 mM AMP-PNP (cyan line). **(B-D)** were measured with all three BiP constructs. BiP-167-519 gives information about the distance between NBD and SBD, BiP-519-638 monitors the lid conformation and BiP-167-519 has labels on the NBD and the lid to watch the distance between NBD and the C-terminal end of the lid.

As a control, spFRET measurements were performed for BiP with ATP $\gamma$ S and AMP-PNP. Figure 5.10A and Table 5.3 reveal that, for all three BiP mutants (Figure 5.10A), the measurement with ATP (Figure 5.10B, dark yellow line) has the same conformation as with ATP $\gamma$ S (blue line) or with AMP-PNP (cyan line). Therefore, we conclude that the chosen non-hydrolyzable ATP analogues can be used instead of ATP to determine the conformation

Table 5.3: Distances calculated using PDA for BiP with ATP analogs. The spFRET mutants (25 pM) were measured in the presence of nucleotides (1 mM ATP, 1 mM ATP $\gamma$ S or 1 mM AMP-PNP) and in the absence and presence of a nucleotide exchange factor (10  $\mu$ M BAP). The photons of a burst were divided into bins of 1 ms, summed up in a FRET histogram, and fitted using a double- or triple-Gaussian model. From the PDA, the distance  $d$  between donor and acceptor, the corresponding width  $\sigma$  and the relative weights of the different populations were calculated. An asterisk (\*) indicates that the respective value was fixed for fitting.

Mutant	Subpopulation 1			Subpopulation 2			Subpopulation 3			Subpopulation 4			Goodness of the fit $\chi^2$
	$d$ [Å]	$\sigma$ [Å]	%										
167/519 ATP				52	4	100							2.0
167/519 ATP $\gamma$ S				51	4	65.4	56	8	34.6				7.4
167/519 AMP-PNP				50	5	73.0	59	8	27.0				2.2
167/519 BAP + ATP				54	6	93.0				79	8*	7.0	3.9
167/519 BAP + ATP $\gamma$ S	41	4	6.1	54	5	29.0	58	13	64.9				1.3
167/519 BAP + AMP-PNP	42	5	18.8				57	7*	54.5	73	12*	26.7	1.2
519/638 ATP	43	6	8.9				85	10	91.1				2.3
519/638 ATP $\gamma$ S	43	4	6.8				85	12	93.2				2.7
519/638 AMP-PNP	45	6	8.0				88	12	92.0				3.0
519/638 BAP + ATP	45	4	13.4				86	12	86.6				12.7
519/638 BAP + ATP $\gamma$ S	44	4	39.9				85	17	60.1				9.5
519/638 BAP + AMP-PNP	45	4	83.0				87*	17	17.0				17.0
167/638 ATP				53	5	96.0	78	5	4.0				1.9
167/638 ATP $\gamma$ S	43	5	17.4	52	4	47.4	66	8	35.2				1.0
167/638 AMP-PNP	39	5*	4.0	53	7	83.6	76	3	12.4				1.0
167/638 BAP + ATP	45	6*	18.1	55	6	58.9	73	8	23.0				1.3
167/638 BAP + ATP $\gamma$ S	43	3	12.6	59	12	87.4							1.4
167/638 BAP + AMP-PNP	43	3	11.7	58	13	88.3							1.3

of BiP in the presence of ATP and the absence of a NEF.

By measuring BiP with BAP and ATP $\gamma$ S (Figure 5.10C and Table 5.3), the FRET efficiency was different than BiP with ATP. In ATP $\gamma$ S, the third oxygen of the phosphate rest is exchanged with a sulfur in comparison to ATP (Figure 5.9). The FRET efficiency histogram for BiP in the presence of BAP and ATP $\gamma$ S is for the interdomain- and the combined-mutant similar to the conformation of BiP with BAP and ADP. The lid-mutant is a mixture of the histogram of BiP with BAP and BiP with BAP and ATP.

By using AMP-PNP and adding this to BiP with BAP, the FRET efficiency and, therefore, the conformation of BiP were again different to the one of BiP with BAP and ATP (Figure 5.10D and Table 5.3). AMP-PNP has an exchange of the oxygen between the  $\beta$ - and  $\gamma$ -phosphorus atom by a nitrogen (Figure 5.9). The FRET efficiency was in the measurements similar to BiP with BAP without a nucleotide. Maybe AMP-PNP cannot bind to BiP anymore. One reason could be that BAP changes the nucleotide binding pocket of BiP and, thus, changes the affinity for AMP-PNP.

Overall, ATP $\gamma$ S and AMP-PNP can be used as non-hydrolyzable ATP analogues for BiP without a NEF or any other interaction partner. If one of these interaction partners, for example BAP, is present, ATP has to be used because the analogues may not be recognized as ATP and, thus, change the conformation.

Nevertheless, it is very unlikely that ATP was hydrolyzed and BiP was measured in the ADP bound state, because the conformation of BiP stayed the same over the whole period of measurement. Thus, the time between hydrolysis and release of the ADP has to be very short in the presence of a high excess of ATP and by the fact that ATP has a higher binding affinity than ADP. Thus, ATP analogues are not necessary to measure ATP conformations.

## 5.6 The N-terminal domain of BAP interacts with the lid

A high FRET population in the interdomain-mutant and the combined-mutant of BiP arised in the presence of BAP in the nucleotide free state (Figure 5.6B and D, first column). This

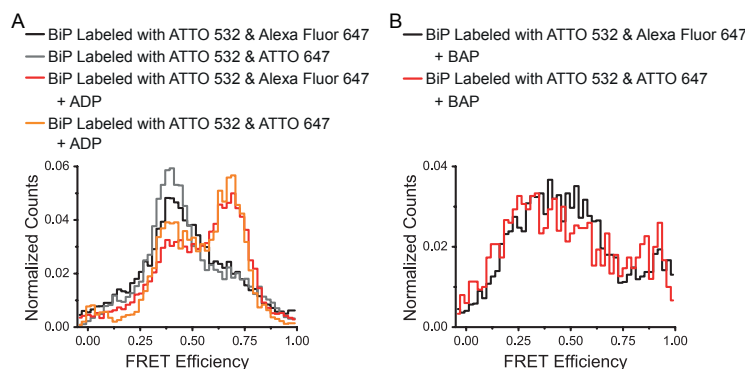


Figure 5.11: SpFRET analysis of BiP-167-519 labeled with ATTO 647 or Alexa Fluor 647. (A) SpFRET distributions of 25 pM BiP were measured without any nucleotide (black and gray line) or in the presence of 1 mM ADP (red and orange line) or (B) with 10  $\mu$ M BAP (black and red line). These different conditions were used for BiP-167-519 labeled with ATTO 532 and Alexa Fluor 647 and BiP-167-519 labeled with ATTO 532 and ATTO 647, respectively.

points towards a possible interaction between BAP and the C-terminal lid of BiP. To rule out if the high FRET efficiency is caused by a dye artifact, the dye ATTO 647 is exchanged by Alexa Fluor 647 (Thermo Fisher Scientific, Waltham, MA, USA). ATTO 647 is known for its high hydrophobic surface, which can result in undesirable interaction with the proteins. Alexa Fluor 647 does not have such a high hydrophobicity and, therefore, is less likely interacting and sticking in undesirable ways to the surrounding molecules. The measurements, where BiP was labeled with Alexa Fluor 647, had a similar FRET efficiency distribution as the one where BiP was labeled with ATTO 647 (Figure 5.11A). The addition of BAP also did not show any difference. The high FRET population was still detectable. This suggest that the subpopulation is not a dye-specific interaction with the protein.

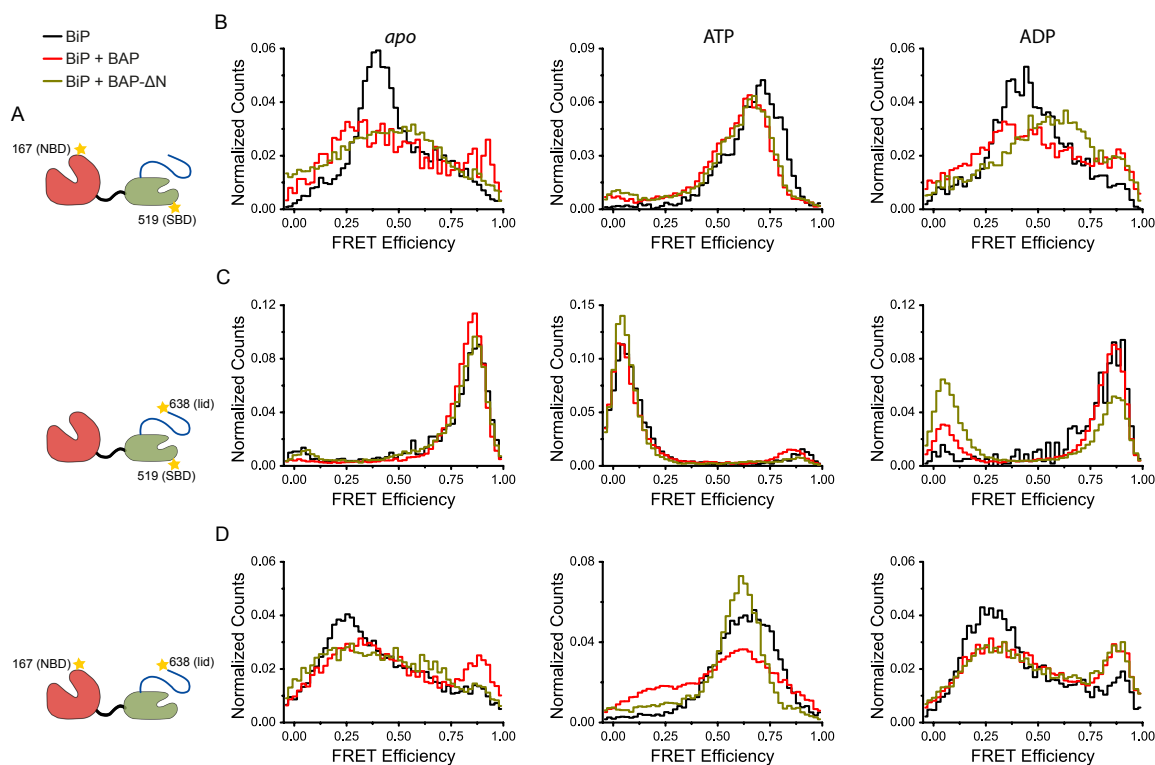


Figure 5.12: SpFRET analysis of BiP in the presence of BAP- $\Delta$ N. (A) The cartoons depict the BiP mutants measured. (B-D) SpFRET distributions of 25 pM BiP were measured in the presence of 10  $\mu$ M BAP- $\Delta$ N (first column, dark yellow line) or 10  $\mu$ M BAP- $\Delta$ N and 1 mM ATP (second column, dark yellow line) or 10  $\mu$ M BAP- $\Delta$ N and 1 mM ADP (last column, dark yellow line). All three labeling constructs were measured under these conditions and compared with the measurements without BAP (black line and Figure 5.2) and with 10  $\mu$ M BAP (red line and Figure 5.6). (B) BiP-167-519 gives information about the distance between NBD and SBD, (C) BiP-519-638 monitors the lid conformation and (D) BiP-167-519 has labels on the NBD and the lid to watch the distance between NBD and the C-terminal end of the lid.

To further determine the interaction between BAP and the C-terminal lid of BiP, experiments with a BAP variant without the N-terminal domain were performed. Therefore, a BAP lacking

the first 104 N-terminal amino acids (BAP- $\Delta$ N) was designed and characterized by Mathias Rosam and Christina Stutzer in the group of Prof. Buchner. This mutant corresponds to the construct used for the structure determination of the yeast ortholog [Yan et al., 2011].

By measuring BiP with BAP- $\Delta$ N instead of BAP without any nucleotide, FRET efficiencies were detected, which were similar to the measurements in the absence of BAP (Figure 5.12B-D (first column, dark yellow line) and Table 5.4). The main distance for the interdomain mutant was  $d = 55 \text{ \AA}$  ( $\sigma = 8 \text{ \AA}$ ), for BiPs lid-mutant  $d = 44 \text{ \AA}$  ( $\sigma = 3 \text{ \AA}$ ) and for the combined-mutant  $d = 64 \text{ \AA}$  ( $\sigma = 15 \text{ \AA}$ ). Thus, no significant difference in the FRET efficiencies of BiP with BAP- $\Delta$ N compared to full-length BAP was observed.

In the case of adding ATP to BiP with BAP- $\Delta$ N, the conformation is similar to the conformation of BiP with ATP. Here, the distance calculated by PDA was  $d = 53 \text{ \AA}$  ( $\sigma = 4 \text{ \AA}$ ) for the interdomain-mutant and  $d = 89 \text{ \AA}$  ( $\sigma = 9 \text{ \AA}$ ) for the lid-mutant. This is in line with the results of the measurements of BiP with BAP and ATP, where BAP cannot bind (Figure 5.12B-C (second column, dark yellow line) and Table 5.4). For the combined-mutant, we detect a difference in the measurement with full length BAP and BAP- $\Delta$ N. The low FRET peak of the measurements with BAP and ATP is not populated anymore. The left over population has a distance of  $d = 55 \text{ \AA}$  ( $\sigma = 3 \text{ \AA}$ ) (Figure 5.12D (second column, dark yellow line) and Table 5.4). Thus, the N-terminus is important for the transient interaction of ATP bound BiP with BAP.

In the ADP conformation, spFRET measurements revealed a difference between BAP- $\Delta$ N and full-length BAP (Figure 5.12B-D (third column, dark yellow line)). The NBD and SBD are closer together and a larger fraction of molecules has a open lid. For further analyzing the effect of BAP- $\Delta$ N in comparison to BAP, the three different mutants are compared. In the presence of BAP- $\Delta$ N and ADP, the interdomain-mutant had a FRET efficiency state of 65 %, which corresponds to  $d = 55 \text{ \AA}$  and has a width of  $\sigma = 8 \text{ \AA}$  (Table 5.4). This distance is smaller than the one measured for full length BAP in the presence of ADP (Figure 5.12B, red line). The FRET efficiencies of the lid-mutant in the presence of BAP- $\Delta$ N and ADP were shifted, compared to full length BiP, for a larger fraction of BiP molecules to the low FRET state. The percentage of the molecules in the open conformation shifted from 18.9 % with BAP to 43.3 % with BAP- $\Delta$ N in the presence of ADP. Furthermore, for BiP-167-638 with BAP- $\Delta$ N and ADP, the same FRET efficiencies from the measurements with BAP and ADP were detected (Table 5.4).

In summary, for measurements with BAP- $\Delta$ N and ADP, we conclude that the two binding domains come closer together in the absence of the N-terminal domain of BAP and the lid shifts more to an open conformation. Hence, the N-terminus of BAP has an effect on the FRET efficiencies and, therefore, on the distances between NBD and SBD and between SBD and lid.

To gain further insight regarding the interaction of BiP and BAP, Mathias Rosam of the group of Prof. Buchner expressed and labeled a BiP variant without the C-terminal lid. SpFRET measurements of the lidless mutant of BiP with BAP were performed (BiP- $\Delta$ lid, Figure 5.13).

By cutting off the lid (BiP- $\Delta$ lid), the low FRET efficiency population of BiP-167-519 with BAP and without a nucleotide was shifted to higher FRET values. This means that the distance between the two binding domains decreased (Figure 5.13B and Table 5.5). This effect was also shown in the presence of ADP. To further address the interaction between the lid of BiP and the N-terminal domain of BAP, BiP- $\Delta$ lid was measured in combination with BAP- $\Delta$ N (Figure 5.13C and Table 5.5). The percentage of molecules with a high FRET efficiency ( $d \sim 40 \text{ \AA}$ ) increased by using BiP- $\Delta$ lid and further increase by using BAP- $\Delta$ N in-

Table 5.4: Distances calculated using PDA for BiP with BAP- $\Delta$ N and in the presence and absence of nucleotides. The spFRET mutants (25 pM) were measured in the absence (*apo*) and presence of nucleotides (1 mM ATP or 1 mM ADP) and a nucleotide exchange factor (10  $\mu$ M BAP- $\Delta$ N). The photons of a burst were divided into bins of 1 ms, summed up in a FRET histogram, and fitted using a double- or triple-Gaussian model. From the PDA, the distance  $d$  between donor and acceptor, the corresponding width  $\sigma$  and the relative weights of the different populations were calculated. An asterisk (\*) indicates that the respective value was fixed for fitting. The error of the fit values was approximated from the measurements without a NEF as the maximum standard deviation for the fit and is given in parenthesis.

Mutant	Subpopulation 1			Subpopulation 2			Subpopulation 3			Goodness of the fit $\chi^2$
	$d$ [Å]	$\sigma$ [Å]	%	$d$ [Å]	$\sigma$ [Å]	%	$d$ [Å]	$\sigma$ [Å]	%	
167/519 BAP- $\Delta$ N	41 ( $\pm$ 4)	3 ( $\pm$ 1)	3.2	55 ( $\pm$ 1)	8 ( $\pm$ 1)	65.5	65 ( $\pm$ 2)	17 ( $\pm$ 2)	31.3	1.7
167/519 BAP- $\Delta$ N + ATP				53 ( $\pm$ 1)	4 ( $\pm$ 1)	88.9	74 ( $\pm$ 2)	13 ( $\pm$ 2)	11.1	5.9
167/519 BAP- $\Delta$ N + ADP	40 ( $\pm$ 4)	3 ( $\pm$ 1)	4.8	55 ( $\pm$ 1)	8 ( $\pm$ 1)	83.4	82 ( $\pm$ 2)	11* ( $\pm$ 2)	11.8	1.3
519/638 BAP- $\Delta$ N	44 ( $\pm$ 1)	3 ( $\pm$ 1)	53.4	48 ( $\pm$ 4)	8 ( $\pm$ 3)	38.7	85 ( $\pm$ 4)	10* ( $\pm$ 5)	7.9	2.2
519/638 BAP- $\Delta$ N + ATP				48 ( $\pm$ 4)	8 ( $\pm$ 3)	10.6	89 ( $\pm$ 4)	9 ( $\pm$ 5)	89.4	25.8
519/638 BAP- $\Delta$ N + ADP	44 ( $\pm$ 1)	4 ( $\pm$ 1)	43.9	53 ( $\pm$ 4)	12 ( $\pm$ 3)	12.8	86 ( $\pm$ 4)	7 ( $\pm$ 5)	43.3	15.5
167/638 BAP- $\Delta$ N	40 ( $\pm$ 2)	3 ( $\pm$ 1)	2.3	54 ( $\pm$ 1)	9 ( $\pm$ 1)	38.9	64 ( $\pm$ 3)	15 ( $\pm$ 4)	58.8	1.7
167/638 BAP- $\Delta$ N + ATP	44 ( $\pm$ 2)	4 ( $\pm$ 1)	5.9	55 ( $\pm$ 1)	3 ( $\pm$ 1)	76.9	69* ( $\pm$ 3)	11 ( $\pm$ 4)	17.2	5.9
167/638 BAP- $\Delta$ N + ADP	43 ( $\pm$ 2)	3 ( $\pm$ 1)	14.9	57 ( $\pm$ 1)	13 ( $\pm$ 1)	85.1				2.0

Table 5.5: Distances calculated using PDA for BiP- $\Delta$ lid with BAP or BAP- $\Delta$ N and in the presence and absence of nucleotides. BiP- $\Delta$ lid (25 pM) was measured in the absence (*apo*) and presence of nucleotides (1 mM ATP or 1 mM ADP) and a nucleotide exchange factor (10  $\mu$ M BAP or 10  $\mu$ M BAP- $\Delta$ N). The photons of a burst were divided into bins of 1 ms, summed up in a FRET histogram, and fitted using a double- or triple-Gaussian model. From the PDA, the distance  $d$  between donor and acceptor, the corresponding width  $\sigma$  and the relative weights of the different populations were calculated. An asterisk (\*) indicates that the respective value was fixed for fitting. The error of the fit values was approximated from the measurements without a NEF as the maximum standard deviation for the fit and is given in parenthesis.

BiP- $\Delta$ lid	Subpopulation 1			Subpopulation 2			Subpopulation 3			Goodness of the fit $\chi^2$
	$d$ [Å]	$\sigma$ [Å]	%	$d$ [Å]	$\sigma$ [Å]	%	$d$ [Å]	$\sigma$ [Å]	%	
BAP	41 ( $\pm$ 4)	3 ( $\pm$ 1)	17.4	54 ( $\pm$ 1)	11 ( $\pm$ 1)	82.6				11.7
BAP + ATP	41 ( $\pm$ 4)	4 ( $\pm$ 1)	8.3	53 ( $\pm$ 1)	4 ( $\pm$ 1)	82.0	69 ( $\pm$ 2)	11* ( $\pm$ 2)	9.7	7.2
BAP + ADP	40 ( $\pm$ 4)	3 ( $\pm$ 1)	18.7	52 ( $\pm$ 1)	11 ( $\pm$ 1)	81.3				3.5
BAP- $\Delta$ N	41 ( $\pm$ 4)	3 ( $\pm$ 1)	30.7	52 ( $\pm$ 1)	10 ( $\pm$ 1)	69.3				11.0
BAP- $\Delta$ N + ATP	41 ( $\pm$ 4)	3 ( $\pm$ 1)	22.1	53 ( $\pm$ 1)	4 ( $\pm$ 1)	69.2	64 ( $\pm$ 2)	9* ( $\pm$ 2)	8.7	3.9
BAP- $\Delta$ N + ADP	40 ( $\pm$ 4)	2 ( $\pm$ 1)	30.5	49 ( $\pm$ 1)	9 ( $\pm$ 1)	69.5				4.4

stead of BAP. In the nucleotide free state, the percentage shifted from 5.2 % for BiP-167-519 with BAP to 17.4 % for BiP- $\Delta$ lid with BAP and to 30.7 % for BiP- $\Delta$ lid with BAP- $\Delta$ N. The relatively high percentage of BiP molecules with a short distance between the two binding domains suggest that the lid keeps the two domains separated from each other.

An additional effect was the shift of a certain percentage of BiP- $\Delta$ lid molecules to the high FRET conformation ( $d \sim 53 \text{ \AA}$ ) either without a nucleotide or when ADP was present. From the measurements of BiP with BAP and ADP, we know that BiP is very inhomogeneous and has a broad distribution of conformations for the linker between the two binding domains. Without the lid, the distribution of conformations gets narrower. By removing the N-terminal domain of BAP, the remaining molecules with low FRET efficiencies were also shifted to the two high FRET conformations ( $d \sim 40 \text{ \AA}$  and  $d \sim 53 \text{ \AA}$ ). This supports the theory that the lid interacts with the N-terminal domain of BAP and pushes the two binding domains apart.

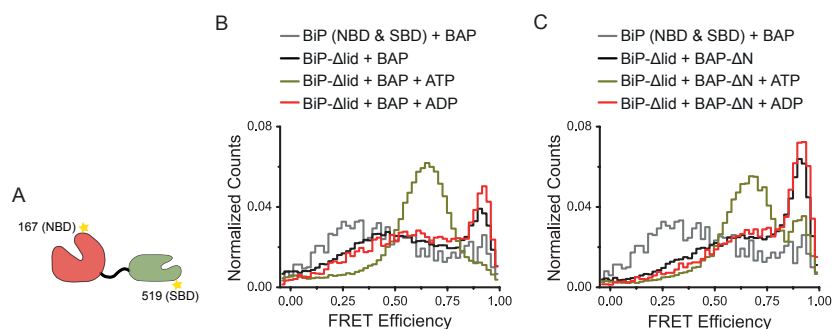


Figure 5.13: SpFRET analysis of BiP- $\Delta$ lid with BAP and BAP- $\Delta$ N. **(A)** A cartoon of BiP- $\Delta$ lid indicating the labeling position is shown. **(B)** SpFRET distributions were measured for 25 pM BiP-167-519 with 10  $\mu$ M BAP (grey line) or 25 pM BiP- $\Delta$ lid with 10  $\mu$ M BAP alone (black line), in the presence of 10  $\mu$ M BAP and 1 mM ATP (dark yellow line) or 10  $\mu$ M BAP and 1 mM ADP (red line). **(C)** SpFRET distributions were measured for BiP-167-519 with 10  $\mu$ M BAP (grey line), BiP- $\Delta$ lid with 10  $\mu$ M BAP- $\Delta$ N (black line), with 10  $\mu$ M BAP- $\Delta$ N and 1 mM ATP (dark yellow line) or with 10  $\mu$ M BAP and 1 mM ADP (red line).

In summary, the effect of deleting the lid of BiP or the N-terminal domain of BAP, suggest that the C-terminal lid of BiP interacts with the N-terminal domain of BAP. They push each other apart and, therefore, increase the distance between the NBD and SBD of BiP. When one or both interaction partners are missing, the two domains come close together.

## 5.7 The function of BAP as a nucleotide exchange factor

A NEF, in our case BAP, is expected to influence the nucleotide cycle and speed it up. This can be done in different ways. One possibility is that BAP, due to the transient interaction with BiP, speeds up the hydrolysis of ATP and, therefore, the whole cycle gets fast. To further address this question, the dissociation constant of BiP with bound ATP in the presence and absence of BAP have to be compared. The comparison is experimentally challenging as total values of the dissociation constant for ATP cannot be determined, due to hydrolysis of ATP. In the used ATP stock, a small percentage of ADP is always present. Another way to determine

the dissociation rate of ATP is to use commercial ADP, which contains a few percent of ATP contamination. For the other measurements, which are presented above, ADP was purified by an anion-exchange column in the Äkta (ÄKTAmicro, GE Healthcare, Uppsala, Sweden) and only the ADP fraction was used. For the determination of the  $K_d$ , we used the commercial ADP, because the measurements contains then two different populations, the ADP and the ATP conformation. Thus, we can only compare the measurements with and without BAP or BAP- $\Delta$ N but cannot determine absolute values.

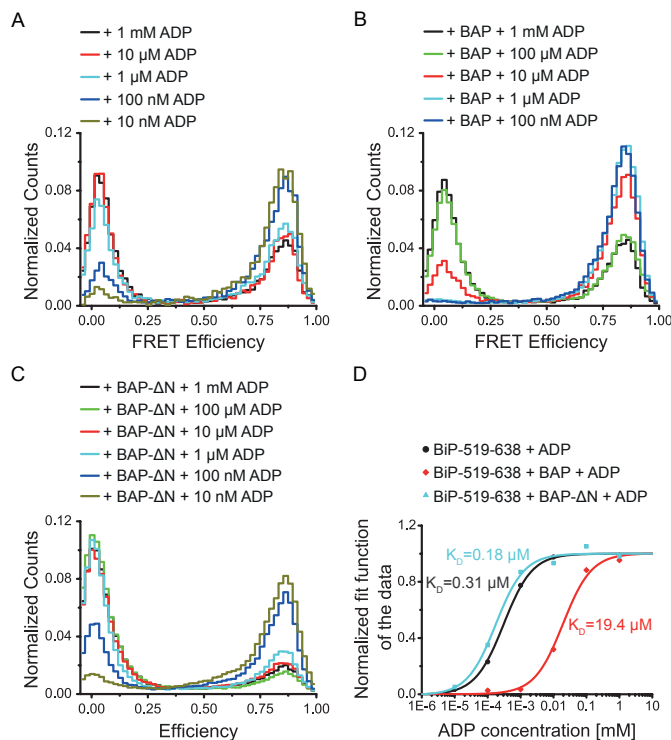


Figure 5.14: Calculation of the  $K_d$  of ATP in the presence and absence of BAP by using spFRET. SpFRET distributions of 25 pM BiP-519-638 were measured with different concentrations of ADP contaminated with a few percent of ATP (**A**) in the absence and (**B**) presence of 10  $\mu$ M BAP and (**C**) presence of 10  $\mu$ M BAP- $\Delta$ N. (**D**) The normalized area under the FRET histograms up to a FRET value of 0.4 was summed up and plotted versus the ADP concentration. The  $K_d$  is given by the fit as  $0.31 \pm 0.03 \mu$ M for BiP alone,  $19.4 \pm 4.8 \mu$ M in the presence of BAP and  $0.17 \pm 0.04 \mu$ M in the presence of BAP- $\Delta$ N.

Different ADP concentrations and, thus, also different ATP concentrations, were measured in the absence of a NEF (Figure 5.14A), in the presence of BAP (Figure 5.14B) and in the presence of BAP- $\Delta$ N (Figure 5.14C). The normalized area under the FRET efficiency histogram up to a FRET efficiency value of 0.4 was plotted versus the ADP concentration. The values were fitted by a sigmoid curve (Figure 5.14D). For BiP alone, a  $K_d$  of  $0.31 \pm 0.03 \mu$ M was determined. By adding BAP to the measurements, the  $K_d$  increased to  $19.4 \pm 4.8 \mu$ M. This is an increase in the dissociation constant of a factor of 65. Therefore, BAP increases the release of ATP. To analyze if this effect is due to the N-terminus of BAP, the same experiment was performed with BAP- $\Delta$ N instead of BAP. The calculated value for the  $K_d$

was  $0.17 \pm 0.04 \mu\text{M}$ . This is in the same range as the value calculated for the measurements without a NEF and, therefore, the increase in the ATP release is due to the N-terminal domain of BAP.

To further address the effect of BAP on the nucleotide cycle, the hydrolysis process is analyzed in more details. When ATP hydrolyzes, an ADP and a pyrophosphate are bound to BiP. In the measurements before, only ADP was added instead of ADP and pyrophosphate. One effect could be that BAP speeds up the process of kicking off the pyrophosphate and, therefore, speeding up the whole nucleotide cycle. To answer this question, pyrophosphate was added to the measurement of the lid-mutant with ADP and to the measurements with BAP and ADP. It was decided to simulate the hydrolyzed state because it is very hard to control the hydrolysis process and, therefore, it is unknown if an ATP or an ADP with pyrophosphate is present. However, these measurements are again performed with the non-purified ADP, which is the reason for the two FRET populations.

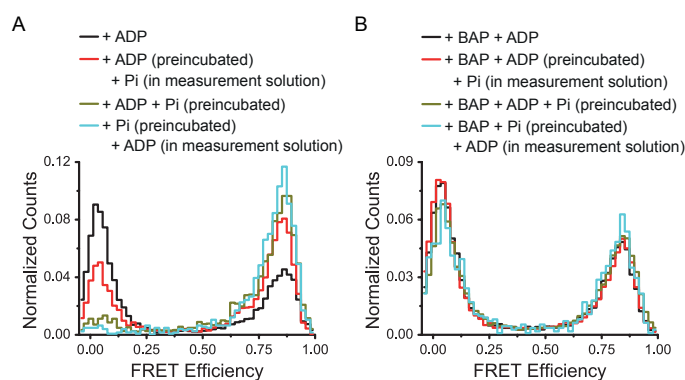


Figure 5.15: Conformational effect of pyrophosphate for BiP with ADP in the presence and absence of BAP. **(A)** SpFRET distributions of 25 pM BiP-519-638 were measured with different ways of incubation with 10 mM pyrophosphate and 1 mM ADP in the absence of BAP or **(B)** in the presence of 10  $\mu\text{M}$  BAP.

To figure out the effect of pyrophosphate, we measured the spFRET distribution of BiP-519-638 in the presence of ADP and a 10-fold Mol excess of pyrophosphate compared to ADP. The incubation process was varied. When we first incubate with ADP at 37°C for 15 min and then add pyrophosphate to the measurement at 20°C (Figure 5.15A, red line) a small shift from low to high FRET efficiencies compared to the measurements without pyrophosphate was detected (Figure 5.15A, black line). By preincubating ADP and pyrophosphate at the same time at 37°C for 15 min, the lid is totally closed (Figure 5.15A, dark yellow line). This does not change anymore when we first incubate with pyrophosphate at 37°C for 15 min and then add ADP to the measurement at 20°C (Figure 5.15A, cyan line). The explanation for this effect can be given by the fact that pyrophosphate is known to increase the affinity of a Hsp70 to ADP. Therefore, as longer BiP is incubated with pyrophosphate as more likely it is that the affinity for ADP is increased.

By adding BAP to the different incubation processes, no changes in the conformation with a mixture of open and closed lid conformations were detected (Figure 5.15B). This means BAP keeps the lid conformation constant, independent of the presence of pyrophosphate. Thus, it is most likely that BAP has a opposite effect on the ADP affinity as the pyrophosphate and the two effects are canceled out.

In summary, we were not able to make statements about the hydrolyzed state and how BAP changes it. However, we detected that BAP can cancel out the increase in the ADP affinity induced by pyrophosphate.

## 5.8 BAP and C<sub>H</sub>1 compete for binding to BiP with each other

BiP interacts in the ER with a substrate, for example, to protect it from unspecific interaction with itself or with other substrates. An authentic substrate protein for BiP is C<sub>H</sub>1, an intrinsically disordered domain of antibodies [Vanhove et al., 2001], [Marcinowski et al., 2013]. In a cell, different factors influence the interaction of BiP with the substrate, one of them is the NEF BAP. BAP interacts with the lid and, therefore, has an effect on the substrate binding pocket. Thus, it is of interest how the conformation of BiP changes, when BAP and C<sub>H</sub>1 are both present.

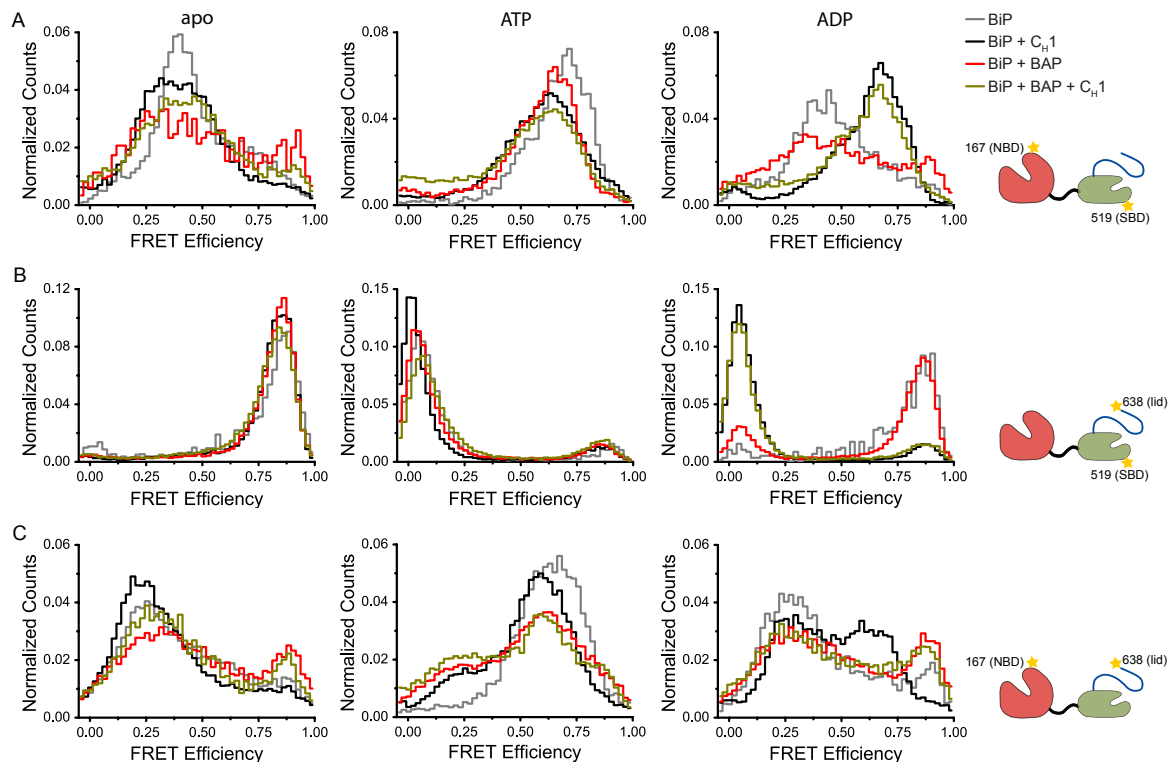


Figure 5.16: SpFRET analysis of BiP with BAP and C<sub>H</sub>1. **(A-C)** SpFRET distributions of 25 pM BiP were measured in the absence of any NEF and substrate (gray line), in the presence of 14  $\mu$ M C<sub>H</sub>1 (black line) or 10  $\mu$ M BAP (red line) or with 10  $\mu$ M BAP and 14  $\mu$ M C<sub>H</sub>1 (dark yellow line) and without nucleotide, with 1 mM ADP or 1 mM ATP, respectively. All three labeling constructs were measured under these conditions. **(A)** BiP-167-519 gives information about the distance between NBD and SBD, **(B)** BiP-519-638 monitors the lid conformation and **(C)** BiP-167-519 has labels on the NBD and the lid to watch the distance between NBD and the C-terminal end of the lid.

As a control, BiP was measured in the presence of C<sub>H1</sub> (Figure 5.16 (black lines)). For BiP with C<sub>H1</sub> but without a nucleotide (Figure 5.16 (first row)), the conformation of all three labeling mutants was similar to the measurements without C<sub>H1</sub>.

Binding of C<sub>H1</sub> to BiP with ATP did not induce conformational changes for all three mutants (Figure 5.16 (second row)). This could be explained by the low binding affinity of C<sub>H1</sub> to BiP in the ATP conformation [Vanhove et al., 2001].

When adding ADP instead of ATP, changes in the conformation were observed (Figure 5.16 (third row) and Table 5.6). The interdomain-mutant, BiP-167-519, had one broad peak, which required two Gaussian functions in a close proximity for proper fitting. One Gaussian with a peak separation of  $d = 52 \text{ \AA}$  and a width of  $\sigma = 4 \text{ \AA}$ . This conformation is equal to the ATP conformation without a substrate. The other Gaussian was calculated with a distance of  $d = 55 \text{ \AA}$  with a width of  $\sigma = 7 \text{ \AA}$ . Thus, upon binding of C<sub>H1</sub>, most of the molecules shifted to a closer interdomain separation. The lid is in an open conformation, similar to the conformation of BiP with ATP. The last mutant, BiP-167-638, consists of two FRET populations in the presence of C<sub>H1</sub> and ADP. One population is similar to the main conformation of BiP in the presence of ADP and the other one is again similar to the ATP state.

In conclusion, the effect of C<sub>H1</sub> on the conformation of BiP was only observable in the ADP bound state. We detected no conformational changes in BiP without a nucleotide or in the presence of ATP, independent of substrate binding. This could be explained by the low binding affinity of BiP to a substrate in those nucleotide states and is in line with the results from [Qi et al., 2013], [Yang et al., 2015]. They show that ATP binding strongly affects substrate release and polypeptide re-binding stimulates ATP hydrolysis. The lid opens completely and the two binding domains finally shifts to a closer distance. In the presence of ADP, the affinity increases due to conformational changes in the substrate binding pocket and the substrate stays bound.

In the presence of both BAP and C<sub>H1</sub>, BiP changed its conformation in a different manner (Figure 5.16 (dark yellow lines) and Table 5.7). In the absence of any nucleotide (Figure 5.16 (first row)), the conformations for BiP with C<sub>H1</sub> and BiP with BAP were similar. We detected no conformational changes by adding both, BAP and C<sub>H1</sub>.

When ATP is bound to BiP, BAP can only interact transiently, which was shown above (Chapter 5.4 on page 59). C<sub>H1</sub> itself did not introduce a conformational change of BiP with ATP. Therefore, no structural changes were detected when BAP and C<sub>H1</sub> were added to BiP with ATP (Figure 5.16 (second row)).

In the presence of ADP (Figure 5.16 (third row)), we detected differences between the measurements of BiP with BAP, BiP with C<sub>H1</sub> and BiP with BAP and C<sub>H1</sub>. The interdomain-mutant, BiP-167-519, had a similar conformation with C<sub>H1</sub> alone and C<sub>H1</sub> with BAP. In the presence of C<sub>H1</sub> the lid was completely open, independent of BAP, which induced alone a partly closed lid. The combined-mutant changed its conformation upon addition of BAP. The distances are similar to the distances measured only in the presence of BAP. Therefore, we can conclude that in the measurements with ADP, either BiP is in the conformations of BiP with BAP or in the conformations of BiP with C<sub>H1</sub>.

To further analyze the interaction between BiP, BAP and the substrate C<sub>H1</sub>, Mathias Rosam from the group of Prof. Buchner performed analytical ultracentrifugation (AUC) experiments. He measured BiP alone as a reference (Figure 5.17 (gray line)). Upon binding of C<sub>H1</sub> to BiP, only a very small change in size was observed (Figure 5.17 (black line)). The sedimentation velocity and, therefore, the sedimentation coefficient  $s_{20,w}$  of this measurement resulted in the same peak value as for BiP alone. Additionally, the peaks for the dimers and

Table 5.6: Distances calculated using PDA for BiP with C<sub>H1</sub> and in the presence and absence of nucleotides. The spFRET mutants (25 pM) were measured in the absence (*apo*) and presence of nucleotides (1 mM ATP or 1 mM ADP) and a substrate (14  $\mu$ M C<sub>H1</sub>). The photons of a burst were divided into bins of 1 ms, summed up in a FRET histogram, and fitted using a double- or triple-Gaussian model. From the PDA, the distance  $d$  between donor and acceptor, the corresponding width  $\sigma$  and the relative weights of the different populations were calculated. An asterisk (\*) indicates that the respective value was fixed for fitting. The error of the fit values was approximated from the measurements with a nucleotide as the maximum standard deviation for the fit and is given in parenthesis.

Mutant	Subpopulation 1			Subpopulation 2			Subpopulation 3			Goodness of the fit $\chi^2$	
	$d$ [Å]	$\sigma$ [Å]	%	$d$ [Å]	$\sigma$ [Å]	%	$d$ [Å]	$\sigma$ [Å]	%		
167/519	C <sub>H1</sub>	40 ( $\pm$ 4)	5 ( $\pm$ 1)	3.7			61 ( $\pm$ 2)	8 ( $\pm$ 2)	96.3	5.9	
167/519	ATP + C <sub>H1</sub>				53 ( $\pm$ 1)	6 ( $\pm$ 1)	95.0	83 ( $\pm$ 2)	14* ( $\pm$ 2)	5.0	7.6
167/519	ADP + C <sub>H1</sub>	52 ( $\pm$ 1)	4 ( $\pm$ 1)	56.5	55 ( $\pm$ 1)	7 ( $\pm$ 1)	38.6	97 ( $\pm$ 2)	12* ( $\pm$ 2)	4.9	2.7
519/638	C <sub>H1</sub>	45 ( $\pm$ 1)	3 ( $\pm$ 1)	84.1	52 ( $\pm$ 4)	11 ( $\pm$ 3)	15.9				8.1
519/638	ATP + C <sub>H1</sub>	45 ( $\pm$ 1)	4 ( $\pm$ 1)	12.3				100 ( $\pm$ 4)	20 ( $\pm$ 5)	87.7	9.6
519/638	ADP + C <sub>H1</sub>	44 ( $\pm$ 1)	4 ( $\pm$ 1)	12.5				96 ( $\pm$ 4)	15 ( $\pm$ 5)	87.5	11.1
167/638	C <sub>H1</sub>	44 ( $\pm$ 2)	6 ( $\pm$ 1)	10.6				66 ( $\pm$ 3)	10 ( $\pm$ 4)	89.4	2.0
167/638	ATP + C <sub>H1</sub>	45 ( $\pm$ 2)	4 ( $\pm$ 1)	13.2	55 ( $\pm$ 1)	4 ( $\pm$ 1)	43.2	67 ( $\pm$ 3)	12 ( $\pm$ 4)	43.6	2.1
167/638	ADP + C <sub>H1</sub>	40 ( $\pm$ 2)	5 ( $\pm$ 1)	2.3	53 ( $\pm$ 1)	3 ( $\pm$ 1)	23.6	62 ( $\pm$ 3)	10 ( $\pm$ 4)	74.1	3.9

Table 5.7: Distances calculated using PDA for BiP with BAP and C<sub>H1</sub> and in the presence and absence of nucleotides. The spFRET mutants (25 pM) were measured in the absence (*apo*) and presence of nucleotides (1 mM ATP or 1 mM ADP), a nucleotide exchange factor (10  $\mu$ M BAP) and a substrate (14  $\mu$ M C<sub>H1</sub>). The photons of a burst were divided into bins of 1 ms, summed up in a FRET histogram, and fitted using a double or triple-Gaussian model. With photon distribution analysis (PDA), the distance  $d$  between donor and acceptor, the corresponding width  $\sigma$  and the relative weights of the different populations were calculated. An asterisk (\*) indicates that the respective value was fixed for fitting. The error of the fit values was approximated from the measurements with a nucleotide as the maximum standard deviation for the fit and is given in parenthesis.

Mutant	Subpopulation 1			Subpopulation 2			Subpopulation 3			Goodness of the fit $\chi^2$	
	$d$ [Å]	$\sigma$ [Å]	%	$d$ [Å]	$\sigma$ [Å]	%	$d$ [Å]	$\sigma$ [Å]	%		
167/519	BAP + C <sub>H1</sub>	42 ( $\pm$ 4)	5 ( $\pm$ 1)	10.5	60 ( $\pm$ 1)	8 ( $\pm$ 1)	80.0	90 ( $\pm$ 2)	11* ( $\pm$ 2)	9.5	1.2
167/519	BAP + ATP + C <sub>H1</sub>				54 ( $\pm$ 1)	6 ( $\pm$ 1)	82.4	78 ( $\pm$ 2)	13* ( $\pm$ 2)	17.6	11.3
167/519	BAP + ADP + C <sub>H1</sub>	53 ( $\pm$ 1)	4 ( $\pm$ 1)	48.3	55 ( $\pm$ 1)	9 ( $\pm$ 1)	41.4	85 ( $\pm$ 2)	13* ( $\pm$ 2)	10.3	1.9
519/638	BAP + C <sub>H1</sub>	45 ( $\pm$ 1)	4 ( $\pm$ 1)	79.3	52 ( $\pm$ 4)	8 ( $\pm$ 3)	18.4	95 ( $\pm$ 4)	10* ( $\pm$ 5)	2.2	1.8
519/638	BAP + ATP + C <sub>H1</sub>	46 ( $\pm$ 1)	4 ( $\pm$ 1)	17.5				84 ( $\pm$ 4)	11 ( $\pm$ 5)	82.5	18.2
519/638	BAP + ADP + C <sub>H1</sub>	45 ( $\pm$ 1)	5 ( $\pm$ 1)	17.1				95 ( $\pm$ 4)	17 ( $\pm$ 5)	82.9	2.7
167/638	BAP + C <sub>H1</sub>	43 ( $\pm$ 2)	3 ( $\pm$ 1)	9.6				61 ( $\pm$ 3)	12 ( $\pm$ 4)	90.4	2.4
167/638	BAP + ATP + C <sub>H1</sub>	44 ( $\pm$ 2)	4 ( $\pm$ 1)	13.7	55 ( $\pm$ 1)	4 ( $\pm$ 1)	38.6	64 ( $\pm$ 3)	14 ( $\pm$ 4)	47.7	2.0
167/638	BAP + ADP + C <sub>H1</sub>	44 ( $\pm$ 2)	4 ( $\pm$ 1)	16.5				59 ( $\pm$ 3)	14 ( $\pm$ 4)	83.5	3.9

higher oligomers disappeared in the presence of  $C_{H1}$ , which was in line with [Blond-Elguindi et al., 1993]. Adding BAP to BiP (Figure 5.17 (red line)) resulted in a larger sedimentation coefficient because of the larger complex size. Surprisingly, the complex peak of BiP with BAP and  $C_{H1}$  shifted towards a smaller sedimentation coefficient than the BiP-BAP complex and was in between the peak of BiP with  $C_{H1}$  and the peak of BiP with BAP (Figure 5.17 (dark yellow line)).

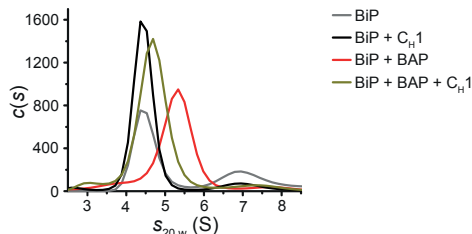


Figure 5.17: Analytical ultracentrifugation measurements of BiP with BAP and  $C_{H1}$ . Complex formation by sedimentation velocity (SV) runs of  $0.37 \mu\text{M}$  ATTO 488-labeled BiP (gray line),  $0.37 \mu\text{M}$  ATTO 488-labeled BiP and  $37 \mu\text{M}$   $C_{H1}$  (black line),  $0.37 \mu\text{M}$  ATTO 488-labeled BiP and  $3.7 \mu\text{M}$  BAP (red line) or  $0.37 \mu\text{M}$  ATTO 488-labeled BiP,  $3.7 \mu\text{M}$  BAP and  $37 \mu\text{M}$   $C_{H1}$  (dark yellow line). The measurements were performed by Mathias Rosam in the group of Prof. Buchner.

Hence, we can conclude that BAP and  $C_{H1}$  cannot bind both at the same time. This result is in line with the experimental spFRET data, where the conformation of BiP with BAP and  $C_{H1}$  is either similar to the conformation of BiP with  $C_{H1}$  alone or to the conformation of BiP with BAP.

## 5.9 Discussion and Outlook

The function of BAP and its interactions on the endoplasmic reticulum-resident Hsp70 chaperone BiP were analyzed in this chapter. BAP was characterized in previous studies as a NEF of BiP [Chung et al., 2002]. NEFs generally facilitate the exchange of ADP to ATP [Cyr, 2008], which lead us to expect that BAP can interact with BiP and speed up the process of nucleotide exchange. From the crystal structure of yeast BiP with yeast BAP, it is known that BAP consists of two domains, the N-terminal and the C-terminal domain and interacts with the NBD of BiP (PDB-ID: 3QML) [Yan et al., 2011].

AUC and spFRET measurements were performed to analyze the effect of BAP on the nucleotide cycle of BiP. BAP was found to bind to BiP in the absence of any nucleotide and in the presence of ADP. When ATP is bound to BiP, BAP interacts transiently due to the N-terminal domain of BAP. The results are in line with the expectation that a NEF facilitates the exchange of ADP to ATP and, therefore, has to be bound in the ADP state of BiP [Behnke et al., 2015]. Furthermore, the lid of BiP and the N-terminus of BAP were identified to interact. By performing spFRET measurements on a lidless mutant of BiP, BiP- $\Delta$ lid, in combination with BAP lacking the N-terminus, BAP- $\Delta$ N, this interaction was identified. The lid and the N-terminal domain of BAP push each other apart and keep the two domains of BiP separated.

In addition, the effect of BAP on the nucleotide cycle was investigated. The dissociation constant of ATP from BiP and from BiP with BAP was indirectly determined. BAP increases the  $K_d$  by a factor of 65 and, thus, speeds up the release of ATP. One possible explanation would be that BAP changes the nucleotide binding pocket to a more open conformation to facilitate the release of the nucleotides. This is in line with the comparison of the crystal structures of the NBD with BAP and the NBD with BAP and ADP [Yan et al., 2011].

Furthermore, by testing to use of non-hydrolyzable ATP analogues, differences in the FRET histograms were identified. For BiP alone the FRET efficiencies measured with ATP and the ATP analogues are similar. By adding BAP, the detected conformations are similar to the ADP conformations. The differences between ATP and the ATP analogues are due to small chemical changes which are recognized by BAP. One possible explanation for the different behavior with and without BAP is that the binding domain of BiP changes from a pocket to a more tunnel-like structure, when BAP binds and, therefore, BAP itself interacts with the nucleotide. Thus, we have to use ATP instead of non-hydrolyzable ATP analogues for studying the ATP conformation of BiP. Nevertheless, the ATP analogues help to understand that the binding pocket in some case changes when BAP binds.

In the presence of a substrate, the intrinsically disordered domain  $C_H1$  of an antibody, the conformation upon binding of ADP changes. The lid has to be open, when  $C_H1$  is bound to the substrate binding pocket. Upon binding of a substrate and BAP, a mixed conformation of the BAP-bound and the  $C_H1$ -bound state was detected. This result is also supported by AUC measurements that showed that either BAP or  $C_H1$  can bind. This is in line with the idea that BAP should assist the chaperone cycle and help a substrate free BiP to accelerate the ADP/ATP exchange and, therefore, makes BiP again able to bind a new substrate [Cyr, 2008].

The overall nucleotide cycle of BiP is given in Figure 5.18. In the ATP state, the lid is in an open conformation and the two binding domains are close together. In this conformation, a substrate, in our case  $C_H1$ , can bind (Figure 5.18, outer cycle) [Marcinowski et al., 2011], but the affinity for the binding is low. When ATP hydrolyzes to ADP, the affinity of BiP for binding a substrate increases. The substrate stays bound to BiP, but the overall structure is very similar to the ATP bound conformation. Upon release of the ADP, the lid closes and catches the substrate. The two binding domains are well separated. By binding new ATP, the substrate is released and the whole nucleotide cycle starts again. Alternatively, BAP can interact transiently with BiP in the ATP conformation (Figure 5.18, inner cycle). When ATP hydrolyzes to ADP, BAP stable binds to BiP and separates the two binding domains and closes the lid. This conformation does not change when ADP is released. Upon binding of a new ATP, BAP is released from the complex. Whenever both interaction partners, BAP and  $C_H1$ , are present, only one can interact with BiP at a time.

The increase in the chaperone cycle due to BAP that was identified in the cooperation with the group of Prof. Buchner was in total much lower than for other NEFs. Other NEFs, for example Bag-1, are known to stimulate the dissociation of ADP from Hsc70 and Hsp70 by up to 100-fold [Mayer and Bukau, 2005]. Thus, BAP may have an additional function in the chaperone cycle. To further analyze the binding and dissociation rates in the presence and absence of BAP, TIRF measurements could be performed. We have already performed first experiments with immobilize BiP in vesicles but the protein seems to interact with the lipids. Direct binding of BiP to the surface was also tried but this results so far in the loss of the functionality of BiP. One idea to overcome this problem would be to use a flow system as described in [Tyagi et al., 2014].

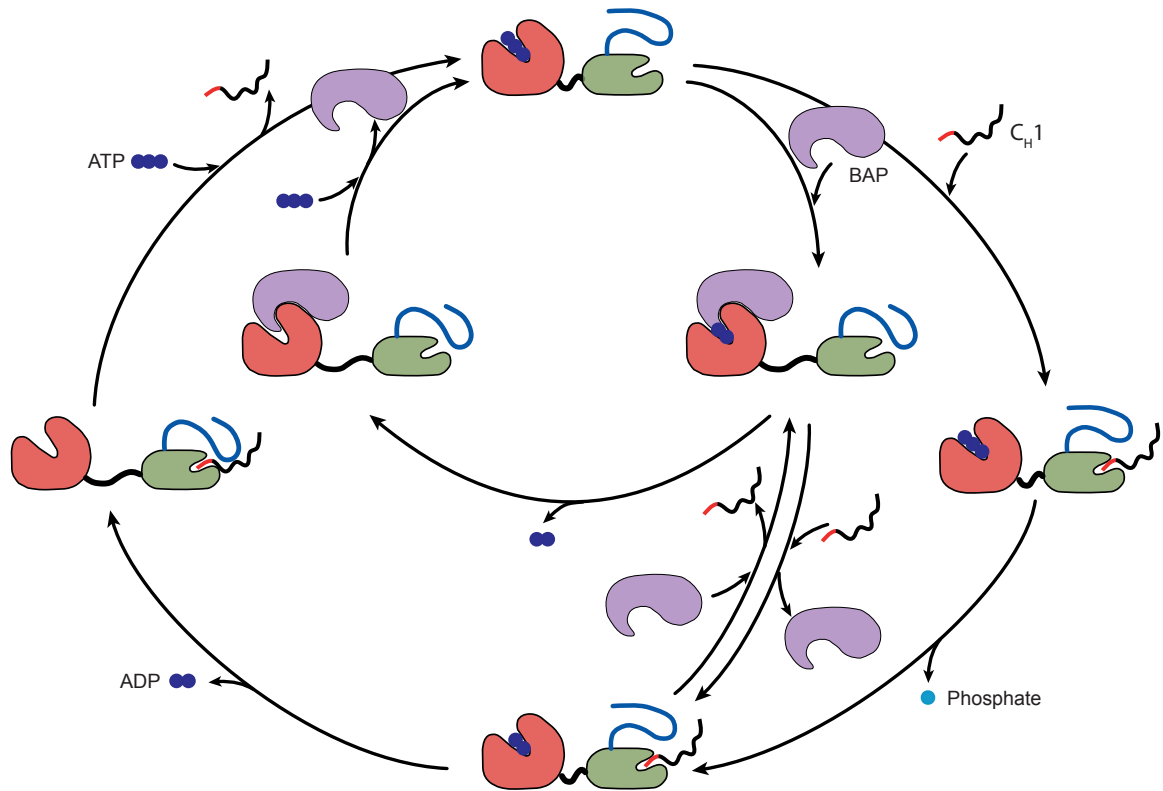


Figure 5.18: Model for the BAP-regulated chaperone cycle of BiP. The different domains of BiP and BAP are color-coded as in Figure 5.1 and in Figure 5.4. For BiP, the NBD is shown in red, the SBD in green and the lid in blue, BAP is depicted in purple. For all combinations of BiP, BAP and C<sub>H</sub>1, which are depicted, the most populated conformation is drawn.

Furthermore, it would be of interest to study the chaperone cycle of BiP in the presence of BAP and other co-chaperones, for example, a J-protein. J-proteins are known to influence the chaperone cycle and are assumed to interact between the two binding domains of BiP [Kampinga and Craig, 2010], [Mapa et al., 2010]. Due to the fact that BAP binds to the NBD and, therefore, is in close proximity to the linker between the NBD and SBD, it would be important to know if both proteins can interact at the same time with BiP or if they are competing with each other.

One of the major open questions is how mutations in BAP, like observed for patients with the disease Marinesco-Sjögren syndrome [Howes et al., 2012], are changing the interaction of BAP with BiP and how they influence the chaperone cycle. BAP was identified as a NEF, which increases the chaperone cycle much less than other NEFs. Furthermore, BiP is known to be functional without BAP. Therefore, the important question is, what is the effect of the mutations that causes the autosomal recessive form of ataxia, cataract and myopathy [Anttonen et al., 2005], [Senderek et al., 2005], [Krieger et al., 2013].

# 6 Sti1 mediates the interaction of Hsp70 and Hsp90

## 6.1 Introduction

Some unfolded proteins need not only the assistance by Hsp70, which was studied in the previous chapter, but rather from multiple chaperones. Therefore, Hsp70 interacts with the client and hands it over to Hsp90. From literature, it is known that Hsp70 and Hsp90 do not interact by its own in solution, they need assistance from a co-chaperone [Hernandez et al., 2002]. The co-chaperone Hop (Hsp-organizing protein) in mammals or its yeast homolog Sti1 (stress-induced protein 1) works as a scaffold and helps to bring Hsp70 and Hsp90 together [Chen and Smith, 1998]. This complex network of Hsp70, Hsp90 and numerous co-factors is not present in all biological systems, except for the prokaryotic and archaeal domains of life [Wegele et al., 2004]. The sequence identity between Hop and Sti1 is 37 % [Wegele et al., 2004]. Hop and Sti1 act in slightly different ways. Hop acts as a passive adapter and Sti1 is a regulatory linker protein for the ATPase of Hsp70 and Hsp90 [Wegele et al., 2004], [Daniel et al., 2007]. Nevertheless, their function is the same: they physically connect the two chaperones, Hsp70 and Hsp90, regulate their activity and enable the transfer of clients.

Sti1 consists of two aspartate and proline rich (DP) domains [Nelson et al., 2003] and three tetratricopeptide repeat (TPR) domains. TPR domains consist of 34-amino acid sequence motifs that are repeated 1 to 16 times per domain [Brinker et al., 2002]. These domains are known to interact with EEVD-COOH sequences, which can be found in Hsp70 and Hsp90. The EEVD motifs vary between Hsp70 and Hsp90. Hsp70 has a PTIEEVD motif and Hsp90 a MEEVD. These differences are the reason for selective interactions between the TPR domains and the Hsps [Scheuffler et al., 2000], [Brinker et al., 2002]. In Sti1, the three domains are named TPR1, TPR2A and TPR2B. Hsp90 interacts specifically with TPR2A and substantial contacts are formed between the Hsp90 M-domain and TPR2B [Lee et al., 2012], [Schmid et al., 2012]. TPR2A and TPR2B stabilize the open conformation of Hsp90 and inhibit the ATPase activity [Richter et al., 2003], [Schmid et al., 2012]. Hsp70 interacts with TPR1 and TPR2B. Thereby, the binding affinity of Hsp70 and Hsp90 varies. Hsp90 has a high affinity to the TPR2A domain, which is for Hop in the range of  $K_d = 90$  nM, independently of the presence of Hsp70, whereas Hsp70 has a lower interaction affinity. In the absence of Hsp90, the binding affinity of Hsp70 to Hop is  $K_d = 1.3$   $\mu$ M and, in the presence of Hsp90, the affinity increases to  $K_d = 250$  nM [Hernandez et al., 2002].

Two modules form a Sti1 molecule [Schmid et al., 2012] (see also Figure 6.1). The first module consists of TPR1 and DP1, which are flexibly connected. This module is the binding domain for Hsp70. The second module comprises the two TPR2 domains and the DP2 domain. TPR2A and TPR2B are connected in a non-flexible way and are connected by a rigid linker with DP2. Thus, the module can bind to Hsp70 and Hsp90. The two modules of Sti1 are connected by a flexible linker, which makes it possible to bring the module TPR1-DP1

in close proximity to the other domains. To resolve the mechanism of the conformational changes of Sti1 due to binding of Hsp70 and/or Hsp90, spFRET measurements were performed. We found that the two modules come together to transfer a bound Hsp70 from one binding domain to the other. The whole chapter is based on [Röhl et al., 2015] published under the license 'creative commons - Attribution 4.0 International'.

## 6.2 Sample Preparation

The protein expression, purification and labeling was done by Alina Röhl in the group of Prof. Buchner (TU Munich, Munich, Germany). A brief summary of the used strategy is presented here.

For the expression of Sti1, a pET28 vector carrying the respective gene and in addition a N-terminal 6xHis-SUMO-tag were transformed into the *E.coli* strain BL21 (DE3) Codon Plus. By addition of 1 mM isopropyl- $\beta$ -D-thiogalactopyranosid (IPTG) over night at 30°C, protein expression was induced at 0.5 of OD<sub>600</sub>. Protein purification was done by a 5 ml Hi-Tap column (GE Healthcare, Freiburg, Germany), then the His-SUMO-tag was cleaved and gel filtration chromatography was performed with a Superdex 200 PrepGrande column (GE Healthcare) preequilibrated in 40 mM Hepes (pH 7.5), 150 mM KCl, 5 mM MgCl<sub>2</sub>. The point mutations for the spFRET mutants were generated by using a QuikChange II Site-Directed Mutagenesis Kit (Agilent, Santa Clara, California, USA).

For yHsp90 (in this chapter only called Hsp90), a pET28 vector, which carries the respective gene, and a Thrombin cleavable 6xHis-tag were used. yHsp70 (in this chapter only called Hsp70) was expressed in *Pichia pastoris* strain KM71H-Ssa1 (aox1::ARG4; arg4; 6xHis-SSA1 gene genomically inserted at AOX1 locus), which was induced with 0.5 % (v/v) methanol. The purification of both Hsps was done in the same way as for Sti1.

For the spFRET measurements, all native cysteine residues in the Sti1-protein were removed and multiple double-cysteine mutants were generated. The double-cysteine mutants were labeled stochastically at the cysteine residues with ATTO 532-maleimide and ATTO 647-maleimide (AttoTec GmbH, Siegen, Germany) by adding a 3-fold excess of dyes in 40 mM Hepes (pH 7.5), 150 mM KCl, 5 mM MgCl<sub>2</sub> for one hour at room temperature. Quenching of the reaction was done by adding a 10-fold excess of cysteine. Afterwards, free dye was separated from the protein on a Superdex 200 10/300 GL HPLC column (GE Healthcare). The attached dyes do not alter the functionality of Sti1, which was tested by Alina Röhl.

The spFRET measurements in solution were performed with fluorescently labeled Sti1, which was diluted to a concentration of approximately 25 pM and then measured alone or in the presence of 25  $\mu$ M Hsp70 and/or 10  $\mu$ M Hsp90. The Hsp70 and Hsp90 concentrations were chosen much higher than the  $K_d$ , which is known from [Scheufler et al., 2000] and [Hernandez et al., 2002]. The sample preparation for the surface based measurements was done as described previously in Chapter 3.5 on page 37.

### 6.3 TPR2A and TPR2B form a rigid module

To monitor the conformational changes of Sti1 and, therefore, to deduce the mechanism that brings Hsp70 and Hsp90 together, different labeling positions for spFRET were tested. The overall structure of Sti1 is not known, but crystal structures of the isolated domains have been resolved. The PDB-ID of the different domains are 1ELW (TPR1), 2LLV (DP1), 3UQ3 (TPR2) and 2LLW (DP2). Combining the domains helps to get an idea of the overall structure. Figure 6.1 shows the combination of the domains and additionally depicts all tested labeling positions.

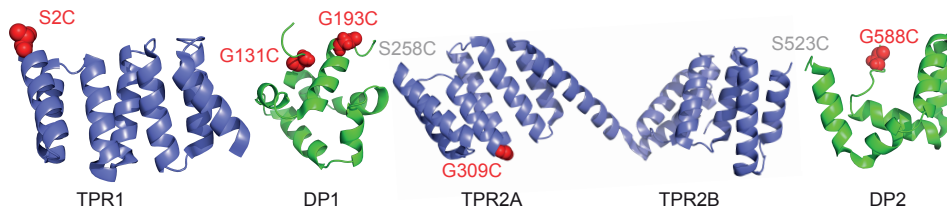


Figure 6.1: Different tested labeling positions of Sti1. The secondary structures of the different domains of Sti1 (PDB-ID: 1ELW, 2LLV, 3UQ3, 2LLW) are combined. The residues mutated to a cysteine are shown in red. The two mutated residues labeled in gray are not solved in the structure.

From the crystal structure, it is known that the two TPR2 domains are rigidly connected [Schmid et al., 2012]. To test if our full length Sti1 behaves in the same way as the isolated TPR2 domain, the TPR2A and TPR2B domains were labeled stochastically with two dye. The mutant, called G309C-S523C, is depicted in the cartoon in Figure 6.2A.

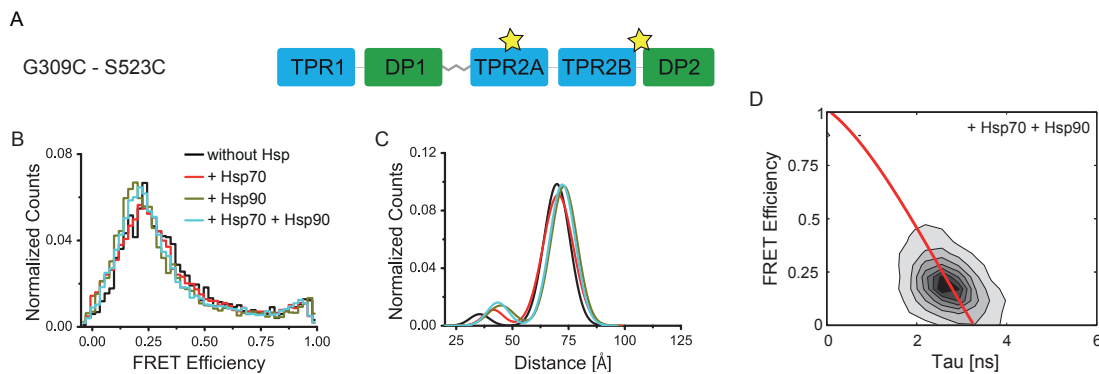


Figure 6.2: SpFRET analysis of the Sti1 mutant G309C-S523C. (A) SpFRET mutant is labeled in both TPR2 domains to monitor the rigidity of the linker between the two modules. (B) SpFRET distributions of 25 pM Sti1 measured in the absence of any interaction partner (black line), in the presence of 25  $\mu$ M Hsp70 (red line), 10  $\mu$ M Hsp90 (dark yellow line) or in the presence of 25  $\mu$ M Hsp70 and 10  $\mu$ M Hsp90 (cyan line). (C) The distance distributions were calculated using PDA. (D) FRET efficiency versus lifetime plot of the Sti1 mutant G309C-S523C. The red line is the theoretical relationship between the lifetime and the FRET efficiency, when the molecule does not change its conformation while it is measured.

We expected no changes by adding Hsp70, Hsp90 or both. Figure 6.2B shows the spFRET efficiency histograms measured in the presence of the different bound Hsps. The maximum in the spFRET efficiency histogram did not depend on the addition of Hsps. The second small FRET efficiency population was occupied by less than 10 % of the Sti1 molecules and could represent misfolded molecules or sticking of the dyes to Sti1.

The distances calculated using PDA from the spFRET efficiency histogram are given in Figure 6.2C and Table 6.1. Upon addition of Hsps, the distances did not change. The FRET peak with the highest population corresponds to a mean dye distance of 70 - 73 Å ( $\sigma$  in the range of 8 - 10 Å).

Table 6.1: Distances calculated using PDA for the Sti1 mutant G309C-S523C. G309C-S523C (25 pM) was measured in the absence of any Hsp, in the presence of 25  $\mu$ M Hsp70, in the presence of 10  $\mu$ M Hsp90 and in the presence of 25  $\mu$ M Hsp70 and 10  $\mu$ M Hsp90. The photons of a burst were divided into bins of 1 ms, summed up in a FRET histogram, and fitted using a double-Gaussian model. From the PDA, the distance  $d$  between donor and acceptor, the corresponding width  $\sigma$  and relative weights of the different populations were calculated. An asterisk (\*) indicates that the respective value was fixed.

G309C-S523C	Subpopulation 1			Subpopulation 2			Goodness of the fit
	$d$ [Å]	$\sigma$ [Å]	%	$d$ [Å]	$\sigma$ [Å]	%	$\chi^2$
without Hsp	35	6*	3.6	70	8	96.4	1.3
+ Hsp70	41	6*	6.0	70	10	94.0	2.9
+ Hsp90	45	8*	7.3	73	8	92.7	1.2
+ Hsp70 + Hsp90	43	7*	7.9	72	8	92.1	2.9

Additionally, FRET efficiency versus the lifetime of the donor was plotted exemplary for the measurement in the presence of Hsp70 and Hsp90 (Figure 6.2D). Dynamic behavior of the molecule on the timescale of the diffusion time can be identified by this method (see Chapter 3.3.3 on page 29). For the measurements of G309C-S523C the population is exactly on the static line and, therefore, no dynamics can be identified.

In summary, we can conclude that the two TPR2 domains (TPR2A and TPR2B) are connected by a rigid linker and do not change their conformation upon binding of Hsps.

## 6.4 End-to-end distances are too large for detecting conformational changes

To address the question of large conformational changes between the two modules of Sti1, both ends of the protein were labeled with fluorescent dyes. Different mutants were tested (Figure 6.3A). The mutants, where the dyes are located at both ends, are S2C-G588C (Figure 6.3B), S2C-S523C (Figure 6.3C) and G131C-S523C (Figure 6.3D). One labeled residue is located either in the TPR1 or in the DP1 domain, the other in the DP2 domain or between TPR2B and DP2.

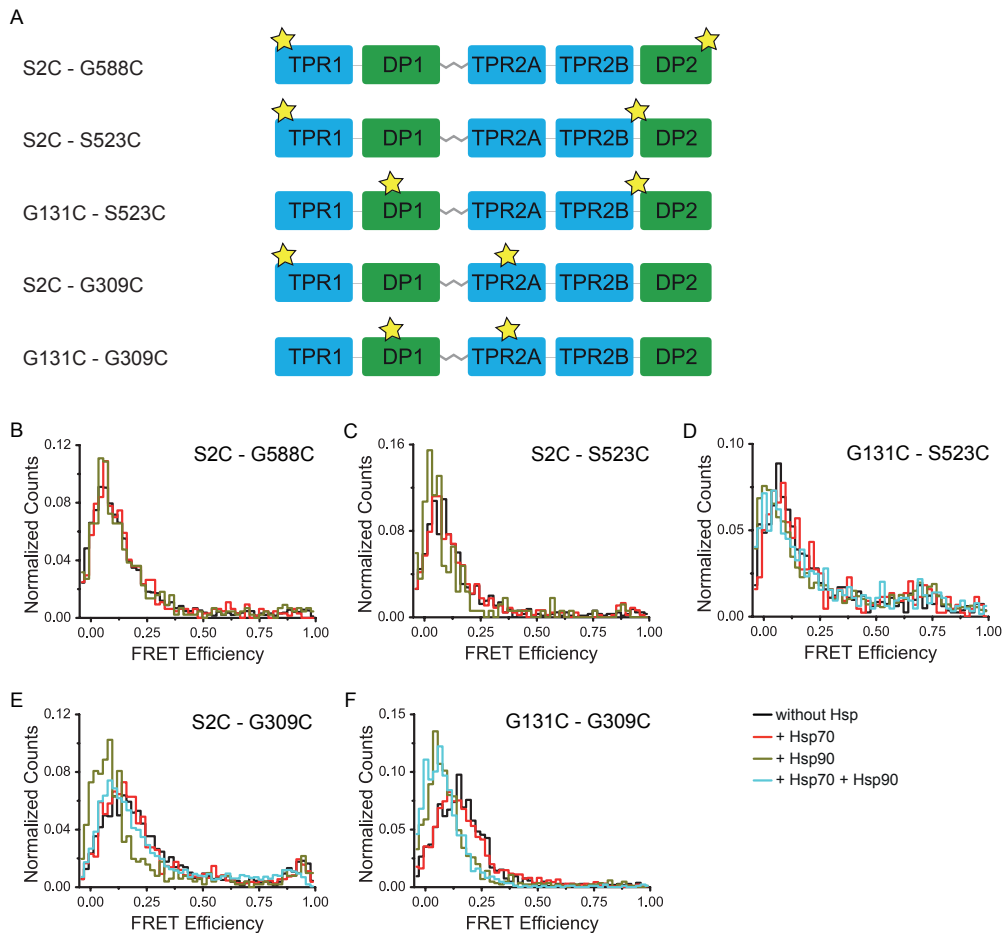


Figure 6.3: SpFRET analysis of StiI mutants with large dye distances. **(A)** Various spFRET mutants are labeled on both sides of the StiI molecule. **(B-F)** SpFRET distributions of 25 pM StiI measured in the absence of any interaction partner (black line), in the presence of 25  $\mu$ M Hsp70 (red line), 10  $\mu$ M Hsp90 (dark yellow line) or in the presence of 25  $\mu$ M Hsp70 and 10  $\mu$ M Hsp90 (cyan line). **(B)** SpFRET histograms for the S2C-G588C mutant, where the dyes are located in the TPR1 and DP2 domains, **(C)** for the S2C-S523C mutant, where the dyes are in the TPR1 domain and between TPR2B and DP2, **(D)** for the G131C-S523C mutant with dyes in the DP1 domain and between TPR2B and DP2, **(E)** for the S2C-G309C mutant with dyes in the TPR1 and TPR2A domain and **(F)** for the G131C-G309C mutant where the dyes are located in the DP1 and TPR2A domain.

The FRET efficiency for all these mutants was below 10 %. Therefore, the distance between the two dyes was much larger than the Förster radius and, thus, the FRET mutants were not sensitive to potential small changes in the conformation and they did not come into proximity. Shifting the dyes closer together shifted the FRET efficiency to slightly higher values. Locating one dye in the TPR1 domain and the other one in the TPR2A domain (Figure 6.3E - S2C-G309C) or shifting the dye positions to the DP1 domain and the TPR2A domain (Figure 6.3F - G131C-G309C) changed the FRET efficiency to approximately 15 %. Thus, the distance was close enough to detect changes in the conformation. By adding Hsp70, no differences in the FRET efficiency histograms were detected. In the presence of Hsp90 or Hsp70 and Hsp90, the maximum value of the FRET efficiency was approximately 0.05 and, thus, smaller than without any Hsp. From this shift, we can conclude that Hsp90 induces a conformational change in Sti1.

## 6.5 Linker length is independent of bound Hsps

To distinguish if the detected shift in the FRET efficiency is due to a change in the linker length or due to a flipping of the rigid module (TPR2A-TPR2B-DP2) and, thus, bringing one module closer to the other parts of the Sti1 molecule, both ends of the linker were labeled.

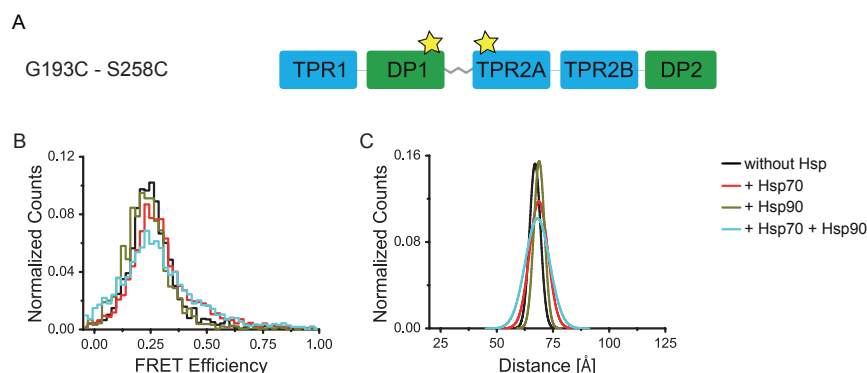


Figure 6.4: SpFRET analysis of the Sti1 mutant G193C-S258C. **(A)** Cartoon of the spFRET mutant, labeled on both ends of the linker to monitor its conformational changes upon binding of Hsp. **(B)** SpFRET distributions of 25 pM Sti1 measured in the absence of any interaction partner (black line), in the presence of 25  $\mu$ M Hsp70 (red line), 10  $\mu$ M Hsp90 (dark yellow line) or in the presence of 25  $\mu$ M Hsp70 and 10  $\mu$ M Hsp90 (cyan line). **(C)** The distance distributions were calculated using PDA.

The mutant G193C-S258C monitors the conformation of the linker upon binding to different Hsps (Figure 6.4A). The maximum value of the FRET efficiency stayed the same, independent of the binding of a Hsp, and was approximately 25 % (Figure 6.4B). For applying a PDA fit to the FRET data, only one Gaussian distribution was needed (Figure 6.4C and Table 6.2). The distance between the two dyes was calculated to be 67 - 69 Å and was constant upon binding of Hsps. However, a change in the width of the distribution was measured. Without Hsp and in the presence of Hsp90, the width was  $\sigma = 3$  Å. This is very narrow for a

PDA distribution and is related to a non flexible conformation. Upon binding of Hsp70 the distribution increases and the width changed to  $\sigma = 6 \text{ \AA}$ . When both Hsps, Hsp70 and Hsp90, were bound, the flexibility increased again and a width of  $\sigma = 8 \text{ \AA}$  was measured. Thus, the binding of Hsp does not change the distance between DP1 and TPR2A, but when Hsp70 is bound independently of Hsp90, the width of the conformation gets larger. Therefore, the linker itself gets more flexible.

Table 6.2: Distances calculated using PDA for the Sti1 mutant G193C-S258C. G193C-S258C (25 pM) was measured in the absence of any Hsp, in the presence of 25  $\mu\text{M}$  Hsp70, in the presence of 10  $\mu\text{M}$  Hsp90 and in the presence of 25  $\mu\text{M}$  Hsp70 and 10  $\mu\text{M}$  Hsp90. The photons of a burst were divided into bins of 1 ms, summed up in a FRET histogram, and fitted using a Gaussian model. From the PDA, the distance  $d$  between donor and acceptor, the corresponding width  $\sigma$  and the relative weights of the different populations were calculated.

G193C-S258C	Subpopulation 1			Goodness of the fit
	$d$ [ $\text{\AA}$ ]	$\sigma$ [ $\text{\AA}$ ]	%	$\chi^2$
without Hsp	67	3	100	2.6
+ Hsp70	69	6	100	7.0
+ Hsp90	69	3	100	1.0
+ Hsp70 + Hsp90	68	8	100	3.4

## 6.6 Distance changes between the two modules of Sti1

To gain further insight in the conformational changes of Sti1, the distance between the two dyes has to be closer to the Förster radius in order to make the FRET efficiency more sensitive to small distance changes. However, the labeling positions have to be far enough apart from the linker to be able to detect a possible flipping of the ridged module (TPR2A-TPR2B-DP2) to the module TPR1-DP1. For these experiments, labeling positions were chosen in the DP1 and the TPR2A domains. The mutant is called G193C-G309C (Figure 6.5A).

The majority of G193C-G309C molecules had a FRET efficiency in a range of about 15 % (Figure 6.5B). By using PDA, the distances for the different measured conditions were calculated (Figure 6.5C and Table 6.3). Without any Hsp, the distance was  $d = 72 \text{ \AA}$  ( $\sigma = 10 \text{ \AA}$ ). This was similar to the distance calculated in the presence of Hsp70 ( $d = 69 \text{ \AA}$  and  $\sigma = 12 \text{ \AA}$ ). In the presence of Hsp90 or both Hsp70 and Hsp90, the FRET efficiency histogram shifted to lower FRET efficiency values. Therefore, the distance between the two dyes increased. The distance value changed to  $d = 80 \text{ \AA}$  ( $\sigma = 11 \text{ \AA}$ ) with Hsp90 and to  $d = 78 \text{ \AA}$  ( $\sigma = 10 \text{ \AA}$ ) with Hsp70 and Hsp90. This trend was already seen in the measurements of the mutants S2C-G309C and G131C-G309C. The width of the spFRET distribution is large suggesting Sti1 has some flexibility in the linker region.

Furthermore, a high FRET peak appeared (Figure 6.5B). This high FRET value represents the case, where both dyes and, therefore, the DP1 and TPR2A domain came close together. The distance for this fraction of Sti1 molecules was calculated to be between 30 and 40  $\text{\AA}$

(Figure 6.5C and Table 6.3). Variations in the distance are due to the fact that, in the range of very low or very high FRET values, the used technique is less sensitive in comparison to distances close to the Förster radius. The low distance between the DP1 and TPR2A domain corresponds to a module flipped close to the other. In the following, this conformation will be called the 'closed conformation'.

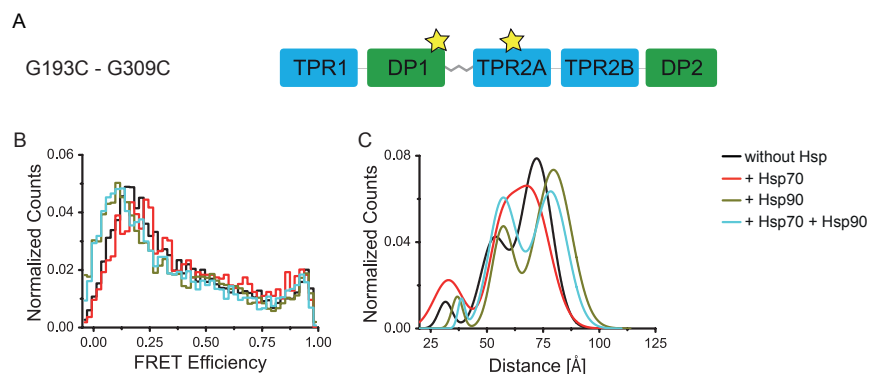


Figure 6.5: SpFRET analysis of the Sti1 mutant G193C-G309C. **(A)** Cartoon of the spFRET mutant, labeled in the DP1 and the TPR2A domain, to monitor the changes between the two modules. **(B)** SpFRET distributions of 25 pM Sti1 measured in the absence of any interaction partner (black line), in the presence of 25  $\mu$ M Hsp70 (red line), 10  $\mu$ M Hsp90 (dark yellow line) or in the presence of 25  $\mu$ M Hsp70 and 10  $\mu$ M Hsp90 (cyan line). **(C)** The distance distribution were calculated using PDA.

Additionally, a third peak in the FRET histogram was detected, an intermediate conformation with a FRET efficiency of 55 % (Figure 6.5B). This FRET value represented a distance  $d$  of 53 - 57 Å ( $\sigma$  between 7 - 9 Å) in the presence and absence of Hsps (Figure 6.5C and Table 6.3). The width of this conformation is again large and, thus, the Sti1 has some flexibility in this conformation, as well.

To address whether there are dynamic transitions between the three conformations, the lifetime of the donor dye was analyzed. By plotting again the FRET efficiency versus the lifetime of the donor, dynamic behavior of the molecule on the timescale of the diffusion time can be identified. The red line in Figure 6.6 illustrates the theoretical relationship between lifetime and FRET efficiency of a static molecule, i.e. the molecule does not interchange its conformation of the millisecond timescale. In the measurement without any Hsps (Figure 6.6A), the measured data followed the theoretical line and, therefore, Sti1 did not interchange between different conformations.

By adding one or more Hsps, the measured distribution deviated from the red line (Figure 6.6B-D). The data is not distributed symmetrically around the static line. Especially between the high and the intermediate state, the measured data are more similar to the green lines, which represents the theoretical case where a molecule interchange between two different states. Thus, Sti1 can change its conformation from a high FRET to an intermediate state, i.e. from a closed conformation to a partly open one. This is the first hint that Sti1 is able to interchange between different conformations. Thus, Sti1 is flexible and its opening and closing can be modulated by Hsp70 and Hsp90.

Table 6.3: Distances calculated using PDA for the Sti1 mutant G193C-G309C. G193C-G309C (25 pM) was measured in the absence of any Hsp, in the presence of 25  $\mu$ M Hsp70, in the presence of 10  $\mu$ M Hsp90 and in the presence of 25  $\mu$ M Hsp70 and 10  $\mu$ M Hsp90. The photons of a burst were divided into bins of 1 ms, summed up in a FRET histogram, and fitted using a triple-Gaussian model. From the PDA, the distance  $d$  between donor and acceptor, the corresponding width  $\sigma$  and the relative weights of the different populations were calculated. An asterisk (\*) indicates that the respective value was fixed.

G193C-G309C	Subpopulation 1			Subpopulation 2			Subpopulation 3			Goodness of the fit
	$d$ [Å]	$\sigma$ [Å]	%	$d$ [Å]	$\sigma$ [Å]	%	$d$ [Å]	$\sigma$ [Å]	%	$\chi^2$
without Hsp	32	4*	4.7	53	8	24.7	72	10	70.6	1.1
+ Hsp70	33	9	9.0	56	8	27.3	69	12	63.7	1.6
+ Hsp90	37	3	5.7	57	7	28.2	80	11	66.1	1.3
+ Hsp70 + Hsp90	39	2	2.3	57	9*	37.3	78	10	57.4	1.1

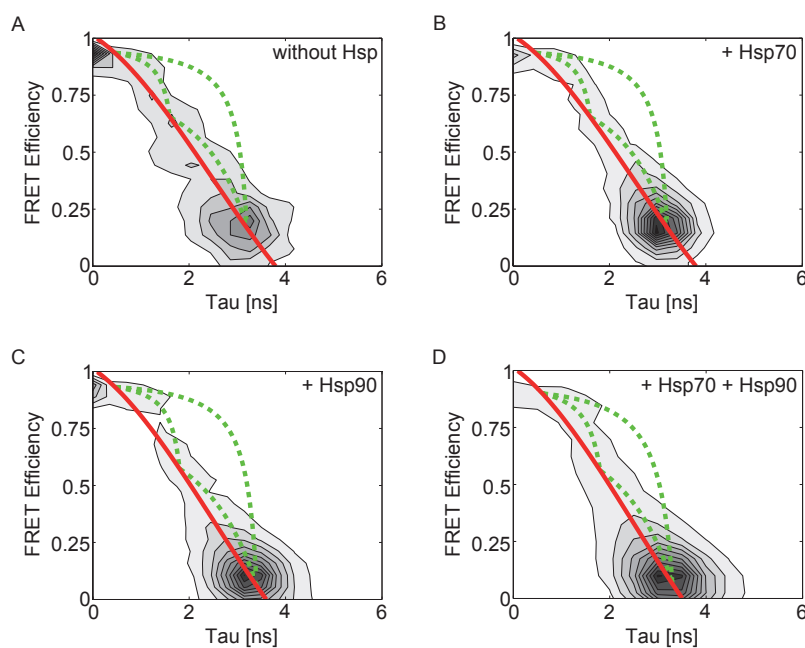


Figure 6.6: FRET efficiency versus lifetime plots of the Sti1 mutant G193C-G309C. SpFRET distributions were measured for 25 pM Sti1 and the FRET efficiency was plotted versus the lifetime of the donor dye (**A**) in the absence of any interaction partner, (**B**) in the presence of 25  $\mu$ M Hsp70, (**C**) in the presence of 10  $\mu$ M Hsp90 and (**D**) in the presence of 25  $\mu$ M Hsp70 and 10  $\mu$ M Hsp90. The red line is the theoretical relationship between the lifetime and the FRET efficiency, when the molecule does not change its conformation during the burst. The green lines illustrate the theoretical case for dynamic molecules, i.e. Sti1 that interchanges its conformation during the time it spends in the focus.

## 6.7 Binding of Hsp70 to multiple domains

To support the hypothesis that Hsp70 and Hsp90 can modulate the opening and closing of Sti1, two new mutants of G193C-G309C were created (Figure 6.7A). Sti1 has two binding domains for the Hsp70, one in the TPR1 and the other in the TPR2B. In addition, one binding domain for Hsp90 in the TPR2A is known. The mutant G193C-G309C N39A has a mutation in the binding pocket for the Hsp70 in the TPR1. This mutation blocks binding of Hsp70 to this domain. Due to the fact that Sti1 has two binding domains for Hsp70, the Hsp70 can only bind to TPR2B in this mutant. The other mutant, G193C-G309C N435A, has a mutation in the TPR2B domain and blocks the binding of Hsp70 in TPR2B. Thus, only interactions between Hsp70 and the TPR1 of Sti1 are possible in this mutant.

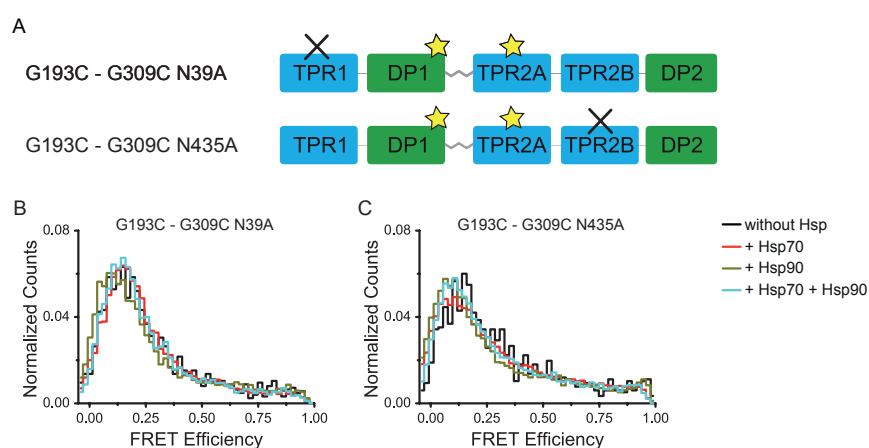


Figure 6.7: SpFRET analysis of the Sti1 mutant G193C-G309C N39A and G193C-G309C N435A. (A) Cartoon of the spFRET mutant, labeled in the DP1 and the TPR2A domains to monitor the changes between the two ridged modules. The X indicates a mutation in the respective Hsp70 binding domain, which results in the loss of Hsp70 binding. (B-C) SpFRET distributions of 25 pM Sti1 measured in the absence of any interaction partner (black line), in the presence of 25  $\mu$ M Hsp70 (red line), 10  $\mu$ M Hsp90 (dark yellow line) or in the presence of 25  $\mu$ M Hsp70 and 10  $\mu$ M Hsp90 (cyan line) for (B) G193C-G309C N39A and (C) G193C-G309C N435A.

Both mutants, G193C-G309C N39A (Figure 6.7B) and G193C-G309C N435A (Figure 6.7C), showed differences in the FRET efficiency compared to the mutant without a blocked binding domain, G193C-G309C (Figure 6.5). Without blocking of the binding of Hsp70, the FRET efficiency was shifted with Hsp70 and Hsp90. This shifting was lost by blocking one of the binding domains, independently of which of the two domains was blocked. A small shift in the FRET efficiency to lower values upon binding of Hsp90 was still detectable, especially for G193C-G309C N39A, but less dominant. Therefore, we can conclude that both binding domains for Hsp70 are important for the conformational changes in Sti1.

## 6.8 TIRF analysis of the dynamic behavior of Sti1

In the last sections snapshots on the millisecond timescale were performed and dynamics of Sti1 are found. To further analyze the dynamic behavior of Sti1, TIRF measurements were performed, which widen up the timescale up to seconds. Fluctuations between different conformations on the millisecond to second timescale can be directly measured with this method. Single Sti1 molecules with and without Hsps were encapsulated in vesicles and immobilized on the surface of a quartz prism. For the detailed measurement procedure see Chapter 3.5 on page 37. To verify that the encapsulation process does not affect the sample and, therefore, the FRET efficiency, burst measurements on the MFD-PIE setup of the vesicles diffusing in solution were performed. Figure 6.8 demonstrates that the FRET histograms look the same and, thus, the encapsulation procedure does not significantly affect the sample.

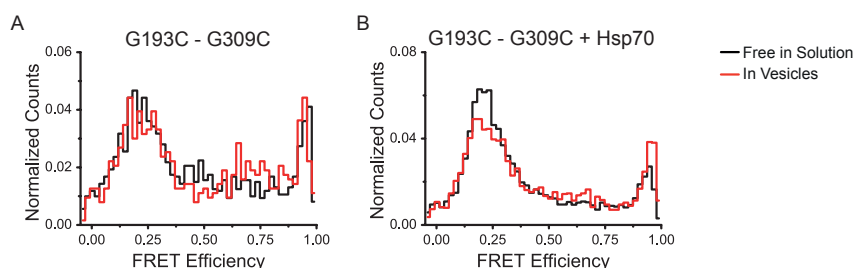


Figure 6.8: Comparison of the spFRET measurement of the Sti1 mutant G193C-G309C free in solution and encapsulated in vesicles. SpFRET distributions of 25 pM Sti1 mutant G193C-G309C measured (A) in the absence of any interaction partner and (B) in the presence of Hsp70 freely diffusing in solution (black line) and in vesicles encapsulated (red line).

In Figure 6.9 (first row), exemplary spFRET traces for G193C-G309C are depicted. We can detect two kinds of traces, static (first column), i.e. one FRET efficiency state is detected until the dye molecules were bleached, and dynamic traces (second column), i.e. molecules that interchanged their conformation during the measurement. Without bound Hsps, 11 % of the molecules that were measured were dynamic (Table 6.4 (first column)). All traces with more than one bleaching step were discarded from the analysis due to the possibility of multiple molecules present per vesicle. Upon the binding of Hsp70 (Figure 6.9 (third column)) or Hsp90 (Figure 6.9 (fourth column)), the percentage of dynamic traces increased to approximately 25 %. When both Hsps were bound, the number of molecules interchanging between different conformations shifted to approximately 30 %. These results are in agreement with the solution-based spFRET measurements and suggest that, upon binding of Hsps, the Sti1 molecule becomes more dynamic and brings the two TPR domains, TPR1 and TPR2, close together.

However, 20 - 30 % of dynamic molecules sounds less for an important process in nature. For spFRET measurements with proteins encapsulated in vesicles this is a very high percent of dynamic molecules. The explanation for this is given in the encapsulation process. The protein extruded 31 times and it is very likely that a large fraction of molecules loses its functionality in this process. Therefore, 20 - 30 % of molecules showing dynamics is related to a real native process.

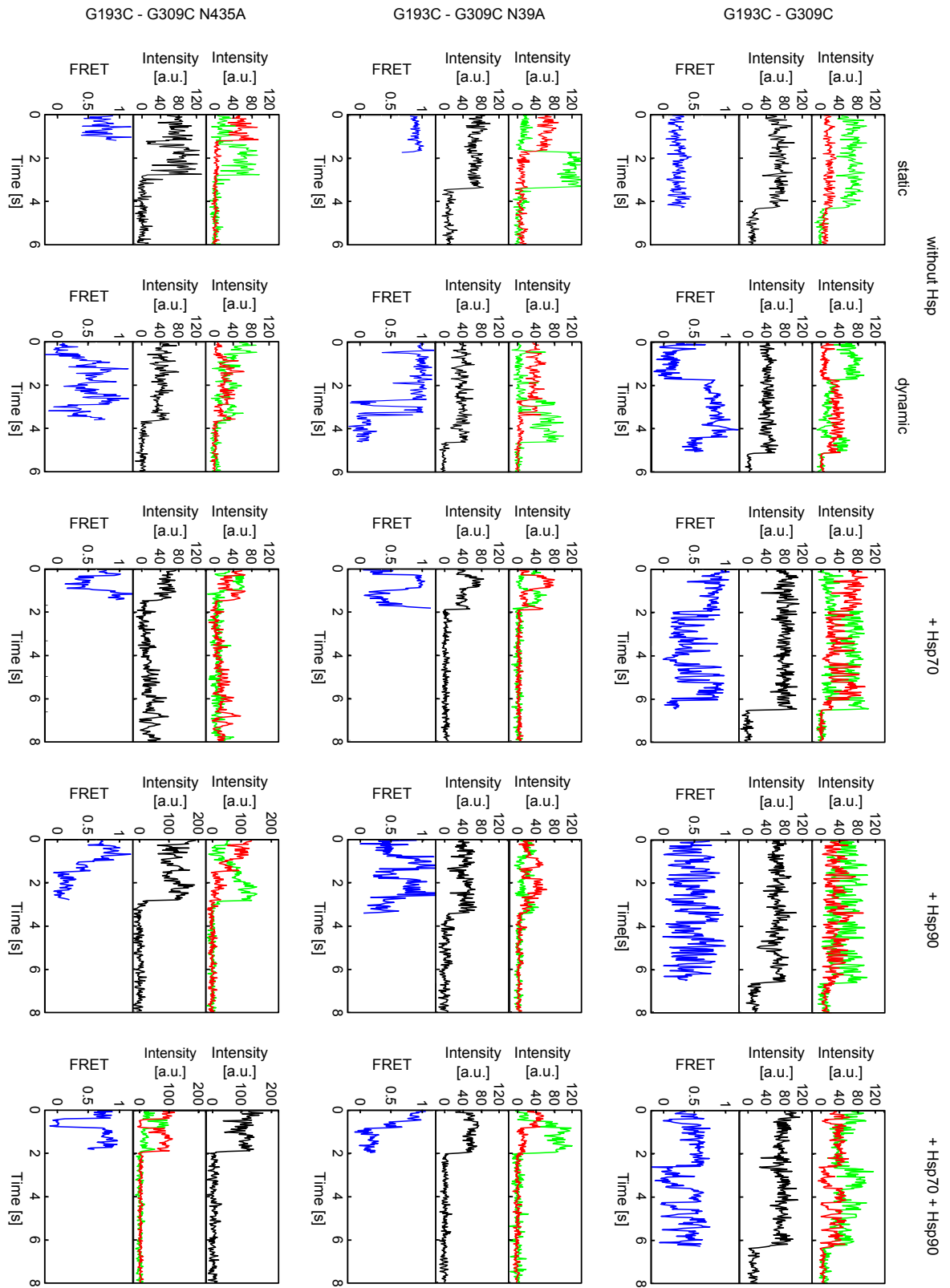


Table 6.4: Percentage of dynamic traces in TIRF measurements of the Sti1 mutant G193C-G309C. G193C-G309C, G193C-G309C N435A and G193C-G309C N39A were measured in the absence of any Hsp and in the presence of 25  $\mu$ M Hsp70, in the presence of 10  $\mu$ M Hsp90 and in the presence of 25  $\mu$ M Hsp70 and 10  $\mu$ M Hsp90.

	G193C-G309C dynamic traces [%]	G193C-G309C N39A dynamic traces [%]	G193C-G309C N435A dynamic traces [%]
without Hsp	11	13	17
+ Hsp70	25	27	15
+ Hsp90	28	27	26
+ Hsp70 + Hsp90	29	23	21

To further support this hypothesis, spFRET measurements of immobilized vesicles containing G193C-G309C N39A (Figure 6.9 (second row)) and G193C-G309C N435A (Figure 6.9 (third row)) were performed. These two mutants also showed two types of traces, static and dynamic traces. However, the percentage of dynamic traces varied when one of the two binding domains of the Hsp70 were blocked. Without any Hsp and upon binding of Hsp90, the percentage of dynamic traces is the same as for G193C-G309C. Without Hsp, approximately 11 - 17 % of the traces showed dynamic behavior, with bound Hsp90, 26 - 28 % of the analyzed traces were dynamic (Table 6.4 (second and third column)). Upon binding of Hsp70, the percentage depends on the blocking of the binding domain. For G193C-G309C N39A, the dynamics were not influenced by the mutation. Hsp70 binding increased the percentage of dynamic traces to 27 % compared to 25 % without the mutation in TPR1. This is different for the G193C-G309C N435A mutant. The blocking of the binding of Hsp70 in the TPR2B domain kept the percentage of dynamic traces in the same range as observed in the absence of Hsp70. By adding Hsp70 and Hsp90 at the same time, the percentage of dynamic traces was significantly reduced compared to the Sti1 mutant without blocked binding domains (G193C-G309C). With blocked binding, the percentage was between 21 and 23 % compared to 29 % with both intact binding domains.

Figure 6.9: Representative traces from spFRET TIRF experiments of Sti1. Time traces of the donor (green) and acceptor intensity (red, upper graphs), total intensity (black, middle graphs) and FRET efficiency (blue, lower graphs) of the Sti1 mutants G193C-G309C, G193C-G309C N39A and G193C-G309C N435A measured in the absence and presence of Hsp70, Hsp90 and/or Hsp70 and Hsp90. The left column represents molecules that do not show any conformational changes during the measurement. The next column shows dynamic spFRET traces for the different Sti1 mutants in the absence of Hsps. The middle column was measured in the presence of 25  $\mu$ M Hsp70 and the following in the presence of 10  $\mu$ M Hsp90. The last column represents traces measured in the presence of 25  $\mu$ M Hsp70 and 10  $\mu$ M Hsp90. Anticorrelated fluctuations in the donor and acceptor fluorescence intensities indicate changes in the FRET efficiency due to movement of Sti1 between different conformations.

From these results, we conclude that the TPR2B domain is important for the dynamics induced by Hsp70 binding, because a mutation in TPR2B influences the dynamics of the whole Sti1. When both Hsps, Hsp70 and Hsp90, are present, both binding domains seem to be important for the mediation of the Sti1 dynamics.

To extract information about the states and the transitions from the traces, a Hidden Markov model analysis (HMM, see Chapter 3.5.5 on page 43) was performed. All dynamic traces from the same Sti1 mutant measured under the same conditions were fitted to a global HMM. Three FRET states were detected with FRET efficiencies of approximately 18 % (low FRET), ~60 % (intermediate FRET) and ~90 % (high FRET) (Table 6.5). All these states can interconvert. The transition density plot is given in Figure 6.10. The FRET efficiency and broadening of the different transitions in the  $x$  and  $y$  direction were given by the HMM analysis. The width of the peaks in the transition density plot corresponds to the width (standard deviation) of the respective FRET state given by the HMM analysis. The majority of the transitions were well defined and had a low standard deviation. This is due to well defined conformations in all molecules.

Table 6.5: FRET values extracted from the HMM analysis of the TIRF measurements of the Sti1 mutant G193C-G309C. G193C-G309C, G193C-G309C N39A and G193C-G309C N435A were analyzed using HMM with a global fit in the presence of 25  $\mu$ M Hsp70, in the presence of 10  $\mu$ M Hsp90 and in the presence of 25  $\mu$ M Hsp70 and 10  $\mu$ M Hsp90.

G193C-G309C	low	intermediate	high
+ Hsp70	0.16	0.52	0.84
+ Hsp90	0.24	0.66	0.92
+ Hsp70 + Hsp90	0.23	0.57	0.86
G193C-G309C N39A	low	intermediate	high
+ Hsp70	0.18	0.62	0.92
+ Hsp90	0.10	0.58	0.91
+ Hsp70 + Hsp90	0.14	0.58	0.91
G193C-G309C N435A	low	intermediate	high
+ Hsp70	0.18	0.65	0.93
+ Hsp90	0.20	0.57	0.92
+ Hsp70 + Hsp90	0.17	0.57	0.92

In addition, the transition rates were calculated by the HMM analysis (Table 6.6). For the mutant G193C-G309C, the transition rates were similar in the presence of Hsp70 and/or Hsp90. They were all in a range of about 0.5 to 1.5  $s^{-1}$  except for the transition from the low to the high FRET state, which was approximately four times faster. For the mutants with one blocked binding domain, G193C-G309C N39A and G193C-G309C N435A, almost all of the transition rates in the presence of Hsp70 with Hsp90 got faster. This increase in dynamic rates was also observed upon binding of Hsp70 to the mutant G193C-G309C N435A with the blocked TPR2B binding domain. However, the kinetics for all three mutants were similar upon Hsp90 binding.

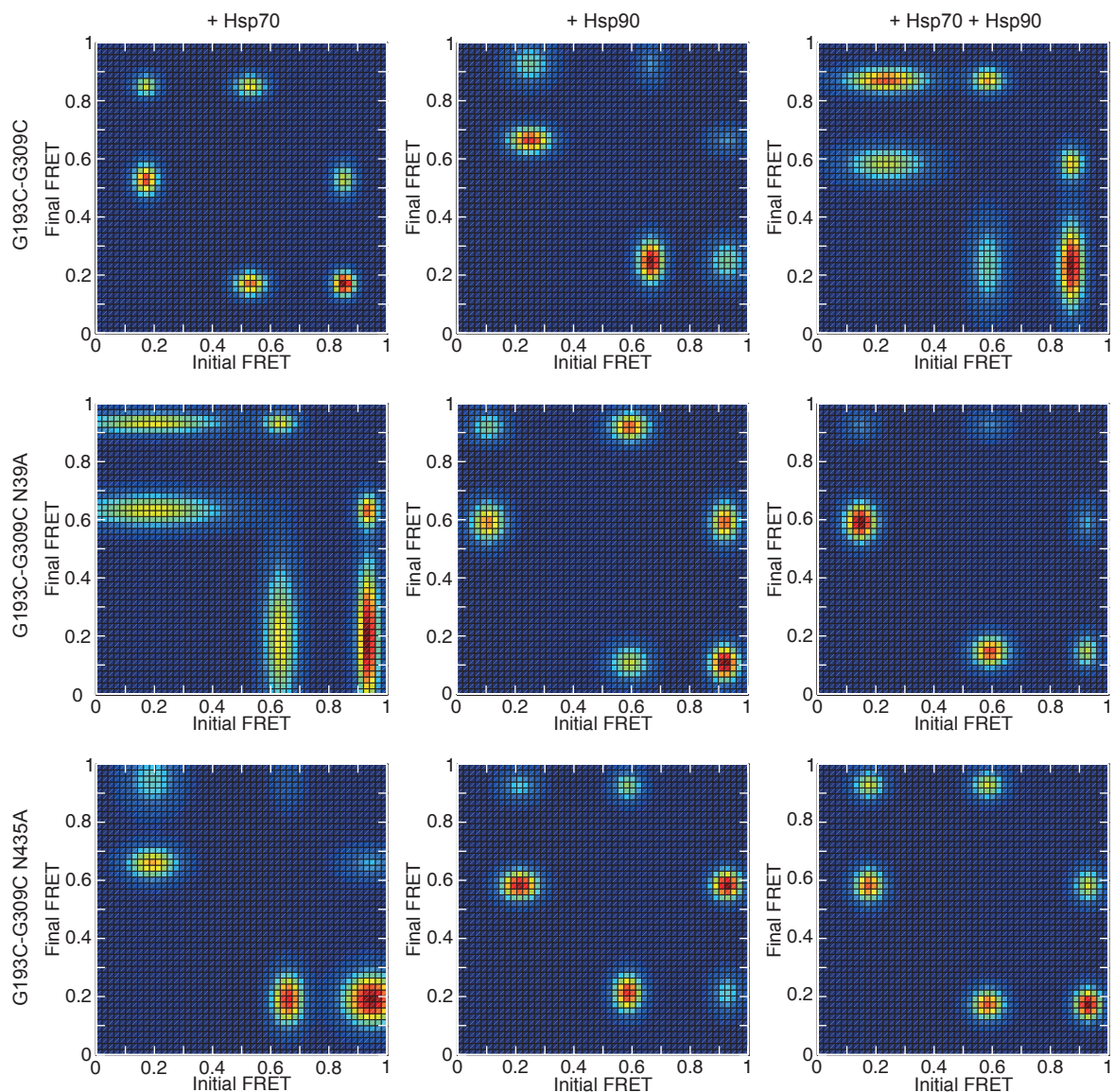


Figure 6.10: Transition density plots from the spFRET TIRF experiments of the Stt1 mutant G193C-G309C. To generate these plots, the dynamic spFRET traces from the TIRF measurements were fitted using a global HMM with three states. The first column shows the plot for the mutants G193C-G309C, G193C-G309C N39A and G193C-G309C N435A in the presence 25  $\mu$ M Hsp70. The next column was measured in the presence of 10  $\mu$ M Hsp90 and the last column in the presence of 25  $\mu$ M Hsp70 and 10  $\mu$ M Hsp90.

Table 6.6: Transition rates extracted from the HMM analysis of the TIRF measurements of the StII mutant G193C-G309C. G193C-G309C, G193C-G309C N435A and G193C-G309C N39A were analyzed by HMM with a global fit in the absence of any Hsp and in the presence of 25  $\mu\text{M}$  Hsp70, in the presence of 10  $\mu\text{M}$  Hsp90 and in the presence of 25  $\mu\text{M}$  Hsp70 and 10  $\mu\text{M}$  Hsp90. The number of measured transitions is given in the parenthesis next to the respective rates. An asterisk (\*) indicates that the respective value has too low statistics and is not determinable.

G193C-G309C	low $\rightarrow$ high [s <sup>-1</sup> ]	high $\rightarrow$ low [s <sup>-1</sup> ]	low $\rightarrow$ intermediate [s <sup>-1</sup> ]	intermediate $\rightarrow$ low [s <sup>-1</sup> ]	intermediate $\rightarrow$ high [s <sup>-1</sup> ]	high $\rightarrow$ intermediate [s <sup>-1</sup> ]	
	+ Hsp70	4.5 (83)	1.0 (49)	1.5 (64)	1.5 (69)	0.9 (48)	1.5 (53)
	+ Hsp90	3.4 (36)	0.6 (35)	1.7 (79)	0.9 (69)	0.9 (22)	0.6 (22)
+ Hsp70 + Hsp90	4.3 (51)	0.9 (41)	1.0 (22)	0.7 (29)	1.0 (34)	0.8 (35)	
G193C-G309C N39A	low $\rightarrow$ high	high $\rightarrow$ low	low $\rightarrow$ intermediate	intermediate $\rightarrow$ low	intermediate $\rightarrow$ high	high $\rightarrow$ intermediate	
	+ Hsp70	3.5 (31)	1.0 (19)	1.5 (20)	0.8 (19)	1.7 (23)	1.0 (18)
	+ Hsp90	3.0 (52)	1.3 (27)	2.1 (28)	2.4 (36)	1.3 (43)	1.3 (39)
+ Hsp70 + Hsp90	5.0 (15)	4.1 (7)	3.1 (22)	2.3 (27)	3.0 (8)	1.9 (7)	
G193C-G309C N435A	low $\rightarrow$ high	high $\rightarrow$ low	low $\rightarrow$ intermediate	intermediate $\rightarrow$ low	intermediate $\rightarrow$ high	high $\rightarrow$ intermediate	
	+ Hsp70	2.5 (20)	2.3 (8)	3.8 (18)	1.5 (14)	3.3 (6)	2.5* (3)
	+ Hsp90	2.7 (10)	0.8 (9)	2.2 (23)	1.8 (25)	1.7 (26)	1.6 (13)
+ Hsp70 + Hsp90	4.1 (32)	4.0 (19)	3.2 (26)	2.4 (26)	2.4 (19)	1.2 (19)	

All these results are in line with the solution-based spFRET measurements on the MFD-PIE system. Three different conformations are possible and the molecule can interchange between all of them. By blocking the binding of Hsp70 to the TPR2B domain, the transitions gets faster when Hsp70 binds to TPR1 independent of the presence of Hsp90. Blocking the TPR1 domain only has an effect when both Hsps are bound. Therefore, TPR2B is the important binding domain when only Hsp70 is bound. By adding Hsp90 to this complex, the second binding domain also becomes important.

## 6.9 Discussion and Outlook

Sti1 consists of two modules, the TPR1-DP1 and the TPR2-DP2 module, which are connected by a flexible and unstructured linker. TPR1-DP1 does not form a rigid unit, but the two domains are flexible concerning their orientation. The TPR2 domain itself consists of two parts, the TPR2A and TPR2B, which are known to be tightly linked and form a structural and functional unit [Schmid et al., 2012]. DP2 is connected in a defined orientation to the TPR2 domain and forms, together with the TPR2 domain, a module with low inter-domain flexibility [Röhl et al., 2015].

Hsp70 and Hsp90 are connected by Sti1, which works as a kind of scaffold and helps Hsp70 and Hsp90 to come close together and transfer the client protein from Hsp70 to Hsp90, where folding continues. Sti1 has two binding domains for Hsp70, one in the TPR1 domain and one with a higher affinity in the TPR2B domain [Schmid et al., 2012]. Hsp90 binds to the TPR2A-TPR2B domain with a large interaction surface, which includes an interaction of TPR2B with the Hsp90 M-domain [Southworth and Agard, 2011], [Schmid et al., 2012]. We saw, that the two TPR2 domains are rigidly connected. From this we assume that the reduction in the accessible space for Hsp70 to TPR2B shifts the preferred binding domain for Hsp70 upon binding of Hsp90 to the TPR1 domain. Furthermore, the presence of Hsp90 induces a slightly more open conformation of Sti1, which increases the distance between the two TPR-DP modules and makes the TPR1 domain better accessible for the Hsp70. This effect is due to a conformational twisting, but not due to a change in the length of the linker. Taken together, this explains why Hsp70, which has a higher affinity to the TPR2B domain, binds also to TPR1 in the presence of Hsp90.

The fact that two binding domains for Hsp70 are available, which are differentially activated and regulated, suggests that Hsp70 can switch between these two binding sides during client transport. Remarkably, an increased dynamics, which brings the two TPR-DP modules close together, was observed in the presence of Hsp70 and Hsp90. Therefore, we suggest that the transfer of the Hsp70 from one TPR binding domain to the other is facilitated. This would explain the existence of the flexible linker. Taken together, our results underline the model known from [Alvira et al., 2014]. The resulting model is depicted in Figure 6.11. Sti1 acts as a scaffold that connects Hsp70 and Hsp90. When Hsp90 binds to Sti1, a Hsp70 with bound client interacts preferably with the TPR1 domain. Due to the dynamics of the linker region of Sti1, which connects the two TPR domains, the Hsp70 is transferred from the TPR1 to the TPR2B domain. There, it hands over its client to Hsp90. Afterwards, we assume that the TPR2B binding domain is freed up again to allow Hsp90 to start the folding of the substrate. Therefore, the Hsp70 is released from the binding complex or is shifted back to the TPR1 binding domain. Next, Sti1 opens up. Due to the low affinity of Hsp70 to the TPR1 binding domain, bound Hsp70 is released again. Thus, the binding domain is free for a new Hsp70

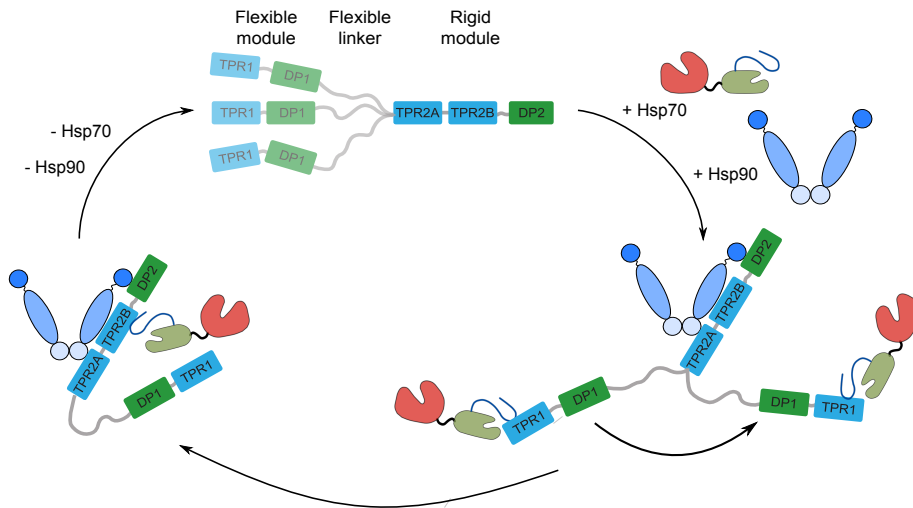


Figure 6.11: Model for the Hsp-mediated cycle of Sti1. Sti1 is color-coded as above, Hsp70 is colored as in Chapter 5 and Hsp90 is depicted as in Chapter 4.2.2. Upon binding of Hsp70 and Hsp90, the two Sti1 modules come close together and Hsp70 changes from the binding site in the TPR1 domain to the binding site in the TPR2B domain. This helps to transfer a possible client from Hsp70 to Hsp90. Afterwards both Hsps are released and the cycle starts again.

with bound client.

In order to complete an overall picture of the cycle, some remaining questions need to be answered. We used a high amount of Hsp70 and Hsp90 to make sure that every Sti1 molecule has a Hsp70 and a Hsp90 molecule bound. To test if this is also the case in the vesicles for the TIRF measurements, one could label the Hsps, each with one additional dye, and use the labels as a control if the respective Hsp is really present in the vesicle.

Additionally, it would be of interest to follow a client through its chaperone cycle. One approach to do that would be to label the client protein with one donor dye and the Hsp70 and Hsp90 each with different acceptor dyes. With this approach, a FRET signal between the three components is generated and can be followed over time by using a spFRET TIRF system. Choosing the labeling positions close to the binding domain of the client would introduce a high FRET signal, when the client is bound to the Hsp. The transfer from Hsp70 to Hsp90 would change the energy transfer from one acceptor to another.

Furthermore, it is of interest to know how other Hsps or cofactors influence the client cycle. It is known that Hsp40 interacts with Hsp70 and helps to bind Hsp70 to Sti1 [Morgner et al., 2015]. However, Hsp40 itself does not interact with Sti1. Therefore, TIRF measurements of the presence of Hsp40 could help to detect if the transition rates of Sti1 changes due to faster binding and unbinding of the Hsp70.

Another interesting interaction partner is the cofactor p23, which is known to interact in a later state of the cycle with the Hsp70-Hsp90-Sti1 complex [Li and Buchner, 2013]. It helps to weaken the binding of Hsp90 to Sti1. By using a labeled p23 in combination with labeled Sti1, differences in the conformation of Sti1 upon binding of p23 can be monitored. Furthermore, changes in the dynamics upon binding of p23 to Hsp90 can be detected on a TIRF setup.

In an additional next step, the found cycle has to be put in the context of a nucleotide. The measurements in this chapter are all performed without a nucleotide. To analyse the effect of

ADP and ATP, the nucleotides have to be added to the measurements. It is already known that Hsp70 can only bind to Sti1 in the ADP or nucleotide free conformation, but not in the ATP bound state [Johnson et al., 1998]. Furthermore, in literature it is found that Hsp90 binding is independent of the nucleotide state, but the maximum velocity of the ATPase reaction is reduced [Richter et al., 2003]. In [Hernandez et al., 2002], they observed that the ATP binding site of Hsp90 is no longer blocked by Hop, when Hsp70 is present. This, together with the finding that ATP changes the conformation of Hop without any interaction with Hsps [Yamamoto et al., 2014], could help to explain the nucleotide cycle of Sti1.



# 7 Microfluidic measurements of the substrate protein MBP

## 7.1 Microfluidics

### 7.1.1 Introduction

The protein studies in the last chapters are all based on single-molecule methods that are limited to equilibrium. This has the advantage of detecting multiple distinguishable conformations at the same time. However, it is only a snapshot of the conformation of the molecule. One idea to overcome this problem is to measure under non-physiological conditions to monitor different conformations. This has the disadvantage that the experimentalist is very often not sure if the respective observation corresponds to a real state in nature. An alternative idea is to use microfluidics. In such a system, the sample is mixed or diluted in a microfluidic device, which allows to monitor fast conformational changes like folding processes or changes induced by exchange of the environment. To realize this concept, small volumes of sample and buffer are mixed in a device by a laminar flow. This approach can be combined with single-molecule microscopy methods [Lipman et al., 2003]. The idea is to perform single-pair Förster Resonance Energy Transfer (spFRET) measurement directly in the device, where the different components are mixed together or the sample is diluted. Therefore, microfluidic allows the determination of fast kinetics of a molecule in the range of a few milliseconds to seconds after mixing or diluting the sample. The timing of the measurable interaction depends on the microfluidic device. This approach has the advantage that proteins that are only stable in higher concentrations ( $\mu\text{M}$  range), can be diluted to single-molecule concentrations directly in the device and, thus, the protein only has to be stable up to a few seconds until it is measured. In addition, buffer conditions can be changed in the device and, thus, a conformational change in the protein can be induced.

An additional feature of microfluidics is the possibility to remove oxygen from the sample and buffer. The design of the device has to be chosen accordingly. Additional channels that are not connected to the sample and buffer channels have to be implemented. These channels can be flushed with nitrogen, which diffuses through the highly permeable silicone elastomer polydimethylsiloxane (PDMS) and forces out the oxygen. The advantage of oxygen removal from the solutions is that the measurement can become more sensitive under optimal buffer conditions. Oxygen is an efficient triplet quencher and, therefore, continuously removing it can increase the photostability of the used dyes and hence increases the number of detected photons by adding a redox component to the buffer [Lemke et al., 2009].

In summary, microfluidics open up a wide range of possibilities. Questions regarding kinetics, which are not solvable in equilibrium, can be addressed with the combination of spFRET fluorescence methods and microfluidics.

## 7.1.2 Design of the microfluidic device

To perform a microfluidic measurement, the used device design has to be chosen according to the biological question. For many open questions in protein folding, different components of a sample need to be mixed inside the device to detect fast kinetics. Therefore, multiple channels that are combined in the device are needed. And additional, the ability to remove oxygen from the different solutions was preferable. Thus, the design of the device is chosen as described in [Lemke et al., 2009], which was already tested for single-molecule studies. The design consists of two different kinds of channels. One for the solutions (black lines), the sample and the buffer, and the other one for the degassing (green lines). Figure 7.1 depicts the design that was used for this thesis. This design offers the opportunity to flush additional channels with nitrogen and, thus, to degas the sample due to the high gas permeability of PDMS. However, for the studies presented here the oxygen was not removed from the solutions.

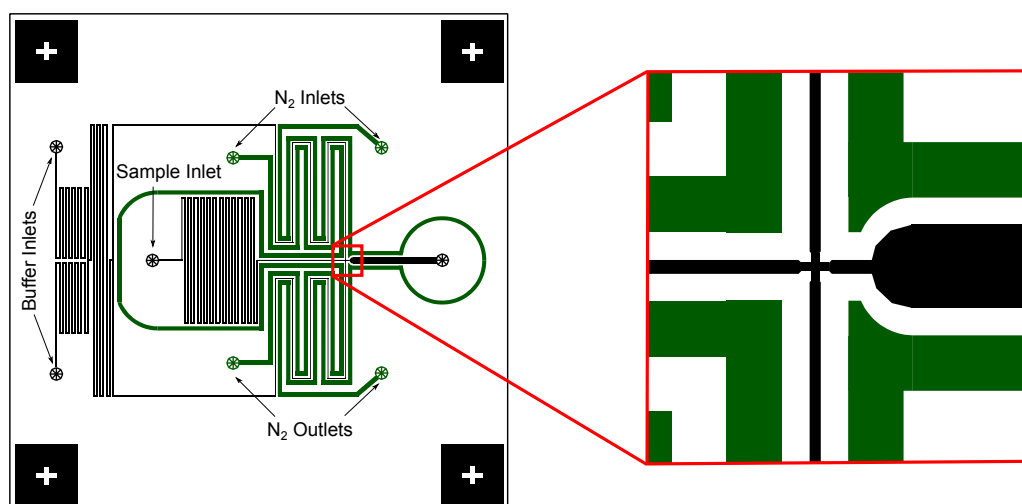


Figure 7.1: Design of the microfluidic device. The sample is connected to the sample inlet and can be mixed in the device with the buffer, connected at the buffer inlets, to measure fast changes of the conformation of the sample (black lines). The zoom in shows the mixing point. The nitrogen source is connected to the N<sub>2</sub> inlets (green lines). It is used to degas the sample solution. The crosses at the edges and the border are used for aligning the masks for the sample/buffer channels and the gas channels to each other.

The sample and buffer channels have a height of 80  $\mu\text{m}$  and a width of 40  $\mu\text{m}$ . The sample, which is the labeled molecule of interest, is fed into the sample inlet. The binding partners or buffers, which are expected to introduce a conformational change, are fed into the buffer inlets. The two different streams are combined and afterwards split up again. This design allows to mix two independent components of the buffer inside the device. Originally, this was used to mix different components of a redox system, to always have it freshly mixed before it is mixed with the sample. Close to the 300  $\mu\text{m}$  wide measuring area, the buffer channels and the sample channel come together and introduce a mixing of all three solution streams. From knowing the speed of the mixed stream and the distance between the measurement and the mixing point, the time between mixing and measuring can be calculated.

The green channels represent the gas channels with a height of 160  $\mu\text{m}$  and a width of 200  $\mu\text{m}$ . They are flushed with nitrogen from the  $\text{N}_2$  inlets. The distance between the gas and buffer or sample channels is very narrow ( $\sim 100 \mu\text{m}$ ). Because of the high gas permeability of PDMS, the material the devices consist of, the oxygen in the sample and buffer solution is exchanged with nitrogen. Removing the oxygen reduces the triplet quenching and increases the photostability of the dyes. This additional feature was not used for the measurements presented on the next pages.

### 7.1.3 Manufacturing of the devices

Different types of microfluidic devices are commonly used. We chose the principle of using a wafer as a negative mask. This has the advantage that, after a wafer is once produced, the production of the devices is easy, inexpensive and reproducible. For producing the PDMS devices, the wafer is poured over with PDMS. After curing and, therefore, polymerizing the PDMS, it is pulled off from the wafer. In the last step the PDMS is connected with a coverslip. In the following, the procedure of producing the chrome mask for the wafer, the wafer itself and afterwards of the PDMS device are described.

The production of the wafer was done with the help of Philipp Altpeter and Charlott Leu in the clean room of the group of Prof. Rädler.

#### Producing the chromium masks

To build up a structure on a wafer, a photoresist is put on top of the wafer. Then, the photoresist is illuminated by a lamp through a mask with the structure. Afterwards, the illuminated areas of the photoresist are crosslinked and then developed. Thus, for the exposure, a mask is needed that protects the parts of the wafer that should not be exposed. This mask can be made out of a print on a foil or by etching chromium on a glass plate. The foil is quick and inexpensive to produce but has the big disadvantage that the printing is not as precise as a chromium mask, which can lead to holes in the structure. This could result in a bad quality of the structure on top of the wafer. Additionally, the foil ages and cannot be used for years. The chromium mask, on the other side, is costly and special equipment is needed, but it is very precise. In the clean room of the group of Prof. Rädler, the needed equipment for producing a chromium mask is available. To work in a reproducible and precise way, the chromium mask was chosen and the production of this is described below.

The structure was drawn in the software 'autocad' (Autodesk, München, Germany) and then send to the ProtoLaser (LPKF, Garbsen, Germany). The ProtoLaser is a laser system, consisting of a diode laser with an emission wavelength of 375 nm, an acousto-optic modulator (AOM) to control the intensity and a scanner for controlling the position of the laser spot. This system illuminates the structure on a chromium mask. The chromium mask consists of a glass plate with a thin layer of chromium on top. The chromium layer is covered with the positive photoresist AZ 1518 (MicroChemicals, Ulm, Germany). To produce the final mask, the structure is exposed on the photoresist. At the illuminated areas, the photoresist is no more polymerized. During developing the photoresist, the exposed areas of the photoresist are freeing up the chromium. Development was done by putting the mask for 40 s in AZ 726 (MicroChemicals) and, afterwards, the mask was washed with water to stop the reaction. Finally, the mask was dried with compressed air.

In the next step, the chromium, which was not covered by the photoresist, had to be etched. For etching, the mask was put for 40 s in 'Chrome etch No.1' (MicroChemicals), which is a mixture of perchloric acid and ceric ammonium nitrate. Afterwards, the mask was washed with water and dried again with compressed air. To remove the photoresist, the wafer was covered with dimethyl sulfoxide (DMSO) in a breaker and the breaker was heated up to 90°C on a hotplate for 30 min. Next, the mask was washed with water. If some photoresist residues remained on the photo mask, a Peroxymonosulfuric acid (Piranha) treatment was done. The cleaned mask can now be used for structuring a wafer.

Due to the two different channel heights used in our design, two masks are required. One mask structured with the sample and buffer channels (Figure 7.1 (black lines)) and the other one with the gas channels (Figure 7.1 (green lines)).

### **Structuring a wafer**

The approach for structuring the wafer with the chosen design is the following: A layer of epoxy-based photoresist, in our case SU-8 100, is spin-coated on top of the wafer, illuminated and developed. The next layer of SU-8 100 is put on top of the first structure, illuminated and also developed. To do this in a reproducible and precise way, the illumination power and the layer thickness have to be optimized.

### **Testing the manufacturing conditions**

For clean, well structured channels, the exposure power has to be chosen correctly. If the exposure power is too low, the degree of crosslinking the photoresist is too low and, therefore, the structures can be washed away [May et al., 2005], [Winterstein et al., 2014]. If the exposure power is too high, the area at the edges of the excited structure will also be cross-linked. This effect is called T-topping or generation of a surface inhibition layer and is caused by an overexposure of the upper layer of the photoresist [Mitra and Chakraborty, 2011]. To minimize this effect, the wavelength below 350 nm should be cut out of the spectrum by a filter (material data sheet of SU-8 100). For the used equipment in the cleanroom it was not possible to add such a filter. An additional way to minimize T-topping is to reduce the excitation time and, thus, reducing the time of cross-linking the upper layer.

The used maskaligner, wherein the illumination source, a lamp, is located, has to be tested due the power of the lamp. This has to be done on a regular base because the power of the lamp decreases by aging. To determine the remaining excitation power and adjust therefore the excitation time, a test structure was excited with different excitation times.

As a photoresist, we chose SU-8 100, which is a negative photoresist. A negative photoresist becomes insoluble to the developer upon illumination. The illuminated areas corresponded to the resulting structures. A layer of SU-8 100 was spin coated on a wafer. Therefore, it is important that the calculated thickness of the layer is equal to the actual thickness of the designed structures. The thickness of the photoresist depends on the viscosity of the SU-8 100 and the spin-coating velocity. The viscosity of SU-8 100 depends on the amount of solvent in the SU-8 100. When the bottle with SU-8 100 is open, parts of the solvent can evaporate and the viscosity increases. By using the same spin coating velocity for the photoresist with a higher viscosity, the layer gets too thick. Thus, the SU-8 100 layer has to be tested for the correct thickness.

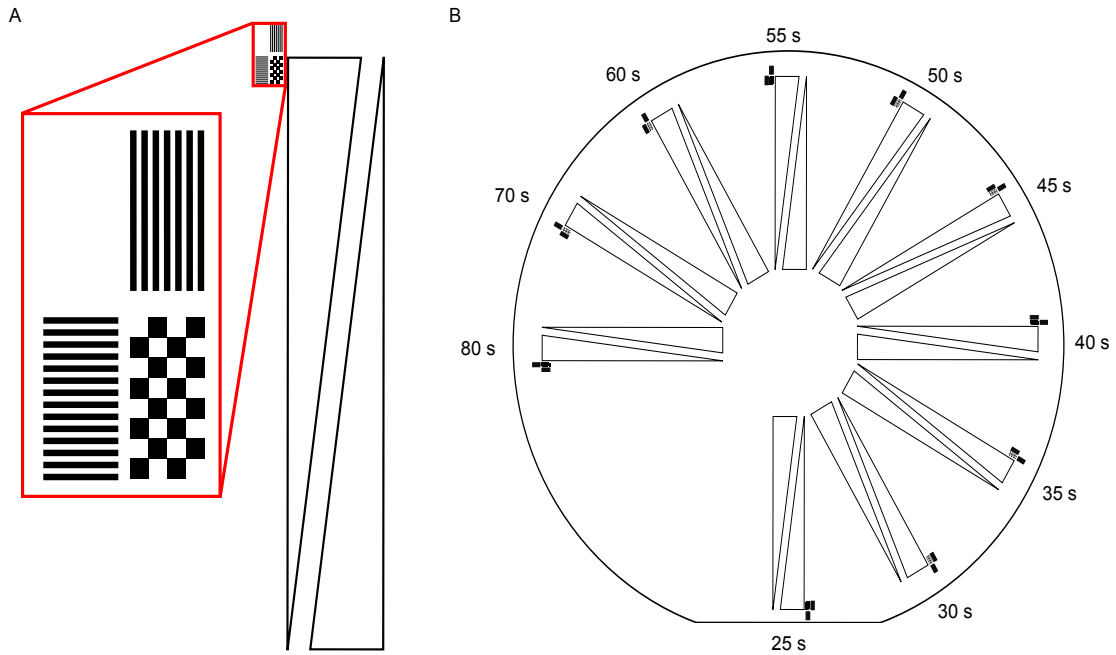


Figure 7.2: Dose test for the maskaligner. (A) The used design for the dose test consists of two triangles, lines in two directions and a checkerboard pattern. (B) For testing different exposure times, the wafer was rotated by  $30^\circ$  after each exposure and the exposure time was changed.

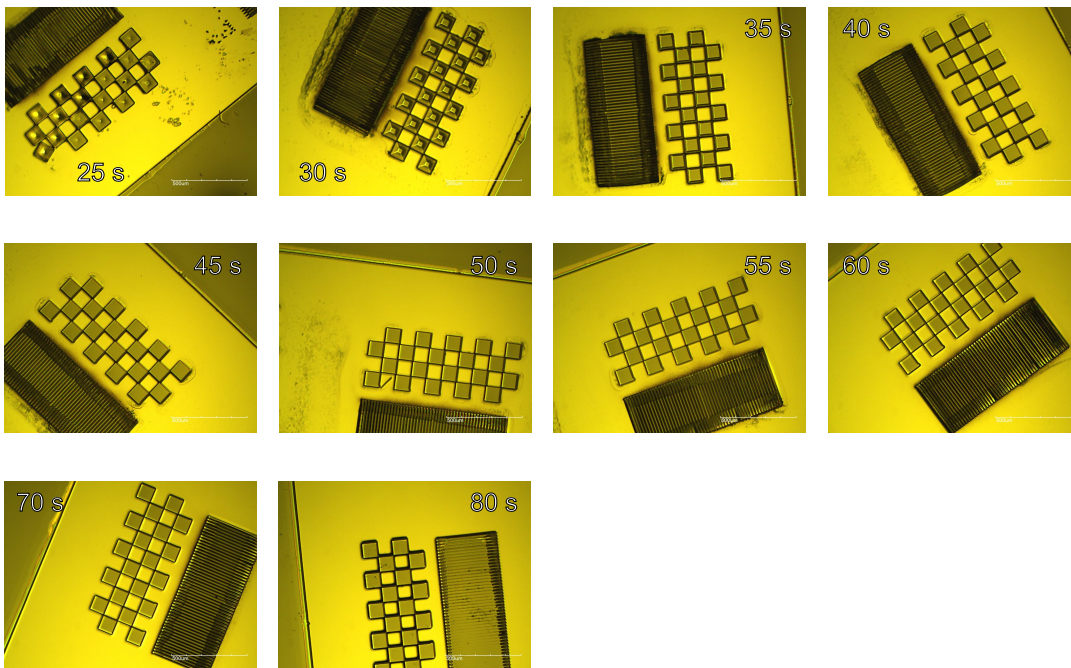


Figure 7.3: Light microscopy images of the dose test sample. The same position in the structure was illuminated for different exposure times and, therefore, different doses. The scale bar refers to  $500 \mu\text{m}$ . Exposure times smaller than 45 s are not long enough because the structures look like pyramids. The longer exposure times look similar, independent of the exposure time.

According to the data sheet of SU-8 100, a spin coating velocity of 3500 rpm is needed for a 80  $\mu\text{m}$  thick layer. The layer of SU-8 100 has to be cured and, afterwards, can be illuminated. The exact process for this is given on page 110. To measure the thickness of the SU-8 100 layer and to verify the correct dose for illumination, a test structure was created and illuminated on a single wafer at different positions with different exposure times. The scheme of the used structure and the positions are shown in Figure 7.2. We chose small lines and a checkerboard pattern in the size of the structures of our device design. We tested if the lines are separated in a proper manner and the squares have vertical edges (Figure 7.2A). Furthermore, these structures were chosen to check for the height of the structure, the SU-8 100 thickness, and, therefore, for the spin velocity of the photoresist.

After development, the structures were checked with a light microscope. In Figure 7.3, snapshots of the different illumination times are depicted. Illumination times smaller than 45 s were too low. The structure had no rectangular edges and the squares look more like pyramids. In particular, an exposure time of 25 s was way too short and parts of the structure were flushed to another position on the wafer. The dose of the longer exposure times looks fine. To check for T-topping and other unwanted effects like connected structures, parts of the wafer with an exposure time of 50 s, 60 s and 80 s were additionally measured in a scanning electron microscope (SEM).

Figure 7.4 shows the SEM measurements of the structures. The bright areas in the figure are due to electrons of the scanning beam, which are collected on the surface of the structure. To avoid this effect, the surface needs to be treated to make it electroconductive but this was not done here. In Figure 7.4A the structure was exposed for 50 s. The area, where the electron beam hits the structure, shows deformation. This could be explained by the fact that the crosslinking was not sufficient and is a hint that an illumination time of 50 s was too short. The test structure after an exposure time of 80 s is depicted in Figure 7.4B. The upper edges of the structure were overhanging. This effect is called T-topping and causes problems, when the structure is used as a mask for PDMS. When the PDMS is pulled off, the photoresist and, therefore, the mask will break. The exposure was therefore too long.

Figure 7.4C and D show the structure after 60 s exposure time. The edges were more or less vertical and the structure kept their shape during the SEM measurement. A height of 86  $\mu\text{m}$  of the structure in Figure 7.4D was calculated. This value corresponds very well to the theoretical value of 80  $\mu\text{m}$ , which is chosen for the sample and buffer channel height, especially by taking into account the possible error in choosing the edges for calculating the height in the image.

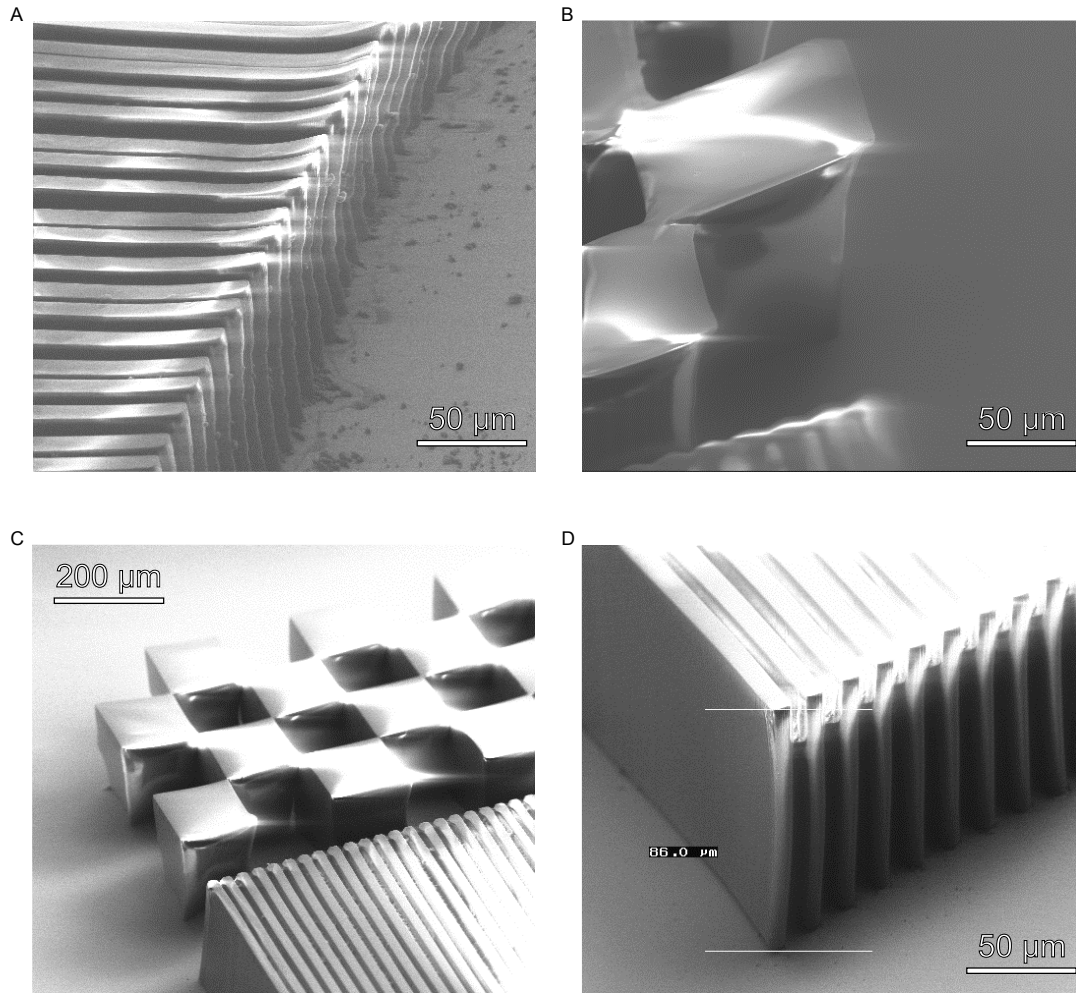


Figure 7.4: SEM images of the dose test pattern. (A) The structure was illuminated for 50 s. The structure might have been deformed by the electron beam. (B) An exposure time of 80 s was tested. The T-topping of the structure indicates the illumination time was too long. (C) and (D) were exposed for 60 s. The edges are vertical and the height can be calculated as 86  $\mu\text{m}$ .

## Protocol for producing a multilayer structured wafer

By knowing the conditions for the height of the structure and the correct illumination dose, a multilayer structured wafer can be produced. A three inch silicon wafer was used, which was polished on one side (MicroChemicals). On this side, the structure was built. Due to the small size of the design compared to the wafer, four times the same design was placed on the wafer (Figure 7.5).

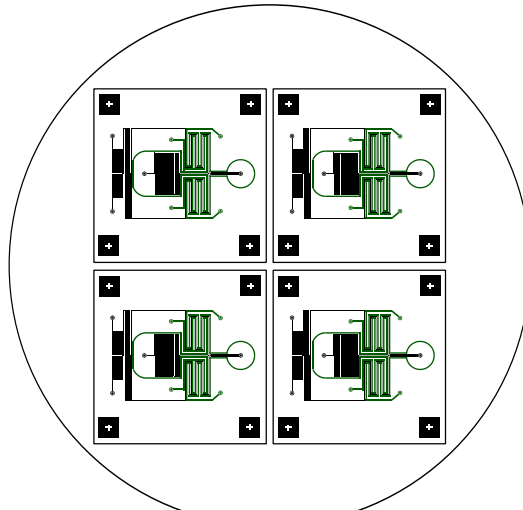


Figure 7.5: Device positions on the wafer. The same design, like in Figure 7.1, is four times positioned on one wafer.

The wafer was first coated with the adhesion promoter TI Prime (MicroChemicals) to change the surface properties in a way that the photoresist SU-8 100 (MircoChem Corp, Westborough, MA, USA) can bind more efficient. A drop of the size of a 2-Euro piece was put on top of the wafer and spin coated with 2000 - 4000 rpm for 20 s. Afterwards, the wafer was cured on a hotplate for 2 min at 120°C.

For spin coating the first 80  $\mu\text{m}$  thick layer of SU-8 100, some resist was poured on top of the wafer. Air bubbles should be avoided. The wafer was spun for 10 s with 500 rpm and an acceleration of 200 rpm for distributing the photoresist on the whole wafer. With an acceleration of 300 rpm, the speed of the spin coater was increased to 3500 rpm and then spun for additional 30 s. The wafer was stored over night on a horizontal plate to ensure SU-8 100 degassing and equilibrating the layer thickness. To cure the photoresist, the wafer was baked the next day for 8 min at 65°C and, afterwards, for 25 min at 95°C. This process is called soft baking.

For exposing the sample and buffer channel structure on the coated wafer, the maskaligner was used. The mask was put in the maskaligner, facing down to have a minimal distance between the mask structure and the wafer to avoid illumination of areas at the edges of the structure. Next, the wafer was put in the wafer slot in the maskaligner and lifted up till the wafer touched the mask. The exposure time was chosen according to the dose test as 60 s. After exposing, the wafer with the SU-8 100 was cured in the post-exposure baking step. The wafer was prewarmed by holding it above the hotplate and was then put on the hotplate at 65°C for 2 min. The temperature was increased to 95°C for additional 9 min.

Afterwards, the temperature was ramped down to avoid fine cracks in the photoresist. The whole post exposure baking has to be done very precisely, because, otherwise, the tendency of delamination of the photoresist from the wafer increases [May et al., 2005].

In order to get rid of the unexposed SU-8 100, the developer mr-Dev 600 (micro resist technology GmbH, Berlin, Germany) was used. The wafer was covered in a breaker with the developer for about 10 min, till all photoresist was removed. Afterwards, the wafer was washed with isopropyl and dried with compressed air.

The second layer of SU-8 100 was 160  $\mu\text{m}$  for the chosen design. The spin coating was calculated from the calibration curve of the material data sheet of SU-8 100 as 60 s at 500 rpm with an acceleration of 200 rpm and, then, with an acceleration of 300 rpm to 1750 rpm for 30 s. To degas the wafer in a proper way, the wafer had to be put in a desiccator for hours till all air bubbles were removed. If this step is not done long enough, small air bubbles between the structures would remain and, thus, a connection between the channels would be created. After the wafer had been totally degassed, soft baking was done for 32 min at 65°C and, afterwards, for 60 min at 95°C.

The second exposure was cured in the same way as the first exposure with the exception that the second structure had to be aligned on top of the first structure. This was done by using the crosses in the edges of the structure. The exposure time was calculated from the dose test of the 80  $\mu\text{m}$  high structure and the material data sheet of SU-8 100 as 70 s for the 160  $\mu\text{m}$  thick layer. The post exposure bake was done in the same way as the first one, but the times were elongated to 4 min at 65°C and 15 min at 95°C. The development was increased to 12 min, due to the thicker structures. Afterwards, the wafer was washed with isopropyl and dried with compressed air.

In the next step, the wafer has to be coated with trimethylchlorosilane (TMCD). The TMCD changes the surface properties of the wafer and, therefore, makes it less sticky for PDMS. This process is important, because otherwise pulling off the PDMS from the wafer after cross-linking could destroy the structures on top of the wafer. This coating is permanent and only has to be applied once before the first use of the wafer as a mask. For coating, a few drops of TMCD were put on the wafer and dried under the fume hood over night.

## PDMS device

For producing a microfluidic device with the help of the structured wafer, multiple steps are necessary, which are described in the following. Thereby, it was figured out that only two of the four devices of the wafer are functional. In the other two designs, the gas and solution channels are connected.

The used material is PDMS, a silicone elastomer. PDMS is obtained from two components, the non cross-linked monomeric material and the cross-linker. The ratio of the two components determines its rigidity. For our design, a 1:10 ratio was used, i.e. ten parts of the non cross-linked material mixed with one part of the cross-linker. When less cross-linker was added, the PDMS would be too soft and the channels would collapse during the procedure of building the devices. When more cross-linker is added, the PDMS is too hard and the device would not permanently stick to the coverslip.

The PDMS was mixed and then poured on the wafer. The wafer was put in a desiccator for degassing for at least 40 min to remove all air bubbles between the structures. After the air had been removed from the PDMS, the PDMS was cured in an oven for 40 min at 80°C. In the meantime, the coverslips were cleaned. They were washed with 100 % acetone and with

100 % isopropyl. For drying, lens cleaning tissues (Thorlabs, Dachau, Germany) were used and touching the coverslip was avoided to keep the glass clean.

After the PDMS had been crosslinked in the oven, it was cooled down. The structure on top of the wafer was cut and peeled off. In the next step, holes with a diameter of 0.6 mm were drilled for the in- and outlets. This is important because, after the device is finalized, the tubes for the sample and buffer are connected by metal pins that fit into the holes of the device. For cleaning the PDMS chips after drilling, the structured side of the PDMS was cleaned from drilling rest using tape (tesa SE, Norderstedt, Germany).

To connect PDMS with the cleaned coverslip, the surface properties have to be changed. Using a zepto plasma cleaner (Diener electronic GmbH + Co. KG, Ebhausen, Germany), the surface is more negatively charged and, thus, hydrophilic. For treatment, the pressure inside the plasma cleaner was decreased to 0.3 bar, the plasma was kindled and treated the surfaces with 20 % power at 0.5 bar for 15 s. By placing the PDMS afterwards on top of the coverslip, the PDMS sticks to the glass. To make the binding permanent, the device was put over night in the oven at 80°C.

The final step in producing the microfluidic devices was the cleaning of the in- and outlets. Due to the drilling, small pieces of PDMS can stick to the in- and outlets. To remove them, a syringe connected to a short piece of tube and a metal pin was pushed into the drilled holes. The remaining PDMS pieces stuck in the metal pin after removing the pin and can be pushed out of the pin by inducing some pressure by the syringe.

#### 7.1.4 Microfluidic flow control system

For measurements with controlled flow rates, the volume of the buffer and the sample, which are flushed through the channels, has to be controlled very precisely. Due to small air bubbles, aggregates in the solutions or differences between the different device positions on the wafer, it is not possible to control the flow manually. To overcome this problem, a commercial flow control system with implemented feedback loops to control the volume flow (OB1 Mk3, Elveflow, Paris, France) is used. The whole setup with all connected components is depicted in Figure 7.6.

A gas bottle filled with nitrogen is connected via a tube with the flow control system with three outlets. The input pressure is split up to the three outlets, which can be controlled separately. Each outlet is connected via a tube with an Eppendorf tube (Eppendorf, Hamburg, Germany), which is filled with the buffer or sample, respectively. Due to the pressure set to the outlet of the flow control system box, the liquid in the Eppendorf tube is pushed into a tube starting at the bottom of the Eppendorf tube. The sample or buffer, respectively, is flushed into the tube and then through the connected flow sensor (MFS 2 - Microfluidic flow sensor, Elveflow, Paris, France). The flow sensors can measure flow rates between 0.2 and 7  $\frac{\mu\text{l}}{\text{min}}$ . They are connected back via a cable to the flow control system. There, the defined and the actual volumes flushed through the sensor are compared and the flow control system can respond and adjust the pressure within 40 ms. This makes the system very fast, sensitive to changes and, thus, stable over a long period of time. The fact that the flow rate can be set at a fixed value makes the system very reproducible even between different measurements. The outlet of the flow sensor is then connected by a tube and a metal pin with the microfluidic device (Figure 7.7). The sample is mixed and measured inside the device and the outlet of the device is connected via a tube with the waste.

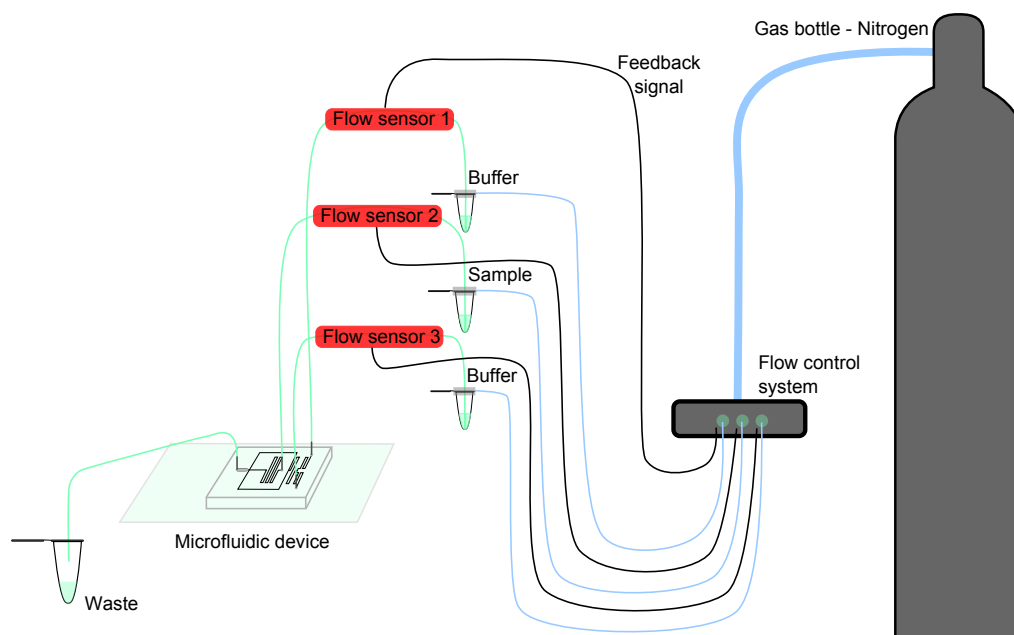


Figure 7.6: Microfluidic flow control system. The pressure of the gas bottle is adjusted by the flow control system, which gets a feedback from the flow sensors. The sample and buffer are flushed from the Eppendorf tubes through the flow sensors and then through the metal pins into the microfluidic device.

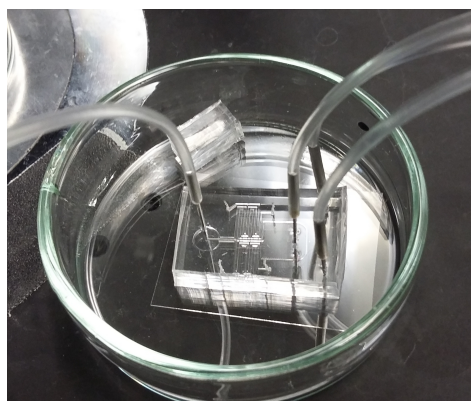


Figure 7.7: Device connected with tubes. The sample and buffer channels are connected with metal pins, which are then connected with the tubes filled with sample and buffer, respectively.

### 7.1.5 Calibration of the flow velocity

For applying a known velocity to the molecules of interest inside the measurement area of the device, the externally applied flow has to be calibrated. During the procedure of calibration it was found that every position on a wafer has its own calibration curve. This is due to small deviations in the SU-8 100 thickness resulting from the manufacturing of the wafer. To account for this, the flow of a device from every position on a wafer has to be calibrated once and can be assumed to stay constant during different batches of PDMS devices. The different positions on the wafer are depicted in Figure 7.5.

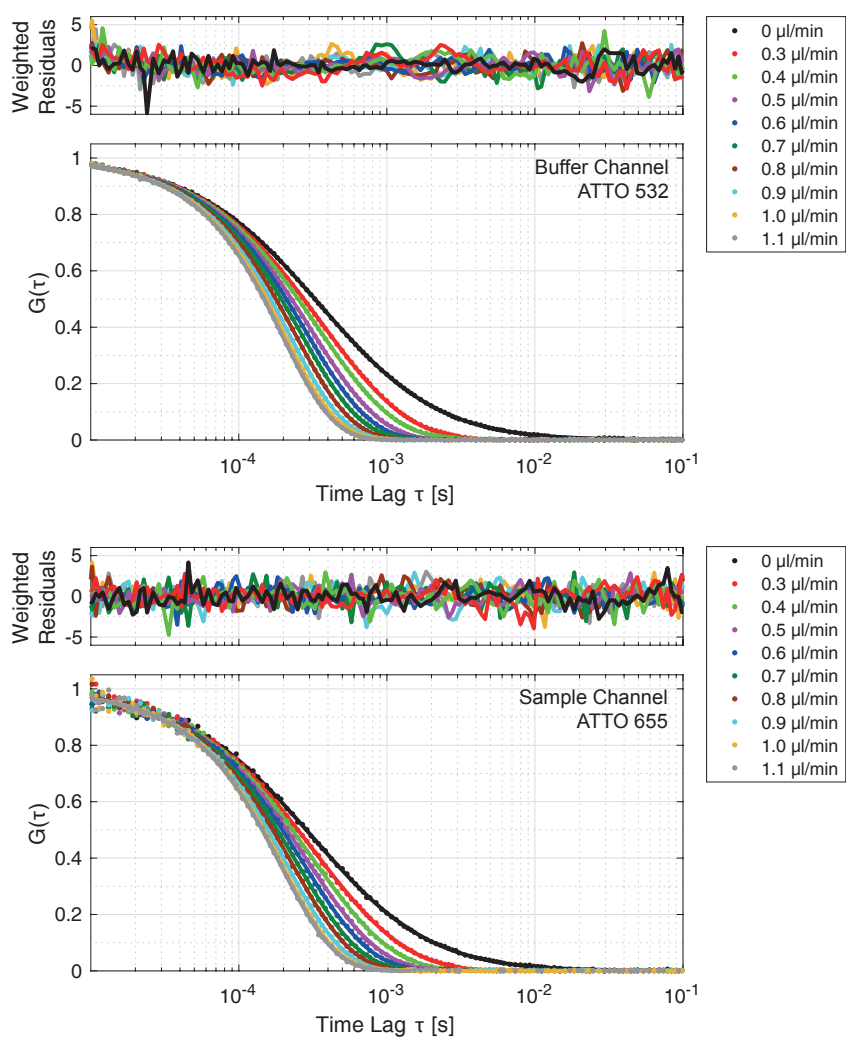


Figure 7.8: FCS curves with different flow rates. ATTO 532 and ATTO 655 were flushed in the buffer and sample channel, respectively. The flow rate was equal in all three channels and is given in the legend. Flow rates were determined by fitting the curves with Equation (3.29) (page 23).

To calibrate the flow rate on a microfluidic device, different dye solutions at a nM concentration were mixed inside the device and measured on a MFD-PIE setup. The flow rate was calculated using the FCS fit with Equation (3.29) (page 23). ATTO 532 (ATTO-TEC

GmbH, Siegen, Germany) was flushed in the two buffer channels and ATTO 655 (ATTO-TEC GmbH) in the sample channel. These two dyes are chosen because they are very photostable and excitable with the available lasers on the used setup. The two dye solutions in the three channels are mixed properly at the point of measurement, which can be seen by the fact that for both dyes, FCS curves are detectable (Figure 7.8 (upper panel: buffer stream, lower panel: sample stream)). The flow rate was chosen for all three channels the same. Therefore, the same velocity is expected for all three solution streams. After mixing in the wider channel, FCS measurements were performed. The change in the curve shape depending on the externally applied flow is depicted in Figure 7.8.

The velocity, calculated from the FCS fit with flow, is plotted versus the externally applied flow rate. The relationship for the FCS measurement in Figure 7.8 is depicted in Figure 7.9. The slope of the fitted curve is  $3.19 \frac{\text{mm}\cdot\text{min}}{\text{l}\cdot\text{s}} = 191400 \frac{\text{m}}{\text{l}}$  for the buffer channel and  $3.09 \frac{\text{mm}\cdot\text{min}}{\text{l}\cdot\text{s}} = 185400 \frac{\text{m}}{\text{l}}$  for the sample channel. Therefore, the mean is calculated as  $3.14 \frac{\text{mm}\cdot\text{min}}{\text{l}\cdot\text{s}}$ . Small deviations are due to variations in the focus z-position between different measurements. With the help of this value and knowledge about the applied velocity and the information of the distance between the mixing and measurement points, the time interval between mixing and measuring is calculated.

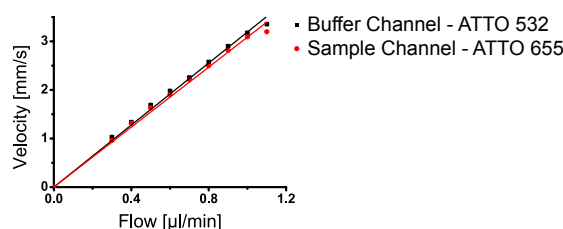


Figure 7.9: Calibration curve for the flow rate. The velocity calculated from the FCS fit is plotted versus the externally applied flow rate.

## 7.2 Folding kinetics of DM-MBP

### 7.2.1 Introduction

The first protein-test system for the microfluidic was MBP. With microfluidics, we wanted to monitor the timescale of refolding of the maltose binding protein (MBP, PDB-ID: 1OMP). The MBP, a 40 kDa protein, consists of two domains, the N-terminal domain and the C-terminal domain (Figure 7.10). Each domain consists of a central core of a five-strand  $\beta$ -sheet with two  $\alpha$ -helices on one side and three  $\alpha$ -helices on the other side. The two domains are connected by a groove, which contains the maltose binding site. Upon binding of maltose to this groove, the MBP changes from an open to a closed conformation. [Spurlino et al., 1991].

We chose a MBP mutant with two mutations in the amino acid residue 52 and 298, which is called in the following DM-MBP. It is known that DM-MBP can fold on its own, but slowly. The folding kinetics of this mutant of MBP can be accelerated by the assistance of GroEL/GroES. From literature, it is known that this chaperone system increases the time of proper folding by a factor of 6 [Sharma et al., 2008] to 10 [Chakraborty et al., 2010].

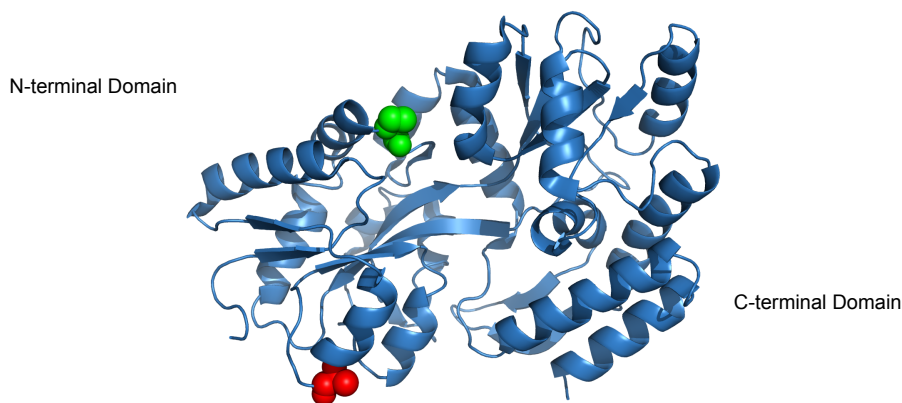


Figure 7.10: Crystal structure of MBP. The labeling sites of MBP (PDB-ID: 1OMP) are depicted as red and green spheres.

The conformation of the DM-MBP upon addition of GroEL or GroEL, GroES and ATP is already known from spFRET measurements in equilibrium [Sharma et al., 2008]. To monitor conformational changes involved in the refolding of DM-MBP bound to GroEL or GroEL, GroES and ATP, microfluidic measurements were performed together with Ganesh Agam from our group.

## 7.2.2 Sample Preparation

DM-MBP expression, purification and labeling was done by Ganesh Agam in our group. GroEL and GroES were expressed and purified in the group of Prof. Hartl (Max Planck Institute of Biochemistry, Martinsried). A short summary of the used strategy is presented here.

DM-MBP (A52C, P298C) was cloned between the NdeI and NheI sites in the pCH vector, pCH-DM-MBP(A52C-P298C). It was expressed under the control of the T7 promoter, inducible with IPTG, in the cytosol. Double-cysteine mutants of MBP were generated by site-directed mutagenesis of the DM-MBP gene. For labeling, ATTO 532-maleimide (ATTO-TEC GmbH) and Alexa Flour 647-maleimide (Thermo Fisher Scientific, Waltham, MA, USA) in 5 mM Tris (pH 7.8), 20 mM KCl and 5 mM Mg[OAc]<sub>2</sub> were mixed for 2 h at 25°C in the presence of a 1.1-fold molar excess of the fluorophore. The protein was stored in 5 mM Tris (pH 7.8), 20 mM KCl and 5 mM Mg[OAc]<sub>2</sub>. The whole protocol is based on the protocol described in [Sharma et al., 2008].

For the expression and purification of GroEL, an *E.coli* strain containing the plasmid pOF39 was used. Cells were grown at 34°C until stationary phase and frozen in a suspension in 50 mM Tris (pH 8.0) and 10 % sucrose in liquid nitrogen. Thawed cells were lysed by sonication with a tip sonicator in 50 mM Tris (pH 8.0), 10 mM EDTA, 10 mM Mg(OAc)<sub>2</sub>, 50 mM KCl, 2 mM dithiothreitol (DTT), 1 mM phenylmethylsulfonylfluoride (PMSF), 1 mg/ml of 150 000 U/mg lysozyme and 50 mg/ml of 3000 U/mg DNase I for 30 min on ice. By centrifugation at 4°C (20 min, 48 000 *g*, followed by 1 h at 257 000 *g*), cell debris and membranes were removed. The supernatant was adjusted to 20 mg/ml in 30 mM Tris (pH 7.8), 50 mM NaCl, 1 mM EDTA and 1 mM DTT. Next, GroEL was fractionated by successive steps of chromatography on a DE52 column in the same buffer, DE52 column in 25 mM

histidine (pH 5.5), 50 mM NaCl, 1 mM DTT (final pH of the loaded sample ~6.0), phenyl-Sepharose CL-4B (Pharmacia, Uppsala, Sweden) in 20 mM 3-(N-morpholino)propanesulfonic acid (MOPS) (pH 7.2), 400 mM NaCl, 1 mM DTT and Sephacryl S300-HR (Pharmacia) in 10 mM MOPS (pH 7.2), 50 mM KCl and 1 mM DTT. GroEL protein eluting at ~800 kDa was pooled. The whole protocol is based on [Hayer-Hartl et al., 1994].

GroES was expressed from a pET-11a vector (Novagen Inc., Madison, Wisconsin, USA) in BL21 cells cultured at 37°C in LB medium containing ampicillin. Expression was induced by addition of isopropyl-P-D-thiogalactopyranoside (IPTG) to 0.8 mM when cells reach a density of 0.6 OD<sub>600</sub> and the cells were further incubated for 3 h. The protein purification was done in three steps. First chromatography was done by a DEAE Sepharose column (buffer: 30 mM Tris (pH 7.5), 10 mM NaCl, 1 mM EDTA and 1 mM DTT), second by a MonoQ column (16/10) (buffer: 20 mM Imidazol (pH 5.8) and 10 mM NaCl) and the last step was done by a 3:HiPrep 26/60 Superdex 200. The protein was stored in 30 mM Tris/Cl (pH 7.5), 100 mM NaCl and 1 mM EDTA. The whole protocol is based on [Hayer-Hartl et al., 1996].

### 7.2.3 Spontaneous refolding of DM-MBP

To monitor the conformational changes of the N-terminal domain of DM-MBP upon refolding, microfluidic measurements were performed. As a reference for the unfolded and properly folded DM-MBP, equilibrium measurements were performed. The DM-MBP was denatured in 3 M GuHCl, a chaotropic agent, and, afterwards, the GuHCl was diluted to 2 M. The spFRET (see Chapter 2.5 on page 11) was determined on a multiparameter fluorescence detection setup (MFD, see Chapter 3.3.2 on page 25) with pulsed interleaved excitation (PIE, see Chapter 3.3.1 on page 24). The distance between the two dyes was calculated by photon distribution analysis (PDA, see Chapter 3.3.3 on page 32).

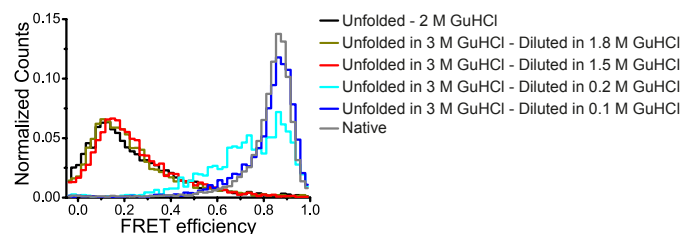


Figure 7.11: DM-MBP measured in different GuHCl concentrations in equilibrium. DM-MBP was denatured in 2 M GuHCl (black line). After denaturation in 3 M GuHCl, 50 pM DM-MBP was measured in 1.8 M GuHCl (dark yellow line), in 1.5 M GuHCl (red line), in 0.2 M GuHCl (cyan line) and in 0.1 M GuHCl (dark blue line). As a reference native DM-MBP was measured (gray line).

The FRET efficiency for the unfolded DM-MBP is approximately 0.1 (Figure 7.11, black line), which corresponds to a distance between the dyes of  $d = 75 \text{ \AA}$  and a width of  $\sigma = 13 \text{ \AA}$  (Table 7.1). This width of the distribution is very broad, which can be explained by multiple subconformations due to the flexibility of the unfolded protein.

By reducing the GuHCl concentration to 0.1 M, the DM-MBP folds properly and the FRET efficiency changes to approximately 0.9 (Figure 7.11, blue line). A GuHCl concentration of 0.2 M emerged to be too high to reach the final, proper folded conformation (Figure 7.11, gray line). The FRET efficiency of the native state corresponds to a distance of  $d = 45 \text{ \AA}$  with a

width of  $\sigma = 4 \text{ \AA}$  (Table 7.1). This width is well defined and, therefore, represents to a single conformation. These results are in line with recently published data [Sharma et al., 2008].

Table 7.1: Distances calculated using PDA for DM-MBP. DM-MBP (50 pM) was measured in the presence of 2 M GuHCl (unfolded) and in the presence of 0.1 M GuHCl (folded). The photons of a burst were divided into bins of 1 ms, summed up in a FRET histogram, and fitted using a Gaussian model. With photon distribution analysis (PDA), the distance  $d$  between donor and acceptor, the corresponding width  $\sigma$  and the relative weights of the different populations were calculated.

	Subpopulation			Goodness of the fit
	$d$ [Å]	$\sigma$ [Å]	%	$\chi^2$
unfolded	75	13	100	1.3
folded	45	4	100	4.2

The timescale of interchanging between the unfolded and the refolded conformation was monitored by a combination of spFRET and microfluidics. The DM-MBP was denatured again in 3 M GuHCl and, afterwards, diluted to 2 M GuHCl in 5 mM Tris (pH 7.8), 20 mM KCl and 5 mM Mg[OAc]<sub>2</sub>. Then, the DM-MBP was connected to the sample inlet of the microfluidic device. The buffer inlets were connected to 5 mM Tris (pH 7.8), 20 mM KCl and 5 mM Mg[OAc]<sub>2</sub>. Additionally, 0.001 % Tween20 was added to all solutions to avoid sticking of the protein to the tubes or the microfluidic device. The sample and buffer solutions were mixed in the device in a 1 to 12 ratio, e.g. 1 part DM-MBP and 12 parts buffer, to a final GuHCl concentration of 0.15 M. With the 1 to 12 ratio, two flow rate combinations of the sample and buffer channels can be measured, i.e.  $0.2 \frac{\mu\text{l}}{\text{min}}$  and  $0.3 \frac{\mu\text{l}}{\text{min}}$  applied to the sample channel and  $1.2 \frac{\mu\text{l}}{\text{min}}$  and  $1.8 \frac{\mu\text{l}}{\text{min}}$  applied to each of the buffer channels, respectively. This was the highest reachable dilution in the used design because higher dilutions would result in only one flow rate combination and, therefore, due to the setup, in only five different distances. The limitation in the distances is due to the used microscope stage. The flow rate in the detection area is limited, because too high flow rates result in too short bursts, because the molecule is flushed too fast through the focal volume and, therefore, the number of detected photons has a too low statistic.

---

Figure 7.12: Spontaneous refolding of DM-MBP. DM-MBP was unfolded in 3 M GuHCl. **(A)** The GuHCl concentration was diluted to 2 M and then mixed in the microfluidic device 1 to 12 with a buffer containing 20 mM KCl to a final concentration of 0.15 M GuHCl. **(B-C)** The GuHCl concentration was diluted to 1.8 M after denaturation. At a mixing ratio of 1 to 12 in the microfluidic device, the concentration of GuHCl was reduced to 0.13 M in the presence of **(B)** 20 mM KCl or **(C)** 200 mM KCl. The concentration of DM-MBP was chosen as 15 pM after mixing.

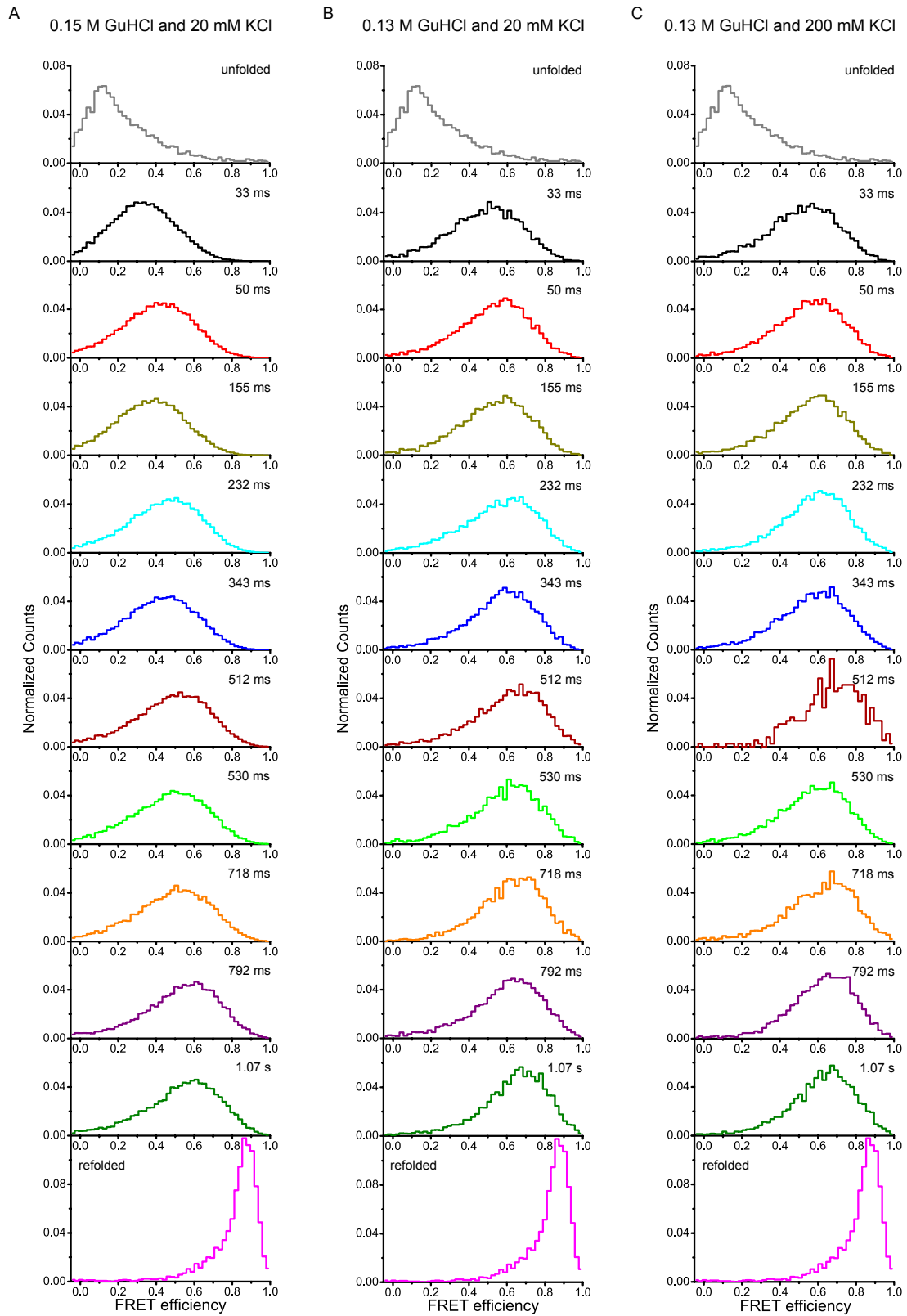


Figure 7.12A depicts the time dependent changes in the FRET efficiency after dilution from 2 M to 0.15 M GuHCl. A reliable PDA analysis cannot be performed due to the high flow rates and, therefore, very narrow bursts with a too low number of photons. The FRET efficiency changes from the unfolded DM-MBP (FRET efficiency  $\sim 0.1$ ) to an intermediate FRET efficiency of  $\sim 0.65$  after approximately 800 ms. Within the maximum timescale, we can reach with the used microfluidic design, the DM-MBP does not change from the intermediate conformation to its finally folded conformation. Thus, the timescale for this last refolding step is much longer than 1 s.

It is known from literature that the refolding of DM-MBP depends on the GuHCl concentration [Chakraborty et al., 2010]. To test if small changes in the final concentration have an effect on the refolding kinetics, the maximum concentration, which is needed to keep the DM-MBP unfolded, was verified. We tested the conformation by the FRET efficiency of equilibrium measurements at a GuHCl concentration of 1.8 M and 1.5 M and compared these measurements with the one with a final GuHCl concentration of 2 M (Figure 7.11, dark yellow and red line). The FRET efficiency of the measurements with 1.8 M GuHCl is similar to the FRET efficiency with 2 M. At a concentration of 1.5 M GuHCl, the FRET efficiency shifts to slightly lower values, which is due to the fact that the degree of refolding and unfolding depends first on the GuHCl concentration and then on the time. Therefore, 1.8 M GuHCl was used, because it is the lowest possible GuHCl concentration at which the DM-MBP stays totally unfolded.

For the following measurements, we first denatured the DM-MBP in 3 M GuHCl and then diluted the concentration to 1.8 M GuHCl in 5 mM Tris (pH 7.8), 20 mM KCl, 5 mM Mg[OAc]<sub>2</sub> and 0.001 % Tween20. This sample was then mixed in the microfluidic device in a ratio of 1 to 12 with buffer, which results in a final GuHCl concentration of 0.13 M. The time-dependent refolding is given in Figure 7.12B. The refolding kinetics is faster than observed for the measurements with a final GuHCl concentration of 0.15 M. The intermediate state at  $\sim 0.65$  FRET efficiency was reached after approximately 500 ms. The final, properly folded conformation was again not reached on the timescale of the microfluidic measurements.

In the next step, we investigated the effect of the concentration of KCl on the refolding kinetics. [Chakraborty et al., 2010] observed that the refolding gets slower by a factor of two when the concentration of KCl is increased from 20 mM to 200 mM. The same measurement as discussed above (finally 0.13 M GuHCl) in the presence of 20 mM KCl was performed in the presence of 200 mM KCl (Figure 7.12C). The timescale for refolding, measured with microfluidics, does not change depending on the tested salt concentration. The intermediate state was again reached in approximately 500 ms after mixing.

To further analyze the data, the FRET efficiency curves are plotted by a Gaussian function. The mean FRET efficiency value of the fit is plotted versus the time after mixing (Figure 7.13). It is clearly visible that the timescale of the refolding is different for the two tested GuHCl concentrations. Fitting the curves using an exponential function results in  $681 \pm 609$  ms,  $509 \pm 244$  ms and  $428 \pm 323$  ms for 0.15 M GuHCl and 20 mM KCl, 0.13 M GuHCl and 20 mM KCl and 0.13 M GuHCl and 200 mM KCl, respectively. The standard errors of the fit are very large and, thus, are not determinable. However, it shows that the refolding time in the presence of 0.15 M GuHCl and 20 mM KCl is the larger one.

In summary, we measured the refolding of DM-MBP from an unfolded to an intermediate conformation. Refolding time for this process depends on the GuHCl concentration, but not on the concentration of the KCl. This is contradictory to the literature. There it is found that the refolding is salt dependent and increases with higher salt concentrations [Chakraborty et al., 2010]. We suggested that when the refolding time from the unfolded to the intermedi-

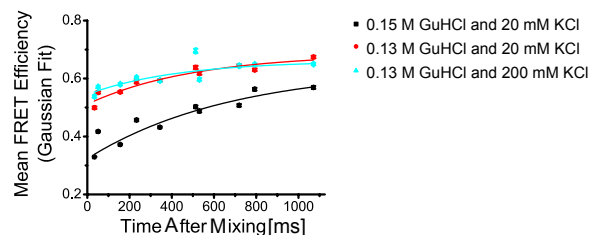


Figure 7.13: Kinetic of the spontaneous refolding of DM-MBP. The FRET efficiency curves of Figure 7.12 were fitted using a Gaussian function. The mean FRET efficiency of the fit and standard error are plotted versus the time after mixing for DM-MBP refolded in 0.15 M GuHCl and 20 mM KCl (black dots), in 0.13 M GuHCl and 20 mM KCl (red dot) and 0.13 M GuHCl and 200 mM KCl (cyan dots). Fitting the mean FRET efficiency using an exponential curve results in refolding times of  $681 \pm 609$  ms,  $509 \pm 244$  ms and  $428 \pm 323$  ms, respectively.

ate state is independent of the salt concentration, then refolding from this point onwards to the final conformation has to be salt dependent.

#### 7.2.4 GroEL mediated conformational changes of DM-MBP

From literature it is known that the chaperone/co-chaperone complex GroEL/GroES change the conformations of DM-MBP [Sharma et al., 2008]. To investigate the effect of GroEL on the conformation of DM-MBP, we tested first how GroEL changes the FRET efficiency in an equilibrium measurement.

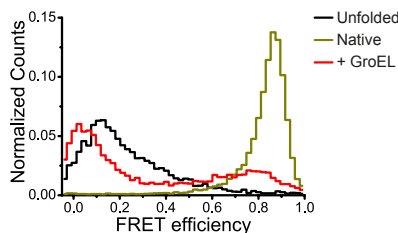


Figure 7.14: DM-MBP measured in equilibrium in the presence of GroEL. The measurement of 50 pM DM-MBP in the presence of 0.13 M GuHCl and 3  $\mu$ M GroEL (red line) is compared with the measurements of 50 pM unfolded DM-MBP in 2 M GuHCl (black line) and the measurement of refolded GuHCl with 0.1 M GuHCl (dark yellow line).

In Figure 7.14, the conformational changes between the folded DM-MBP and the GroEL bound DM-MBP are depicted. Upon addition of GroEL, the FRET efficiency shifts from a high FRET peak to two populations, one with a low FRET mean value at approximately 0.05 and one with a high FRET mean value at approximately 0.8. The low FRET peak is shifted to slightly smaller FRET values compared to the unfolded DM-MBP and the high FRET peak is a bit lower than the spontaneously refolded DM-MBP. The distances are calculated using PDA as  $d = 50$  Å with a  $\sigma = 7$  Å for the higher FRET state and as  $d = 84$  Å with a  $\sigma = 15$  Å for the lower FRET population (Table 7.2). The second width of the distribution

is again very broad and corresponds to multiple subconformations. Thus, we conclude that GroEL unfolds a fraction of DM-MBP to a larger degree than GuHCl is able to do and the other fraction changes the conformation resulting in a slightly wider distance between the two labeling positions. These results are in line with the previously published data for the used DM-MBP mutant [Sharma et al., 2008].

Table 7.2: Distances calculated using PDA for DM-MBP with GroEL. DM-MBP (50 pM) was measured in the presence of 0.13 M GuHCl and 3  $\mu$ M GroEL. The photons of a burst were divided into bins of 1 ms, summed up in a FRET histogram, and fitted using a double-Gaussian model. With photon distribution analysis (PDA), the distance  $d$  between donor and acceptor, the corresponding width  $\sigma$  and the relative weights of the different populations were calculated.

	Subpopulation			Subpopulation			Goodness of the fit
	$d$ [Å]	$\sigma$ [Å]	%	$d$ [Å]	$\sigma$ [Å]	%	$\chi^2$
+ GroEL	50	7	35.5	84	15	64.5	3.6

Next, the temporal progress of refolding in the presence of GroEL was investigated by using microfluidics. DM-MBP was again denatured in 3 M GuHCl, diluted to a final GuHCl concentration of 1.8 M in a buffer containing 20 mM KCl and 0.001 % Tween20 and, then, connected to the sample inlet of the microfluidic device. The buffer, connected to the buffer inlets, contained 20 mM KCl, 0.001 % Tween20 and 3.25  $\mu$ M GroEL, which resulted after mixing in a final GroEL concentration of 3  $\mu$ M. The GuHCl concentration was again 0.13 M after mixing.

The FRET efficiency of the DM-MBP was determined 33 ms after mixing as  $\sim 0.6$  (Figure 7.15, black line). This is a similar value as the one detected in measurements without GroEL (Figure 7.12B, black line). Therefore, the GroEL is not bound, which is in line with the timescale of GroEL binding measured with a halftime of  $\sim 100$  ms [Sharma et al., 2008].

For comparison the time for mixing is estimated as the following: The channel in the mixing point is 40  $\mu$ m wide. The solutions are combined 1 to 12. Therefore, the width of the middle stream is approximately 3  $\mu$ m. Due to the fact that the buffer is mixed from both sides with the sample stream, the GroEL and ATP only have to diffuse half of the way, i.e. 1.5  $\mu$ m. The diffusing coefficient for ATP can be approximated as  $1 \cdot 10^{-5} \frac{\text{cm}^2}{\text{s}}$  [Wang et al., 2012] and for GroEL as  $560 \cdot 10^{-9} \frac{\text{cm}^2}{\text{s}}$  [Lakowicz, 2006]. With  $\tau_D = \frac{\omega^2}{4D}$ , the time the molecule diffuses in the sample stream can be approximated as 0.5 ms for ATP and 10 ms for GroEL. Thus, mixing of GroEL is much faster than binding found in literature and our first measurement timepoint.

After 50 ms (Figure 7.15, red line), an additional population with a low FRET efficiency value appears. Two populations are detectable, one at lower FRET values, which is induced by binding of GroEL, and the second population at the same FRET efficiency as detected in the measurements in the absence of GroEL (Figure 7.12B, red line).

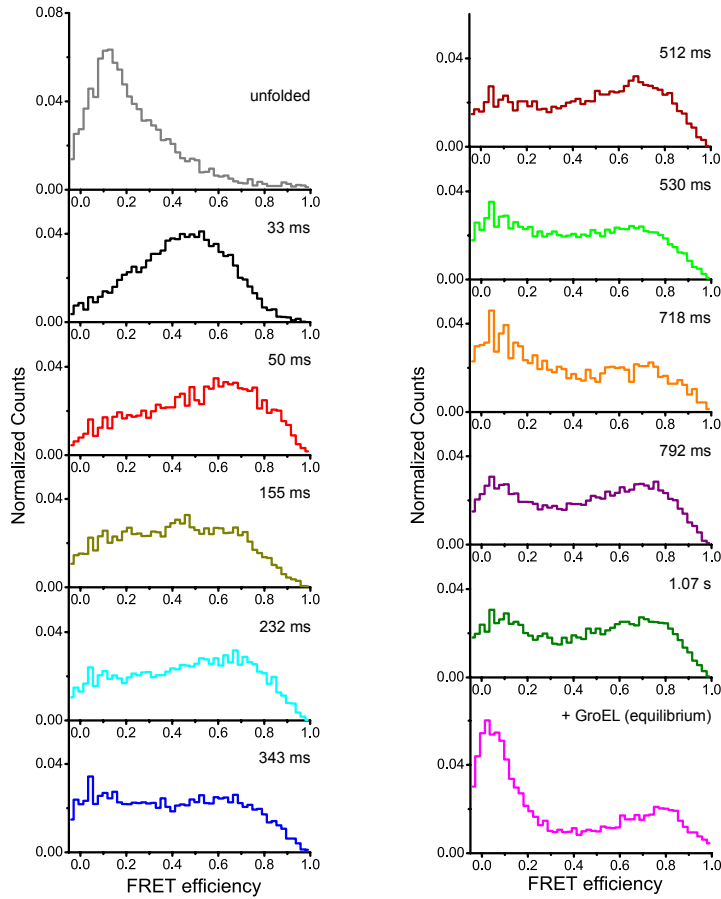


Figure 7.15: Timescale of the refolding kinetic of DM-MBP mediated by GroEL. DM-MBP was unfolded in 3 M GuHCl. The GuHCl concentration was diluted to 1.8 M and then mixed in the microfluidic device 1 to 12 with a buffer containing 20 mM KCl, 0.001 % Tween20 and 3.25  $\mu\text{M}$  GroEL (after mixing 3  $\mu\text{M}$  GroEL) to a final concentration of 0.13 M GuHCl. The concentration of DM-MBP as to be 15 pM after mixing.

To further investigate the binding of GroEL, the measurements after 33 ms, 50 ms, 155 ms and 232 ms were analyzed with fluorescence correlation spectroscopy (FCS). In Figure 7.16 the four autocorrelation functions are depicted. Due to the fact that the measurements were done with two different flow rates, only the measurement after 33 ms and 155 ms or 50 ms and 232 ms can be easily compared. 33 ms and 50 ms after mixing the DM-MBP diffuses faster than 155 ms and 232 ms after mixing, respectively, indicating a binding of GroEL faster than 155 ms. For a detailed analysis, the FCS curves were fitted with the correlation function with flow (Equation (3.29)). The diffusing coefficients were calculated as 147.5  $\frac{\mu\text{m}^2}{\text{s}}$  for 33 ms, 108,4  $\frac{\mu\text{m}^2}{\text{s}}$  for 50 ms, 76.5  $\frac{\mu\text{m}^2}{\text{s}}$  for 155 ms and 82.6  $\frac{\mu\text{m}^2}{\text{s}}$  for 232 ms. Thus, the diffusing coefficient changes around 50 ms after mixing, which is a hint for binding of GroEL.

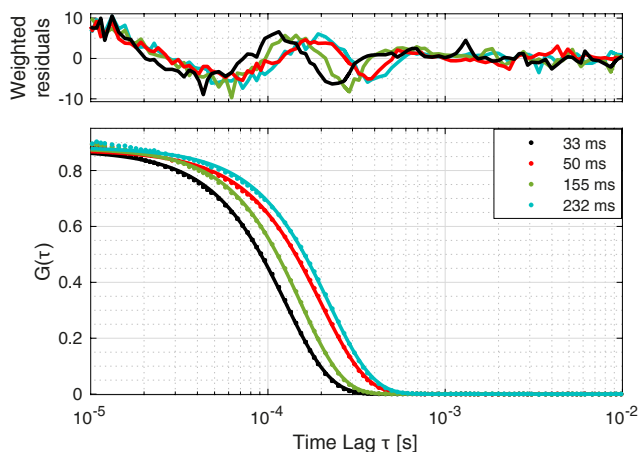


Figure 7.16: FCS curves of DM-MBP mixed with GroEL. DM-MBP was unfolded in 3 M GuHCl. The GuHCl concentration was diluted to 1.8 M and then mixed in the microfluidic device 1 to 12 with a buffer containing 20 mM KCl, 0.001 % Tween20 and 3.25  $\mu\text{M}$  GroEL (after mixing 3  $\mu\text{M}$  GroEL) to a final concentration of 0.13 M GuHCl. The concentration of DM-MBP was chosen as 15 pM after mixing. FCS autocorrelation was performed 33 ms, 50 ms, 155 ms and 232 ms after mixing. The diffusing coefficients were calculated as 147.5  $\frac{\mu\text{m}^2}{\text{s}}$  for 33 ms, 108,4  $\frac{\mu\text{m}^2}{\text{s}}$  for 50 ms, 76.5  $\frac{\mu\text{m}^2}{\text{s}}$  for 155 ms and 82.6  $\frac{\mu\text{m}^2}{\text{s}}$  for 232 ms.

After binding the FRET histogram changes. The amplitude of the low FRET population is increased up to  $\sim 300$  ms and the FRET efficiency value decreases over time. The high FRET population stays at its FRET efficiency value. From 343 ms onwards, the FRET efficiency is stable over time and does not change anymore. To analyze the changes in a more precise way, two Gaussian functions were fitted to the data. The means of the two FRET efficiencies are plotted versus the time after mixing (Figure 7.17). The mean of the high FRET population stays constant over time. The mean of the low FRET population can be fitted using an exponential function and results in a reaction time of  $168 \pm 59$  ms.

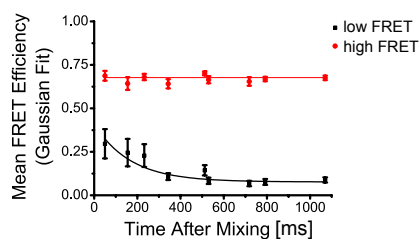


Figure 7.17: Kinetic of the GroEL mediated refolding of DM-MBP. The FRET efficiency curves of Figure 7.15 were fitted using two Gaussian functions. The two mean FRET efficiencies of the fit and the corresponding standard error are plotted versus the time after mixing for DM-MBP refolded in 0.15 M GuHCl and 20 mM KCl. The low FRET population was fitted using an exponential curve resulting in kinetic times of  $168 \pm 59$  ms.

Compared to the equilibrium measurement of DM-MBP with GroEL, the FRET populations are broader and molecules can be detected between the two main peaks. This could be

because of interchanging molecules between the two FRET populations or more likely due to a the low number of photons. The applied flow decreases the time the molecule spends in the focus and, thus, the number of photons is decreased.

In summary, the binding of GroEL to DM-MBP happens on a timescale of approximately 50 ms, which is larger than the diffusing time we calculated of GroEL. After binding, first the low FRET population is filled, which corresponds to unfolded proteins (Figure 7.15). Till approximately 300 ms, the low FRET peak shifts to slightly lower FRET values with a kinetic time of  $168 \pm 59$  ms. From 343 ms onwards, the conformation stays stable over time.

## 7.2.5 GroEL and GroES mediated refolding of DM-MBP

Following the chaperone cycle, next conformational changes of DM-MBP introduced by binding of GroEL and GroES were studied. In literature, it is stated that the GroEL, closed by GroES, assists the caught substrate in folding to its native conformation [Sigler et al., 1998]. The rate of folding was found to be up to 10-times faster in the presence of GroEL, GroES and ATP than for spontaneous folding [Chakraborty et al., 2010]. To analyze changes in the refolding kinetics with the help of microfluidics, first equilibrium measurements were performed (Figure 7.18).

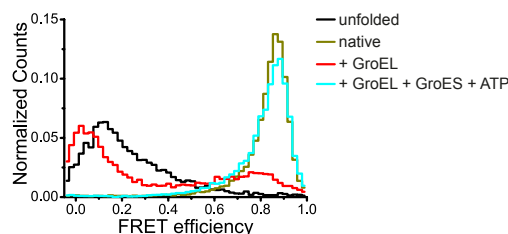


Figure 7.18: DM-MBP measured in equilibrium in the presence of GroEL, GroES and ATP. The measurement of 50 pM refolded DM-MBP in the presence of 0.13 M GuHCl and 3  $\mu$ M GroEL, 6  $\mu$ M GroES and 2 mM ATP (cyan line) is compared with the measurements of 50 pM unfolded DM-MBP in 2 M GuHCl (black line), the measurement of refolded DM-MBP with 0.1 M GuHCl (dark yellow line) and the measurement of DM-MBP in the presence of 0.13 M GuHCl and 3  $\mu$ M GroEL (red line).

Similar to [Sharma et al., 2008], we found that, when GroEL binds to DM-MBP, the FRET efficiency shifts for the majority of DM-MBP molecules to lower FRET values compared to the unfolded, denatured DM-MBP. The addition of GroES and ATP changes the conformation and shifts the FRET efficiency to higher FRET values. This FRET efficiency is equal to the value found for properly folded DM-MBP. Using PDA, we determined the distance for these populations as  $d = 45 \text{ \AA}$  with  $\sigma = 3 \text{ \AA}$  and as  $d = 48 \text{ \AA}$  with  $\sigma = 7 \text{ \AA}$  (Table 7.3). The first population is the same as for the native DM-MBP and the second population is needed to fit the fraction of proteins that are in the intermediate state and not fully folded. This is in line with the fact that only a small fraction of substrate proteins leave the chaperone cycle per time properly folded [Sigler et al., 1998].

Table 7.3: Distances calculated using PDA for DM-MBP with GroEL, GroES and ATP. DM-MBP (50 pM) was measured in the presence of 0.13 M GuHCl and 3  $\mu$ M GroEL, 6  $\mu$ M GroES and 2 mM ATP. The photons of a burst were divided into bins of 1 ms, summed up in a FRET histogram, and fitted by a double-Gaussian model. With photon distribution analysis (PDA), the distance  $d$  between donor and acceptor, the corresponding width  $\sigma$  and the relative weights of the different populations were calculated.

	Subpopulation			Subpopulation			Goodness of the fit
	$d$ [Å]	$\sigma$ [Å]	%	$d$ [Å]	$\sigma$ [Å]	%	
+ GroEL + GroES + ATP	45	3	61.0	48	7	39.0	1.7

To analyze the function of GroEL, GroES and ATP complex on the folding kinetics in more details, microfluidic measurements were performed. Therefore, DM-MBP was denatured in 3 M GuHCl and then diluted to 1.8 M GuHCl in buffer containing 20 mM KCl and 0.001 % Tween20. This solution was then connected to the sample inlet of the microfluidic device. The buffer inlets were each connected to a buffer solution containing 20 mM KCl, 0.001 % Tween20, 3.25  $\mu$ M GroEL, 6.5  $\mu$ M GroES and 10.85 mM ATP. This results in a final concentration of 3  $\mu$ M GroEL, 6  $\mu$ M GroES, 10 mM ATP and 0.13 M GuHCl after mixing.

The FRET efficiency histograms measured at different time points after mixing are depicted in Figure 7.19. After 33 ms, the FRET efficiency histogram is similar to that in the absence of GroEL, GroES and ATP. This can be explained by the fact that binding of GroEL takes longer than 33 ms. Furthermore, it can be seen that already after 50 ms a FRET efficiency of  $\sim 0.65$  was reached. This FRET value was identified in the measurements without a chaperone as the intermediate state, which was reached after approximately 500 ms without a chaperone. Thus, GroEL, GroES and ATP speed up the fast collapse to the intermediate state by a factor of 10.

After 232 ms, the FRET efficiency starts shifting to higher values and gets asymmetric. Between 232 ms and 343 ms, the mean FRET efficiency is  $\sim 0.75$ . From there onwards the mean FRET efficiency value is stable at 0.8. The reason for this observation might be that a second peak at approximately 0.85 is gradually populated. This peak would correspond to the completely folded DM-MBP. After 1.07 s, the second population is clearly visible.

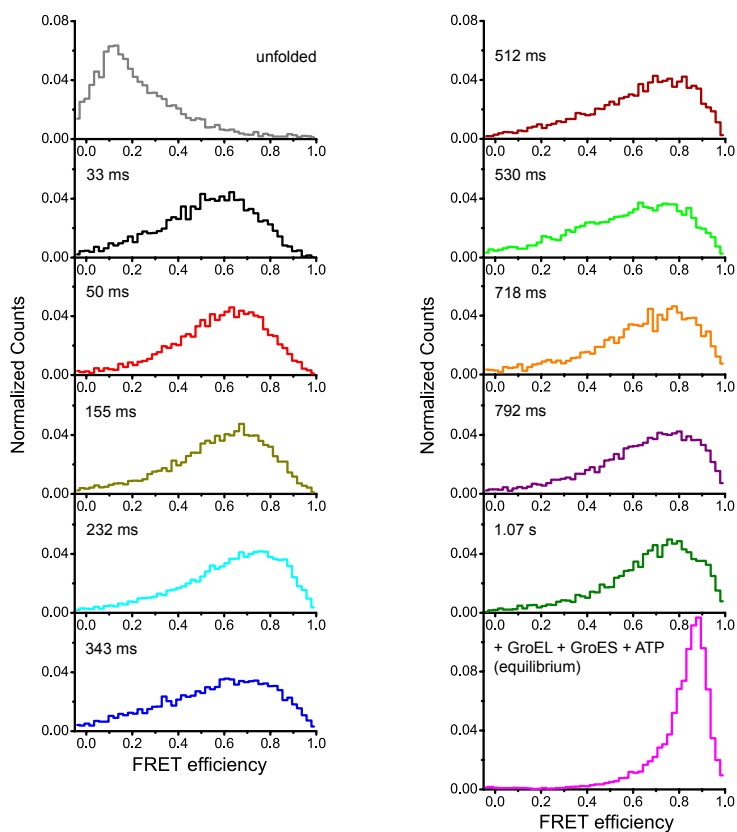


Figure 7.19: Timescale of the refolding kinetics of DM-MBP mediated by GroEL, GroES and ATP. DM-MBP was unfolded in 3 M GuHCl. The GuHCl concentration was diluted to 1.8 M and then mixed in the microfluidic device 1 to 12 with a buffer containing 20 mM KCl, 3.25  $\mu$ M GroEL, 6.5  $\mu$ M GroES, 10.85 mM ATP and 0.001 % Tween20 (after mixing 3  $\mu$ M GroEL, 6  $\mu$ M GroES and 10 mM ATP) to a final concentration of 0.13 M GuHCl. The concentration of DM-MBP was chosen as 15 pM after mixing.

To further analyze the kinetics, the FRET histograms of the different time points after mixing were fitted using Gaussian functions. For the first three measurements, until 155 ms after mixing, only two Gaussian functions were needed to approximate the FRET efficiency histogram. For the remaining measurements, three Gaussian functions were used. For estimating the mean FRET efficiency values, all FRET efficiency histograms were fitted independently and the mean of the FRET values was determined. The FRET efficiency of the first population was determined as 0.47, the second as 0.71, which is similar to the collapsed state, and the last one as 0.87, which corresponds to the folded state. Next, the FRET efficiency histograms were fitted a second time and the mean FRET efficiency value were fixed and the width and the amplitude of the Gaussian were kept free for fitting. The resulting amplitude of the Gaussian functions were plotted versus the time after mixing (Figure 7.20). The individual populations can be approximated using a linear function. The slope of the curves was determined as  $-4.48 \cdot 10^{-6} \pm 2.43 \cdot 10^{-6}$  for the low FRET population,  $-6.93 \cdot 10^{-7} \pm 2.44 \cdot 10^{-6}$  for the intermediate FRET population and  $3.07 \cdot 10^{-6} \pm 1.36 \cdot 10^{-6}$  for the high FRET state. The standard errors were too large to be significant. However, we suggest that the low

FRET population shifts depending on the time after mixing to the folded population and the collapsed population stays on the measured time scale independent.

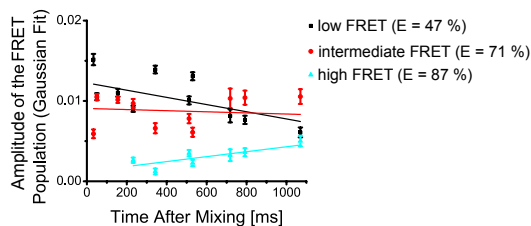


Figure 7.20: Kinetic of the GroEL, GroES and ATP mediated refolding of DM-MBP. The FRET efficiency curves of Figure 7.19 were fitted using two or three Gaussian functions. The mean FRET efficiency values were fixed to 0.47, 0.71 and 0.87. The amplitude of the mean FRET efficiencies of the fit and the corresponding standard error are plotted versus the time after mixing for DM-MBP refolded in 0.15 M GuHCl and 20 mM KCl. The three FRET population were fitted using a linear function resulting in a slope of  $-4.48 \cdot 10^{-6} \pm 2.43 \cdot 10^{-6}$ ,  $-6.93 \cdot 10^{-7} \pm 2.44 \cdot 10^{-6}$  and  $3.07 \cdot 10^{-6} \pm 1.36 \cdot 10^{-6}$ , respectively.

Thus, the chaperone system GroEL in combination with its co-chaperone binds between 33 ms and 50 ms and speeds up the folding to a collapsed state by a factor of 10. Furthermore, GroEL-GroES shifts the DM-MBP from an unfolded, i.e. low FRET, conformation to a folded, i.e. more condensed, conformation starting 232 ms after mixing and, after 1.07 s, a fraction of DM-MBP molecules is already, properly folded in its native conformation.

### 7.3 Discussion and Outlook

Microfluidic opens up a new dimension in spFRET measurements. As a first application, the time dependent refolding conformations of a double-mutant of the maltose binding protein (DM-MBP) were studied. DM-MBP consists of two domains, the N-terminal and the C-terminal domain, and a deep cleft in between, which is the maltose binding site [Spurlino et al., 1991].

DM-MBP can fold on its own or the refolding can be mediated by a chaperone system called GroEL/GroES. Using microfluidics, it is possible to analyze the timescale of the conformation changes introduced upon refolding. For spontaneous refolding of a denatured DM-MBP, we detected a GuHCl concentration dependency. After denaturation, the GuHCl concentration was diluted. The final GuHCl concentration determined the refolding kinetics of the protein. We detected that the N-terminal domain of DM-MBP changes from an unfolded conformation to an intermediate conformation within the timescale that was within the measurement range. In the presence of 0.15 M GuHCl, the folding to an intermediate state took 800 ms. By decreasing the concentration of GuHCl to 0.13 M, the folding appeared already within approximately 500 ms. Thus, the timing of the folding is highly dependent on the GuHCl concentration during the refolding.

Furthermore, previous studies state that the time for proper refolding depends on the concentration of KCl. In the presence of 200 mM KCl instead of 20 mM KCl, in literature it was shown that the folding takes two times longer [Chakraborty et al., 2010]. Moreover, with the

help of microfluidic experiments, we were able to detect that the time for the first refolding step, from the unfolded to an intermediate state, is independent of the salt concentration. Combining our results with those from [Chakraborty et al., 2010], we conclude that the first collapse to the intermediate state is independent of the salt concentration, but the folding time needed from this intermediate state to the folded conformation increases in the presence of higher salt concentrations.

In addition, the effect of GroEL alone and in the presence of GroES was analyzed. GroEL was found to bind within approximately 50 ms to DM-MBP. After 50 ms, a fraction of DM-MBP molecules are folded. In the first 300 ms, the DM-MBP molecules in the collapsed state get slightly more compact and then stay in this conformation. Upon addition of GroEL, GroES and ATP, which is required for GroES binding, the kinetics change. Until GroEL binds, the conformation is equal to the measurements without GroEL. After GroEL binding also GroES seems to interact with the complex, because the conformation differs from the measurements of DM-MBP bound only to GroEL. The binding of GroEL-GroES was found to speed up the initial collapse of the DM-MBP from the unfolded to the intermediate conformation by a factor of 10. Afterwards, GroEL-GroES shifts the unfolded DM-MBP more and more to a folded state until, after approximately 1 s, molecules begin to reach their properly folded conformation. Thus, the GroEL-GroES chaperone complex shifts the DM-MBP faster in the intermediate state and does not first unfold parts of the DM-MBP molecules. Afterwards, GroEL-GroES folds the unfolded molecules to their finally folded conformation.

Here, we showed that a microfluidic measurement needs a lot of producing steps. The design of the microfluidic device, which was chosen, consists of two different types of channels with different heights, one for the sample and the other one for the gas channels. These two heights made it necessary to produce a two layer structured wafer. The process for the wafer production is for one layer: spin coating the wafer with a layer of SU 8-100 photoresist, baking it, exposing the structure, baking it again and then finally developing the photoresist. This protocol makes a lot of tests necessary before starting the process. The exact thickness of the SU 8-100 layer was measured on a scanning electron microscope (SEM). A test structure was used to determine the optimal excitation dose of the used maskaligner by testing the structure with light microscopy and SEM. The second layer introduces additional problems such as air bubbles in the SU 8-100 between the structures of the first layer. To get rid of these air bubbles, a desiccator was found to be the best solution. Additionally, the baking steps of the second layer has to be done carefully to avoid stress in the structure of the first layer. In summary, processing of a multilayer wafer needs the fine tuning of all possible parameters, but when the protocol for the wafer is once optimized, producing the next wafer can be done easily.

Next, the actual PDMS devices have to be produced and need to be calibrated. For reproducible measurements, a feedback based flow control system is needed to adjust the flow independently of small aggregates and air bubbles, which requires higher pressure for a short period of time. With the help of a known sample, the relationship between the externally applied flow and the velocity of the solution in the device can be calculated. By knowing the distance between mixing and measuring point, the externally applied flow and the relationship between flow and velocity, the time after mixing can be calculated. This makes it possible to work in a reproducible way and compare different measurements, even in different devices.

Microfluidic is a great tool to study protein folding on a fast timescale. Fast collapse of a protein or conformational changes due to mixing with different interaction partners opens up a wide range of interesting questions that can now be addressed. One of them, related to

the above described proteins, would be how fast BAP changes the conformation of BiP. Is it possible to monitor the opening of the lid of BiP upon ATP binding?

To further improve the microfluidic tool, a more precised microscope table is needed. Due to the unprecise microscope table, only five positions in the device can be measured. The first position is after 350  $\mu\text{m}$  after mixing, which can be found in the ocular of the microscope and is visible as the place where the distance to the side walls is similar to the distance to the beginning of the measurement channel. In addition, the distance of one, two, three and four millimeter after mixing can be adjusted. A microscope table with a micrometer screw would increase the accuracy and precision of possible positions for measurements. This would have multiple positive effects. With only one flow rate combination, multiple time points after mixing, more than five, can be measured. Therefore, the time between two data points can be chosen as always the same and a 1 to 19 dilution can be performed without the loose of half of the data points, due to the fact that only one batch of flow rates is needed for enough statistics.

Additionally, a different design of the microfluidic device would make a few critical steps in producing the wafer more easy and allow to observe a protein over longer timescales. The edges should be round to avoid trapping of air bubbles. Furthermore, the crossmarks for the alignment of the two structures, the sample and gas channels, in the process of producing a wafer, need to be changed to make the alignment more precise. This could result in a wafer with four useable positions. The used wafers for this work only have two usable designs each (Figure 7.5). The other positions on the wafer have a connection between the sample and gas channels. Another point, which could be optimized in the design of the device, is the length of the channel for the measurements. If it is longer, longer timescales can be observed.

In summary, microfluidics is a highly promising addition to equilibrium spFRET measurements to understand the folding process of proteins. Nevertheless, it needs a lot of controls to produce the microfluidic devices in a reproducible way and perform reliable measurements. The calibration of the devices has to be done carefully for each new wafer. However, microfluidics in combination with spFRET provide a measurement system that allows to analyze conformational changes in proteins induced by changing the environment conditions by mixing.

## 8 Summary

Different chaperone systems were studied with respect to their conformational changes and interactions on a single-molecule level. Two different types of microscopes were used in combination with single-pair Förster Resonance Energy Transfer (spFRET). On the one side, a confocal setup with a combination of 'pulsed interleaved excitation' (PIE) and 'multiparameter fluorescence detection' (MFD) was used to study snapshots of the protein diffusing in solution. On the other side, total internal reflection fluorescence (TIRF) microscopy was applied to study the dynamics and conformational changes of a single-molecule over time introduced by interactions with different cofactors.

The first chaperon system that was studied, was the heat shock protein 70 (Hsp70) in the human endoplasmic reticulum (ER). This protein, called BiP, consists of two domains, the nucleotide binding domain (NBD) and the substrate binding domain (SBD) with a  $\alpha$ -helical lid that can open and close the binding pocket. BiP changes its conformation upon addition of a nucleotide. Nevertheless, to control the wide range of sometimes contradictory functions like protein folding and degradation, BiP interacts with different co-chaperones. One of these co-chaperones is a nucleotide exchange factor (NEF), the BiP Associated Protein BAP. Here, we analyzed the function of BAP as a NEF. BAP interacts with the NBD of BiP and introduces conformational changes in BiP. In the ADP and the nucleotide free state, it interacts stably, but in the presence of ATP, only a transient interaction was detected. The transient interaction of BAP with BiP is mediated by the N-terminal domain of BAP. This domain was identified together with the lid of BiP to separate the NBD and SBD from each other. Furthermore, the assumption arises that BAP mediates an open nucleotide binding pocket, which increases the release of the nucleotides. This would speed up the nucleotide cycle, as is expected for a NEF. Furthermore, the addition of a substrate reveals that BAP and the substrate compete with each other. In summary, BAP is an important interaction partner for BiP and essential for mediating the nucleotide cycle of BiP.

The Hsp70 is known to catch unfolded proteins and then hands them over to the next interaction partner in the folding machinery, the Hsp90. This process is mediated by the co-chaperone Sti1. Sti1 consist of two modules, which are flexible connected by a linker. The first module consist of an aspartate and proline rich (DP) and a tetratricopeptide repeats (TPR) domain, the DP1 and TPR1 domains. The second module comprise two TPR domains, the TPR2A and the TPR2B domain, and the DP2 domain. Hsp70 has two possible binding positions, one in the TPR1 domain and one in the TPR2B domain. This domain is next to the TPR2A domain, which is responsible for binding Hsp90. By using spFRET methods, it was found that Hsp70 prefers to bind to the TPR1 domain when Hsp90 is bound to Sti1. Due to the dynamics in the linker region, the two modules come close together and the Hsp70 can interchange the binding domain from TPR1 to TPR2B. We speculate that in the case of a bound substrate, this can be transferred to the close by Hsp90. To free up the binding domain TPR2B again, the Hsp70 is released or transferred back to the TPR1 binding domain and Sti1 opens up. Due to the low affinity of Hsp70 to the TPR1 binding domain, remaining Hsp70 is released and the cycle can start again. Sti1 was detected to show

dynamics on its own, but upon binding of Hsp70, Hsp90 or both, the percentage of dynamic molecules detected by spFRET TIRF measurements increases. Thus, Sti1 has the important role binding Hsp70 and Hsp90, dynamically connect the two chaperones as a scaffold and assisting in the substrate transfer.

Another chaperone system studied here, is the Hsp60 in bacteria, GroEL. GroEL consists of two identical rings stacked together. Each ring forms a cavity wherein unfolded proteins are encapsulated and can fold. GroEL on its own does not mediate proper folding, but in combination with GroES unfolded proteins are assisted in folding. When a substrate is captured, the ring structure of GroEL can be closed by binding a GroES, which is mediated by ATP binding to GroEL. In this chaperone cage, the substrate is encapsulated for several seconds and can reach its final conformation. As a substrate we chose a double-mutant of the maltose binding protein (DM-MBP). This protein is not a natural substrate, because it can fold without assistance. However, interaction with GroEL and GroES, increases the folding. The equilibrium conformations of DM-MBP, without and with GroEL are already known from literature, how the conformation changes over time is not studied till now. To analyze this changes, a microfluidic approach was implemented. This requires that microfluidic devices were produced, including the required wafer, and then calibrated for the flow. In combination with microfluidics and MFD-PIE, it was possible to detect conformational changes on a timescale from 33 ms to 1.07 s. DM-MBP was found to collapse on this timescale to an intermediate state. The folding step from the intermediate state to the finally folded state takes much longer than 1 s and, thus, could not be monitored with the used microfluidic design. Furthermore, it was found that the refolding of DM-MBP to the intermediate state depends on the GuHCl concentration, the denature reagent, and not on the KCl concentration, which maybe changes the time from the intermediate to the final conformation. The addition of GroEL starts shifting a fraction of DM-MBP molecules to an unfolded and the other fraction to a slightly different compacter state than in the measurements without GroEL. The shifting starts on the same timescale as binding of GroEL occurs. When GroES is bound to the complex, DM-MBP folds in a similar way than spontaneous folding of DM-MBP occurs, to the intermediate state, but the timescale increased by 10 times. Thus, DM-MBP is not first unfolded and then refolded like expected from the measurements in the presence of only GroEL. From the intermediate state, the DM-MBP gets more condensed until approximately 1 s after mixing, then a fraction of molecules are totally folded. Thus, with the help of microfluidics, it was found that folding of DM-MBP depends on the GuHCl concentration and the first collapse to an intermediate state is independent of the KCl concentration. Adding GroEL to DM-MBP unfolds a fraction of the substrate and the rest changes slightly the conformation on a timescale of approximately 300 ms. When GroES is additionally bound to the complex, DM-MBP first collapses to the intermediate state and then proper folding starts around 1 s after mixing.

To further analyze the studied chaperone systems of this theses, multiple still unknown interactions could be studied. For example, it would be interesting to add different co-factors to the measurements. For the measurements with BiP and BAP, the Hsp40, also known as J-protein, could be one interesting interaction partner. A competition experiment by using Hsp40 and BAP at the same time in microfluidic devices on the MFD-PIE setup would reveal further insights into the function of BiP in a more native situation. Furthermore, the addition of a labeled substrate to the measurements with Sti1 would result in a three-color experiment, where the transfer of the substrate from one Hsp to the other could be visualized. For studying the DM-MBP refolding in more details, the timescale that is detectable in the microfluidic measurements needs to be increased and the time intervals between two

measurements should be changed to equal time steps. For this propose, a new microfluidic device has to be designed with a longer detection area and the microscope stage has to be exchanged to one with  $\mu\text{m}$  precision.

In summary, different chaperone systems were analyzed according to their interaction with nucleotide exchange factors, co-chaperones and the conformational changes they introduce in a substrate. By establishing a microfluidic platform as an add-on for the MFD-PIE setup, the timescale of conformational changes can be additionally studied by spFRET. Overall, spFRET in combination with MFD-PIE and single-molecule TIRF microscopy allows the analysis of conformational changes in a precise way and collects information that would be hidden in ensemble measurements. Thus, spFRET is an important tool to study the conformation of chaperones and their interaction with co-factors and substrates.



# Bibliography

- Alder, N. N., Shen, Y., Brodsky, J. L., Hendershot, L. M., and Johnson, A. E. (2005). The molecular mechanisms underlying BiP-mediated gating of the Sec61 translocon of the endoplasmic reticulum. *The Journal of Cell Biology*, 168(3):389–399.
- Alvira, S., Cuellar, J., Röhl, A., Yamamoto, S., Itoh, H., Alfonso, C., Rivas, G., Buchner, J., and Valpuesta, J. M. (2014). Structural characterization of the substrate transfer mechanism in Hsp70/Hsp90 folding machinery mediated by Hop. *Nat Commun*, 5.
- Antonik, M., Felekyan, S., Gaiduk, A., and Seidel, C. A. (2006). Separating structural heterogeneities from stochastic variations in fluorescence resonance energy transfer distributions via photon distribution analysis. *J Phys Chem B*, 110(13):6970–8.
- Anttonen, A.-K., Mahjneh, I., Hamalainen, R. H., Lagier-Tourenne, C., Kopra, O., Waris, L., Anttonen, M., Joensuu, T., Kalimo, H., Paetau, A., Tranebjaerg, L., Chaigne, D., Koenig, M., Eeg-Olofsson, O., Udd, B., Somer, M., Somer, H., and Lehesjoki, A.-E. (2005). The gene disrupted in Marinesco-Sjögren syndrome encodes SIL1, an HSPA5 cochaperone. *Nat Genet*, 37(12):1309–1311.
- ATTO-TEC GmbH (04.07.2016). <https://www.atto-tec.com/>.
- Axelrod, D. (1981). Cell-substrate contacts illuminated by total internal reflection fluorescence. *The Journal of Cell Biology*, 89(1):141–145.
- Bagshaw, C. (2001). ATP analogues at a glance. *J Cell Sci*, 114(Pt 3):459–60.
- Baum, L. E. and Petrie, T. (1966). Statistical inference for probabilistic functions of finite state Markov chains. *Ann. Math. Statist.*, 37(6):1554–1563.
- Behnke, J., Feige, M. J., and Hendershot, L. M. (2015). BiP and its nucleotide exchange factors Grp170 and Sil1: Mechanisms of action and biological functions. *Journal of Molecular Biology*, 427(7):1589 – 1608. Molecular Chaperones and Protein Quality Control (Part I).
- Blond-Elguindi, S., Fourie, A. M., Sambrook, J. F., and Gething, M. J. (1993). Peptide-dependent stimulation of the ATPase activity of the molecular chaperone BiP is the result of conversion of oligomers to active monomers. *Journal of Biological Chemistry*, 268(17):12730–5.
- Born, M. and Oppenheimer, R. (1927). Zur Quantentheorie der Molekeln. *Annalen der Physik*, 389(20):457–484.
- Boukobza, E., Sonnenfeld, A., and Haran, G. (2001). Immobilization in surface-tethered lipid vesicles as a new tool for single biomolecule spectroscopy. *The Journal of Physical Chemistry B*, 105(48):12165–12170.

- Brinker, A., Scheuffer, C., von der Mülbe, F., Fleckenstein, B., Herrmann, C., Jung, G., Moarefi, I., and Hartl, F. U. (2002). Ligand discrimination by TPR domains: Relevance and selectivity of EEVD-recognition in Hsp70·Hop·Hsp90 complexes. *Journal of Biological Chemistry*, 277(22):19265–19275.
- Buck, T. M., Wright, C. M., and Brodsky, J. L. (2007). The activities and function of molecular chaperones in the endoplasmic reticulum. *Semin Cell Dev Biol*, 18(6):751–61.
- Chakraborty, K., Chatila, M., Sinha, J., Shi, Q., Poschner, B. C., Sikor, M., Jiang, G., Lamb, D. C., Hartl, F. U., and Hayer-Hartl, M. (2010). Chaperonin-catalyzed rescue of kinetically trapped states in protein folding. *Cell*, 142(1):112 – 122.
- Chen, S. and Smith, D. F. (1998). Hop as an adaptor in the heat shock protein 70 (Hsp70) and Hsp90 chaperone machinery. *Journal of Biological Chemistry*, 273(52):35194–35200.
- Chung, K. T., Shen, Y., and Hendershot, L. M. (2002). BAP, a mammalian BiP-associated protein, is a nucleotide exchange factor that regulates the ATPase activity of BiP. *J Biol Chem*, 277(49):47557–63.
- Condon, E. U. (1928). Nuclear motions associated with electron transitions in diatomic molecules. *Phys. Rev.*, 32:858–872.
- Cyr, D. M. (2008). Swapping nucleotides, tuning Hsp70. *Cell*, 133(6):945–7.
- Daniel, S., Söti, C., Csermely, P., Bradley, G., and Blatch, G. L. (2007). *Networking of Chaperones by Co-Chaperones*, chapter Hop: An Hsp70/Hsp90 Co-Chaperone That Functions Within and Beyond Hsp70/Hsp90 Protein Folding Pathways, pages 26–37. Springer New York, New York, NY.
- Doyle, S. M., Genest, O., and Wickner, S. (2013). Protein rescue from aggregates by powerful molecular chaperone machines. *Nat Rev Mol Cell Biol*, 14(10):617–629.
- Eggeling, C., Berger, S., Brand, L., Fries, J. R., Schaffer, J., Volkmer, A., and Seidel, C. A. (2001). Data registration and selective single-molecule analysis using multi-parameter fluorescence detection. *J Biotechnol*, 86(3):163–80.
- Feige, M. J., Groscurth, S., Marcinowski, M., Shimizu, Y., Kessler, H., Hendershot, L. M., and Buchner, J. (2009). An unfolded CH1 domain controls the assembly and secretion of IgG antibodies. *Molecular Cell*, 34(5):569 – 579.
- Feldman, D. E. and Frydman, J. (2000). Protein folding in vivo: the importance of molecular chaperones. *Current Opinion in Structural Biology*, 10(1):26 – 33.
- Förster, T. (1948). Zwischenmolekulare Energiewanderung und Fluoreszenz. *Annalen der Physik*, 437(1-2):55–75.
- Franck, J. and Dymond, E. G. (1926). Elementary processes of photochemical reactions. *Trans. Faraday Soc.*, 21:536–542.
- Gansen, A., Valeri, A., Hauger, F., Felekyan, S., Kalinin, S., Tóth, K., Langowski, J., and Seidel, C. A. M. (2009). Nucleosome disassembly intermediates characterized by single-molecule FRET. *Proceedings of the National Academy of Sciences*, 106(36):15308–15313.
- Hartl, F. U., Bracher, A., and Hayer-Hartl, M. (2011). Molecular chaperones in protein folding and proteostasis. *Nature*, 475(7356):324–332.

- Hayer-Hartl, M. K., Ewbank, J. J., Creighton, T. E., and Hartl, F. U. (1994). Conformational specificity of the chaperonin GroEL for the compact folding intermediates of alpha-lactalbumin. *The EMBO Journal*, 13(13):3192–3202.
- Hayer-Hartl, M. K., Weber, F., and Hartl, F. U. (1996). Mechanism of chaperonin action: GroES binding and release can drive GroEL-mediated protein folding in the absence of ATP hydrolysis. *The EMBO Journal*, 15(22):6111–6121.
- Hebert, D. N. and Molinari, M. (2007). In and out of the ER: protein folding, quality control, degradation, and related human diseases. *Physiol Rev*, 87(4):1377–408.
- Hernandez, M. P., Sullivan, W. P., and Toft, D. O. (2002). The assembly and intermolecular properties of the Hsp70-Hop-Hsp90 molecular chaperone complex. *Journal of Biological Chemistry*, 277(41):38294–38304.
- Howes, J., Shimizu, Y., Feige, M. J., and Hendershot, L. M. (2012). C-terminal mutations destabilize SIL1/BAP and can cause Marinesco-Sjogren syndrome. *J Biol Chem*, 287(11):8552–60.
- Ichhaporia, V. P., Sanford, T., Howes, J., Marion, T. N., and Hendershot, L. M. (2015). Sil1, a nucleotide exchange factor for BiP, is not required for antibody assembly or secretion. *Molecular Biology of the Cell*, 26(3):420–429.
- Jablonski, A. (1933). Efficiency of anti-stokes fluorescence in dyes. *Nature*, 131:839–840.
- Jablonski, A. (1935). Über den Mechanismus der Photolumineszenz von Farbstoffphosphoren. *Zeitschrift für Physik*, 94(1):38–46.
- Johnson, B. D., Schumacher, R. J., Ross, E. D., and Toft, D. O. (1998). Hop modulates hsp70/hsp90 interactions in protein folding. *Journal of Biological Chemistry*, 273(6):3679–3686.
- Kalinin, S., Felekyan, S., Antonik, M., and Seidel, C. A. (2007). Probability distribution analysis of single-molecule fluorescence anisotropy and resonance energy transfer. *J Phys Chem B*, 111(34):10253–62.
- Kalinin, S., Valeri, A., Antonik, M., Felekyan, S., and Seidel, C. A. M. (2010). Detection of structural dynamics by FRET: A photon distribution and fluorescence lifetime analysis of systems with multiple states. *The Journal of Physical Chemistry B*, 114(23):7983–7995.
- Kampinga, H. H. and Craig, E. A. (2010). The HSP70 chaperone machinery: J proteins as drivers of functional specificity. *Nat Rev Mol Cell Biol*, 11(8):579–92.
- Kapanidis, A. N., Laurence, T. A., Lee, N. K., Margeat, E., and Kong, Xiangxu and Weiss, S. (2005). Alternating-laser excitation of single molecules. *Accounts of Chemical Research*, 38(7):523–533.
- Kim, Y. E., Hipp, M. S., Bracher, A., Hayer-Hartl, M., and Hartl, F. U. (2013). Molecular chaperone functions in protein folding and proteostasis. *Annu Rev Biochem*, 82:323–55.
- Krieger, M., Roos, A., Stendel, C., Claeys, K. G., Sonmez, F. M., Baudis, M., Bauer, P., Bornemann, A., de Goede, C., Dufke, A., Finkel, R. S., Goebel, H. H., Häussler, M., Kingston, H., Kirschner, J., Medne, L., Muschke, P., Rivier, F., Rudnik-Schöneborn, S., Spengler, S., Inzana, F., Stanzial, F., Benedicenti, F., Synofzik, M., Lia Taratuto, A., Pirra, L., Tay, S. K.-H., Topaloglu, H., Uyanik, G., Wand, D., Williams, D., Zerres, K.,

- Weis, J., and Senderek, J. (2013). SIL1 mutations and clinical spectrum in patients with Marinesco-Sjögren syndrome. *Brain*, 136(12):3634–3644.
- Kudryavtsev, V., Sikor, M., Kalinin, S., Mokranjac, D., Seidel, C. A., and Lamb, D. C. (2012). Combining MFD and PIE for accurate single-pair Förster resonance energy transfer measurements. *Chemphyschem*, 13(4):1060–78.
- Lakowicz, J. R., editor (2006). *Principles of Fluorescence Spectroscopy*. Third edition.
- Lee, C.-T., Graf, C., Mayer, F. J., Richter, S. M., and Mayer, M. P. (2012). Dynamics of the regulation of Hsp90 by the co-chaperone Sti1. *The EMBO Journal*, 31(6):1518–1528.
- Lee, Y.-K., Brewer, J. W., Hellman, R., and Hendershot, L. M. (1999). BiP and immunoglobulin light chain cooperate to control the folding of heavy chain and ensure the fidelity of immunoglobulin assembly. *Molecular Biology of the Cell*, 10(7):2209–2219.
- Lemke, E. A., Gambin, Y., Vandelinder, V., Brustad, E. M., Liu, H.-W., Schultz, P. G., Groisman, A., and Deniz, A. A. (2009). Microfluidic device for single-molecule experiments with enhanced photostability. *Journal of the American Chemical Society*, 131(38):13610–13612.
- Levinthal, C. (1969). How to fold graciously. *Mössbaun Spectroscopy in Biological Systems Proceedings*, 67(41):22–24.
- Li, J. and Buchner, J. (2013). Structure, function and regulation of the Hsp90 machinery. *Biomedical Journal*, 36(3):106–117.
- Lindquist, S. and Craig, E. A. (1988). The heat-shock proteins. *Annual Review of Genetics*, 22(1):631–677.
- Lipman, E. A., Schuler, B., Bakajin, O., and Eaton, W. A. (2003). Single-molecule measurement of protein folding kinetics. *Science*, 301(5637):1233–1235.
- Magde, D., Elson, E., and Webb, W. W. (1972). Thermodynamic fluctuations in a reacting system - measurement by fluorescence correlation spectroscopy. *Phys. Rev. Lett.*, 29:705–708.
- Mapa, K., Sikor, M., Kudryavtsev, V., Waegemann, K., Kalinin, S., Seidel, C. A., Neupert, W., Lamb, D. C., and Mokranjac, D. (2010). The conformational dynamics of the mitochondrial Hsp70 chaperone. *Mol Cell*, 38(1):89–100.
- Marcinowski, M., Holler, M., Feige, M. J., Baerend, D., Lamb, D. C., and Buchner, J. (2011). Substrate discrimination of the chaperone BiP by autonomous and cochaperone-regulated conformational transitions. *Nat Struct Mol Biol*, 18(2):150–8.
- Marcinowski, M., Rosam, M., Seitz, C., Elferich, J., Behnke, J., Bello, C., Feige, M. J., Becker, C. F., Antes, I., and Buchner, J. (2013). Conformational selection in substrate recognition by Hsp70 chaperones. *J Mol Biol*, 425(3):466–74.
- Marcion, G., Seigneure, R., Chavanne, E., Artur, Y., Briand, L., Hadi, T., Gobbo, J., Garrido, C., and Neiers, F. (2014). C-terminal amino acids are essential for human heat shock protein 70 dimerization. *Cell Stress and Chaperones*, 20(1):61–72.

- May, G. S., Han, S.-S., and Hong, S.-J. (2005). Characterization of low-temperature SU-8 negative photoresist processing for MEMS applications. *Transactions on Electrical and Electronic Materials*, 6(4):135–139.
- Mayer, M. P. and Bukau, B. (2005). Hsp70 chaperones: cellular functions and molecular mechanism. *Cell Mol Life Sci*, 62(6):670–84.
- McKinney, S. A., Joo, C., and Ha, T. (2006). Analysis of single-molecule FRET trajectories using Hidden Markov Modeling. *Biophysical Journal*, 91(5):1941 – 1951.
- Minsky, M. (1961). Microscopy apparatus.
- Mitra, S. K. and Chakraborty, S. (2011). *Microfluidics and Nanofluidics Handbook: Fabrication, Implementation, and Applications*.
- Morgner, N., Schmidt, C., Beilstein-Edmands, V., Ebong, I.-o., Patel, N., Clerico, E., Kirschke, E., Daturpalli, S., Jackson, S., Agard, D., and Robinson, C. (2015). Hsp70 forms antiparallel dimers stabilized by post-translational modifications to position clients for transfer to Hsp90. *Cell Reports*, 11(5):759–769.
- Müller, B. K., Zaychikov, E., Bräuchle, C., and Lamb, D. C. (2005). Pulsed interleaved excitation. *Biophysical Journal*, 89(5):3508 – 3522.
- Nelson, G. M., Huffman, H., and Smith, D. F. (2003). Comparison of the carboxy-terminal DP-repeat region in the co-chaperones Hop and Hip. *Cell Stress & Chaperones*, 8(2):125–133.
- Nir, E., Michalet, X., Hamadani, K. M., Laurence, T. A., Neuhauser, D., Kovchegov, Y., and Weiss, S. (2006). Shot-noise limited single-molecule FRET histograms: Comparison between theory and experiments . *The Journal of Physical Chemistry B*, 110(44):22103–22124.
- Okumus, B., Wilson, T. J., Lilley, D. M., and Ha, T. (2004). Vesicle encapsulation studies reveal that single molecule ribozyme heterogeneities are intrinsic. *Biophysical Journal*, 87(4):2798 – 2806.
- Otero, J. H., Lizak, B., and Hendershot, L. M. (2010). Life and death of a BiP substrate. *Semin Cell Dev Biol*, 21(5):472–8.
- Press, W. H., Teukolsky, S., Vetterling, W., and Flannery, B. (1992). *Numerical Recipes in C: the art of scientific computing, Second Edition*. Cambridge Univ. Press, New York.
- Qi, R., Sarbeng, E. B., Liu, Q., Le, K. Q., Xu, X., Xu, H., Yang, J., Wong, J. L., Vorvis, C., Hendrickson, W. A., Zhou, L., and Liu, Q. (2013). Allosteric opening of the polypeptide-binding site when an Hsp70 binds ATP. *Nat Struct Mol Biol*, 20(7):900–7.
- Ramachandran, S., Cohen, D. A., Quist, A. P., and Lal, R. (2013). High performance, led powered, waveguide based total internal reflection microscopy. *Scientific Reports*, 3:2133–.
- Richter, K. and Buchner, J. (2006). Hsp90: Twist and fold. *Cell*, 127(2):251 – 253.
- Richter, K., Muschler, P., Hainzl, O., Reinstein, J., and Buchner, J. (2003). Sti1 is a non-competitive inhibitor of the Hsp90 ATPase: Binding prevents the N-terminal dimerization reaction during the ATPase cycle. *Journal of Biological Chemistry*, 278(12):10328–10333.

- Röhl, A., Wengler, D., Madl, T., Lagleder, S., Tippel, F., Herrmann, M., Hendrix, J., Richter, K., Hack, G., Schmid, A. B., Kessler, H., Lamb, D. C., and Buchner, J. (2015). Hsp90 regulates the dynamics of its cochaperone Sti1 and the transfer of Hsp70 between modules. *Nat Commun*, 6.
- Sauer, M., Hofkens, J., and Enderlein, J. (2011). *Handbook of Fluorescence Spectroscopy and Imaging*.
- Scheufler, C., Brinker, A., Bourenkov, G., Pegoraro, S., Moroder, L., Bartunik, H., Hartl, F., and Moarefi, I. (2000). Structure of TPR domain-peptide complexes: Critical elements in the assembly of the Hsp70-Hsp90 multichaperone machine. *Cell*, 101(2):199 – 210.
- Schmid, A. B., Lagleder, S., Gräwert, M. A., Röhl, A., Hagn, F., Wandinger, S. K., Cox, M. B., Demmer, O., Richter, K., Groll, M., Kessler, H., and Buchner, J. (2012). The architecture of functional modules in the Hsp90 co-chaperone Sti1/Hop. *The EMBO Journal*, 31(6):1506–1517.
- Senderek, J., Krieger, M., Stendel, C., Bergmann, C., Moser, M., Breitbach-Faller, N., Rudnik-Schoneborn, S., Blaschek, A., Wolf, N. I., Harting, I., North, K., Smith, J., Muntoni, F., Brockington, M., Quijano-Roy, S., Renault, F., Herrmann, R., Hendershot, L. M., Schroder, J. M., Lochmuller, H., Topaloglu, H., Voit, T., Weis, J., Ebinger, F., and Zerres, K. (2005). Mutations in SIL1 cause Marinesco-Sjögren syndrome, a cerebellar ataxia with cataract and myopathy. *Nat Genet*, 37(12):1312–4.
- Sharma, S., Chakraborty, K., Müller, B. K., Astola, N., Tang, Y.-C., Lamb, D. C., Hayer-Hartl, M., and Hartl, F. U. (2008). Monitoring protein conformation along the pathway of chaperonin-assisted folding. *Cell*, 133(1):142 – 153.
- Shiau, A. K., Harris, S. F., Southworth, D. R., and Agard, D. A. (2006). Structural analysis of *E. coli* Hsp90 reveals dramatic nucleotide-dependent conformational rearrangements. *Cell*, 127(2):329 – 340.
- Sigler, P. B., Xu, Z., Rye, H. S., Burston, S. G., Fenton, W. A., and Horwich, A. L. (1998). Structure and function in GroEL-mediated protein folding. *Annual Review of Biochemistry*, 67(1):581–608. PMID: 9759498.
- Southworth, D. and Agard, D. (2011). Client-loading conformation of the Hsp90 molecular chaperone revealed in the Cryo-EM structure of the human Hsp90:Hop complex. *Molecular Cell*, 42(6):771 – 781.
- Spurlino, J. C., Lu, G. Y., and Quijcho, F. A. (1991). The 2.3-Å resolution structure of the maltose- or maltodextrin-binding protein, a primary receptor of bacterial active transport and chemotaxis. *Journal of Biological Chemistry*, 266(8):5202–5219.
- Tokunaga, M., Imamoto, N., and Sakata-Sogawa, K. (2008). Highly inclined thin illumination enables clear single-molecule imaging in cells. *Nat Meth*, 5(2):159–161.
- Tomov, T., Tsukanov, R., Masoud, R., Liber, M., Plavner, N., and Nir, E. (2012). Disentangling subpopulations in single-molecule FRET and ALEX experiments with photon distribution analysis. *Biophysical Journal*, 102(5):1163 – 1173.
- Tyagi, S., VanDelinder, V., Banterle, N., Fuertes, G., Milles, S., Agez, M., and Lemke, E. A. (2014). Continuous throughput and long-term observation of single-molecule fret without immobilization. *Nat Meth*, 11(3):297–300.

- Vanhove, M., Usherwood, Y.-K., and Hendershot, L. M. (2001). Unassembled Ig heavy chains do not cycle from BiP in vivo but require light chains to trigger their release. *Immunity*, 15(1):105 – 114.
- Viterbi, A. (1967). Error bounds for convolutional codes and an asymptotically optimum decoding algorithm. *Information Theory, IEEE Transactions on*, 13(2):260–269.
- Wang, Z., Kriegs, H., and Wiegand, S. (2012). Thermal diffusion of nucleotides. *The Journal of Physical Chemistry B*, 116(25):7463–7469. PMID: 22663072.
- Wegele, H., Müller, L., and Buchner, J. (2004). *Reviews of Physiology, Biochemistry and Pharmacology*, chapter Hsp70 and Hsp90 - a relay team for protein folding, pages 1–44. Springer Berlin Heidelberg, Berlin, Heidelberg.
- Widengren, J., Kudryavtsev, V., Antonik, M., Berger, S., Gerken, M., and Seidel, C. A. M. (2006). Single-molecule detection and identification of multiple species by multiparameter fluorescence detection. *Analytical Chemistry*, 78(6):2039–2050.
- Widengren J., M. . (2002). *Single Molecule Detection in Solution: Methods and Applications*.
- Widengren J., Rigler R., M. . (1994). Triplet-state monitoring by fluorescence correlation spectroscopy. *Journal of Fluorescence*, 4(3):255–258.
- Widengren J., Mets Ü., R. R. (1995). Fluorescence correlation spectroscopy of triplet states in solution: A theoretical and experimental study. *J. Phys. Chem.*, 99(36):13368–13379.
- Winterstein, T., Staab, M., Nakic, C., Feige, H.-J., Vogel, J., and Schlaak, H. F. (2014). SU-8 electrothermal actuators: Optimization of fabrication and excitation for long-term use. *Micromachines*, 5(4):1310.
- Yamamoto, S., Subedi, G. P., Hanashima, S., Satoh, T., Otaka, M., Wakui, H., Sawada, K.-i., Yokota, S.-i., Yamaguchi, Y., Kubota, H., and Itoh, H. (2014). ATPase activity and ATP-dependent conformational change in the co-chaperone HSP70/HSP90-organizing protein (HOP). *Journal of Biological Chemistry*, 289(14):9880–9886.
- Yan, M., Li, J., and Sha, B. (2011). Structural analysis of the Sil1-BiP complex reveals the mechanism for Sil1 to function as a nucleotide-exchange factor. *Biochem J*, 438(3):447–55.
- Yang, J., Nune, M., Zong, Y., Zhou, L., and Liu, Q. (2015). Close and allosteric opening of the polypeptide-binding site in a human Hsp70 chaperone BiP. *Structure*, 23(12):2191 – 2203.



# Acknowledgments

An erster Stelle möchte ich mich ganz herzlich bei meinem Doktorvater, Prof. Don C. Lamb, bedanken. Du hast es mir ermöglicht, meine Doktorarbeit in Deiner Arbeitsgruppe zu schreiben und meine Ergebnisse auf zahlreichen Konferenzen zu präsentieren. Ich habe in der Zeit viel lernen dürfen und bei Dir immer ein offenes Ohr gefunden, wann immer sich ein neues wissenschaftliches Problem aufgetan hat. Vielen Dank für Deine Unterstützung!

Weiter möchte ich mich auch bei Prof. Christoph Bräuchle bedanken. Sie haben ein unfassbar breites wissenschaftliches Wissen, von dem unser ganzer Arbeitskreis in den vielen Diskussionen in den Montagsseminaren profitieren durfte. Vielen Dank, dass Sie sich ohne lange zu zögern bereit erklärt haben, mein Zweitgutachter zu werden.

Ich möchte mich auch bei Prof. Buchner bedanken. Mit Ihrem unglaublichen Fachwissen über Chaperone haben Sie in jedem Meeting zu BiP und BAP, aber auch Sti1, immer wieder neue Aspekte eingeworfen, die meine wissenschaftliche Arbeit bereichert haben und sich in dieser Doktorarbeit wiederfinden. Ich bin Ihnen sehr dankbar, dass ich Teil einer so ergiebigen Kollaboration sein durfte und Sie sich darüber hinaus bereit erklärt haben, ein Teil meiner Prüfungskommission zu sein.

Weiter möchte ich Prof. Hartl danken. Auch Sie haben sich direkt bereit erklärt, Teil der Prüfungskommission zu werden, obwohl Sie an dem Prüfungsgespräch selbst leider nicht teilnehmen können. Vielen Dank, dass Sie es ermöglicht haben, dass ich mit GroEL und GroES arbeiten konnte und ich für meine zusätzlichen Versuche Nachschub bekommen habe.

Natürlich möchte ich auch den weiteren Mitgliedern meiner Prüfungskommission, Herr Prof. Hartschuh und Frau Prof. de-Vivie-Riedle, herzlich danken, dass Sie sich die Zeit nehmen und meiner Prüfung beiwohnen.

Ich möchte hier auch die vielen Geldgeber meiner wissenschaftlichen Arbeit dankend erwähnen: den SFB 1035, NIM, CeNS und CIPSM. Ohne diese Unterstützung wäre das Microfluidic Projekt niemals realisiert worden und ich hätte keinen regen wissenschaftlichen Austausch auf den verschiedenen Konferenzen führen können.

Weiter möchte ich meinen Kooperationspartnern danken: Alina Röhl, Mathias Rosam, Christina Stutzer und Daniel Rutz. Vielen Danke, dass Ihr mich immer wieder mit neuem Protein versorgt habt und mit mir so rege und ergiebig über die Daten diskutiert habt.

Prof. Rädler, ich bin Ihnen sehr dankbar, dass ich Ihren Reinraum für die Herstellung der für die Microfluidic benötigten Wafer benutzen durfte. Vielen Dank auch an Philipp Altpeter und Charlott Leu. Danke, dass Ihr mir so viel erklärt habt und dass Ihr nicht aufgegeben habt. Nach den vielen Versuchen war es dann doch endlich möglich, zwei gute Wafer herzustellen. Weiter möchte ich auch Rafal Krzyszton dafür danken, dass er seine Erfahrungen mit der Microfluidic und vor allem mit der Durchflusskontrolle mit mir geteilt hat. Ich habe viel Zeit dadurch gespart, dass ich Deinem Tipp mit dem Durchflusskontrollsystem gefolgt bin.

Nicht vergessen möchte ich aber auch den ganzen Arbeitskreis der Professoren Lamb und Bräuchle. Ich hatte eine tolle Zeit bei Euch mit vielen wissenschaftlich relevanten Diskussionen und manchmal auch einfach nur netten Gesprächen.

Aber der Reihe nach: zu aller erst möchte ich Dir, Jens, danken. Du bist in den letzten

drei Jahren ein guter Freund geworden und hast mir immer mit einem offenen Ohr und zahlreichen Tipps geholfen. Und natürlich nicht zu vergessen, Du hast diese ganze Arbeit korrigiert. Danke auch für all die gemeinsamen Teepausen, am Anfang noch mit Euch, Aurelie und Niko, dann wurde Vroni ein fester Bestandteil der "Tee-Gruppe" und zuletzt sind nur wir zwei von dem morgendlichen Ritual übrig geblieben. Euch allen vielen Dank für die erheiternden Themen und so manches Lachen. An Dich, Niko, an dieser Stelle noch ein dickes Danke: Wenn du mich vor dreieinhalb Jahren nicht verwirrt auf dem Flur eingesammelt hättest, dann wäre ich vermutlich niemals ein Teil von dieser Gruppe geworden, weil ich nicht mal den Raum für meine Vorstellung gefunden hätte.

Weiter möchte ich auch Dir, Lena, danken. Du hast mir immer mit Rat und Tat zur Seite gestanden. Wenn mein Protein "komische Sachen" gemacht hat oder ich ein Problem im Biolab hatte, dann wusstest Du immer eine Antwort.

Danke auch an euch, Jelle und Anders, dass Ihr mir zusammen mit Waldi bei all meinen Setup-Fragen zur Seite gestanden seid und mir erklärt haben, wie ich meine MFD-Daten richtig auswerten muss.

Nicht zuletzt möchte ich Ganesh danken. Ohne Dich hätte ich nie das DM-MBP messen können. Du hast ein beeindruckendes Literaturwissen und ich bin Dir dankbar, dass Du mich daran hast teilhaben lassen. Danke, dass Du zusammen mit mir die Microfluidic-Messungen gemacht hast.

Und natürlich möchte ich auch all den anderen ehemaligen und aktuellen Mitgliedern des AK Lamb und Bräuchle danken. Ihr habt mir in vielen großen und kleinen Dingen geholfen und es erst ermöglicht, dass ich mich hier wohl gefühlt habe und in eine so gute Atmosphäre aufgenommen wurde.

Als letzten aus den beiden Arbeitskreisen möchte ich noch Dir, Moritz, danken für Deine Hilfe bei so manch einer Anschaffung, bei Problemen mit der Reisekostenrückerstattung und Hilfe in jeder Lebenslage.

Ich möchte hier noch ein herzliches Dankeschön an meine Familie und Freunde sagen, die immer an mich geglaubt und mich stets unterstützt haben. Die meisten von Euch sind zwar weit weg, aber trotzdem wusste ich die ganze Zeit, dass ich mich auf Euch verlassen kann.

Zu guter Letzt möchte ich mich noch bei Dir, Daniel, bedanken. Ohne Dich und Deine stete Unterstützung hätte ich die letzten Monate nicht geschafft. Ich weiß, dass es nicht immer einfach war, wenn sich wieder alles nur um diese Arbeit gedreht hat, aber Du hast mir trotz allem immer gut zugehört. Danke, dass Du so ein wichtiger Teil in meinem Leben geworden bist.